

# Optimization of the Beam Screen for the FCC Injection Kicker Magnets

Thèse N° 8079

Présentée le 10 décembre 2019  
à la Faculté des sciences de base  
Laboratoire de physique des accélérateurs de particules  
Programme doctoral en physique

pour l'obtention du grade de Docteur ès Sciences

par

**Agnieszka CHMIELIŃSKA**

Acceptée sur proposition du jury  
Prof. F. Carbone, président du jury  
Prof. L. Rivkin, Dr M. J. Barnes, directeurs de thèse  
Dr G. Rumolo, rapporteur  
Dr S. Calatroni, rapporteur  
Dr M. Paraliiev, rapporteur

2019





Nothing in life is to be feared, it is only to be understood.  
Now is the time to understand more, so that we may fear less.  
— Marie Skłodowska-Curie

To my family and friends...



# Acknowledgements

This was a long and challenging journey. However, at the end of my work I feel very satisfied and extremely lucky to have had the chance to carry out doctoral studies at CERN and EPFL. I would like to thank all the people who have helped and supported me during this time.

First and foremost, I would like to thank Mike Barnes for accepting me to carry out the PhD under his supervision. His experience in the field of kicker magnets and his guidance throughout my research studies were vital for this work. During these three years he has always shown great support and patience. He always had time for my questions and made this journey an enjoyable one. Also, he pushed me to grow as a scientist by posing many open-ended questions and motivating me to answer them.

I would like to express my sincere gratitude to my thesis director, Prof. Leonid Rivkin. He gave me this unique opportunity to carry out my doctoral studies at EPFL. I am very grateful for his support, encouragement and advice throughout my PhD.

I would like to extend my thanks to Fabrizio Carbone (EPFL, President of the jury), Giovanni Rumolo (CERN), Sergio Calatroni (CERN) and Martin Paraliev (PSI) for accepting to be the members of the examining committee, and for their useful comments on my thesis work.

To Giovanni Rumolo I am also very grateful for providing valuable feedback on my project during my stay at CERN. His suggestions and ideas were always of great help.

I would like to thank my group leader Brennan Goddard and my section leader Thomas Kramer for creating opportunities for me to participate in many schools and conferences, where I could learn and share my work.

The work presented here would not have been possible without the help of many colleagues. A special thanks I would like to give to Fritz Caspers. During my PhD, he has always shown great willingness to share his knowledge and experience with me. I really appreciated his support during measurements, many valuable life lessons and inspiring coffee discussions.

A big thank you goes to Branko Kosta Popovic. It was a great pleasure working with him, he was always making my days more enjoyable and became a true friend. Also, I thank Christine Vollinger and Aaron Farricker for always being available and willing to share their expertise.

The spiral beam screen measurements would not have been possible without several people. First, I would like to thank Wim Weterings for his enthusiasm and commitment to test the prototype. Also, I am very grateful to Laurent Ducimetière for his great support of this idea. A special thanks goes to Salim Bouleghlimat, Gael Bellotto and Yves Sillanoli for the preparation

## Acknowledgements

---

of the measurement setup. In addition, I would like to thank Vasileios Vlachodimitropoulos for performing measurements on the LHC MKI with me and for his input during my PhD.

I would like to express my sincere gratitude to Alexandre Lasheen. I really appreciated his time for many interesting discussions about longitudinal beam dynamics, as well as his support and advice on different matters. Furthermore, I thank Elena Shaposhnikova and Ivan Karpov for their valuable input into my studies.

Throughout my PhD at CERN I was able to profit from the experience and knowledge of many ABP colleagues. I would like to thank Sergey Arsenyev and Carlo Zannini for always being available for me, as well as to Benoît Salvant for always providing valuable remarks on my project. To Elias Métral for his advice and openness.

I would like to thank the BTP section colleagues, especially to Wolfgang Bartman and Florian Burkart for their helpful input regarding the optimization of the FCC injection kicker system.

I am grateful to Nicolas Magnin for his supervision and help in developing Python tools for the LHC MKI. This project was a great experience for me and allowed me to attain new skills.

The essential part of my work required high performance computing resources. I am very thankful to IT colleagues, especially to Maria Alandes Pradillo and Pablo Llopis Sanmillan for great collaboration when setting up a new cluster. They both made a lot of effort to help me run my simulations. In this context, I am also grateful to Micha Dehler from PSI for his help and kindly recognising me in Melbourne.

I am indebted to my septa colleagues for making me feel included and smiling every day, especially to Alejandro Sanz Ull, Louise Olivia Jorat, Miroslav Atanasov, Ole-Kristian Berge and Michael Hourican. A special thanks I would like to give to Jan Borburgh for his great support during my PhD.

Also, I would like to thank Mauro Tadorelli for always supporting me during my stay at CERN.

Finally, I would like to thank all of my friends, not mentioned before, for accompanying me in this journey and the time spent together inside and outside of CERN, especially to Christoph Wiesner, Oskar Björkqvist, Eino Juhani Oltedal, Elisa Garcia-Tabares Valdivieso, Luis Gonzalez, Alban Sublet, Joël Repond and Michael Schenk. A big thanks to Janne Holma for sharing his passion for cross-country skiing. Also, to David Woog, Martin Geppert and Matthew Fraser for motivating me to new challenges – I am really, really looking forward to my first Ironman 70.3!

To my parents, Teresa and Adam, I would like to thank for their unconditional support, which I was receiving every day.

My greatest thank I want to give to Michał for all his love, endless support and faith in me. Also, I thank him for sharing with me his passion to mountains and all the great times spent in the Jura, the French and Swiss Alps and the Pyrenees doing triathlon and cross-country skiing.

*Grindelwald, September 2019*

Agnieszka

# Abstract

The Future Circular Collider for hadrons (FCC-hh) is a proposed high-energy frontier particle accelerator, which would be built in a new  $\sim 100$  km circumference tunnel and would enable proton-proton collisions at a centre-of-mass energy of 100 TeV. The baseline injection energy is 3.3 TeV. The FCC-hh will require a fast injection kicker system that is highly reliable and does not limit accelerator performance. To achieve low ripple and fast rise and fall time field pulses, the injection system will use ferrite loaded transmission line type magnets. The FCC-hh will operate at high beam intensity: hence, the beam coupling impedance will be an issue. The problems are twofold: longitudinal and transverse impedance may drive beam instabilities, while the real part of the longitudinal impedance gives rise to beam induced heating. The power deposition in the kicker magnet can cause a temperature increase of the ferrite yoke above its Curie point: this would affect the ability to inject beam. For a high beam current and a short bunch length, a high power deposition would occur in unshielded FCC-hh injection kicker magnets: hence, a beam screen is a critical feature. Amongst the most challenging requirements for the beam screen are: low broadband beam coupling impedance, fast field rise and fall time, low field ripple during the flat-top field and good high voltage behaviour. In this thesis, we propose and develop a novel concept of a spiral beam screen. The fundamental advantage of the new design, in comparison to the conventional straight screen conductors used for example in the LHC injection kickers, is a significant reduction of the maximum voltage induced on the conductors, thus a greatly reduced probability of an electrical breakdown of the beam screen. Also, the spiral screen design allows a reduction of the maximum transverse beam coupling impedance of the kicker system. Both the conventional and spiral designs are studied from a theoretical, a numerical, and an experimental point of view. Important new contributions brought to the field of kicker magnets include: real-time data analysis of the output waveform of the LHC kicker magnet to ensure the ferrite yoke is below its Curie point; a new CST and PSpice model of the FCC-hh injection kicker magnets; proposal and development of new calculation and measurement methods for determining power loss distribution in the ferrite of a kicker magnet; and novel measurements of the electromagnetic properties of ferrites as a function of frequency and temperature.

**Keywords:** Future Circular Collider, LHC, injection kicker systems, kicker magnets, PSpice, beam screen, spiral, beam coupling impedance, beam induced heating, beam instability, EM simulations, CST Particle Studio, Opera 2D, impedance measurements, power deposition distribution, EM characterization of ferrites.



# Résumé

Le FCC-hh (Future Circular Collider for hadrons) est une proposition d'accélérateur de particules à la frontière des hautes-énergies, qui serait construit dans un nouveau tunnel de  $\sim 100$  km de circonférence et permettrait des collisions proton-proton à une énergie centrale de masse de 100 TeV. L'énergie d'injection prévue est de 3.3 TeV. Le FCC-hh nécessitera un système d'aimants d'injection rapides d'une grande fiabilité et qui ne limite pas les performances de l'accélérateur. Pour obtenir des impulsions magnétiques avec une faible ondulation et des temps de montée et de descente rapides, le système d'injection utilisera des aimants de type ligne de transmissions (kickers) dont le circuit magnétique est constitué de ferrites. Le FCC-hh fonctionnera avec un faisceau de haute intensité : par conséquent, l'impédance de couplage du faisceau avec ces aimants sera problématique. Le problème est double : d'un part les impédances longitudinale et transversale peuvent entraîner des instabilités du faisceau, et d'autre part la partie réelle de l'impédance longitudinale donne lieu à un échauffement des ferrites induit par le faisceau. Cet échauffement peut conduire au dépassement du point de Curie des ferrites, ce qui affecte la capacité d'injecter le faisceau. Pour un faisceau de courant élevé et constitué de paquets courts, le dépôt de puissance dans les aimants kickers d'injection non protégés du FCC-hh serait très élevé. Pour cette raison, un écran de faisceau est un élément critique. Parmi les exigences requises pour l'écran de faisceau, les plus difficiles sont : une faible impédance de couplage avec le faisceau, une bonne préservation des temps de montée et de descente et du faible taux d'ondulation du champ magnétique, ainsi qu'un bon comportement à haute tension. Dans cette thèse, nous proposons et développons un nouveau concept d'écran de faisceau avec conducteurs hélicoïdaux. L'avantage fondamental de cette nouvelle conception, par rapport aux écrans conventionnels dont les conducteurs sont droits, utilisés par exemple dans les kickers d'injection du LHC, est une réduction significative de la tension maximale induite sur les conducteurs. La probabilité d'un claquage électrique au niveau de l'écran du faisceau est ainsi considérablement réduite. En outre, l'écran hélicoïdal permet une réduction du maximum de l'impédance de couplage transversale du faisceau des aimants kickers. Les conceptions conventionnelle et hélicoïdale sont étudiées d'un point de vue théorique, numérique et expérimental. Parmi les nouvelles contributions importantes apportées au domaine des aimants kickers, nous pouvons mentionner : l'analyse en temps réel des données de la forme d'impulsion produite par l'aimant kicker du LHC pour assurer que la température des ferrites reste inférieure au point Curie ; un nouveau modèle CST et PSpice des aimants kickers d'injection du FCC-hh ; la proposition et mise au point de nouvelles méthodes de calcul et de mesure pour déterminer la distribution des pertes de puissance dans

## Acknowledgements

---

les ferrites d'un aimant kicker ; de nouvelles mesures des propriétés électromagnétiques des ferrites en fonction de la fréquence et de la température.

**Mots clefs :** Futur Collisionneur Circulaire, LHC, système d'aimants d'injection, aimants kickers, PSpice, écran de faisceau, hélicoïdal, impédance de couplage de faisceau, échauffement induit par le faisceau, instabilité du faisceau, simulations EM, CST Particle Studio, Opera 2D, mesures d'impédance, distribution de dépôt de puissance, caractérisation EM des ferrites.



# Contents

<b>Acknowledgements</b>	<b>v</b>
<b>Abstract</b>	<b>vii</b>
<b>List of figures</b>	<b>xxi</b>
<b>List of tables</b>	<b>xxiii</b>
<b>List of symbols</b>	<b>xxv</b>
<b>Acronyms</b>	<b>xxxvi</b>
<b>1 Introduction</b>	<b>1</b>
1.1 The Future Circular Collider for hadrons . . . . .	2
1.1.1 Baseline design . . . . .	2
1.1.2 Baseline parameters . . . . .	3
1.2 Motivation and objectives of this thesis . . . . .	3
<b>2 Theoretical foundation</b>	<b>9</b>
2.1 Linear beam dynamics . . . . .	9
2.1.1 Betatron motion . . . . .	10
2.1.2 Synchrotron motion . . . . .	11
2.2 Wake function and beam coupling impedance . . . . .	12
2.2.1 Longitudinal direction . . . . .	14
2.2.2 Transverse planes . . . . .	19
2.2.3 Resonator model . . . . .	20
2.2.4 The Panofsky-Wenzel theorem . . . . .	21
2.2.5 Effect on beam dynamics . . . . .	21
2.3 Basic electromagnetic theory . . . . .	23
<b>3 Fast pulsed kicker systems in particle accelerators at CERN</b>	<b>27</b>
3.1 General overview . . . . .	27
3.1.1 Single turn injection . . . . .	27
3.1.2 Technological aspects . . . . .	27
3.1.3 Kicker magnet aperture . . . . .	28
	xi

3.1.4	Transmission line topology . . . . .	29
3.1.5	Beam coupling impedance considerations . . . . .	31
3.2	Injection kicker magnets of the Large Hadron Collider (LHC MKI) . . . . .	31
3.2.1	LHC injection kicker system parameters . . . . .	31
3.2.2	Conventional beam screen design . . . . .	33
3.2.3	High voltage issues . . . . .	34
3.2.4	Heating problems . . . . .	36
3.3	Analysis of thermal data and the LHC MKI waveforms . . . . .	37
3.3.1	Soft Start . . . . .	37
3.3.2	PyMKITemp . . . . .	38
3.3.3	PyMKISS . . . . .	42
3.3.4	Achievements . . . . .	42
<b>4</b>	<b>Design of the injection kicker magnet for FCC-hh</b>	<b>45</b>
4.1	The FCC-hh injection system at 3.3 TeV . . . . .	45
4.1.1	Injection layout . . . . .	46
4.1.2	Optimization of the injection kicker system . . . . .	46
4.2	Beam coupling impedance of the unshielded kicker . . . . .	51
4.2.1	FCC beam spectrum . . . . .	51
4.2.2	Tsutsui model . . . . .	53
4.2.3	Power deposition in an unshielded kicker . . . . .	54
4.3	Design of the injection kicker magnet . . . . .	56
4.3.1	PSpice simulations . . . . .	56
4.3.2	Equivalent circuit . . . . .	57
4.3.3	Field flat-top quality assessment . . . . .	58
4.3.4	Optimization of the kicker magnet module . . . . .	59
4.3.5	20-cell kicker magnet module . . . . .	59
<b>5</b>	<b>Beam coupling impedance of the FCC injection kicker magnet</b>	<b>63</b>
5.1	CST Studio Suite . . . . .	63
5.2	Computing resources at CERN . . . . .	65
5.3	Conventional beam screen: initial design . . . . .	65
5.3.1	Dispersive materials modelling . . . . .	67
5.3.2	Longitudinal beam coupling impedance . . . . .	67
5.3.3	Total power loss . . . . .	68
5.3.4	Power deposition distribution . . . . .	69
5.3.5	Investigation of the simplified model and the cut-down model . . . . .	74
5.3.6	Impact of the ferrite rings . . . . .	75
5.3.7	The low frequency mode . . . . .	76
5.4	Optimization of the conventional beam screen . . . . .	77
5.4.1	Overlap length reduction . . . . .	77
5.5	Spiral beam screen . . . . .	80
5.5.1	New concept . . . . .	80

5.5.2	Induced voltage analysis . . . . .	81
5.5.3	Longitudinal beam coupling impedance . . . . .	82
5.5.4	Optimization process . . . . .	83
5.6	Impact on longitudinal beam stability . . . . .	86
5.6.1	Coupled bunch instability . . . . .	86
5.6.2	Loss of Landau damping . . . . .	88
5.7	Transverse beam coupling impedance . . . . .	89
5.7.1	Wakefield simulations . . . . .	89
5.7.2	Eigenmode simulations . . . . .	89
5.7.3	Results . . . . .	90
5.7.4	Transverse impedance budget considerations . . . . .	93
<b>6</b>	<b>Impact of a beam screen upon the field response of the kicker magnet</b>	<b>95</b>
6.1	General considerations . . . . .	95
6.1.1	Beam screen with longitudinal or spiral screen conductors . . . . .	95
6.1.2	Beam screen with continuous coating . . . . .	96
6.2	Opera-2D . . . . .	97
6.3	Unshielded kicker magnet . . . . .	97
6.3.1	Opera-2D model . . . . .	98
6.3.2	Frequency dependent inductance and resistance . . . . .	99
6.3.3	Field homogeneity . . . . .	102
6.3.4	Field rise time . . . . .	103
6.4	FCC injection kicker magnet with a beam screen . . . . .	104
6.4.1	Opera-2D model . . . . .	104
6.4.2	Frequency dependent inductance . . . . .	104
6.4.3	Estimate of power dissipation due to the beam image current and eddy currents . . . . .	108
6.4.4	Field homogeneity . . . . .	108
6.4.5	PSpice equivalent circuit . . . . .	109
6.4.6	Benchmark simulations of field-rise time and field flat-top quality . . . . .	112
<b>7</b>	<b>Experimental validation of predictions using LHC MKI</b>	<b>115</b>
7.1	Single wire measurement techniques . . . . .	115
7.1.1	Classical method . . . . .	115
7.1.2	Resonant method . . . . .	116
7.2	Longitudinal impedance of the conventional beam screen . . . . .	118
7.2.1	Experimental setup . . . . .	118
7.2.2	Results . . . . .	119
7.3	Novel power deposition distribution measurements . . . . .	120
7.3.1	Measurement method . . . . .	121
7.3.2	Experimental setup . . . . .	121
7.3.3	Results . . . . .	122
7.4	Benchmark measurements of the spiral beam screen . . . . .	124

## Contents

---

7.4.1	Prototype . . . . .	124
7.4.2	CST model . . . . .	126
7.4.3	Experimental setup . . . . .	126
7.4.4	Results . . . . .	128
<b>8</b>	<b>Characterization of electromagnetic properties of ferrites</b>	<b>131</b>
8.1	Specification of magnetic materials for pulsed kicker magnets . . . . .	131
8.2	Electromagnetic characterization of materials . . . . .	132
8.3	Transmission method . . . . .	133
8.4	Short-circuit line method . . . . .	135
8.5	Results . . . . .	135
8.5.1	Measurements at room temperature . . . . .	136
8.5.2	Heated sample measurements . . . . .	137
8.6	Importance of the results . . . . .	140
<b>9</b>	<b>Conclusions</b>	<b>141</b>
9.1	Summary of work achievements . . . . .	141
9.2	Scientific contributions . . . . .	145
9.3	Recommendations for future research . . . . .	146
<b>A</b>	<b>The Panofsky-Wenzel theorem</b>	<b>147</b>
<b>B</b>	<b>PSpice macros and goal functions</b>	<b>149</b>
<b>C</b>	<b>Prototype spiral beam screen</b>	<b>151</b>
	<b>Bibliography</b>	<b>161</b>
	<b>Curriculum Vitae</b>	

# List of Figures

1.1	Baseline location of the FCC. . . . .	3
1.2	Conceptual layout of the FCC. . . . .	3
2.1	Curvilinear coordinate system to describe particle motion in circular accelerators.	9
2.2	Schematic drawing of the bunch passing through the accelerator component [28]. If the beam pipe is smooth and perfectly conducting (left), there are no fields induced. However, a discontinuity in the structure (right) causes wake fields to be generated. . . . .	13
2.3	The reference system with two point charges travelling parallel to each other with the constant velocity $\vec{v}$ . The test particle $q$ is at the distance $z$ behind the source particle $q_1$ . . . . .	13
2.4	Schematic drawing of the longitudinal bunch distribution $\lambda(s)$ . The witness slice (red) is affected by the wake function $W_{  }(s - s_1)$ generated by the source slice (green). . . . .	16
3.1	Diagram of a single turn injection (reproduced from Ref. [49]). The deflection angle provided by the septum and kicker is denoted by $\Theta_{\text{septum}}$ and $\Theta_{\text{kicker}}$ , respectively. . . . .	28
3.2	Schematic diagram of the kicker system. . . . .	28
3.3	Cross section of C-core kicker magnet. . . . .	29
3.4	Simplified equivalent electric circuit of a transmission line kicker magnet. . . .	29
3.5	Build-up of the magnetic flux inside the kicker magnet. . . . .	30
3.6	Drawing of the LHC MKI cross-section [51]. . . . .	32
3.7	Photograph of the upstream end of the LHC MKI. . . . .	32
3.8	Photograph of the prototype LHC MKI during assembly. . . . .	32
3.9	Photograph of the upstream end of the beam screen with capacitively coupled screen conductors. . . . .	33
3.10	Photograph of the downstream end of the beam screen with grounded screen conductors connected all together. . . . .	33
3.11	LHC MKI beam screen at the upstream end of the kicker magnet (CATIA model).	34
3.12	Screen conductors inside the kicker magnet aperture. . . . .	35
3.13	Magnet voltage and voltage of screen conductor adjacent to HV busbar (for 60 kV PFN voltage) [56]. . . . .	35

## List of Figures

---

3.14	Maximum conductor and inter-conductor voltages (for 60 kV PFN voltage) [56].	35
3.15	Example of filtered SS data for MKI8D (collected for 1 month of LHC operation). A single SS is indicated in the black rectangular window (zoomed in Fig. 3.16).	40
3.16	MKI8D parameters during a single SS. The temperature is interpolated at IPOC timestamps (grey dots).	40
3.17	Temperature measurements at the upstream end of MKI8D with respect to time.	40
3.18	Average rise time at TMR during each SS with respect to time (MKI8D).	41
3.19	Average rise time at TMR versus average temperature during each SS (MKI8C).	41
3.20	Average delay time versus average temperature during each SS (MKI8C).	41
4.1	Schematic layout of the FCC double plane injection system.	46
4.2	Schematic drawing of the IA [75].	48
4.3	Magnetic flux density in the magnet aperture as a function of the effective length.	49
4.4	Current as a function of the magnetic flux density (effective length of 20 and 30 m for a 32 mm and 48 mm aperture, respectively).	50
4.5	Ideal beam spectrum of equally spaced bunches ( $\sigma_{\text{RMS}} = 0.08$ m, bunch spa- cing: 25 ns)	52
4.6	Zoom at main lines in the beam spectrum shown in Fig. 4.5 occurring every 40 MHz.	52
4.7	FCC beam spectrum including gaps for the kicker rise time ( $\sigma_{\text{RMS}} = 0.08$ m, bunch spacing: 25 ns).	53
4.8	Zoom at main lines in the beam spectrum shown in Fig. 4.7 occurring every 40 MHz.	53
4.9	Zoom at the side-band harmonics occurring every 0.41 MHz due to the gaps for the kicker field rise time.	53
4.10	Tsutsui model of the unshielded kicker magnet.	54
4.11	Relative complex permeability of ferrite 8C11 [85].	55
4.12	Longitudinal impedance per unit length of unshielded kicker (analytic calcula- tion), for aperture dimensions of $32 \times 32$ mm and $48 \times 48$ mm, together with the FCC nominal beam spectrum.	55
4.13	Equivalent circuit of the transmission line kicker magnet - detailed schematic.	57
4.14	Schematic diagram of the kicker magnet waveform. The flat-top ripple excur- sions outside of the acceptance limits are marked in red.	58
4.15	Magnetic field flat-top FOM as a function of $R_{\text{cell}}$ investigated for different num- ber of cells (see Table 4.3).	59
4.16	Normalized magnetic flux as a function of time for different $R_{\text{cell}}$ ( $C_{\text{cell}} = 2.84$ nF, $C_{\text{in}} = C_{\text{out}} = 1.42$ nF, $L_{\text{cell}} = 111$ nH and $L_{\text{end}} = 126$ nH). All waveforms are crossing $\pm 0.5\%$ threshold of the normalized magnetic flux at $\sim 15$ ns.	60
4.17	Normalized magnetic flux as a function of time for different $C_{\text{out}}$ ( $R_{\text{cell}} = 23 \Omega$ , $C_{\text{cell}} = 2.84$ nF, $C_{\text{in}} = 1.42$ nF, $L_{\text{cell}} = 111$ nH and $L_{\text{end}} = 126$ nH). All waveforms are crossing $\pm 0.5\%$ threshold of the normalized magnetic flux at $\sim 15$ ns.	61

4.18 Normalized magnetic flux in the optimized configuration of a 20-cell FCC injection kicker magnet ( $R_{\text{cell}} = 25.5 \, \Omega$ , $C_{\text{cell}} = 2.84 \, \text{nF}$ , $C_{\text{in}} = 1.42 \, \text{nF}$ , $C_{\text{out}} = 1.82 \, \text{nF}$ , $L_{\text{cell}} = 111 \, \text{nH}$ and $L_{\text{end}} = 126 \, \text{nH}$ ). . . . .	61
5.1 FCC injection kicker magnet with the conventional beam screen (full model). .	66
5.2 Magnet upstream end (zoom). . . . .	66
5.3 Magnet downstream end (zoom). . . . .	66
5.4 Real part of the longitudinal beam coupling impedance of the FCC injection kicker magnet with the initial beam screen design (full model) together with the FCC beam spectrum. . . . .	68
5.5 Imaginary part of the longitudinal beam coupling impedance of the FCC injection kicker magnet with the initial beam screen design (full model). . . . .	68
5.6 Decay of the longitudinal wake potential ( $WL = 500 \, \text{m}$ ) . . . . .	68
5.7 Real part of the longitudinal beam coupling impedance of the FCC injection kicker magnet with the initial beam screen design: original data is compared with the worst case scenario model assuming that first fundamental harmonic is at 880 MHz or at 920 MHz. . . . .	69
5.8 Power loss at different frequencies. . . . .	71
5.9 Cumulative power loss. . . . .	71
5.10 Comparison of the FCC injection kicker magnet power deposition distribution calculated using CST power loss monitors at selected $f_0$ multiples and at 40 MHz multiples. . . . .	72
5.11 Comparison of the FCC injection kicker magnet power deposition distribution calculated using data-sheet of magnetic properties at ambient temperature and measured magnetic properties at 150°C. . . . .	73
5.12 Real part of the longitudinal beam coupling impedance of the FCC injection kicker magnet taking into account temperature dependence of magnetic properties. . . . .	73
5.13 Real part of the longitudinal beam coupling impedance of the initial beam screen design evaluated for the full model, the simplified model and the cut-down model. .	74
5.14 Real part of the longitudinal beam coupling impedance of the initial beam screen design with ferrite rings placed at both ends of the beam screen in comparison with ferrite rings placed only at the downstream or the upstream end (simplified model). . . . .	75
5.15 Real part of the longitudinal beam coupling impedance of the initial beam screen design along with modified designs (cut-down model). . . . .	77
5.16 Real part of the longitudinal beam coupling impedance for different $L_{\text{overlap}}$ , investigated on the simplified model with graded screen conductors. . . . .	78
5.17 Cumulative power loss for different $L_{\text{overlap}}$ (graded conductors). . . . .	78
5.18 Total power loss as a function of $L_{\text{overlap}}$ (graded conductors). . . . .	78
5.19 Real part of the longitudinal beam coupling impedance for different $L_{\text{overlap}}$ investigated on the simplified model with ungraded screen conductors. . . . .	79

## List of Figures

---

5.20 Cumulative power loss for different $L_{\text{overlap}}$ (no grading). . . . .	79
5.21 Total power loss as a function of $L_{\text{overlap}}$ (no grading). . . . .	79
5.22 Schematic of a single spiral conductor. . . . .	80
5.23 Cross-section of the beam screen. . . . .	81
5.24 Spiral beam screen (cut-down model). . . . .	82
5.25 Real part of the longitudinal beam coupling impedance of the spiral beam screen in comparison with the conventional design, evaluated on the cut-down model with ungraded screen conductors, a non-symmetric vacuum gap and $L_{\text{overlap}} = 56$ mm. . . . .	83
5.26 Spiral beam screen with ungraded screen conductors, a symmetric vacuum gap and $L_{\text{overlap}} = 44$ m (simplified model). . . . .	84
5.27 Initial design of the conventional beam screen with graded screen conductors, a non-symmetric vacuum gap and $L_{\text{overlap}} = 56$ mm (simplified model). . . . .	84
5.28 Spiral beam screen with screen conductors connected together in the overlap region, a symmetric vacuum gap and $L_{\text{overlap}} = 44$ mm (simplified model). . . . .	85
5.29 Real part of the longitudinal impedance of the spiral beam screen with a symmetric vacuum gap, ungraded screen conductors and $L_{\text{overlap}} = 44$ mm in comparison with the initial design of the conventional beam screen (simplified model). . . . .	86
5.30 Cumulative power loss for the spiral beam screen of different number of turns, with ungraded screen conductors, a symmetric vacuum gap and $L_{\text{overlap}} = 44$ mm in comparison with the initial design of the conventional beam screen (simplified model). . . . .	86
5.31 Threshold for the longitudinal coupled bunch instability as a function of resonant frequency. The frequency ranges at which we expect resonances for different beam screen designs are indicated in rectangular windows (in grey). . . . .	87
5.32 $\text{Im}(Z_{  }/n)$ as a function of frequency for different beam screen designs. . . . .	88
5.33 Spectral power densities of Gaussian and parabolic bunch for $m = 0$ and $m = 1$ . . . . .	89
5.34 Real part of the horizontal dipolar transverse impedance of the conventional beam screen with a non-symmetric vacuum gap and $L_{\text{overlap}} = 56$ mm (simplified model). . . . .	91
5.35 Electric field distributions at a) 20 MHz and b) 61 MHz. . . . .	91
5.36 Real part of the horizontal quadrupolar transverse impedance of the conventional beam screen with a non-symmetric vacuum gap and $L_{\text{overlap}} = 56$ mm (simplified model). . . . .	92
5.37 Real part of the horizontal dipolar transverse impedance of a spiral with 3 turns, a symmetric vacuum gap and $L_{\text{overlap}} = 44$ mm (simplified model). . . . .	92
5.38 Electric field distribution at 193 MHz (spiral beam screen with 3 turns). . . . .	93
5.39 Real part of the horizontal quadrupolar transverse impedance of a spiral with 3 turns, a symmetric vacuum gap and $L_{\text{overlap}} = 44$ mm (simplified model). . . . .	93
5.40 Comparison of the real part of the horizontal dipolar transverse impedance of the spiral with 1 and 3 turns, a symmetric vacuum gap and $L_{\text{overlap}} = 44$ mm (simplified model). . . . .	94



6.1	Geometry of the unshielded kicker magnet (Opera-2D model). Due to the top-bottom symmetry only the upper part is modelled. The specific properties of materials are marked with different colours, i.e. conductor (colour red), ferrite (colour blue), free space (colour grey) and the individual regions into which the entire model is divided are numbered. . . . .	98
6.2	Mesh grid required for simulations up to 5 MHz (zoom of part of HV conductor). . . . .	99
6.3	Current density at 10 Hz (unshielded kicker magnet). . . . .	99
6.4	Current density at 1 MHz (unshielded kicker magnet). . . . .	99
6.5	Lines of magnetic flux at 10 Hz (unshielded kicker magnet). . . . .	100
6.6	Lines of magnetic flux at 1 MHz (unshielded kicker magnet). . . . .	100
6.7	Relative magnetic flux density in aperture of the kicker magnet plotted along the $x$ -axis for $y = \{0, 4, 8\}$ mm at both 10 Hz and 1 MHz. . . . .	100
6.8	Predicted inductance as a function of frequency evaluated for (a) the entire model of an unshielded kicker magnet, (b) with the internal inductance of busbars excluded and (c) only the internal inductance of busbars. . . . .	101
6.9	Field homogeneity in the aperture of an unshielded FCC injection kicker magnet at $0.43 \mu\text{s}$ (i.e. at the beginning of the flat-top), w.r.t. $B_0$ at $2.43 \mu\text{s}$ . . . . .	103
6.10	Field homogeneity in the aperture of an unshielded FCC injection kicker magnet at $2.43 \mu\text{s}$ (i.e. at the end of the flat-top), w.r.t. $B_0$ at $2.43 \mu\text{s}$ . . . . .	103
6.11	Geometry of the kicker magnet with a beam screen (Opera-2D model). Due to the top-bottom symmetry only the upper part is modelled. The individual regions are numbered. . . . .	104
6.12	Current density at 10 Hz (shielded kicker magnet). . . . .	105
6.13	Current density at 5 MHz (shielded kicker magnet). . . . .	105
6.14	Magnetic flux lines at 10 Hz (shielded kicker magnet). . . . .	105
6.15	Magnetic flux lines at 5 MHz (shielded kicker magnet). . . . .	105
6.16	Relative magnetic flux density in the aperture of the kicker magnet with a beam screen plotted along the $x$ -axis for $y = \{0, 4, 8\}$ mm, both at 10 Hz and 5 MHz. . . . .	106
6.17	Cell inductance, excluding internal inductance of busbars, as a function of frequency for the FCC injection kicker magnet, with a beam screen, analyzed for different material, width and thickness of the screen conductors. . . . .	107
6.18	Predicted field homogeneity in the aperture of the FCC injection kicker magnet with a beam screen composed of 24 screen conductors (Cu coating, $30 \mu\text{m}$ thickness, $1.3 \text{ mm}$ width) at $0.43 \mu\text{s}$ (i.e. at the beginning of the flat-top). . . . .	109
6.19	Predicted field homogeneity in the aperture of the FCC injection kicker magnet with a beam screen composed of 24 screen conductors (Cu coating, $30 \mu\text{m}$ thickness, $1.3 \text{ mm}$ width) at $2.43 \mu\text{s}$ (i.e. at the end of the flat-top). . . . .	109
6.20	Frequency dependent inductance and resistance of the FCC injection kicker magnet with a beam screen composed of 24 Cu screen conductors ( $30 \mu\text{m} \times 1.3 \text{ mm}$ ). Opera-2D data is compared with the fit of the equivalent circuit obtained using PSpice Optimizer. . . . .	110

## List of Figures

---

6.21	Equivalent circuit of the frequency dependent inductance composed of four building blocks. The initial and optimized ("Current") values of component parameters are indicated below the equivalent circuit. . . . .	112
6.22	Comparison of the normalized magnetic flux for a 20-cell FCC injection kicker magnet with the beam screen (red curve) and without the beam screen (green curve): the waveform of the unshielded kicker magnet is the same as in Fig. 4.18.	113
7.1	Schematic drawing of the experimental setup for a classical single wire method. In the resonant method, the matching resistors are replaced by capacitive coupling.	117
7.2	Measurement results of the real longitudinal impedance of the post-LS1 and upgraded LHC MKI (classical method). . . . .	119
7.3	Measurement results of the real longitudinal impedance of the post-LS1 and upgraded LHC MKI (resonant method). . . . .	120
7.4	Photograph of the measurement setup for the power deposition distribution analysis. The conductive wire is mounted around 5 <sup>th</sup> ring (with respect to the upstream end). . . . .	122
7.5	Forward transmission coefficient as a function of frequency measured at the 1 <sup>st</sup> and the 5 <sup>th</sup> rings of the post-LS1 LHC MKI design. . . . .	123
7.6	Forward transmission coefficient as a function of frequency measured at the 1 <sup>st</sup> and the 5 <sup>th</sup> rings of the upgraded LHC MKI design. . . . .	123
7.7	Comparison of the forward transmission coefficient as a function of frequency measured at 1 <sup>st</sup> yoke of the post-LS1 and upgraded LHC MKI. . . . .	124
7.8	Photograph of the prototype spiral beam screen with 21 screen conductors applied using Ag paint and ~4.5 turns along the length of the alumina tube installed in an LHC MKI. . . . .	125
7.9	CST model of the spiral beam screen (simplified model). . . . .	126
7.10	Metallization at the capacitively coupled end. . . . .	126
7.11	Metallization at the grounded end. . . . .	126
7.12	Photograph of the experimental setup with the individual elements indicated. .	127
7.13	Sucobox with a wire connected to a 220 $\Omega$ matching resistor. . . . .	127
7.14	Sucobox with the capacitive coupling. . . . .	127
7.15	Results of the longitudinal impedance measurements performed on the LHC MKI with a prototype spiral beam screen using classical and resonant single wire methods. The experimental data is compared with the CST predictions. . . . .	128
8.1	Coaxial line test fixture with Dezifix in transmission. . . . .	133
8.2	Coaxial line test fixture with Dezifix terminated in short. . . . .	133
8.3	Ferrite sample ( $x = 3.0$ mm, $d_i = 9.2$ mm, $d_o = 20.9$ mm). . . . .	134
8.4	Ferrite sample placed inside Dezifix connector. . . . .	134
8.5	Simplified diagram of the measurement setup. . . . .	134
8.6	Measured $\epsilon'_r$ for three types of ferrites at 25°C. . . . .	136
8.7	Measured $\mu_r^*$ of CMD5005 ferrite at 25°C in comparison with data-sheet [64]. .	136
8.8	Measured $\mu'_r$ of ferrites at 25°C. . . . .	137

8.9	Measured $\mu_r''$ of ferrites at 25°C. . . . .	137
8.10	Coaxial line test fixture with Dezifix terminated in short, PT100 temperature sensor, heating braid with temperature sensor and non-reversible temperature indicators. . . . .	137
8.11	Measured temperature dependence of $\mu_r'$ for CMD5005. . . . .	138
8.12	Measured temperature dependence of $\mu_r''$ for CMD5005. . . . .	138
8.13	Measured temperature dependence of $S_{11}$ for CMD5005. . . . .	139
8.14	Measured $\mu_r'$ at 50°C set, for the three types of ferrites. . . . .	139
8.15	Measured $\mu_r'$ at 150°C set, for the three types of ferrites. . . . .	140
C.1	Schematic drawing of the prototype spiral beam screen. . . . .	151
C.2	Schematic cross-section of the prototype spiral beam screen. . . . .	151



# List of Tables

1.1	Main parameters of FCC-hh, compared to LHC, HL-LHC and HE-LHC. . . . .	4
2.1	Electrical conductivity of materials commonly used in kicker systems [46, 47]. .	25
2.2	Skin depth of materials commonly used in kicker systems at different frequencies.	25
3.1	LHC injection kicker system parameters [51]. . . . .	32
4.1	FCC injection kicker system parameters including a comparison of the require- ments for unshielded and shielded injection kicker magnets. . . . .	51
4.2	Power deposition estimation, for unshielded kicker magnets with 8C11 ferrite, with an aperture of 32 mm or 48 mm. The predictions for ideal and nominal beam spectrum are compared. . . . .	56
4.3	Central cell parameters for selected numbers of cells ( $L_m = 2.2 \times 10^{-6}$ H). . . . .	58
5.1	Results of the low frequency mode analysis (cut-down model). . . . .	77
5.2	Parameters of the spiral beam screen. . . . .	83
5.3	FCC beam and machine parameters at top energy [7]. . . . .	87
5.4	Contribution of the imaginary longitudinal effective impedance of 18 kicker mag- nets to the threshold for loss of Landau damping (expressed as a % of 200 m $\Omega$ ). . . . . .	88
7.1	Results of quality assessment of the prototype spiral beam screen. . . . .	129
C.1	Dimensions of the prototype spiral beam screen. . . . .	152



# List of symbols

## Physical constants:

$\epsilon_0$	Permittivity of free space, $\epsilon_0 = 8.854 \times 10^{-12} \text{ F} \cdot \text{m}^{-1}$ .
$\mu_0$	Permeability of free space, $\mu_0 = 4\pi \times 10^{-7} \text{ H} \cdot \text{m}^{-1}$ .
$c$	Speed of light in vacuum, $c = 299792458 \text{ m} \cdot \text{s}^{-1}$ .
$Z_0$	Characteristic impedance of free space, $Z_0 = 377 \Omega$ .

## Particle motion and machine parameters:

$\alpha_c$	Momentum compaction factor.
$\beta$	Relativistic beta.
$\beta_x(s), \beta_y(s)$	Beta function in horizontal or vertical plane, respectively.
$\gamma$	Relativistic gamma.
$\gamma_t$	Relativistic gamma at transition.
$\epsilon_x, \epsilon_y$	Beam emittance in horizontal or vertical plane, respectively.
$\eta$	Slippage factor.
$\rho$	Bending radius.
$\sigma$	Cross-section of the process.
$\sigma_{\text{RMS}}$	RMS bunch length.
$\tau_L$	$4\sigma_{\text{RMS}}$ bunch length.
$\phi$	Longitudinal phase angle.
$\phi_0$	Longitudinal synchronous phase.
$\psi_x(s), \psi_y(s)$	Phase advance in horizontal or vertical plane, respectively.
$\psi_{x0}, \psi_{y0}$	Initial phase in horizontal or vertical plane, respectively.
$\omega_0$	Angular frequency of the synchronous particle.
$\omega_{s0}$	Synchrotron angular frequency.

## List of symbols

---

$\omega_{\text{RF}}$	Angular frequency of the RF system.
$C$	Length of the closed orbit.
$C_0$	Length of the nominal closed orbit.
$E_0$	Energy of the synchronous particle.
$f$	Revolution frequency of the particle.
$f_0$	Revolution frequency of the synchronous particle.
$h$	Harmonic number.
$I_0$	Average beam current.
$K_x(s), K_y(s)$	Focusing parameter in horizontal or vertical plane, respectively.
$\mathcal{L}$	Luminosity.
$\mathcal{L}_{\text{int}}$	Integrated luminosity.
$N_b$	Number of bunches per beam in a collider.
$N_p$	Number of particles per bunch.
$p$	Momentum of the particle.
$p_0$	Momentum of the synchronous particle.
$\vec{r}(s)$	Particle location vector.
$\vec{r}_0(s)$	Reference orbit vector.
$q$	Charge of a particle.
$Q_s$	Synchrotron tune.
$Q_x, Q_y$	Betatron tune in horizontal or vertical plane, respectively.
$s$	Orbit path parameter.
$\vec{v}$	Particle velocity vector.
$V_{\text{RF}}$	Amplitude of the RF voltage.
$x$	Horizontal coordinate.
$y$	Vertical coordinate.

### Beam coupling impedance and related quantities:

$\alpha_{\text{line}}$	Line attenuation.
$\alpha_{\text{wire}}$	Wire attenuation.
$\lambda$	Bunch line density.
$\hat{\lambda}$	Bunch spectrum.



---

$\hat{\lambda}_{\text{beam}}$	Beam spectrum.
$\omega_{  }$	Resonator angular frequency in longitudinal direction.
$\omega_x, \omega_y$	Resonator angular frequency in horizontal or vertical plane, respectively.
$d_{\text{wire}}$	Diameter of the wire stretched along the DUT.
$\Delta E$	Total energy loss.
$\vec{F}$	Lorentz force vector.
$\vec{F}_{  }$	Longitudinal component of the Lorentz force vector.
$\vec{F}_{\perp}$	Transverse component of the Lorentz force vector.
$F_{\text{CB}}$	Form factor.
$G_m$	Bessel function of order $m$ .
$h_m$	Spectral power density of the $m$ -th bunch mode.
$\text{Im}\left(\frac{Z_{  }}{n}\right)_{\text{eff}}^m$	Imaginary longitudinal effective impedance for the $m$ -th bunch mode.
$k$	Coupling coefficient.
$L_{\text{DUT}}$	Length of the DUT.
$P$	Total power loss.
$\vec{r}$	Transverse vector position of a test particle.
$\vec{r}_1$	Transverse vector position of a source particle.
$q$	Test particle.
$q_1$	Source particle.
$q_{\text{total}}$	Total charge of a bunch distribution.
$R_{  }$	Resonator shunt impedance in longitudinal direction.
$R_x, R_y$	Resonator shunt impedance in horizontal or vertical plane, respectively.
$s$	Longitudinal position of a test particle.
$s_1$	Longitudinal position of a source particle.
$S_{11}$	Input reflection coefficient.
$S_{21}$	Forward transmission coefficient.
$S_{21,\text{DUT}}$	Forward transmission coefficient measured across the DUT.
$S_{21,\text{REF}}$	Forward transmission coefficient of a reference line.
$Q$	Quality factor.
$Q_0$	Unloaded quality factor.

## List of symbols

---

$Q_L$	Loaded quality factor.
$W_{  }$	Longitudinal wake function.
$W_{  }^{\text{pot}}$	Longitudinal wake potential.
$\vec{W}_{\perp} = \{W_x, W_y\}$	Transverse wake function.
$W_x^{\text{const}}, W_y^{\text{const}}$	Constant term of transverse wake function in horizontal or vertical plane, respectively.
$W_x^{\text{dip}}, W_y^{\text{dip}}$	Dipolar term of transverse wake function in horizontal or vertical plane, respectively.
$W_x^{\text{quad}}, W_y^{\text{quad}}$	Quadrupolar term of transverse wake function in horizontal or vertical plane, respectively.
$W_x^{\text{pot}}, W_y^{\text{pot}}$	Transverse wake potential in horizontal or vertical plane, respectively.
$WL$	Wakelength.
$z$	Distance between source and test particle.
$Z_0$	Characteristic impedance of the measurement system.
$Z_L$	Impedance of the coaxial line.
$Z_{\text{match}}$	Impedance of the matching resistors.
$Z_{  }$	Longitudinal beam coupling impedance.
$\vec{Z}_{\perp} = \{Z_x, Z_y\}$	Transverse beam coupling impedance.
$Z_x^{\text{dip}}, Z_y^{\text{dip}}$	Dipolar component of transverse beam coupling impedance in horizontal or vertical plane, respectively.
$Z_x^{\text{quad}}, Z_y^{\text{quad}}$	Quadrupolar component of transverse beam coupling impedance in horizontal or vertical plane, respectively.

### Electromagnetic quantities:

$\alpha$	Attenuation coefficient.
$\beta$	Phase coefficient.
$\gamma$	Propagation constant.
$\delta$	Skin depth.
$\varepsilon^*$	Complex permittivity.
$\varepsilon_r^*$	Relative complex permittivity.
$\varepsilon', \varepsilon''$	Real or imaginary part of complex permittivity, respectively.
$\varepsilon_r', \varepsilon_r''$	Real or imaginary part of the relative complex permittivity, respectively.
$\mu^*$	Complex permeability.

---

$\mu_r^*$	Relative complex permeability.
$\mu', \mu''$	Real or imaginary part of complex permeability, respectively.
$\mu_r', \mu_r''$	Real or imaginary part of the relative complex permeability, respectively.
$\rho$	Resistivity.
$\sigma$	Electric conductivity.
$\vec{B}$	Magnetic field density.
$\vec{D}$	Electric flux density.
$\vec{E}$	Electric field vector.
$\vec{H}$	Magnetic field vector.
$\vec{J}$	Total current density.
$\vec{J}_0$	Source current density.
$k$	Wave number.
$R_{AC}$	AC resistance.
$R_{DC}$	DC resistance.
$R_s$	Sheet resistance.

**Kicker magnet parameters:**

$\Theta$	Beam deflection angle.
$\tau_c$	Rise time of the pulse from the pulse generator.
$\tau_m$	Fill time of the kicker magnet.
$\tau_p$	Single-way delay time of the PFN or PFL.
$\tau_r$	Rise time of the magnetic field.
$\Phi$	Magnetic flux in the aperture of the kicker magnet.
$A_c$	Cross-section of the air gap.
$B_0$	Magnetic flux density at the center of the kicker magnet aperture.
$B_c$	Magnetic flux density in the ferrite core.
$B_x, B_y$	Magnetic flux density in $x$ or $y$ direction, respectively.
$C_{cell}$	Capacitance of a central cell.
$C_{in}, C_{out}$	Capacitance value at the entrance or output of the kicker magnet, respectively.
$E_m$	Stored magnetic energy per unit length, calculated with Opera-2D.

## List of symbols

---

$f_c$	Cut-off frequency of a cell.
$H_{\text{ap}}$	Horizontal aperture dimension.
$I$	Driving current.
$l_{\text{add}}$	Additional effective length of an end cell.
$l_{\text{cell}}$	Physical length of a central cell.
$l_{\text{unit}}$	Length of the kicker magnet module.
$L_{\text{cell}}$	Inductance of a central cell.
$L_{\text{cell}}^{\text{Opera-2D}}$	Equivalent inductance of a central cell calculated with Opera-2D.
$L_{\text{end}}$	Inductance of an end cell.
$L_{\text{eff}}$	Effective length of the kicker system.
$L_m$	Inductance of the kicker magnet.
$L_{m/m}$	Inductance of the kicker magnet per unit length.
$L_p$	Parasitic inductance.
$n$	Number of cells.
$N$	Number of coil turns.
$P_m$	Power per unit length calculated with Opera-2D.
$R_{\text{cell}}$	Resistance associated with a cell.
$R_{\text{cell}}^{\text{Opera-2D}}$	Equivalent resistance associated with a central cell calculated with Opera-2D.
$t$	Thickness of the ferrite, in the direction perpendicular to the direction of propagation of the beam.
$T_C$	Curie temperature.
$TCC$	Capacitance temperature coefficient.
$V_{\text{ap}}$	Vertical aperture dimension.
$V_{\text{in}}, V_{\text{out}}$	Voltage at the input or output of the kicker magnet, respectively.
$Z$	Characteristic impedance of the kicker magnet.

### Beam screen parameters:

$\alpha$	Angle of the spiral screen conductor.
$\delta_{\text{fringe}}$	Effective increase in length due to fringe fields.
$\epsilon_{r,\text{eff}}$	Effective real relative permittivity.
$A_e$	Effective cross-sectional area of the magnetic core.

---

$d$	Distance between the upper part of the beam screen and GND busbar.
$d_i$	Inner diameter of a toroidal ferrite ring.
$d_o$	Outer diameter of a toroidal ferrite ring.
$D_{\text{beam screen}}$	Inner diameter of a beam screen.
$f_r$	Resonant frequency.
$f_r^{\text{CST}}$	Resonant frequency predicted by CST.
$f_{\text{conv}}^{(n)}$	Harmonic of the fundamental resonance of the longitudinal impedance spectrum of the conventional beam screen ( $n \in \mathbb{Z}$ ).
$f_{\text{spiral}}^{(n)}$	Harmonic of the fundamental resonance of the longitudinal impedance spectrum of the spiral beam screen ( $n \in \mathbb{Z}$ ).
$l_e$	Effective magnetic path length of the magnetic core.
$L$	Length of the screen conductor within a uniform magnetic field.
$L_{\text{overlap}}$	Overlap length.
$L_{\text{total}}$	Total distance along which the spiral spans.
$N_{\text{turn}}$	Number of turns of the spiral conductor along the length of the aperture of the kicker magnet.
$N_{\text{total}}$	Total number of turns along the beam screen.
$p$	Pitch of the spiral.
$P_i$	Predicted total power dissipated in the $i$ -th solid.
$P_i^{\text{CST}}(\omega_n)$	Predicted power dissipated in the $i$ -th solid at angular frequency $\omega_n$ .
$R$	Radius of the beam screen.
$s$	Length of the spiral screen conductor.
$t$	Thickness of the rectangular conductor.
$V_i$	Voltage induced on the $i$ -th screen conductor.
$W$	Width of the rectangular conductor.
$x$	Length of a toroidal ferrite ring.
$x_{\text{overlap}}$	Length of a screen conductor in the overlap region.



# Acronyms

**ATLAS** A Toroidal LHC ApparatuS. 1

**BSM** Physics Beyond the Standard Model. 1, 2

**CDR** Conceptual Design Report. 2

**CERN** European Organization for Nuclear Research. 1, 2, 4, 42, 45, 54, 124, 132, 145, 151

**CLIC** Compact Linear Collider. 2

**CMS** Compact Muon Solenoid. 1

**DUT** Device Under Test. 115–117, 120, 121, 127

**EM** Electromagnetic. 3, 5–7, 12, 54, 63, 71, 96, 97, 115, 121, 132, 143, 145, 146

**ESPP** European Strategy for Particle Physics. 2

**FCC** Future Circular Collider. xix, 2–6, 45, 47, 50–52, 54, 56–60, 64–72, 76, 78, 85–89, 93, 94, 96–99, 102, 103, 107, 108, 112, 119, 121, 125, 132, 139, 141–143, 145, 146

**FCC-ee** Future Circular Collider (electron-positron configuration). 2

**FCC-he** Future Circular Collider (hadron-electron configuration). 2

**FCC-hh** Future Circular Collider (hadron-hadron configuration). 2–4, 45, 46, 85, 141, 149

**FEM** Finite Element Method. 95, 97

**FOM** Figure Of Merit. 58, 59, 149

**GFR** Good Field Region. 102, 106, 108, 109, 144

**GND** Ground conductor. 28, 35, 81, 84, 98, 100

**HE-LHC** High-Energy Large Hadron Collider. 2, 3

**HEB** High Energy Booster. 2, 45

## Acronyms

---

- HL-LHC** High-Luminosity Large Hadron Collider. 2, 3, 45
- HV** High Voltage. 4–6, 28, 35–37, 39, 79, 81–84, 98, 105, 122, 125
- IA** Inductive Adder. 47–49, 112, 113
- ILC** International Linear Collider. 2
- IPOC** Internal Post Operational Check. 38, 39
- LDB** Timber Logging DataBase. 38
- LHC** Large Hadron Collider. 1–4, 6, 31, 34, 36, 37, 43, 45, 47, 57, 72, 76, 85, 88, 96, 97, 108, 132, 139, 141, 142, 144–146
- LHC MKI** Large Hadron Collider Injection Kicker Magnet. 4–6, 31, 33–39, 47, 51, 56, 66, 67, 70, 71, 76–78, 86, 95, 96, 115–123, 125–128, 139, 141–144, 146
- MDB** Timber Measurement DataBase. 38, 42
- MG** Marx Generator. 47, 49
- PEC** Perfect Electric Conductor. 53, 64
- PFL** Pulse Forming Line. 27, 28, 47
- PFN** Pulse Forming Network. 27, 28, 31, 36, 37, 47
- QD** Defocusing Quadrupole. 46
- RCPS** Resonant Charging Power Supply. 27, 31
- RF** Radio Frequency. 11, 15, 16, 38, 39, 83, 127
- RMS** Root Mean Square. 22, 46, 51, 52, 110, 111
- SC** SemiConductor. 47
- SEY** Secondary Electron Yield. 4, 31, 36
- SIS** Software Interlock System. 37, 38, 40, 42
- SM** Standard Model. 1
- SPS-MKE** Super Proton Synchrotron Extraction Kicker Magnet. 53
- SPS-MKP** Super Proton Synchrotron Injection Kicker Magnet. 132
- SS** Soft Start. 37–40, 42, 43



**TEM** Transverse ElectroMagnetic. 115, 118

**TMR** TerMinating Resistor. 38–40

**VNA** Vector Network Analyzer. 115, 118, 121, 127, 133, 138

**YETS** Year End Technical Stop. 34, 36, 39



# 1 Introduction

The Large Hadron Collider (LHC) at CERN has greatly advanced our understanding of matter and the Standard Model (SM) of elementary particles and the fundamental forces. The discovery of the long-sought particle, the Higgs boson, was announced by ATLAS and CMS experiments on 4<sup>th</sup> July 2012 at CERN and completed predictions of the SM [1]. The SM has demonstrated huge success and the underlying theories have been heavily benchmarked experimentally, however it also opened new questions. This is commonly referred to as Physics Beyond the Standard Model (BSM). Observations that remain unexplained include: the imbalance between matter and antimatter, non-zero neutrino masses, the nature of dark matter and the cosmological inflation [2]. Amongst theoretical issues that need to be addressed is, for example, the hierarchy problem: a large discrepancy between aspects of the weak force and gravity [3].

Particle accelerators help explore the fundamental structure of the universe. The accelerator based experiments include fixed target experiments and particle colliders: the latter are relevant for this thesis. In the collider, two counter-rotating beams of particles are accelerated and brought into collision at the experiments installed in the machine. The analysis of the useful interactions, the so-called "events", allows to examine the subatomic world. To increase the discovery potential of particle accelerators, scientists aim to develop high-intensity and high-energy frontiers. In general, the high-energy frontiers produce heavier particles with greater chances of new discoveries, while high-intensity machines allow to probe already known processes with better precision [4].

The quantity that measures the ability of a particle collider to produce the required number of interactions is called luminosity ( $\mathcal{L}$ ) and is expressed in the units of  $\text{area}^{-1}\text{time}^{-1}$  [5]:  $\mathcal{L}$  is the proportionality factor between the collision rate and the cross-section ( $\sigma$ ) of the process. As the experiments collect data over a period of time, the integrated luminosity is given by [5]:

$$\mathcal{L}_{\text{int}} = \int \mathcal{L}(t) dt, \quad (1.1)$$

and is defined in units of  $\text{area}^{-1}$ . The dimensionless product  $\mathcal{L}_{\text{int}}\sigma$  gives the total number of events.

At CERN, the High-Luminosity Large Hadron Collider (HL-LHC) will be a major upgrade of the LHC, in order to sustain and extend its discovery reach. The HL-LHC aims to explore the 14 TeV energy region with the the peak luminosity and integrated luminosity per year increased by a factor of 5 with respect to the LHC design value [6]. However, the HL-LHC will reach its full discovery potential after 2035 [7]. To open a path for research BSM and maximize the potential for new findings, accelerators with higher energy and precision are required.

### 1.1 The Future Circular Collider for hadrons

In 2013, The European Strategy for Particle Physics (ESPP) stated: “*To stay at the forefront of particle physics, Europe needs to be in a position to propose an ambitious post-LHC accelerator project at CERN by the time of the next Strategy update*” [7]. The Future Circular Collider (FCC) study has been launched in response to the above recommendation. The aim of the project is to provide detailed design and feasibility studies for a next-generation circular collider, as part of an international collaboration including more than 135 institutes from 34 countries [7]. Within this study, several machines have been investigated, i.e.: the lepton collider (FCC-ee), the hadron collider (FCC-hh) and the hadron-electron collider (FCC-he). Also, an option to upgrade the energy of the LHC (HE-LHC), by using the technology developed for FCC-hh, has been assessed [7]. In 2019, the FCC Conceptual Design Report (CDR) [7] was released and includes descriptions of the proposed machines. The FCC project will be reviewed together with other proposals – including the linear lepton colliders, i.e. the Compact LLinear Collider (CLIC) [8] and the International Linear Collider (ILC) [9] – during the next ESPP in May 2020.

#### 1.1.1 Baseline design

In this thesis, the focus is on the FCC-hh: below, the baseline parameters are discussed. The collider will be built in a new tunnel of approximately 100 km circumference at CERN. The FCC-hh is foreseen to provide proton-proton collisions at a centre-of-mass energy of 100 TeV, with a much higher luminosity than in HL-LHC. The integrated luminosity is expected to be  $30 \text{ ab}^{-1}$  in 25 years of operation, assuming 160 days scheduled for proton physics per year, as it is currently for the LHC [7, 10]. To reach the nominal energy, Nb<sub>3</sub>Sn dipole magnets with a field of 16 T will be used [7]. However, since each accelerator has a limited dynamic range, a chain of stages will be required to reach the nominal energy. Although different injector options are being considered, the baseline is to use an upgraded LHC as a High Energy Booster (HEB) and to inject the beam at an energy of 3.3 TeV into the FCC [7]. This choice requires modifications to the LHC, to allow a faster ramp up of the LHC [11]. To place the bunches newly injected into the FCC onto the correct trajectory, a combination of septa and kickers magnets will be used. The septa provide slower magnetic field rise and fall times, but stronger field, than kicker magnets. On the contrary, kicker magnets provide fast field rise and fall times, but relatively weak fields. A design of the injection kicker system and, in particular, the beam screen for the kicker magnets is in the scope of this thesis.

The schematic drawing of the FCC, located in the Geneva area, is presented in Fig. 1.1 [12]. The conceptual layout of the collider, indicating the main insertions, is shown in Fig. 1.2 [7]. Two main experiments are located in opposite insertions (PA and PG). The injection insertions are located near two lower luminosity experiments (PL and PB). Also, the collimation systems (PJ and PF), the radio frequency system (PH) and the extraction system (PD) are indicated.

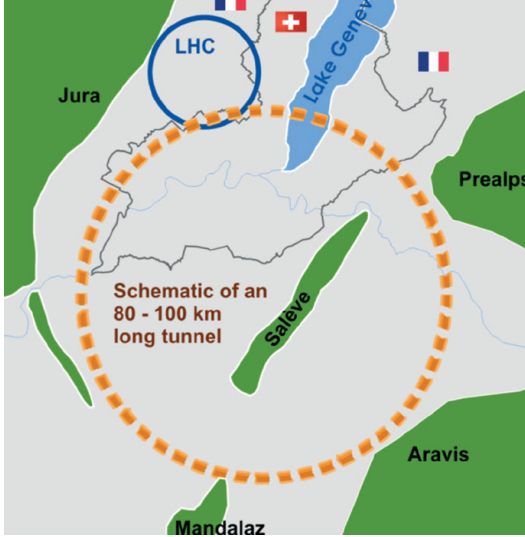


Figure 1.1 – Baseline location of the FCC.

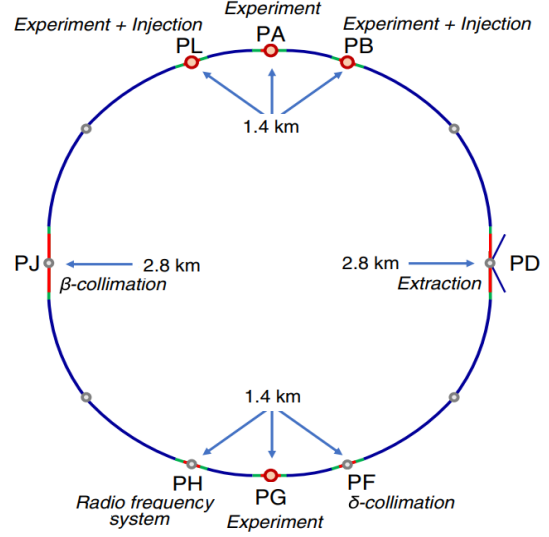


Figure 1.2 – Conceptual layout of the FCC.

### 1.1.2 Baseline parameters

The main FCC-hh baseline parameters are shown in Table 1.1. The values in brackets refer to the initial phase of its operation. For comparison, the corresponding values for LHC, HL-LHC and HE-LHC are presented. All values, except for the injection energy, refer to top collision energy.

## 1.2 Motivation and objectives of this thesis

The FCC-hh will require injection kicker systems that are highly reliable and that do not limit accelerator performance. To circulate many trains of bunches, the kicker magnets must provide magnetic field pulses with fast rise and fall times, and good flat-top quality. Hence, the transmission line ferrite-loaded kicker magnets will be used for FCC. The circulating beam passing through the aperture of the kicker magnet will deposit energy in the form of an electromagnetic (EM) perturbation (wake field), which generally depends on the geometry and the material of the given component. In the frequency domain, the wakefield is known as the beam coupling impedance and, typically, this is a critical aspect in high intensity particle accelerators. The problems are twofold: longitudinal and transverse impedance may drive beam instabilities, leading to beam quality degradation and hence a decrease in the luminosity production. Moreover, the real part of the longitudinal impedance gives rise to beam induced

Table 1.1 – Main parameters of FCC-hh, compared to LHC, HL-LHC and HE-LHC.

Parameter	Unit	LHC	HL-LHC	HE-LHC	FCC-hh
Centre-of-mass energy	TeV	14	14	27	100
Injection energy	TeV	0.45	0.45	1.3	3.3
Circumference	km	26.7	26.7	26.7	97.75
Arc dipole field	T	8.33	8.33	16	16
Beam current	A	0.58	1.12	1.12	0.5
Bunch intensity	$10^{11}$	1.15	2.2	2.2	1.0
Number of bunches / beam	–	2808	2760	2808	10400
RMS bunch length	cm	7.55	9.0	9.0	8.0
Bunch spacing	ns	25	25	25	25
Stored energy / beam	GJ	0.36	0.7	1.4	8.4
Peak luminosity	$10^{34} \text{ cm}^{-2}\text{s}^{-1}$	1	5	16	(5) 30
Integrated luminosity / day	$\text{fb}^{-1}$	0.47	2.8	3.1	(2.2) 8

heating [13]. Power deposition in the kicker magnet can cause a temperature rise of the ferrite yoke, which could exceed its Curie temperature. In such a case, ferrites temporarily lose their magnetic properties until they cool below their Curie temperature: this can impact the ability to inject the beam and hence the runtime of the machine. For a high beam current and short bunches, a high power deposition is expected in the FCC injection kicker magnet: hence, impedance shielding is a critical feature. The beam screen must satisfy the challenging requirements of (1) adequately low, broadband, beam coupling impedance, (2) fast field rise and fall times, (3) adequately small field ripple during the flat-top, (4) good high voltage (HV) behaviour, (5) low Secondary Electron Yield (SEY), (6) compatibility with ultra-high vacuum, (7) radiation resistance, and (8) good mechanical and thermal performance at temperatures from  $10^\circ\text{C}$  to  $350^\circ\text{C}$ . The main objective of this PhD is to design and optimize a beam screen, which will meet the demanding and often conflicting requirements of items (1) to (4), above.

This thesis reports on the research performed and the results achieved during the three-year Doctoral Student programme at CERN and EPFL. First we analyzed the so-called "conventional" beam screen design, with straight screen conductors, used for example in the LHC injection kicker magnets (LHC MKI). Next, we proposed a novel concept of the spiral beam screen. The analysis of both designs has been performed from the theoretical, numerical and experimental point of view. The main goals, highlighting the crucial aspects that had to be analyzed, are listed below.

### (I) Design of the FCC-hh injection kicker system (theoretical and numerical studies)

- Identification of the FCC injector requirements and analysis of proposed scenarios for beam transfer into the FCC. For instance, the required deflection angle, the maximum available length of the injection system and the minimum aperture dimensions depend on lattice parameters. The number of bunches that can be safely transferred into the FCC, per injection, is limited by machine protection constraints, which determine the

kicker field flat-top duration. The acceptable kicker field rise time depends on the proposed machine filling factor and thus spacing between batches of the injected beam.

- Determine hardware parameters for the FCC injection kicker magnet, such as characteristic impedance. Importantly, the characteristic impedance of the kicker magnet and pulse generator must be matched. Otherwise, the resulting reflections can cause voltage and current waveform distortions, which in turn will distort the magnetic field, leading to beam emittance blow-up. However, characteristic impedance must be consistent with field rise time demands and pulse power generator limits. This choice also influences the total length of the injection kicker magnets and thus the beam coupling impedance.
- Analytical calculations to choose the kicker magnet module length and subsequent design of a module, with the aid of PSpice [14], to identify the optimal number of cells needed to achieve the required cut-off frequency. An excessive number of cells leads to increased cost and complexity: in addition, a cell too short can result in HV breakdowns. In the event of a breakdown, the injected beam can be mis-kicked, possibly damaging injection protection or the downstream equipment. In the best case scenario, the consequence would be to dump the already circulating beam, thus reducing machine availability.

### **(II) Beam impedance of the kicker magnet (analytical, numerical, experimental studies)**

- Estimation of the longitudinal impedance of an unshielded kicker magnet, using analytical models [15], together with an analysis of the FCC beam spectrum to evaluate power deposition in the ferrite yoke. These studies verify the necessity of the beam screen.
- Development of a new, proposed, FCC injection kicker magnet model in CST Particle Studio [16]. EM simulations of a kicker magnet with the conventional beam screen to analyse and verify the initial beam coupling impedance predictions.
- Analysis of the measured thermal data and waveform parameters of the LHC MKI to verify whether the temperature rise of any of the yoke exceeds its Curie temperature: this knowledge is critical for the proper design of the beam screen.
- Beam impedance measurements on an LHC MKI to benchmark theoretical predictions and existing CST models. Development of new numerical and experimental methods to determine longitudinal power deposition distribution along the magnet. This analysis is crucial for a beam screen design, as it is important that the power dissipation must not be excessive in any part of the ferrite.
- Evaluation of the injection kicker magnet beam coupling impedance impact on beam stability, in the FCC, and the reduction of the kicker impedance contribution to the overall machine impedance budget. This is an innovative, but challenging, approach as it is not usually of primary importance at the initial design stage of the kicker magnet system.

### **(III) Development of a beam screen design (numerical and experimental studies)**

- Exploration of a novel impedance mitigation techniques and application of possible solutions to improve the HV performance of a beam screen and thus the ability to significantly reduce the possibility of a HV breakdown during injection.
- Development and optimisation of the proposed beam screen such that it meets the required, demanding criteria. In particular, the analysis of the field response of the shielded kicker magnet is crucial and is performed using both Opera 2D [17] and PSpice.
- Design of a dedicated experimental setup for beam coupling impedance measurements of the prototype beam screen installed in LHC MKI, to verify CST predictions.

### Structure and content of this document

First, the basics of accelerator physics and EM theory relevant for the understanding of the research project are reviewed in Chapter 2.

In Chapter 3, the operational principles of fast pulsed kicker magnets are explained. In addition, we introduce the conventional beam screen model, with an emphasis on the HV and heating issues associated with this design. Also, we present a new operation tool developed to validate that the yoke of each MKI is below its Curie point, for safely injecting into the LHC, based on thermal data and kicker waveform real time analysis. This online analysis was crucial to reducing the time before re-injecting beam, when interlock thresholds were exceeded.

Chapter 4 presents the design and optimization of the FCC injection kicker system. Based on the derived FCC beam spectrum and analytical model of the longitudinal impedance of an unshielded kicker, a first estimate of total power loss in the ferrite yoke is provided. Also, a PSpice model of a kicker magnet is developed, to ensure that the field rise time and flat-top quality requirements are met. The work presented in this chapter is published in Ref. [18].

In Chapter 5, the new CST model of the FCC injection kicker magnet with a beam screen is presented. In particular, two different beam screen designs are studied: the conventional design and the novel concept of a spiral beam screen. Also, the impedance contribution of shielded injection kicker magnets to the overall FCC impedance budget is studied and optimized. The main results presented in this chapter are published in Ref. [19].

Chapter 7 discusses the results from measurements performed on an LHC MKI. It is shown that the behaviour of the conventional beam screen is well-understood and correctly predicted. In addition, we present a new experimental method developed to determine power deposition distribution along the yoke, to benchmark the predicted power dissipation distribution. These results are published in Ref. [20]. Finally, the first experimental benchmark to prove the feasibility of the spiral beam screen is presented. The benefits of the spiral screen over the conventional one, for future and existing machines, were highlighted during FCC Week 2019 [21].

In Chapter 6, the field response of the FCC injection kicker magnet with a beam screen is assessed, using Opera-2D and PSpice. The studies show the sensitivity of the field rise time



and field flat-top quality to the conductivity, width and thickness of the screen conductors. A detailed analysis explaining the results is presented. Finally, the optimal design of the beam screen is proposed.

Chapter 8 presents novel measurements of the EM properties of ferrites as a function of frequency and temperature. We discuss two different measurements methods. These studies are vital input for beam coupling impedance simulations and to understand the kicker magnet performance. The results presented in this chapter are published in Ref. [22]

Finally, the main achievements of this project and conclusions are summarized in Chapter 9.



## 2 Theoretical foundation

### 2.1 Linear beam dynamics

In accelerator physics, to describe the motion of beam particles, a curvilinear coordinate system is used, which follows the reference (nominal) orbit of the machine (see Fig. 2.1). The nominal orbit is defined for a reference particle travelling with the designed energy or momentum. The horizontal and vertical displacements of the particle from the reference orbit are denoted by  $x$  and  $y$ , respectively. The coordinate that is pointing into the direction of the longitudinal motion is denoted by  $s$ . In this reference system, any point can be described by:  $\vec{r}(s) = \vec{r}_0(s) + x\vec{e}_x + y\vec{e}_y$ , where  $\vec{r}_0(s)$  indicates the reference orbit.

A synchrotron is a circular accelerator, where the magnetic field is used to modify the trajectory of the beam and the electric field is used to accelerate the beam. The Lorentz force acting on the particle is:

$$\vec{F} = q(\vec{E} + \vec{v} \times \vec{B}), \quad (2.1)$$

where  $q$  is the charge,  $\vec{E}$  and  $\vec{B}$  are the electric and magnetic fields at the location of the particle, and  $\vec{v}$  is the particle velocity.

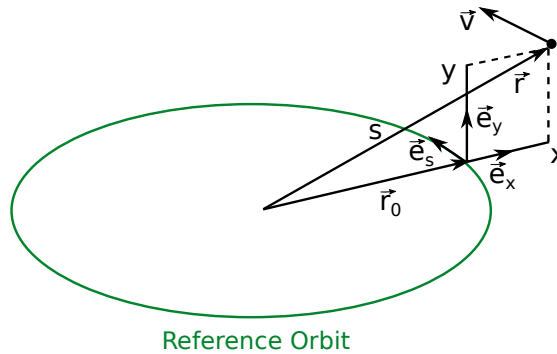


Figure 2.1 – Curvilinear coordinate system to describe particle motion in circular accelerators.

### 2.1.1 Betatron motion

In a synchrotron, the beam particles are guided by dipole magnets, which curve the beam trajectory. To keep the beam on the reference orbit, the magnetic force must be compensated by the centrifugal force. The necessary magnetic field to bend particles travelling with the momentum  $p$  around the radius  $\rho$  defines the beam rigidity ( $B\rho$ ):

$$B\rho = \frac{p}{q}. \quad (2.2)$$

In terms of typical units used in accelerator physics we can write:

$$B\rho[\text{Tm}] = \frac{1}{0.3} p[\text{GeV}/c]. \quad (2.3)$$

Inside a dipole magnet, the trajectory of the particle changes its direction by an angle:

$$\theta = \frac{\int ds}{\rho}. \quad (2.4)$$

In practice, the trajectory of a particle may diverge from the reference orbit. To focus the beam, the quadrupole magnets are used, which produce magnetic field in the horizontal and vertical plane that linearly increases with the distance from the reference orbit. Until now, only linear magnetic fields are considered. The motion of a single particle in a horizontal plane can be therefore described by the Hill's equation [23, 24]:

$$x''(s) + K_x(s)x(s) = \frac{1}{\rho(s)} \frac{\Delta p}{p_0}. \quad (2.5)$$

Note, identical equation holds for the vertical plane. Here,  $K_x(s)$  is the focusing parameter and  $\Delta p = p - p_0$  is the momentum offset from the nominal momentum  $p_0$ . The solution of this equation is [23, 24]:

$$x(s) = \sqrt{\epsilon_x \beta_x(s)} \cos(\psi_x(s) + \psi_{x0}) + D_x(s) \frac{\Delta p}{p_0}, \quad (2.6)$$

where  $\beta_x(s)$  is the beta function,  $D_x(s)$  is the dispersion function and  $\psi_x(s) = \int_{s_0}^s \frac{ds}{\beta_x(s)}$  is the phase advance. In particular,  $\epsilon_x$  is called the beam emittance. Both  $\epsilon_x$  and  $\psi_{x0}$  are constants defined by initial conditions.

From the above expression, a particle performs transverse oscillations around the reference orbit, which are called betatron oscillations. One betatron oscillation is performed for the phase advance equal to  $2\pi$ . The number of betatron oscillations for one revolution period is called a betatron tune [23, 24]:

$$Q_x = \frac{1}{2\pi} \int_{s_0}^{s_0+2\pi\rho} \frac{ds}{\beta_x(s)}. \quad (2.7)$$

### 2.1.2 Synchrotron motion

In a synchrotron, the nominal orbit is fixed at a constant physical radius, by variation of the magnetic field and the radio frequency (RF) electric field, to account for the energy variation. The revolution frequency of the reference particle is:

$$f_0 = \frac{\beta c}{C_0}, \quad (2.8)$$

where  $\beta$  is the relativistic factor,  $c$  is the speed of light and  $C_0$  is the length of the nominal orbit.

The particle is accelerated in an RF cavity where the longitudinal electric field is oscillating sinusoidally with an angular frequency  $\omega_{\text{RF}}$ . The reference particle is synchronized with the RF field and each turn it arrives at the RF cavity at the same phase  $\phi_0 = \omega_0 t$ , where the angular revolution frequency is  $\omega_0 = 2\pi f_0$ . Hence, the synchronism condition requires that:

$$\omega_{\text{RF}} = h\omega_0, \quad (2.9)$$

where  $h$  is an integer, called a harmonic number. In a stationary case, the synchronous phase corresponds to a zero electric field in an RF cavity. However, during acceleration, the revolution frequency of the synchronous particle changes with  $\beta$ , hence the frequency of the RF field must be adjusted accordingly.

The energy gain of the synchronous particle is:

$$\Delta E_0 = qV_{\text{RF}}\sin\phi_0, \quad (2.10)$$

where  $q$  is the particle charge and  $V_{\text{RF}}$  is the amplitude of the RF voltage.

In reality, a beam particle has a certain momentum deviation:  $\Delta p = p - p_0$  with respect to the synchronous particle, hence it travels along a closed orbit of different length  $\Delta C = C - C_0$ . This effect is accounted by the momentum compaction factor [24, 25]:

$$\alpha_c = \frac{\Delta C/C}{\Delta p/p}. \quad (2.11)$$

Analogously, a non-synchronous beam particle has a different revolution frequency  $\Delta f = f - f_0$ . The relative revolution frequency change is proportional to the relative momentum change through the slippage factor [24, 25, 26]:

$$\eta = -\frac{\Delta f/f}{\Delta p/p} = \alpha_c - \frac{1}{\gamma^2}, \quad (2.12)$$

where  $\gamma = 1/(\sqrt{1 - \beta^2})$ . For  $\eta = 0$ , the energy corresponding to  $\gamma = \gamma_t = 1/\sqrt{\alpha_c}$  is called the transition energy. Below transition energy ( $\gamma < \gamma_t, \eta < 0$ ), the velocity increase due to energy increase is dominant with respect to the increase of the path length, hence higher momentum corresponds to a higher revolution frequency. However, above transition energy ( $\gamma > \gamma_t, \eta > 0$ ),

the velocity is roughly constant, so the higher momentum leads to a longer orbit length and therefore a lower revolution frequency. Beam particles with small deviations from the longitudinal synchronous phase  $\Delta\phi = \phi - \phi_0$  follow bounded trajectories and perform so-called synchrotron oscillations around the reference particle. Their equation of motion is [27]:

$$\frac{d^2\phi}{dt^2} + \frac{\omega_{s0}^2}{\cos\phi_0} (\sin\phi - \sin\phi_0) = 0, \quad (2.13)$$

where the synchrotron angular frequency is [25, 26]:

$$\omega_{s0} = \sqrt{-\frac{h\eta q\omega_0^2 V_{RF} \cos\phi_0}{2\pi\beta^2 E_0}}, \quad (2.14)$$

where  $E_0$  is the nominal energy. This equation describes a harmonic oscillator, provided that  $\omega_{s0}$  is a real and positive number. As  $\eta$  and  $\cos\phi_0$  are the only components under the root which might be negative, the stability condition requires that  $\eta\cos\phi_0 < 0$ .

## 2.2 Wake function and beam coupling impedance

Until now, we have discussed the impact of the electromagnetic (EM) fields on beam particle, which are purposely applied and controlled. In general, the external electromagnetic fields generated by the lattice elements do not depend on beam intensity. However, in a real machine, there is another important source of electromagnetic fields to be considered, i.e. the fields generated by the beam itself. In general, a charged beam particle passing through the accelerator, may interact with the machine surroundings and generate electromagnetic fields. Importantly, these fields depend on the beam intensity and charge distribution. Because of the causality principle, the electromagnetic fields induced by an ultrarelativistic charged particle are left behind, hence they are commonly called the *wake fields*.

The wake fields are produced due to finite conductivity of the walls or discontinuities in the beam pipe. Let us remind, the electric field of the static charge radiates outward isotropically. However, when the velocity of the particle approaches the speed of light, the electric field is radial and the magnetic field is azimuthal. Therefore, inside a smooth and perfectly conducting beam pipe the so-called "pancake" field pattern is not disturbed and the opposite charges (image current) formed inside the walls travel along the beam pipe with the same velocity. In such a case, the beam particles and image charges travel side by side, hence the electric and magnetic fields cancel out and there is no net force acting on the beam particles. However, if the wall of the beam pipe is not perfectly conducting or contains discontinuities, the image current is slowed down. From electromagnetic theory it is known that a charge emits radiation, once its trajectory is bent. Therefore, the wake fields can be identified as the radiation fields of the image current (see Fig. 2.2). In turn, the excited wake fields act back on beam particles.

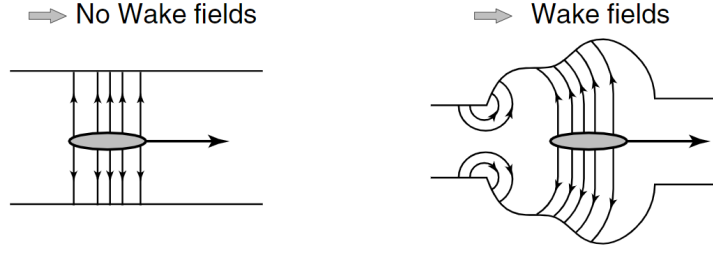


Figure 2.2 – Schematic drawing of the bunch passing through the accelerator component [28]. If the beam pipe is smooth and perfectly conducting (left), there are no fields induced. However, a discontinuity in the structure (right) causes wake fields to be generated.

The concept of wake fields is based on two important approximations introduced below [26]:

1. **Rigid Beam Approximation:** The beam particles are highly relativistic and their trajectories are parallel to the reference orbit in the region of interest. Hence, the beam is rigid, so the shape of the beam is unchanged and the beam velocity remains constant. In particular, this implies that the relative distance between source and test particle is constant.

2. **Impulse Approximation:** As the electromagnetic interaction between the generated wake field and the test particle is localized in a very small region compared to the length of the beam orbit, the force acting on the test particle can be considered in the impulse approximation and quantified as the amount of momentum transferred to the particle.

With the above considerations, we will introduce formal notations to discuss wake fields. First, let us consider two point charges travelling along the  $s$  axis with the velocity  $\vec{v} = (0, 0, \beta c)$ , where  $c$  is the speed of light and  $\beta$  is the relativistic factor. At any time  $t$ , the source particle  $q_1$  is at the longitudinal position  $s_1 = \beta ct$  and at the transverse vector position  $\vec{r}_1$ , whereas the test particle  $q$  is at the distance  $s = z + \beta ct$  with  $z < 0$  behind the source charge and at the transverse vector position  $\vec{r}$ . The source particle excites electric  $\vec{E}$  and magnetic  $\vec{B}$  fields. The wake fields can be computed by solving Maxwell equations with proper boundary conditions.

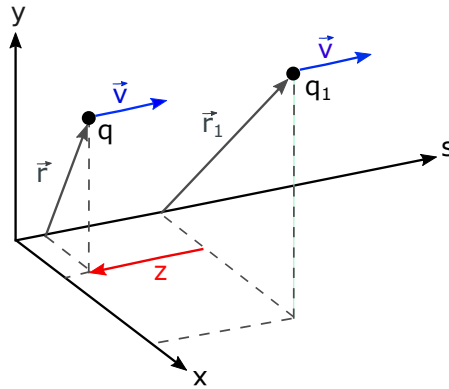


Figure 2.3 – The reference system with two point charges travelling parallel to each other with the constant velocity  $\vec{v}$ . The test particle  $q$  is at the distance  $z$  behind the source particle  $q_1$ .

The Lorentz force acting on the test charge  $q$  is given by:

$$\vec{F}(\vec{r}_1, s_1, \vec{r}, s, t) = q \left[ \vec{E}(\vec{r}_1, s_1, \vec{r}, s, t) + \vec{v} \times \vec{B}(\vec{r}_1, s_1, \vec{r}, s, t) \right] \equiv \vec{F}_{\parallel} + \vec{F}_{\perp}. \quad (2.15)$$

It can be decomposed into longitudinal  $\vec{F}_{\parallel}$  and transverse  $\vec{F}_{\perp}$  vector. The longitudinal force changes the energy of the test charge, while the transverse force deflects its trajectory. Since the beam dynamics is different in the longitudinal direction and transverse planes, we will discuss them separately.

### 2.2.1 Longitudinal direction

#### Longitudinal wake function

The longitudinal wake function  $W_{\parallel}(\vec{r}_1, \vec{r}, z)$  associated with a certain accelerator component is defined as the integral of the longitudinal Lorentz force acting on the test charge  $q$  along the effective length  $L$  due to the electromagnetic fields produced by the source charge  $q_1$ , normalized by the product of both charges  $q_1$  and  $q$  [29, 30, 31]:

$$W_{\parallel}(\vec{r}_1, \vec{r}, z)[V/C] = -\frac{1}{q_1 q} \int_0^L \vec{F}_{\parallel}(\vec{r}_1, s_1, \vec{r}, s, t) \Big|_{t=\frac{s-z}{\beta c}, s_1=s-z} ds. \quad (2.16)$$

As the integral of the longitudinal Lorentz force is the energy change  $\Delta E(\vec{r}_1, \vec{r}, z)$  experienced by the test charge  $q$  due to the wake field produced by the source charge  $q_1$ , the longitudinal wake function can be also defined in the following way [30, 31]:

$$W_{\parallel}(\vec{r}_1, \vec{r}, z)[V/C] = -\frac{\Delta E(\vec{r}_1, \vec{r}, z)}{q_1 q_2}. \quad (2.17)$$

For ultrarelativistic particles ( $\beta = 1$ ), the longitudinal wake function must vanish in front of the source charge because of the causality principle. Hence,  $W_{\parallel}(\vec{r}_1, \vec{r}, z) = 0$  for  $z > 0$ . In addition, the longitudinal wake function is positive for negative energy change, due to the minus sign introduced in the definition. Such a convention can be explained considering a special case:  $z = 0$ . In the origin, the particle cannot gain energy from its own field, thus longitudinal wake function  $W_{\parallel}(\vec{r}_1, \vec{r}, 0)$  must cause energy loss. It can be shown that  $W_{\parallel}(\vec{r}_1, \vec{r}, 0) = \frac{1}{2} W_{\parallel}(\vec{r}_1, \vec{r}, 0^-)$ . This property is called the fundamental beam loading theorem [26]. In physical terms, it means that the ultrarelativistic charge can see only half of its wake field. The real accelerator is designed in such a way, that deviations from the ideal closed orbit are relatively small. Hence, it can be assumed that the longitudinal wake function depends only on  $z$ :  $W_{\parallel}(z) = W_{\parallel}(0, 0, z)$ .



### Longitudinal wake potential

The longitudinal wake function allows to compute the wake field produced by a bunch of particles at the position of the test particle, which is called the longitudinal wake potential. In the longitudinal direction, the bunch line density is denoted by  $\lambda(s)$  and it satisfies condition:  $\int_{-\infty}^{+\infty} \lambda(s) ds = 1$ . By definition, the longitudinal wake potential is the convolution of the longitudinal wake function and the normalized line density [32, 33]:

$$W_{\parallel}^{\text{pot}}(s)[V/C] = \int_{-s}^{+\infty} \lambda(s_1) W_{\parallel}(s - s_1) ds_1. \quad (2.18)$$

In fact, the longitudinal wake potential corresponds to the induced voltage by the bunch. Hence, for a bunch distribution of a total charge  $q_{\text{total}}$ , the following relation holds:

$$V_{\text{ind}}(s)[V] = q_{\text{total}} W_{\parallel}^{\text{pot}}(s). \quad (2.19)$$

As a consequence, the beam particles travelling along the accelerator sees the total voltage as the sum of purposely applied RF voltage  $V_{\text{RF}}(s)$  and the induced voltage  $V_{\text{ind}}(s)$  due to the interaction of the bunch distribution with the accelerator environment:

$$V_{\text{total}}(s)[V] = V_{\text{RF}}(s) + V_{\text{ind}}(s). \quad (2.20)$$

### Longitudinal beam coupling impedance

In certain cases, it may be advantageous to analyze the electrodynamics in the frequency domain. Especially, if circular machines are considered. In addition, the material properties, such as conductivity, permeability and permittivity are frequency dependent. The Fourier transform of the wake function is known as the beam coupling impedance [26, 29, 30, 31, 32, 34, 35]. Here, we introduce a definition of the longitudinal beam coupling impedance [30]:

$$Z_{\parallel}(\omega)[\Omega] = \frac{1}{\beta c} \int_{-\infty}^{+\infty} W_{\parallel}(z) e^{j\omega \frac{z}{\beta c}} dz. \quad (2.21)$$

### Energy loss

The longitudinal wake fields can cause a significant reduction of the total beam energy. The energy loss is usually compensated by the RF system. However, the power extracted from the beam ultimately leads to power dissipation and heating of different elements of the accelerator ring. In this section, we aim to present an analytic expression for the beam energy loss due to multiple passages through the accelerator component characterized by the wake function  $W_{||}(z)$  and beam coupling impedance  $Z_{||}(\omega)$ .

Let us consider a single bunch that consists of  $N_p$  particles. The normalized longitudinal bunch distribution is  $\lambda(s)$  (see figure 2.4). Since the particles at the head of the bunch are expected to affect the trailing ones, the energy change of the witness slice  $qN_p\lambda(s)ds$  due to the wake functions generated by all the preceding source slices  $qN_p\lambda(s_1)ds_1$  is expressed as:

$$\Delta E(s) = -qN_p\lambda(s) \int_s^{\infty} qN_p\lambda(s_1)W_{||}(s-s_1)ds_1. \quad (2.22)$$

The total bunch energy loss is calculated by integrating  $\Delta E(s)$  over the entire bunch length:

$$\Delta E = \int_{-\infty}^{+\infty} \Delta E(s)ds = - \int_{-\infty}^{+\infty} qN_p\lambda(s) \int_s^{+\infty} qN_p\lambda(s_1)W_{||}(s-s_1)ds_1ds \quad (2.23)$$

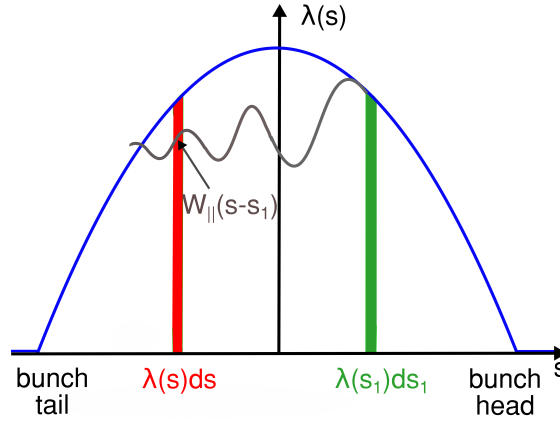


Figure 2.4 – Schematic drawing of the longitudinal bunch distribution  $\lambda(s)$ . The witness slice (red) is affected by the wake function  $W_{||}(s-s_1)$  generated by the source slice (green).

## 2.2. Wake function and beam coupling impedance

It is convenient to analyze the energy loss in the frequency domain. A transfer from time domain to the frequency domain is performed by applying the Fourier transform. In addition, the convolution theorem, Fubini's theorem and Plancherel's theorem are applied. Below, we briefly reviewed the aforementioned statements.

The Fourier transform of function  $f$ , denoted by  $\hat{f}$ , is given by [36]:

$$\hat{f}(\omega) = \int_{-\infty}^{+\infty} f(t) e^{j\omega t} dt. \quad (2.24)$$

The convolution of two functions  $f$  and  $g$  by definition is [36]:

$$(f * g)(t) = \int_{-\infty}^{+\infty} f(u) g(t - u) du. \quad (2.25)$$

By Fubini's theorem, for  $f$  and  $g$  with their Fourier transforms  $\hat{f}$  and  $\hat{g}$ , the following holds [36]:

$$\widehat{(f * g)}(\omega) = \hat{f}(\omega) \hat{g}(\omega). \quad (2.26)$$

From Plancherel theorem it follows that [36]:

$$\int_{-\infty}^{+\infty} \bar{f}(t) g(t) dt = \frac{1}{2\pi} \int_{-\infty}^{+\infty} \bar{\hat{f}}(\omega) \hat{g}(\omega) d\omega. \quad (2.27)$$

Now, let bunch spectrum  $\hat{\lambda}(\omega)$  be defined as the Fourier transform of the bunch longitudinal distribution. In addition, we recall that the longitudinal beam coupling impedance  $Z_{||}(\omega)$  is the Fourier transform of the longitudinal wake function (see Eq. 2.16). In order to analyze energy loss in the frequency domain, Eq. 2.23 can be rewritten using Eqs. 2.25-2.27 in the following steps:

$$\begin{aligned} \Delta E &= -q^2 N_p^2 \int_{-\infty}^{+\infty} \bar{\lambda}(s) \int_s^{+\infty} \lambda(s_1) W_{||}(s - s_1) ds_1 ds = \\ &\stackrel{2.25}{=} -q^2 N_p^2 \int_{-\infty}^{+\infty} \bar{\lambda}(s) [(\lambda * W_{||})(s)] ds = \\ &\stackrel{2.27}{=} -\frac{q^2 N_p^2}{2\pi} \int_{-\infty}^{+\infty} \bar{\hat{\lambda}}(\omega) [\hat{\lambda}(\omega) Z_{||}(\omega)] d\omega = \\ &\stackrel{2.26}{=} -\frac{q^2 N_p^2}{2\pi} \int_{-\infty}^{+\infty} |\hat{\lambda}(\omega)|^2 \text{Re}[Z_{||}(\omega)] d\omega. \end{aligned} \quad (2.28)$$

## Chapter 2. Theoretical foundation

---

However, the above expression is valid only for a single passage through the accelerator component characterized by the longitudinal beam coupling impedance  $Z_{||}(\omega)$ . In the circular accelerator, the bunch is supposed to travel multiple times through the same object. Hence, the contributions from all previous passages of the bunch must be considered. For particles travelling with the speed of light  $c$  around the orbit with the length  $C_0$ , Eq. 2.23 should be generalized in the following way:

$$\Delta E = \int_{-\infty}^{+\infty} \Delta E(s) ds = -q^2 N_p^2 \int_{-\infty}^{+\infty} \lambda(s) \int_s^{+\infty} \lambda(s_1) \sum_{k=-\infty}^{\infty} W_{||}(kC_0 + s - s_1) ds_1 ds. \quad (2.29)$$

As the following relation holds [31]:

$$\sum_{k=-\infty}^{\infty} W_{||}(kC_0 + s - s_1) = \frac{\omega_0}{2\pi} \sum_{p=-\infty}^{\infty} Z_{||}(p\omega_0) \exp\left[-\frac{ip\omega_0(s - s_1)}{c}\right], \quad (2.30)$$

in which  $\omega_0 = \frac{2\pi c}{C_0}$  is the angular revolution frequency, Eq. 2.29 can be expressed as:

$$\Delta E = -\frac{q^2 N_p^2 \omega_0}{2\pi} \sum_{p=-\infty}^{+\infty} |\hat{\lambda}(p\omega_0)|^2 \text{Re}[Z_{||}(p\omega_0)]. \quad (2.31)$$

Since the real part of the longitudinal beam coupling impedance is an even function and  $\omega_0 = 2\pi f_0$ , we obtain:

$$\Delta E = -2q^2 N_p^2 f_0 \left[ \left( \sum_{p=1}^{+\infty} |\hat{\lambda}(p\omega_0)|^2 \text{Re}[Z_{||}(p\omega_0)] \right) + \frac{1}{2} |\hat{\lambda}(0)|^2 \text{Re}[Z_{||}(0)] \right]. \quad (2.32)$$

The last expression can be extended when we consider a beam to be a train of  $N_b$  bunches. In this case, the bunch spectrum  $\hat{\lambda}(p\omega_0)$  in Eq. 2.32 should be replaced with the beam spectrum  $\hat{\lambda}_{\text{beam}}(p\omega_0)$ , calculated as the Fourier transform of the normalized longitudinal beam distribution. In addition, the intensity of the bunch  $N_p$  should be substituted with the intensity of the beam equal to  $N_p N_b$ . Finally, the power loss  $P = \Delta E f_0$  of the beam is given by:

$$P = -2q^2 N_p^2 N_b^2 f_0^2 \left[ \left( \sum_{p=1}^{+\infty} |\hat{\lambda}_{\text{beam}}(p\omega_0)|^2 \text{Re}[Z_{||}(p\omega_0)] \right) + \frac{1}{2} |\hat{\lambda}_{\text{beam}}(0)|^2 \text{Re}[Z_{||}(0)] \right]. \quad (2.33)$$

The power loss of the beam is equal to the power deposition in the accelerator component characterized by the real longitudinal impedance shown in Eq. 2.33.

### 2.2.2 Transverse planes

#### Transverse wake function

Let us refer to the configuration presented on Fig. 2.3, and consider two ultrarelativistic particles travelling inside the accelerator structure along the  $s$  axis with the constant velocity  $\vec{v} = (0, 0, \beta c)$ . The test charge  $q$  is at a distance  $z$  behind the source charge  $q_1$ . The transverse wake fields appear when a charged particle is travelling inside a non symmetric structure or when it is off-centered inside a symmetric vacuum chamber. Below we introduce a definition of the transverse wake function [29, 30]:

$$\vec{W}_\perp(\vec{r}_1, \vec{r}, z)[V/C] = -\frac{1}{q_1 q} \int_0^L \vec{F}_\perp(\vec{r}_1, s_1, \vec{r}, s, t) \Big|_{t=\frac{s-z}{\beta c}, s_1=s-z} ds. \quad (2.34)$$

In order to evaluate the effect of wake fields on the transverse motion, the transverse wake field is usually expanded into a power series along the transverse position of the source and test particle [37], provided that transverse offsets  $\vec{r}_1 = (x_1, y_1)$  and  $\vec{r} = (x, y)$  are relatively small. Taking into account only the lowest order terms and neglecting coupling, for horizontal and vertical plane we obtain:

$$W_x(x_1, x, z) \approx W_x^{\text{const}}(0, 0, z) + W_x^{\text{dip}}(x_1, 0, z)x_1 + W_x^{\text{quad}}(0, x, z)x, \quad (2.35)$$

$$W_y(y_1, y, z) \approx W_y^{\text{const}}(0, 0, z) + W_y^{\text{dip}}(y_1, 0, z)y_1 + W_y^{\text{quad}}(0, y, z)y. \quad (2.36)$$

The first term of the expansion is the constant term and it equals zero when the structure is axisymmetric. The second term is called dipolar or driving wake function, as the test particle is driven by the source particle displacement and it experiences a transverse force independently from its own position. The last term is called quadrupolar or detuning wake function, because the test particle sees a transverse detuning force, which is linearly proportional to its displacement. Since the dipolar and quadrupolar wake functions are defined with respect to the transverse position of the source and test particle, the following relation holds:

$$W_x^{\text{dip}}(x_1, 0, z) = \frac{W_x(x_1, 0, z) - W_x^{\text{const}}(0, 0, z)}{x_1}, \quad (2.37)$$

$$W_y^{\text{dip}}(y_1, 0, z) = \frac{W_y(y_1, 0, z) - W_y^{\text{const}}(0, 0, z)}{y_1}, \quad (2.38)$$

$$W_x^{\text{quad}}(0, x, z) = \frac{W_x(0, x, z) - W_x^{\text{const}}(0, 0, z)}{x}, \quad (2.39)$$

$$W_y^{\text{quad}}(0, y, z) = \frac{W_y(0, y, z) - W_y^{\text{const}}(0, 0, z)}{y}. \quad (2.40)$$

### Transverse wake potential

The transverse wake potential produced by a bunch distribution with longitudinal normalized bunch line density  $\lambda(s)$  is defined as [38]:

$$W_x^{\text{pot}}(s)[V/C] = \int_{-\infty}^{+\infty} \lambda(s_1) \langle x(s_1) \rangle W_x(s - s_1) ds_1, \quad (2.41)$$

where  $\langle x(s_1) \rangle = \int_{-\infty}^{+\infty} x \sigma(x, s_1) dx$  with  $\sigma(x, s_1)$  being the horizontal distribution at  $s = s_1$ . Note, the analogous definition holds for the vertical plane.

### Transverse beam coupling impedance

The transverse beam coupling impedance is found as a Fourier transform of the transverse wake function. Hence, we obtain [30, 35]:

$$\vec{Z}_\perp(\vec{r}_1, \vec{r}, \omega)[\Omega] = \frac{-j}{\beta c} \int_{-\infty}^{+\infty} \vec{W}_\perp(\vec{r}_1, \vec{r}, z) e^{j\omega \frac{z}{\beta c}} dz. \quad (2.42)$$

By convention, the  $-j$  is introduced in the definition. Analogously, we define dipolar and quadrupolar components of transverse beam coupling impedance for horizontal and vertical plane:

$$Z_x^{\text{dip}}(\omega)[\Omega/m] = \frac{-j}{\beta c} \int_{-\infty}^{+\infty} W_x^{\text{dip}}(z) e^{j\omega \frac{z}{\beta c}} dz, \quad (2.43)$$

$$Z_y^{\text{dip}}(\omega)[\Omega/m] = \frac{-j}{\beta c} \int_{-\infty}^{+\infty} W_y^{\text{dip}}(z) e^{j\omega \frac{z}{\beta c}} dz, \quad (2.44)$$

$$Z_x^{\text{quad}}(\omega)[\Omega/m] = \frac{-j}{\beta c} \int_{-\infty}^{+\infty} W_x^{\text{quad}}(z) e^{j\omega \frac{z}{\beta c}} dz, \quad (2.45)$$

$$Z_y^{\text{quad}}(\omega)[\Omega/m] = \frac{-j}{\beta c} \int_{-\infty}^{+\infty} W_y^{\text{quad}}(z) e^{j\omega \frac{z}{\beta c}} dz. \quad (2.46)$$

### 2.2.3 Resonator model

The beam coupling impedance of either the accelerator component or of the entire machine can be approximately represented as a sum of equivalent resonators. Each of them can be

modelled as [29]:

$$Z_{\parallel}(\omega) = \frac{R_{\parallel}}{1 + iQ(\frac{\omega}{\omega_{\parallel}} - \frac{\omega_{\parallel}}{\omega})}, \quad (2.47)$$

$$Z_x(\omega) = \frac{\omega_x}{\omega} \frac{R_x}{1 + iQ(\frac{\omega}{\omega_x} - \frac{\omega_x}{\omega})}, \quad (2.48)$$

$$Z_y(\omega) = \frac{\omega_y}{\omega} \frac{R_y}{1 + iQ(\frac{\omega}{\omega_y} - \frac{\omega_y}{\omega})}. \quad (2.49)$$

where  $R_{\parallel}$ ,  $R_x$  and  $R_y$  are the shunt impedances,  $\omega_{\parallel}$ ,  $\omega_x$  and  $\omega_y$  are the angular resonant frequencies and  $Q$  is the quality factor. In general, the broad-band (low  $Q$ ) beam coupling impedance is associated with short range wake fields, which can potentially lead to single-bunch instabilities. On the contrary, the narrow-band (high  $Q$ ) beam coupling impedance corresponds to long range wake fields, which do not decay when the next bunch arrives and can cause multi-bunch and/or multi-turn coupling.

### 2.2.4 The Panofsky-Wenzel theorem

There is a relationship between longitudinal and transverse wake functions, known as the Panofsky-Wenzel theorem [39]. The details of the derivation can be found in Appendix A. In the time domain, it is expressed as [29]:

$$\frac{\partial}{\partial z} \vec{W}_{\perp}(\vec{r}_1, \vec{r}, z) = \vec{\nabla}_{\perp} W_{\parallel}(\vec{r}_1, \vec{r}, z). \quad (2.50)$$

By applying the Fourier transform to the formula above, the longitudinal and transverse beam coupling impedance are related by [29]:

$$\vec{Z}_{\perp}(\vec{r}_1, \vec{r}, z) = \frac{v}{\omega} \vec{\nabla}_{\perp} Z_{\parallel}(\vec{r}_1, \vec{r}, z), \quad (2.51)$$

where  $\vec{\nabla}_{\perp} = \{\frac{\partial}{\partial x}, \frac{\partial}{\partial y}\}$ . Note, in the formula above, we consider transverse gradients of the longitudinal impedance, hence zero order longitudinal impedance does not contribute to the transverse impedance.

### 2.2.5 Effect on beam dynamics

#### Longitudinal coupled bunch instability

The long range wake fields can cause coupled bunch instability. For equally spaced bunches, the threshold for the longitudinal coupled bunch instability is given by [40]:

$$R_{\parallel} < \frac{|\eta|E_0}{I_0\beta^2} \left( \frac{\Delta E}{E_0} \right)^2 \frac{\Delta\omega_{s0}}{\omega_{s0}} \frac{F_{CB}}{f_0\tau_L} G(f_r\tau_L), \quad (2.52)$$

## Chapter 2. Theoretical foundation

where  $I_0 = qN_b N_p f_0$  is the average beam current,  $F_{CB}$  is the form factor depending on the bunch distribution: here we assume  $F_{CB} = 0.3$  [40]. In addition,  $\frac{\Delta E}{E_0}$  is the energy spread and  $\frac{\Delta\omega_{s0}}{\omega_{s0}}$  is the synchrotron angular frequency spread in the bunch. Also,  $\tau_L = \frac{4\sigma_{RMS}}{c}$ , where  $\sigma_{RMS}$  is the root mean square (RMS) bunch length. The function  $G_m(f_r \tau_L) = (f_r \tau_L) \min\{J_m^{-2}(\pi f_r \tau_L)\}$  is the Bessel function of order  $m$ . In particular, index  $m$  corresponds also to the bunch perturbation mode number.

In a stationary case, the relative energy spread can be calculated using analytical formula [41]:

$$\frac{\Delta E}{E_0} = \sqrt{\frac{2\beta^2 U(\phi)}{h\eta E_0}}, \quad (2.53)$$

where  $\phi = \phi_0 + \Delta\phi$  and  $U(\phi)$  is the potential energy [41]:

$$U(\phi) = \frac{qV_{RF}}{2\pi} [\cos(\phi) - \cos(\phi_0) + (\phi - \phi_0)\sin(\phi_0)]. \quad (2.54)$$

The relative angular synchrotron frequency spread can be estimated as [41]:

$$\frac{\Delta\omega_{s0}}{\omega_{s0}} = \frac{\Delta\phi^2}{16}. \quad (2.55)$$

To determine relative energy spread and relative angular synchrotron frequency spread, Eqs. 2.53-2.55 are evaluated assuming  $\Delta\phi = \frac{\omega_{RF}\tau_L}{2}$ .

### Longitudinal loss of Landau damping

In synchrotrons, there is a mechanism that can stabilize the beam, known as Landau damping [41, 42]. In the longitudinal direction, for a bunched beam, the Landau damping is provided by the spread in synchrotron frequencies of particles inside the bunch. However, at high intensities, the induced voltage due to the wake fields (see Eq. 2.19) leads to the synchrotron frequency shift [43], which will modify the frequency spread: this can cause a loss of Landau damping. To evaluate the contribution of the accelerator element to the total impedance budget for the loss of Landau damping, the imaginary longitudinal effective impedance is calculated. For the  $m$ -th bunch mode, it is defined as [29]:

$$\text{Im}\left(\frac{Z_{||}}{n}\right)_{\text{eff}}^m = \frac{\sum_{p=-\infty}^{\infty} \frac{\text{Im}Z_{||}(\omega_p)}{n} h_m(\omega_p)}{\sum_{p=-\infty}^{\infty} h_m(\omega_p)}, \quad (2.56)$$

where  $n = f/f_0$ ,  $h_m(\omega)$  is the power spectral density of mode  $m$ ,  $\omega_p = \omega_0(N_b p + n_b + mQ_s)$ , where  $n_b$  is the coupled bunch mode number ( $0 \leq n_b < N_b$ ) and  $Q_s = \frac{\omega_{s0}}{\omega_0}$  is the synchrotron tune. For a single bunch,  $N_b = 1$  and  $n_b = 0$ . Hence, it follows that  $\omega_p = \omega_0 p + m\omega_{s0}$ . For a Gaussian and parabolic bunch, the spectral power density is [29]:

$$h_m(\omega) = \begin{cases} (\omega\sigma_{RMS})^{2m} \exp(-\omega^2\sigma_{RMS}^2) & \text{for a Gaussian bunch,} \\ (m+1)^2 \frac{1+(-)^m \cos(\omega\tau_L)}{[(\omega\tau_L)^2 - \pi^2(m+1)^2]^2} & \text{for a parabolic bunch.} \end{cases} \quad (2.57)$$



## 2.3 Basic electromagnetic theory

The macroscopic Maxwell equations for the electric  $\vec{E}$  and magnetic  $\vec{H}$  fields in a linear, homogeneous and isotropic medium are given by [44]:

$$\vec{\nabla} \times \vec{E} = -\frac{\partial \vec{B}}{\partial t}, \quad (\text{Faraday's Law of Induction}) \quad (2.58)$$

$$\vec{\nabla} \times \vec{H} = \frac{\partial \vec{D}}{\partial t} + \vec{J}, \quad (\text{Ampere's Law}) \quad (2.59)$$

$$\vec{\nabla} \cdot \vec{D} = \rho, \quad (\text{Gauss' Law for Electricity}) \quad (2.60)$$

$$\vec{\nabla} \cdot \vec{B} = 0, \quad (\text{Gauss' Law for Magnetism}) \quad (2.61)$$

where  $\vec{D}$  is the electric flux density,  $\vec{J}$  is the total current density and  $\rho$  is the total charge density. By taking the divergence of Eq. 2.59 and applying Eq. 2.60, we obtain the so-called continuity equation:

$$\vec{\nabla} \cdot \vec{J} = -\frac{\partial \rho}{\partial t}. \quad (2.62)$$

In general, the total current density is the superposition of the source current density  $\vec{J}_0$  and the conduction current density induced by the electric fields in the conducting material, where  $\sigma$  is the electric conductivity of the medium, in siemens per meter (S/m):

$$\vec{J} = \vec{J}_0 + \sigma \vec{E}. \quad (2.63)$$

In the frequency domain, Eqs. 2.58-2.61 become [44]:

$$\vec{\nabla} \times \vec{E} = -j\omega \vec{B}, \quad (2.64)$$

$$\vec{\nabla} \times \vec{H} = j\omega \vec{D} + \vec{J}, \quad (2.65)$$

$$\vec{\nabla} \cdot \vec{D} = \rho, \quad (2.66)$$

$$\vec{\nabla} \cdot \vec{B} = 0. \quad (2.67)$$

The constitutive relations are:  $\vec{D} = \epsilon^*(\omega) \vec{E}$  and  $\vec{B} = \mu^*(\omega) \vec{H}$ , where  $\epsilon^*(\omega) \equiv \epsilon'$  and  $\mu^*(\omega) \equiv \mu'$  are frequency dependent complex permittivity and permeability, respectively. Since  $\epsilon^*$  and  $\mu^*$  are complex, the real and imaginary parts can be separated:

$$\epsilon^* = \epsilon' - j\epsilon'', \quad (2.68)$$

$$\mu^* = \mu' - j\mu'' . \quad (2.69)$$

In general, the real parts of the complex permittivity and permeability are related to the stored energy within the medium, while the imaginary parts account for the energy dissipation within the medium. In addition,  $\epsilon^*$  and  $\mu^*$  are related to free space parameters by relative parameters:

$$\epsilon^* = \epsilon_0 \epsilon_r^* = \epsilon_0 (\epsilon_r' - j\epsilon_r''), \quad (2.70)$$

$$\mu^* = \mu_0 \mu_r^* = \mu_0 (\mu_r' - j\mu_r''), \quad (2.71)$$

where  $\epsilon_0 \simeq 8.854 \times 10^{-12} \text{ F} \cdot \text{m}^{-1}$  is permittivity of free space and  $\mu_0 = 4\pi \times 10^{-7} \text{ H} \cdot \text{m}^{-1}$  is permeability of free space. For the material with non-zero conductivity, Eq. 2.65 can be re-written using constitutive relations and Eq. 2.68 as follows:  $\vec{\nabla} \times \vec{H} = j\omega(\epsilon' - j\epsilon'')\vec{E} + \sigma\vec{E} + \vec{J}_0$ . In this case, the complex permittivity of the lossy medium is given by [44, 45]:

$$\epsilon^* = \epsilon' - j\epsilon'' - j\frac{\sigma}{\omega\epsilon_0} = \epsilon'(\omega) - j\left(\epsilon''(\omega) - \frac{\sigma}{\omega\epsilon_0}\right). \quad (2.72)$$

The propagation of the EM field in a source-free, lossy media is described by solving complex wave equations [44]:

$$\vec{\nabla}^2 \vec{E} + k^2 \vec{E} = 0, \quad (2.73)$$

$$\vec{\nabla}^2 \vec{H} + k^2 \vec{H} = 0, \quad (2.74)$$

where  $k = \omega\sqrt{\mu^*\epsilon^*}$  is the wave number. The propagation constant is defined as  $\gamma = jk = \alpha + j\beta$ , where  $\alpha$  denotes attenuation coefficient in nepers per meter (Np/m) and  $\beta$  denotes phase coefficient in radians per meter (rad/m). The losses in the medium give rise to exponential decaying of the electric (or magnetic) field in the direction of wave propagation. The distance required for the field to be attenuated to  $e^{-1}$  (about 37%) of its original value is defined as the skin depth. It follows that 63% ( $1 - e^{-1}$ ) of the current flows through the conductor between the surface and one skin depth, 86% ( $1 - e^{-2}$ ) between the surface and two skin depths, 95% ( $1 - e^{-3}$ ) between the surface and three skin depths, etc. In highly conductive media, such as the busbars of the kicker magnet, the skin depth can be calculated as:

$$\delta = \sqrt{\frac{2}{\omega\mu_0\mu_r\sigma}}, \quad (2.75)$$

where  $\mu_r \equiv \mu_r'(0)$ .

The skin depth in the screen conductors is important for EM shielding. During the propagation of the EM wave through the metallic shielding, eddy currents are induced in the metal, which takes energy out of the wave. Hence, most of the energy is removed within a few skin

depths. Note, the skin depth increases at lower frequencies. Hence, the material for EM shielding must have high conductivity and high permeability, but also sufficient thickness to achieve the required number of skin depths at the lowest frequency of concern. The electrical conductivity of several materials used in kicker system applications is shown in Table 2.1. The corresponding skin depth in the MHz range is presented in Table 2.2.

Table 2.1 – Electrical conductivity of materials commonly used in kicker systems [46, 47].

Material	$\sigma$ [S/m] at 20°C
Silver (Ag)	$6.30 \times 10^7$
Copper (Cu)	$5.96 \times 10^7$
Titanium (Ti)	$2.38 \times 10^6$
Stainless steel	$1.45 \times 10^6$
Nickel–Chromium 80%/20% (NiCr)	$0.92 \times 10^6$

Table 2.2 – Skin depth of materials commonly used in kicker systems at different frequencies.

Freq. [MHz]	Skin depth [μm]				
	Ag	Cu	Ti	Stainless steel	NiCr
1	63	65	326	418	525
5	28	29	145	187	234
10	20	21	103	132	166
40	10	10	52	66	83

The resistivity ( $\rho$ ) of the material (in  $\Omega \cdot \text{m}$ ) is defined as the inverse of electrical conductivity:

$$\rho = \frac{1}{\sigma}. \quad (2.76)$$

The sheet resistance ( $R_s$ ) of the material (in  $\Omega/\square$ ) is the resistance of thin films, which are uniform in thickness ( $t$ ). The thickness and the resistivity of the material are related to the sheet resistance by:

$$R_s = \frac{\rho}{t}. \quad (2.77)$$

The DC resistance ( $R_{\text{DC}}$ ) of the rectangular conductor (in  $\Omega$ ), which is characterized by the length  $L$ , width  $W$  and thickness  $t$ , is written as:

$$R_{\text{DC}} = \frac{\rho}{t} \frac{L}{W}. \quad (2.78)$$

At high frequency, the skin effect causes the resistance of the conductor to increase. The AC resistance ( $R_{\text{AC}}$ ) of an isolated rectangular conductor (in  $\Omega/\text{m}$ ), assuming  $t > 2\delta$ , is [48]:

$$R_{\text{AC}} = \frac{\rho}{2(W + t)\delta}. \quad (2.79)$$



## 3 Fast pulsed kicker systems in particle accelerators at CERN

### 3.1 General overview

#### 3.1.1 Single turn injection

A detailed description of the injection systems in particle accelerators is presented in Ref. [49]. In this chapter, the most important aspects of fast pulsed kicker systems used for a single turn injection are reviewed. Figure 3.1 shows a schematic diagram of a single turn injection in one plane. The beam to be injected passes through the homogeneous field region of the septum and is deflected towards the kicker magnet, which deflects the beam onto a nominal orbit. The septum magnet and the kicker magnet are installed either side of a quadrupole, which is defocusing in the injection plane, thereby reducing the required kicker strength. Note, the circulating beam passes through the aperture of the kicker magnet. The magnetic field produced by the kicker magnet must then rise between the circulating beam and the start of the injected beam and fall between the end of the injected beam and the start of the next train of the circulating beam bunches. The field should not deviate from the flat-top by more than a specified percentage (typically  $\pm 0.5\%$ ) to avoid beam emittance blow-up at injection, and from the zero field, so as to not unduly deflecting the circulating beam. To achieve magnetic field rise and fall times below a few microseconds, transmission line kicker magnets are typically used.

#### 3.1.2 Technological aspects

Figure 3.2 presents a schematic diagram of a fast pulsed kicker system. The main sub-systems are the Resonant Charging Power Supply (RCPS), Pulse Forming Network (PFN) or Pulse Forming Line (PFL), transmission line, kicker magnet, fast high-power switches (thyratrons), terminating and dump resistors. During typical operation, the PFN or PFL is charged by the RCPS to double the nominal voltage required for the kicker magnet operation. To avoid reflections the system has to be matched, hence all the components have the same characteristic impedance  $Z$ . When the main switch closes, a pulse of approximately half of the PFN/PFL

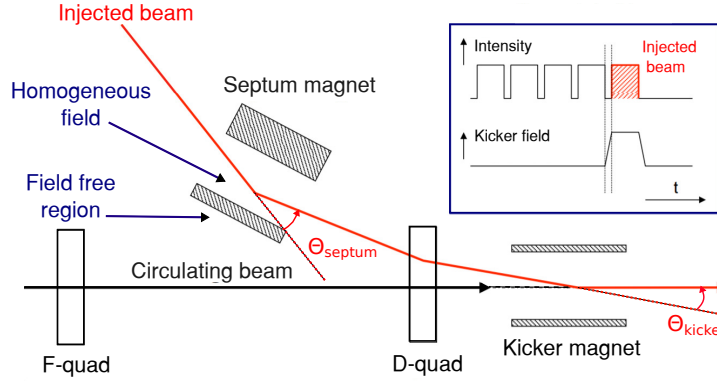


Figure 3.1 – Diagram of a single turn injection (reproduced from Ref. [49]). The deflection angle provided by the septum and kicker is denoted by  $\Theta_{\text{septum}}$  and  $\Theta_{\text{kicker}}$ , respectively.

voltage is launched through the transmission line towards the kicker magnet. Once the pulse reaches the matched terminating resistor, full magnetic field is established in the kicker magnet. Let us introduce  $\tau_p$  as the single delay time of the PFN or PFL. The pulse duration in the kicker magnet is controlled by adjusting the timing of turn-on of the dump switch relative to the main switch: the pulse duration in the kicker magnet can vary between 0 and  $2\tau_p$ .

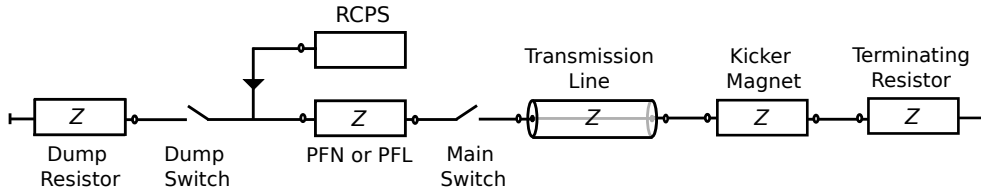


Figure 3.2 – Schematic diagram of the kicker system.

### 3.1.3 Kicker magnet aperture

Transmission line kicker magnets are typically ferrite loaded C-core magnets with rectangular shaped aperture of dimensions  $H_{\text{ap}}$  and  $V_{\text{ap}}$  (see Figure 3.3). Ferrite NiZn is a typical material used for the core of fast pulsed kicker magnets. The specification of magnetic materials for pulsed kicker magnets is discussed in Chapter 9. The driving current  $I$  flows through the high voltage (HV) conductor and returns through the ground (GND) conductor. Assuming a relative permeability ( $\mu_r$ ) of the ferrite yoke  $\gg 1$ , the magnetic flux density inside the aperture of the kicker magnet is:

$$B_y \simeq \mu_0 \left( \frac{NI}{V_{\text{ap}}} \right), \quad (3.1)$$

where  $N$  is the number of coil turns. The inductance of the kicker magnet per unit length is:

$$L_{m/m} \simeq \mu_0 \left( \frac{N^2 H_{\text{ap}}}{V_{\text{ap}}} \right). \quad (3.2)$$

Since kicker magnets must be fast, typically  $N = 1$ . In this case, the inductance is determined by kicker magnet aperture dimensions. The minimum dimensions of the aperture are determined by the beam parameters. However,  $V_{ap}$  cannot be significantly increased, as the current would have to be increased as well to achieve the required magnetic flux density (see Eq. 3.1). For a given characteristic impedance, the current increase would impose a voltage increase and therefore require stronger insulation throughout the kicker magnet system.

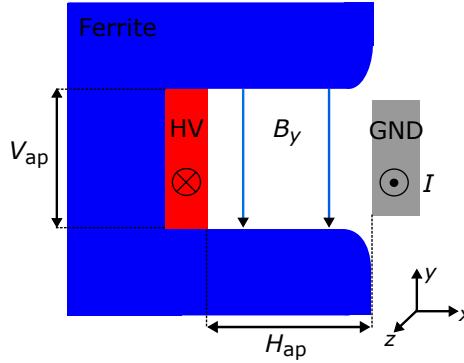


Figure 3.3 – Cross section of C-core kicker magnet.

The beam deflection in  $x$  direction, due to a magnetic field, is:

$$\theta = \left[ \frac{0.3}{p} \right] \int_{z_0}^{z_1} B_y dz = \left[ \frac{0.3 L_{eff}}{p} \right] B_y, \quad (3.3)$$

where  $p$  is expressed in GeV/c,  $B_y$  is given in T and  $L_{eff}$  is the effective length of the magnet (usually different from the mechanical length due to fringe fields at both ends of the magnet).

### 3.1.4 Transmission line topology

A transmission line kicker magnet resembles a distributed electrical transmission line. The C-core ferrites are interleaved with high voltage capacitance plates and form individual cells of the kicker magnet. A simplified equivalent electric circuit of a transmission liner kicker magnet consisting of  $n$  cells is presented in Fig. 3.4. The cell's inductance and capacitance are denoted by  $L_{cell}$  and  $C_{cell}$ , respectively. The voltage pulse at the entrance and at the output of the kicker magnet is denoted by  $V_{in}$  and  $V_{out}$ .

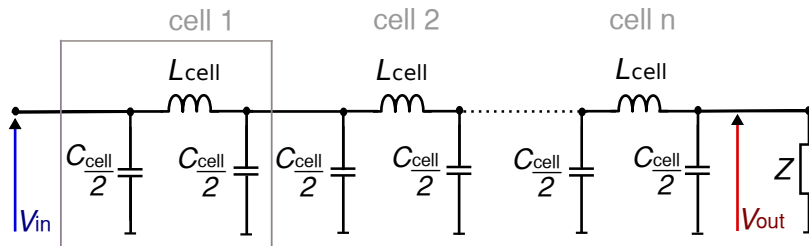


Figure 3.4 – Simplified equivalent electric circuit of a transmission line kicker magnet.

To avoid reflections, the characteristic impedance of the entire system is matched: the characteristic impedance of each central cell of the kicker magnet is given by:

$$Z = \sqrt{\frac{L_{\text{cell}}}{C_{\text{cell}}}}. \quad (3.4)$$

Neglecting end effects, the total inductance of the magnet is:

$$L_m = nL_{\text{cell}}. \quad (3.5)$$

The length of the kicker magnet module ( $l_{\text{unit}}$ ), can be calculated as:

$$l_{\text{unit}} = \frac{L_m}{L_m/m}. \quad (3.6)$$

The "fill time" ( $\tau_m$ ) of the magnet is the delay required for the pulse to travel either one way, if the magnet is terminated in its characteristic impedance, or two ways, if the magnet is terminated in a short circuit. For the first case:

$$\tau_m = n\sqrt{L_{\text{cell}}C_{\text{cell}}} = n\frac{L_{\text{cell}}}{Z} = \frac{L_m}{Z}. \quad (3.7)$$

The magnetic flux ( $\Phi$ ) inside the aperture of the magnet starts to build-up at the beginning of the rising edge of the pulse entering the kicker magnet. For a magnet terminated in its characteristic impedance, neglecting any flat-top ripple, the magnetic flux reaches its flat-top value with the end of the rising edge of the same pulse exiting the kicker magnet (see Fig. 3.5). The magnetic flux is calculated as:

$$\Phi = \int (V_{\text{in}} - V_{\text{out}}) dt. \quad (3.8)$$

Let us introduce  $\tau_c$  as the rise time of the pulse from the pulse generator. In general, it holds that  $\tau_c \ll \tau_m$  (see Fig. 3.5). The rise time of the magnetic flux is:

$$\tau_r \simeq \tau_c + \tau_m. \quad (3.9)$$

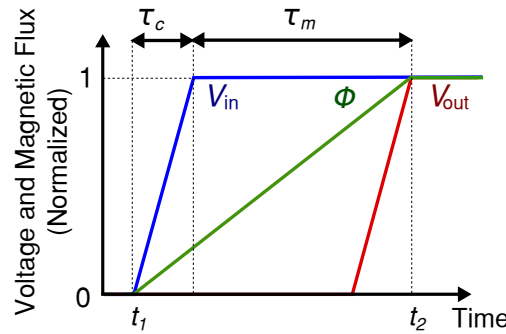


Figure 3.5 – Build-up of the magnetic flux inside the kicker magnet.



### 3.2. Injection kicker magnets of the Large Hadron Collider (LHC MKI)

The pulse cannot significantly degrade while travelling through the kicker magnet, thus the cut-off frequency is an important parameter. Let us introduce  $L_p$  as parasitic inductance in series with the capacitance of each cell of the kicker magnet. The cut-off frequency of a cell is:

$$f_c \simeq \frac{1}{\sqrt{(L_{\text{cell}} + 4L_p)C_{\text{cell}}}}. \quad (3.10)$$

To achieve a high cut-off frequency,  $L_p$  should be minimized. In addition,  $L_{\text{cell}}$  must be small, therefore the cell's length should be minimized. However, the cells cannot be too short in order to provide adequate insulation between high voltage and ground capacitance plates and to limit the complexity and cost of the kicker magnet.

In general, the required  $\tau_r$  determines the choice of characteristic impedance, for a given available length of the kicker magnet. The higher  $Z$ , the smaller the value of  $\tau_m$  (see Eq. 3.7) and hence  $\tau_r$  (see Eq. 3.9) can be achieved, but a longer length of the kicker installation and/or higher voltage is necessary.

#### 3.1.5 Beam coupling impedance considerations

Kicker magnets with ferrite cores are known to have significant beam coupling impedance. In particular, interaction of a high intensity beam with the real component of the longitudinal beam coupling impedance can result in high power deposition in the ferrite yoke [13, 15, 50]. This carries a significant risk that the ferrite yoke will exceed its Curie temperature: hence, electromagnetic shielding is necessary. In addition, kicker magnets typically used at CERN are installed in machine vacuum [49]. Hence, the beam screen has to satisfy often conflicting requirements of fast field rise and fall times with low ripple, low beam coupling impedance, good high voltage performance, low secondary electron yield (SEY), radiation resistance, high temperature resistance to withstand temperatures up to 350°C during bake-out to provide compatibility with ultra-high vacuum. Below, the main features of the so-called "conventional" beam screen design used for the injection kicker magnets of the Large Hadron Collider (LHC MKIs) will be reviewed together with the specification of the LHC MKI parameters.

## 3.2 Injection kicker magnets of the Large Hadron Collider (LHC MKI)

### 3.2.1 LHC injection kicker system parameters

The LHC has two injection kicker systems, named MKI2 and MKI8, to inject two counter rotating beams. For proton beams, the injection energy is 450 GeV. Each system consists of 4 transmission line kicker magnets named A, B, C and D, 4 PFNs and 2 RCPS: magnet D is the first to see the injected beam. The LHC kicker system parameters are summarized in Table 3.1. Figure 3.6 shows a schematic drawing of the LHC MKI cross-section. A photograph of the upstream end of the LHC MKI is shown in Fig. 3.7. Here, the injected beam and the counter rotating circulating beam are depicted. The LHC MKI during assembly is shown in Fig. 3.8.

Table 3.1 – LHC injection kicker system parameters [51].

Parameter	Value	Unit
Number of magnets per system	4	-
Kicker strength per magnet	0.3	T·m
Number of cells per magnet	33	-
Characteristic impedance	5	$\Omega$
Designed magnet voltage	27	kV
Aperture height/width	54/54	mm
Magnetic field flat-top duration	up to 7.86	$\mu$ s
Designed field rise time 0.5%-99.5%	0.9	$\mu$ s
Designed field fall time 99.5%-0.5%	3	$\mu$ s
Beam screen inside diameter	38	mm
Magnet length	2.7	m

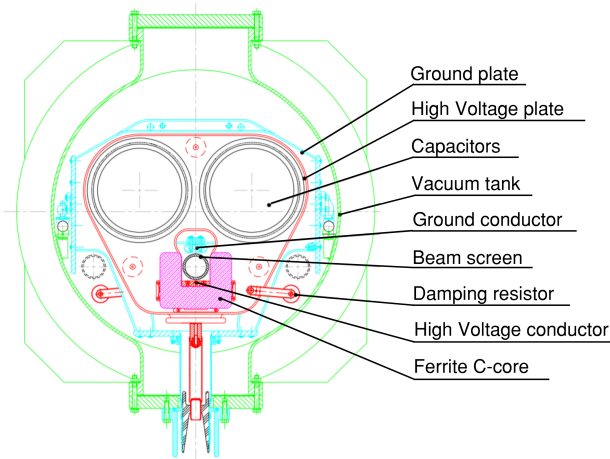


Figure 3.6 – Drawing of the LHC MKI cross-section [51].

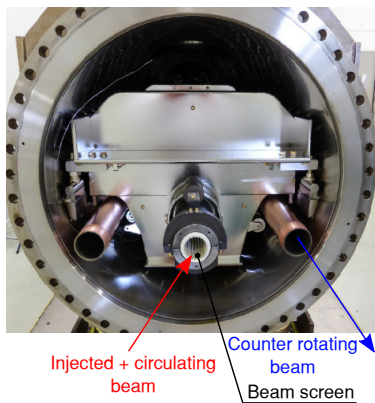


Figure 3.7 – Photograph of the upstream end of the LHC MKI.

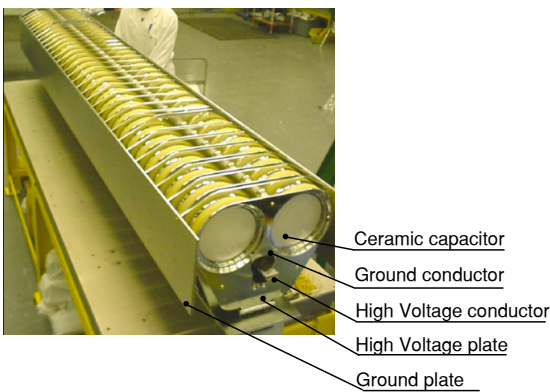


Figure 3.8 – Photograph of the prototype LHC MKI during assembly.

### 3.2.2 Conventional beam screen design

The LHC MKI beam screen consists of 24 NiCr (80%/20%) conductive wires, which are straight, 2.7 mm wide and 0.8 mm thick. The screen conductors are inserted into grooved slots in the inner wall of a ceramic tube (99.7% alumina) that is placed in the aperture of the kicker magnet (see Fig. 3.7). The screen conductors provide a path for the beam image current and therefore screen the ferrite yoke from the electromagnetic fields induced by the circulating beam. In order to preserve a fast magnetic field rise time, the screen conductors are capacitively coupled to a grounded metallic cylinder at the upstream end of the kicker magnet, at which the beam enters the kicker magnet (see Fig. 3.9), and are directly connected to the, grounded, vacuum chamber at the other end (see Fig. 3.10). A CATIA model of the LHC MKI beam screen at the upstream end of the kicker magnet is shown in Fig. 3.11.

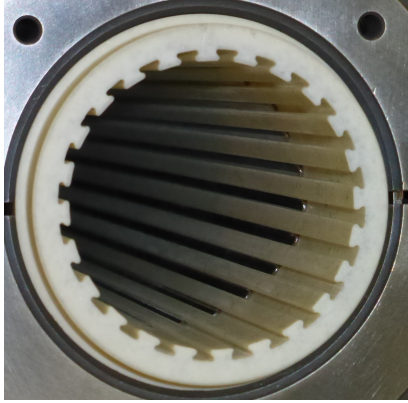


Figure 3.9 – Photograph of the upstream end of the beam screen with capacitively coupled screen conductors.

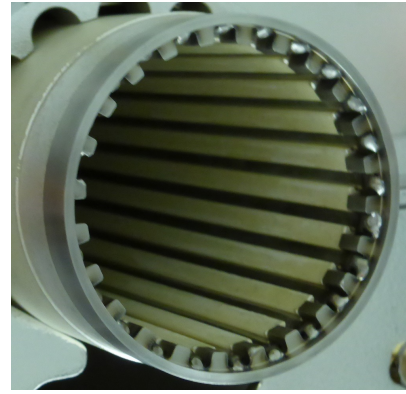


Figure 3.10 – Photograph of the downstream end of the beam screen with grounded screen conductors connected all together.

Due to the capacitive coupling, an open-ended resonating cavity is formed in the region where the screen conductors overlap with the outer metallic cylinder. Hence, the structure exhibits resonant behaviour. The resonances in the longitudinal beam coupling impedance spectrum of the kicker magnet with the conventional beam screen are expected to occur at the frequencies [52]:

$$f_{\text{conv}}^{(n)} = \frac{nc}{2\sqrt{\epsilon_{r,\text{eff}}}(L_{\text{overlap}} + \delta_{\text{fringe}})}. \quad (3.11)$$

In the above formula,  $n$  is an integer,  $\epsilon_{r,\text{eff}}$  is the effective relative permittivity of the volume between the outer metallic cylinder and the overlap of the screen conductors,  $L_{\text{overlap}}$  is the length of the overlap between the metallic cylinder and longest screen conductor,  $\delta_{\text{fringe}}$  is the effective increase in length due to fringe fields.

Another feature of the LHC MKI beam screen are toroidal ferrite rings mounted around each end of the ceramic tube, outside of the aperture of the kicker magnet. Each set of nine rings consists of two types of alternatively arranged Ferroxcube NiZn ferrites: 4M2 and 4B3, with

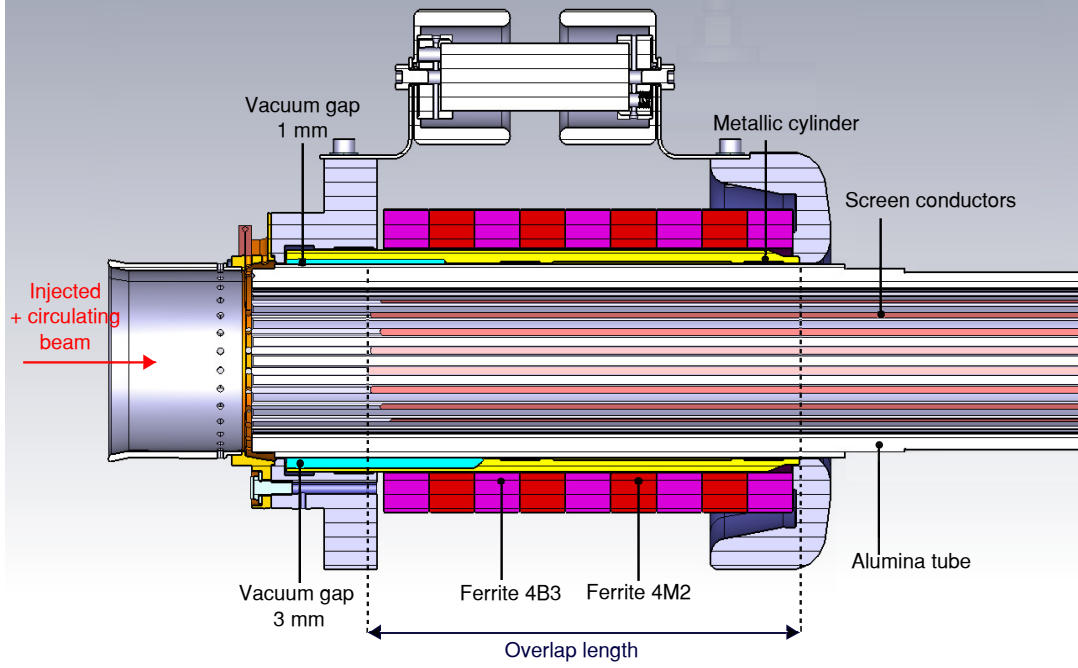


Figure 3.11 – LHC MKI beam screen at the upstream end of the kicker magnet (CATIA model).

a Curie temperature of 200°C [53] and 250°C [54], respectively. Originally, these ferrites were mounted to damp low frequency modes [19]. Importantly, they can serve as a damping material to absorb beam induced power before it is deposited in the ferrite yoke.

At the upstream end, between the alumina tube and the metallic cylinder, there is a vacuum gap (see Fig. 3.11), which has been introduced to reduce electric field associated with screen conductors. The vacuum gap is of 1 mm width at the top of the beam screen and of 3 mm width at the bottom. To further reduce the electric field, and hence decrease the probability of electrical breakdown, the conductive wires have graded lengths at the upstream end. The vacuum gap extends 22.5 mm beyond the end of the longest screen conductor at the top of the beam screen and 33.5 mm at the bottom. The vacuum gap and graded lengths were introduced in 2013 [55] and are part of the so-called "post-LS1" design. In the LHC, all the injection kicker magnets have such a design. For all LHC MKIs, except the MKI8D installed during the Year End Technical Stop (YETS) 2017/18,  $L_{\text{overlap}} = 130$  mm.

### 3.2.3 High voltage issues

During magnetic field rise and fall, a significant voltage is induced on the beam screen conductors. Figure 3.12 presents a drawing of the beam screen inside of the aperture of the kicker magnet. The voltage induced ( $V_i$ ) on the  $i$ -th screen conductor is:

$$V_i = \frac{d\Phi}{dt} = \frac{dB}{dt} (d + R - y_i) L, \quad (3.12)$$

### 3.2. Injection kicker magnets of the Large Hadron Collider (LHC MKI)

where  $L$  is the length of the screen conductor within a uniform magnetic field  $B$  inside the aperture of the kicker magnet,  $R$  is the beam screen radius,  $d$  is the distance from the GND busbar to the beam screen and  $y_i$  is the coordinate of the screen conductor on the  $y$ -axis. Hence, the highest voltage is induced on the screen conductor furthest from the GND busbar, which is the conductor adjacent to the HV busbar (#1 in Fig. 3.12), while the lowest voltage is induced on the screen conductor closest to the GND busbar (#13).

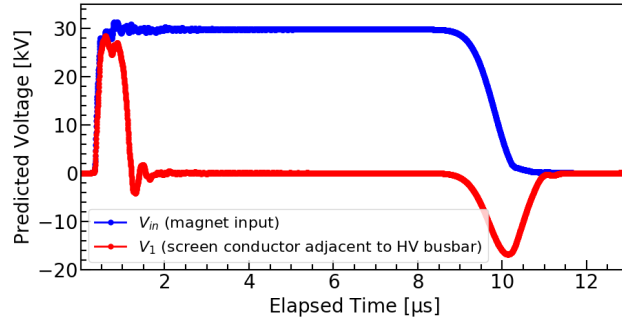
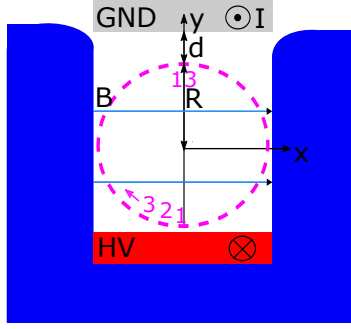


Figure 3.12 – Screen conductors inside the kicker magnet aperture. Figure 3.13 – Magnet voltage and voltage of screen conductor adjacent to HV busbar (for 60 kV PFN voltage) [56].

The voltage is induced during the rise and fall of the magnetic field, when the time derivative of the magnetic field is non-zero. In particular, the induced voltages are positive during magnetic field rise and negative during magnetic field fall. Figure 3.13 presents voltage induced on a single screen conductor adjacent to the HV busbar (red curve). The positive peak is approximately twice the magnitude of the negative peak: for the LHC MKI, the rate of change of the magnetic field during field rise is faster than during field fall. The magnet input voltage is also indicated in Fig. 3.13 (blue curve). Figure 3.14 shows the maximum induced voltage for each of the 24 screen conductors (blue curve), as well as the maximum induced voltage for every two neighbouring screen conductors (pink curve). Voltage breakdowns, along the surface of the alumina tube, between neighbouring screen conductors or between screen conductors and metallic cylinder are a concern during kicker magnet operation, and issues have occurred [55, 57].

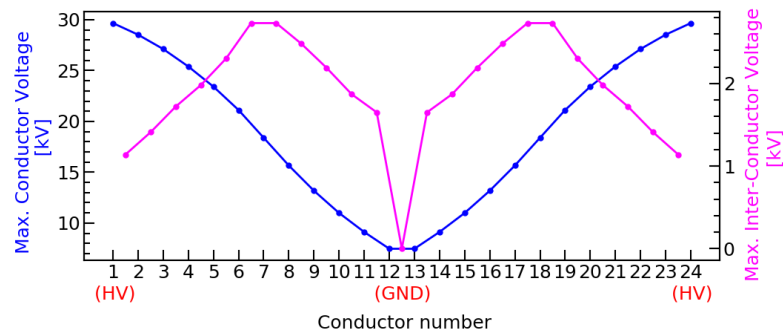


Figure 3.14 – Maximum conductor and inter-conductor voltages (for 60 kV PFN voltage) [56].

Extensive studies have been carried out to optimize the HV performance of the LHC MKI. The initial design of the beam screen consisted of 24 straight silver painted stripes, which provided low beam coupling impedance, but did not flashover on the beam screen until only 15 kV PFN voltage (54 kV required). In 2006, an improved design was developed with 24 solid screen conductors  $0.7 \text{ mm} \times 2.4 \text{ mm}$  with rounded corners allowing for 30 kV PFN voltage without flashover [58]. In 2008, 9 conductors closest to the HV busbar were removed to reduce the maximum electric field by 20%. In addition, the lengths of the 15 remaining screen conductors were graded, to further reduce the maximum electric field. This allowed to achieve 49 kV PFN voltage without flashover, but the total beam induced power deposition into the magnet was increased by a factor of  $\sim 3$  with respect to the initial design. In 2012, a total of 5 conductors closest to the HV busbar of one MKI were removed allowing to sustain 50 kV PFN voltage, however the missing screen conductors increased total deposited power by a factor of  $\sim 1.5$  with respect to 24 screen conductors [55]. Note, the increase in beam induced powers are based on resonant measurements, which we now know may miss resonant peaks – hence the increase is approximate. Finally, the "post-LS1" design permitted installation of 24 solid screen conductors: the required PFN voltage, without flashover, was achieved by introducing the aforementioned vacuum gap and grading of the screen conductor lengths at the upstream end (see Fig. 3.11) [56]. In 2017, for MKI8D magnet,  $\text{Cr}_2\text{O}_3$  coating was applied on the inner surface of the alumina tube, to increase by  $\sim 30\%$  the breakdown voltage in vacuum. In addition, the maximum SEY of virgin alumina is  $\sim 9$ . Experimental studies show that  $\text{Cr}_2\text{O}_3$  coating reduces the maximum SEY to 2.3 or less: this decreases to 1.4 with beam conditioning. Hence, dynamic pressure rise, due to electron cloud, is reduced and therefore the probability of an electrical breakdown [59].

#### 3.2.4 Heating problems

During Run 2, the measured temperatures at the upstream end of the LHC kicker magnets were significantly higher than those at the downstream end [19]. Subsequently electromagnetic simulations predicted that the power deposition in the LHC MKI is expected to be non-uniform [60]. From Eq. 3.11, reducing  $L_{\text{overlap}}$  by shortening the length of the metallic cylinder allows to shift impedance peaks to higher frequencies. Hence, a design with  $L_{\text{overlap}} = 70 \text{ mm}$  was suggested [60], which could reduce the total power deposition by 20%. Next, a reduction to  $L_{\text{overlap}} = 56 \text{ mm}$  was proposed and a prototype magnet (MKI8D), with this overlap, was installed in the LHC in YETS 2017/18. In comparison with the post-LS1 design, the power in the upgraded magnet is expected to be deposited mostly in the ferrite rings at the upstream end of the magnet, leading to a significant reduction of the heat load in the ferrite yokes [61]. Nonetheless, for Run 3 with High Luminosity type beams, unless other mitigating measure were taken, the power deposition in the kicker magnets will be unacceptably high, therefore a water cooling circuit for the ferrite rings has been developed [62]. To provide an experimental verification of the predicted power deposition, novel power deposition distribution measurements have been performed using a single wire frequency domain method. The experimental technique and the results will be discussed in Chapter 5.

### 3.3 Analysis of thermal data and the LHC MKI waveforms

#### 3.3.1 Soft Start

Mis-injection of the beam into the LHC can result in damage to downstream equipment. For this reason, a so-called "Soft Start" (SS) operation mode was originally foreseen to ensure the kicker magnets are properly HV conditioned, prior to injection, to minimize the probability of a breakdown in the kicker magnet during injection. The SS mode is executed when there is no beam in the LHC, before filling the LHC. During the SS, the PFN voltage is gradually increased, until the voltage holding capability is approximately 6% above the nominal required for injection into the LHC. At a relatively low SS voltage, an increase in pressure can be observed following a period with high intensity circulating beam: this effect is attributed to release of charge trapped in the alumina tube during a physics run. Hence, pulsing of the magnet, starting at a relatively low voltage, is necessary to release this charge. Otherwise, if the kicker magnet is pulsed directly at HV, a more serious surface flashover could occur, resulting in possible damage to the alumina tube. During the SS, after voltage ramping, the pulse duration is enlarged at a voltage a few percent above the nominal value [63], until the pulse duration is approximately 10% greater than the maximum pulse duration (7.86  $\mu$ s) required for injection. During a SS, the time between pulses is typically 10 s.

The beam induced power deposition can result in a temperature increase of the ferrite yoke above its Curie temperature ( $T_C$ ), which would impact the ability to inject the beam. Due to HV reasons, PT100 temperature sensors cannot be mounted on the ferrite yoke, instead they are on the side plates of the MKI, so no direct measurement of the ferrite yoke temperature is available [59]. Hence, importantly, the SS mode is now also used as a diagnostic tool to verify whether the temperature of any part of the ferrite yoke is at the Curie temperature following a long physics run. The MKI magnet yoke is made of either CMD5005 or 8C11 ferrite. Both types have  $T_C \sim 125^\circ\text{C}$  [64, 65]. In dedicated measurements, it has been shown that electromagnetic properties of ferrites are temperature dependent (see Chapter 8). In particular, the magnetic permeability drastically decreases once the temperature of the ferrite approaches its  $T_C$ . In this case, Eqs. 3.1-3.2 are no longer valid. Also, the kicker magnet inductance significantly reduces [66]. In turn, an inductance reduction leads to a decrease of the magnet fill time (see Eq. 3.7). A more rapid reduction in the magnet fill time is a clear indication to prohibit injection, as one or more ferrite cells may have exceeded their  $T_C$ .

The analysis of LHC MKI waveform parameters during the SS is the only reliable method to verify the state of the ferrite yoke. For machine protection reasons, Software Interlock System (SIS) thresholds inhibit beam injection into the LHC if any of the MKI temperature sensors indicate a temperature above pre-set interlock limits. Hence, a rapid evaluation of the ferrite yoke status is crucial, as this can affect machine turn-around time. To assess the ferrite status, a representative distribution of analysed SS events is required in order to distinguish an abrupt downward trend in magnet delay time. The SIS thresholds are gradually increased, from a low level, as experience demonstrates that the measured temperature is consistent with a yoke

temperature below its Curie point. If an interlock threshold is reached, and provided that the temperature of the yoke is below its  $T_C$ , the SIS temperature limit is typically increased by  $1^\circ\text{C}$  above the measured temperature. An increase of  $1^\circ\text{C}$  is chosen as, if the first ferrite yoke reaches its  $T_C$ , as a result of the non-linear power deposition, the second yoke is expected to be almost  $10^\circ\text{C}$  cooler [59]: thus only one yoke (3.03% of a magnet, 0.75% of a kicker system) would exceed the  $T_C$ . Studies show that this would give an acceptable mis-kick [67]. Until now, the SS data analysis has been associated with several limitations, i.e. long analysis time and limited amount of data that can be analysed at once. Hence, a dedicated Python code PyMKITemp has been developed to quickly analyse all the historical SS data. In addition, PyMKISS code has been implemented in order to provide a real-time SS data analysis and storage of the results in the CERN Timber Database (MDB), thus allowing rapid validation of the LHC MKI ferrite yoke state for a safe injection.

#### 3.3.2 PyMKITemp

The PyMKITemp is used for long-term SS data analysis. The data is imported from the CERN Timber Measurement DataBase (MDB) or Timber Logging DataBase (LDB) using PyTimber [68]. The parameters of the LHC MKI waveform are recorded by the Internal Post Operational Check (IPOC) system. For each of the 16 magnets, the following IPOC variables are imported and analyzed:

- **T\_RISETIME:**

The rise time (in  $\mu\text{s}$ ) of the pulse is measured at the terminating resistor (TMR) (see Fig. 3.2) from 5% to 95% of the average flat-top magnitude. It is significantly longer than the rise time of the pulse produced by the power generator ( $\sim 30\text{ ns}$ ), as the higher frequency components of this pulse are attenuated during propagation through the magnet. The exact frequency content which is preserved, depends on the cut-off frequency of each cell and the number of cells. Note, the ceramic capacitors have a temperature coefficient  $TCC = -800\text{ ppm}/^\circ\text{C}$  [69]. Thus, a temperature increase leads to a decrease in the cell's capacitance. Until the ferrite approaches  $T_C$ , the inductance of the magnetic circuit of the cell does not vary significantly. If this occurs, the inductance can decrease rapidly, which leads to a more rapid increase in the cut-off frequency. Hence, as the cut-off frequency increases (see Eq. 3.10), the rise time of the pulse at the TMR reduces.

- **T\_DELAY:**

The delay time (in  $\mu\text{s}$ ) is defined as the time between the RF injection pre-pulse and 95% of the pulse rise time at the TMR. In fact, it is a combination of the thyatron switch turn-on delay, propagation delay time through transmission cables and magnet and TMR pulse rise time: hence it is susceptible to time jitter due to the thyatron turn-on delay.

- **CPU-UP - CPU-DOWN:**

The magnet delay time (in  $\mu\text{s}$ ) is measured by capacitive pickups (CPUs) installed at the input and output of the kicker magnet, respectively. The measured signals are each



obtained using a CPU which faces the HV input and output busbars, respectively. Each of these two signals is the delay time between RF injection pre-pulse and 50% of the maximum voltage measured at the pickup. Since both measured signals include the same thyatron time jitter, the difference of these signals eliminates this potential error. The delay time measured in this way is the most sensitive parameter to temperature of the ferrite yoke, as it is proportional to the square root of the cell's inductance (Eq. 3.7), whereas the cut-off frequency of the cells, which directly influences the rise time of the output waveforms of the kicker magnet, depends also on parasitic inductance (Eq. 3.10) and is thus less sensitive to the cell inductance. Note, magnet delay time is also sensitive to the cell capacitance variation with temperature. The LHC MKI delay time measurement by CPUs was implemented in YETS 2017/18.

- **I\_STRENGTH**

The magnitude of the flat-top (in kA) of the TMR current.

- **T\_LENGTH:**

The duration (in  $\mu\text{s}$ ) of the pulse in the TMR, measured at the 95% level.

- **T\_MAGNET\_UP, T\_MAGNET\_DOWN:**

The temperatures measured (in  $^{\circ}\text{C}$ ) at the upstream and the downstream end, respectively, of each MKI.

To distinguish each SS from the nominal operation, the IPOC data is filtered by the Python routine according to certain criteria. In particular, there are two different values for T\_DELAY, one for nominal operation and one for the SS. For the SS, T\_DELAY is in the range 50  $\mu\text{s}$  to 56  $\mu\text{s}$ . In addition, the Python routine selects data for which I\_STRENGTH is above 4.8 kA and T\_LENGTH is greater than 4.3  $\mu\text{s}$ . As the measured waveforms are not ideal trapezoids, and include features such as overshoot or undershoot, filtering on T\_LENGTH ensures that average magnitude of the flat-top calculated by IPOC is not significantly affected by the aforementioned factors. Note: this is important for the rise time and delay time measurement at the TMR. To reduce statistical noise, the values of analyzed variables calculated for each pulse during a SS, which meets the criteria, are averaged. In particular, the results are averaged from 17 pulses or 34 pulses, depending whether a short SS or long SS is executed.

The temperatures at the upstream and downstream end of each magnet are recorded at pre-set time slots, every 5 minutes. These readings are not synchronized with IPOC data. This requires that the Python processing interpolates the temperature values at the timestamps from IPOC: there is very little loss in accuracy, as the thermal time-constants for the ferrite yoke are tens of hours [69]. The filtered data represents all of the points belonging to any individual SS. Provided there is time interval of 500 s between consecutive filtered points, the data is treated as belonging to separate SS events. In fact, it could be any time interval shorter than this, but longer than the time between two pulses (typically 10 s). Once all of the SS events are distinguished, the data is analyzed (see Figs. 3.15, 3.16).

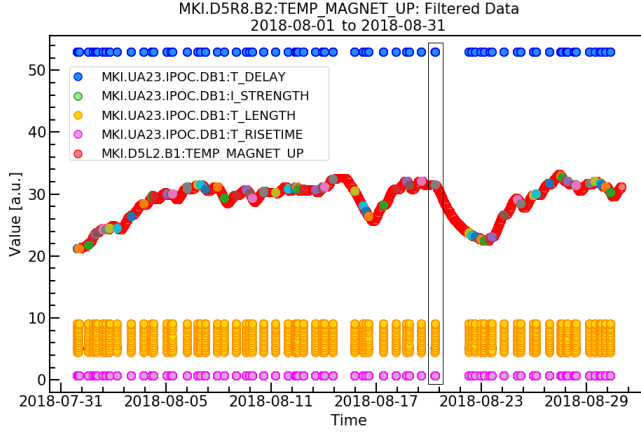


Figure 3.15 – Example of filtered SS data for MKI8D (collected for 1 month of LHC operation). A single SS is indicated in the black rectangular window (zoomed in Fig. 3.16).

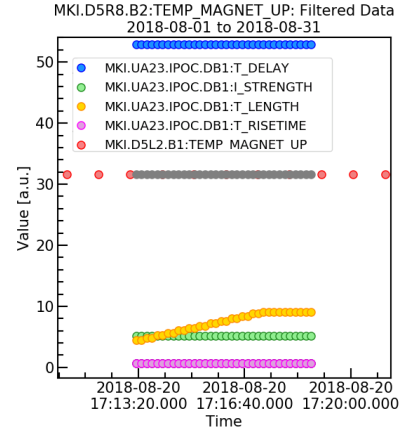


Figure 3.16 – MKI8D parameters during a single SS. The temperature is interpolated at IPOC timestamps (grey dots).

The temperature dependent variables are the rise time of the pulse, delay time with respect to RF injection pre-pulse and delay time of the kicker magnet. The output of the analysis, for each pulse in a SS which meets the analysis criteria, is the average value of each parameter and the average temperature during the SS. Figure 3.17 presents the temperatures measured at the upstream end of MKI8D during the period of 01.06.2017 - 01.09.2017, as well as the SIS interlock limits. The average rise time during each SS is depicted in Fig. 3.18. A strong correlation between the increase in temperature and the decrease in the average rise time is observed.

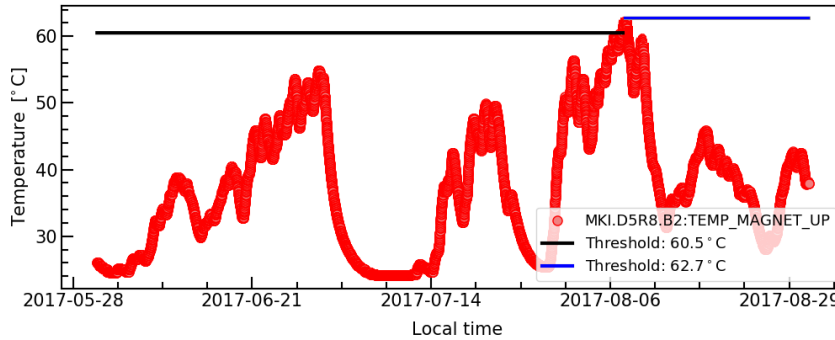


Figure 3.17 – Temperature measurements at the upstream end of MKI8D with respect to time.

In addition, we show also the average rise time measured at the TMR and average delay time measured by capacitive pickups as a function of average temperature during each SS (see Figs. 3.19-3.20). In this case, the analysis is performed for the time period of 25.06.2018 - 15.09.2018 for the magnet MKI8C. In particular, this magnet reaches the highest temperatures after the upgrade of MKI8D. It can be observed that the temperature variation of the delay time measured by capacitive pickups is much less susceptible to noise.

### 3.3. Analysis of thermal data and the LHC MKI waveforms

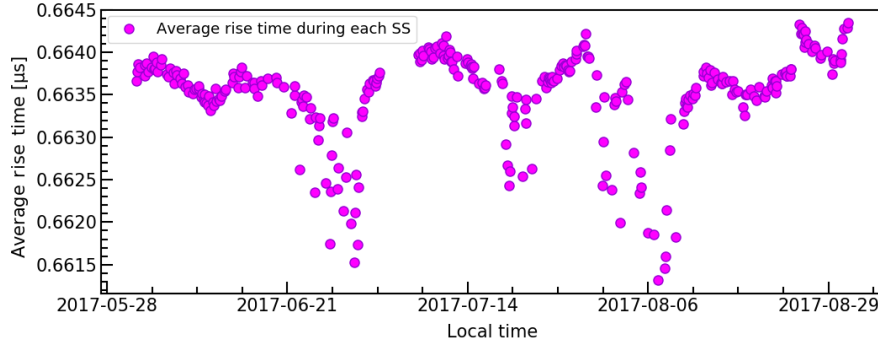


Figure 3.18 – Average rise time at TMR during each SS with respect to time (MKI8D).

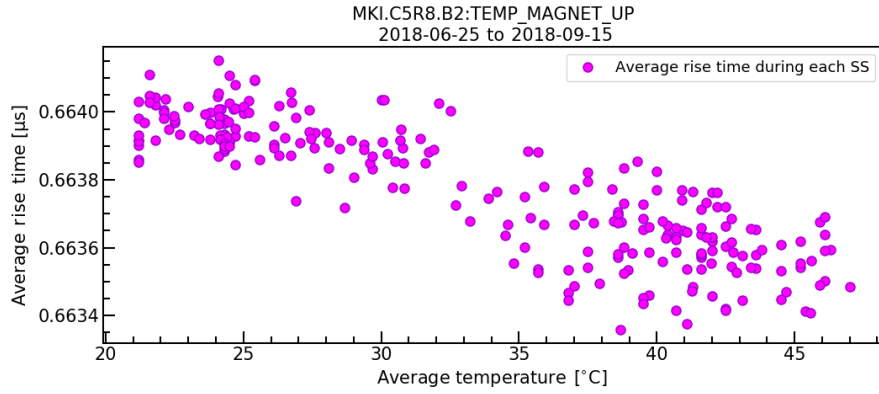


Figure 3.19 – Average rise time at TMR versus average temperature during each SS (MKI8C).

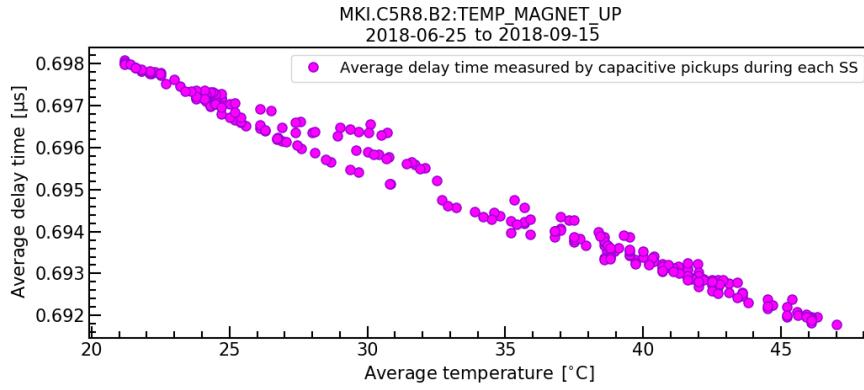


Figure 3.20 – Average delay time versus average temperature during each SS (MKI8C).

In Figure 3.20, the data points follow along a line. As mentioned, the capacitance of each cell of the kicker magnet linearly decreases with temperature. The temperature coefficient of ceramic capacitors is  $TCC = -800 \text{ ppm}/^\circ\text{C}$  [69]. Let us define, the values of  $C_{\text{cell}}$  and  $L_{\text{cell}}$  are measured at an ambient temperature  $T_0 = 20^\circ\text{C}$ . Hence, the magnet delay time (see Eq. 3.7) at

temperature  $T \geq T_0$  is:

$$\tau_m(T) = n\sqrt{L_{\text{cell}}C_{\text{cell}}(1 + (T - T_0)TCC)} = A\sqrt{1 + (T - T_0)TCC} \stackrel{TCC < 1}{=} A\left(1 + \frac{T - T_0}{2}TCC\right), \quad (3.13)$$

where  $A = \tau_m(20^\circ\text{C}) = n\sqrt{L_{\text{cell}}C_{\text{cell}}}$  is a constant. Hence, we expect a linear behavior of the average delay time as a function of temperature. Note: if the first cell of the kicker magnet were to be above its  $T_C$ , the delay time would decrease by 20 ns. However, in Fig. 3.20, no abrupt changes in the average delay time are observed. Hence, the temperature of the ferrite yoke is below its  $T_C$ .

#### 3.3.3 PyMKISS

The PyMKISS module has been designed to provide real-time data analysis. It uses several Python libraries developed at CERN, i.e. PyLSA, PyJapc and PyTimber [68, 70]. In addition, it is supported by PyMKITemp library. The PyMKISS project constitutes of two executable scripts: one for the SS analysis (SoftStartAnalysis.py) and one for SIS temperature interlock monitoring (SISTemperatures.py) [71].

For the SS analysis, the strategy is to query information every minute about the last SS end timestamp using PyJapc. This information can be accessed only through the CERN Technical Network. When a SS occurs, measurement data is collected from CERN Timber Database (MDB) for the following time interval: 5 minutes before the SS end until 30 seconds after the SS end. In particular, the margin of 30 seconds after the SS end ensures that the MKI waveform data is already logged to the CERN Timber Database. The analysis of each SS takes only a few seconds. The outcome is saved back into the Front End Software Architecture (FESA) server, from which the CERN Timber Database reads the data. Using this algorithm, the SS analysis results are present in the CERN Timber Database no later than 1.5 minutes after the SS end.

For SIS temperature interlock monitoring, the current SIS temperature interlock thresholds are imported via PjLSA package. The program queries the temperature measurement and SIS interlock thresholds, for both the upstream and the downstream end of each kicker magnet, every minute, using PyTimber. The outcome of the analysis are the temperature thresholds and the relative temperatures with respect to the interlocks. These values are saved back into CERN Timber Database every 1 minute.

#### 3.3.4 Achievements

The PyMKITemp code has shown great capability to analyse large amounts of data in a short period of time. It proved to be valuable on 8<sup>th</sup> August 2017, when the temperature of the magnet MKI8D exceeded its SIS interlock threshold (see Fig. 3.17). The analysis allowed to confirm that the temperature of ferrite was below its  $T_C$  and thus it was permissible to

### **3.3. Analysis of thermal data and the LHC MKI waveforms**

---

increase the interlock threshold within minutes, hence there was no need for the magnet to cool down and no need to prevent injection into the LHC. Based on the SS analysis algorithm implemented in PyMKISS, the SS analysis has been extended into a real-time process: the results are continuously stored in the CERN Timber Database.



## 4 Design of the injection kicker magnet for FCC-hh

This chapter provides an overview of the beam injection into the FCC-hh with a particular focus on the injection kicker system. In the first section, the baseline design of the injection insertion is discussed. Next, the requirements, design goals and challenges for the injection kicker magnets are identified and explained. Finally, the proposed optimization of the FCC-hh injection kicker system is described and the hardware parameters of the kicker magnets are presented. In the second section, an analytical estimate of the power deposition in the unshielded kicker magnet is presented and the need for a beam screen is confirmed. In the last section, the design of a single kicker magnet module is discussed. This part of the thesis is partially based on the work published in Ref. [18].

### 4.1 The FCC-hh injection system at 3.3 TeV

The baseline injection energy for the FCC-hh at CERN is 3.3 TeV. In this case, the LHC is expected to be modified and used as a High Energy Booster (HEB) injector [72]. Lower injection energies have also been studied, for instance beam injection at 1.3 TeV [7]. Nevertheless, the baseline option is in the scope of this thesis and will be discussed further. The main constraint for the injection system at 3.3 TeV is the beam energy of 560 MJ for HEB to FCC transfer. Studies have shown that LHC injection protection absorbers, during operation with HL-LHC beam parameters, can survive a maximum beam impact of  $\sim 5$  MJ [7] with the expected beam sizes. In particular, the same threshold is foreseen for the protection devices in FCC [72]. Due to machine protection constraints, it follows that a maximum of 80 bunches can be safely transferred at a time. The target FCC fill factor is 80% (10400 bunches). Hence, each FCC ring will be filled by 130 batches of 80 bunches. The revolution period of the machine is 326  $\mu\text{s}$ . Within this time, approximately 10  $\mu\text{s}$  of beam free gaps is foreseen for low intensity beam, a so-called pilot beam, injections and abort gap(s). To enable a faster synchronous beam abort in case of an erratic triggering of a single extraction kicker, the possibility of introducing 4 equally distributed abort gaps is also considered [73].

### 4.1.1 Injection layout

The FCC-hh baseline foresees a double plane injection with a schematic layout shown in Fig. 4.1. The Lambertson septum vertically deflects the injected beam and the kicker magnet compensates for the remaining angle in the horizontal plane: a defocusing quadrupole in the horizontal plane (QD) bends the beam outward in the horizontal plane, thereby reducing the necessary kick strength. The required deflection takes into account the quadrupole cryostat radius of 540 mm. The RMS beam size at injection is  $\sigma_{\text{RMS}} = 0.8$  mm. Assuming  $\pm 15\sigma_{\text{RMS}}$  for beam diameter,  $\pm 2.5$  mm for orbit distortion and alignment errors and  $\pm 1.5$  mm for injection oscillations, the minimum beam pipe diameter is 32 mm. The injection beam dump is located downstream of the kicker magnet and provides protection against a mis-kicked beam. The injection region has a FODO lattice with a half-cell length of 150 m. The initial length of the injection kicker system was foreseen to be from 120 m to 130 m [74, 75]. However, it is desirable to utilize a shorter kicker system length due to beam impedance reasons. Nevertheless, the length must be consistent with the ability of a pulse generator to supply the required current. In addition, the required deflection angle decreases when reducing the physical length of the kicker magnets. Hence, in the proposed design, the kicker magnet system length has been reduced to  $\sim 40$  m and moved to the end of the half-cell, with a phase advance of  $90^\circ$  in both planes to the internal dump. The required deflection angle for the kicker system, having a physical length in the range of 30 m to 40 m, is 0.18 mrad.

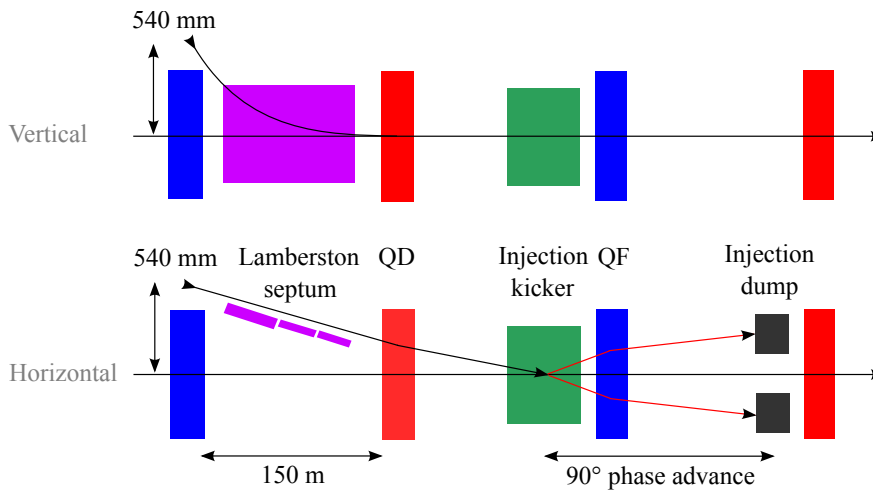


Figure 4.1 – Schematic layout of the FCC double plane injection system.

### 4.1.2 Optimization of the injection kicker system

The design of the injection kicker system has to be optimized for numerous requirements. The hardware parameters are determined by the beam size at injection and the compatibility with the pulse power generator. As already mentioned, the length of the injection kicker system should be minimized to limit the beam coupling impedance for the installation, but



consistent with the capabilities of the pulse generator. In addition, for a high beam current and short bunch length, the real component of the longitudinal beam coupling impedance together with the beam spectrum, is expected to result in a high power deposition in the kicker magnet: hence impedance shielding might be a critical feature. However, a suitable beam screen, placed in the aperture of each kicker magnet, will increase the aperture dimensions. Hence, for the FCC injection kicker system, two options have been studied. In the first approach, we analyzed parameters of the kicker system composed of unshielded magnets, thus assuming that the horizontal and vertical dimensions of the rectangular aperture are equal to the minimum FCC beam pipe diameter of 32 mm. In the second case, the aperture has been increased to 48 mm, to allow for a beam screen with a thickness of 8 mm (as per the LHC MKI beam screen [51]).

To inject 80 bunches separated by 25 ns, the field flat-top duration is specified to be 2  $\mu$ s. To limit beam emittance blow-up due to injection oscillations, the reflections and the flat-top ripple of the field must be lower than  $\pm 0.5\%$ . Based on the proposed filling scheme, the field rise time of the kicker magnet must not be greater than 0.43  $\mu$ s (including any field overshoot, undershoot or ripple outside of the tolerance of  $\pm 0.5\%$ ). The field fall time requirements are less strict. The kicker field fall time must be no longer than the length of the abort gap, so as to not disturb the circulating beam. Hence, with a single abort gap, the field fall time cannot exceed  $\sim 6 \mu$ s, whereas for the design with 4 distributed abort gaps, the field fall time cannot exceed  $\sim 1.75 \mu$ s [73]. To meet the requirements for fast field rise and fall times, ferrite loaded transmission line type magnets will be used, similar to the ones used for the injection into the LHC (see Chapter 3).

The pulse generator of the injection kicker system must be highly reliable in order to achieve a low probability of any misfiring (also known as an erratic, or untriggered, turn-on). In a conventional kicker system design, the PFN or PFL is discharged through a thyatron switch to generate the current pulse for the kicker magnet (see Fig. 3.2). However, a significant drawback of the conventional design is the occasional erratic turn-on of the thyatron switch. In accelerators such as the LHC, the PFNs are rapidly charged starting a few milliseconds before the injection kickers are required: this keeps to a reasonable minimum the time for which high voltage is across the thyatrons [76]. Nevertheless, erratic turn-ons of the thyatrons still occasionally occur: the observed probability of a main switch thyatron erratic during injection, for the LHC, is  $\sim 1.6 \times 10^{-5}$  per injection [19]. Hence, novel pulse generator technologies based on semiconductor (SC) switches are being developed to reach short rise times and low failure rates. However, SC switches are characterized by their relatively low ratings for voltage and current, hence a modular design, consisting of series and parallel SC switches, is required [77]. The most promising designs of pulse power generator based on SC switches are the Inductive Adder (IA) [78, 79] and the Marx Generator (MG) [80]. The baseline parameters of the FCC injection kicker system have been selected in coordination with the IA design to ensure compatibility. However, the MG for FCC injection is being designed to the same specifications as the IA, and thus it will also be compatible with the injection kicker magnets. A schematic drawing of the IA is shown in Fig. 4.2.

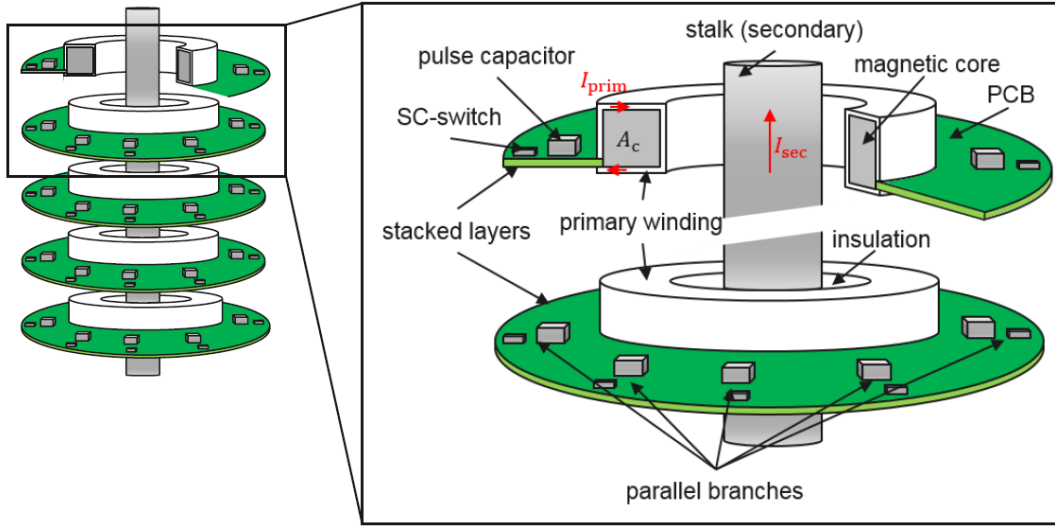


Figure 4.2 – Schematic drawing of the IA [75].

The IA consists of 1:1 pulse transformers with the secondary windings connected in series. The number of parallel branches of the primary windings, together with the repetitive pulse current capability of each branch, determines the maximum output current of the IA. The output voltage is approximately the sum of the voltages of each primary voltage layer. The rise time of the output pulse of the IA, and hence the rise time of the field in the kicker magnet, is dependent upon the propagation delay through the IA stack: this propagation delay depends upon the number of layers and the delay per layer [77]. The IA uses magnetic cores [81]: to limit the size, cost and propagation delay through the stack, the output voltage must be kept at a reasonably low value [82]. In general, to aim for low voltage, the fast kicker magnets have low characteristic impedance, to achieve the required current, but consistent with the field rise time requirements: hence, a characteristic impedance of  $6.25 \Omega$  has been chosen. For the IA, the propagation delay per stack for  $6.25 \Omega$  is comparable with the delay for a  $5 \Omega$  characteristic impedance: however, an important advantage of  $6.25 \Omega$ , in comparison with  $5 \Omega$ , is the larger gap of the secondary insulation, which significantly reduces the electric field in this region [78].

To provide the required deflection angle, several aspects have to be considered in the kicker system design. Reducing the effective magnetic length requires a higher magnetic flux density and thus a larger pulse current. For the yoke of a fast kicker magnet, a NiZn ferrite is typically used: a suitable ferrite has a saturation flux density of  $\sim 0.3 \text{ T}$  [83] at ambient temperature, and a lower value at higher temperatures (e.g.  $0.16 \text{ T}$  at  $100^\circ\text{C}$  [64]). The properties of magnetic materials for fast pulsed kicker systems are further discussed in Chapter 9. Importantly, the design of the kicker magnet should limit the average value of the flux density in the ferrite yoke, including fringe fields at the ends, to a value comfortably below the saturation flux density.

It is desirable to minimize the surface area of the ferrite yoke: the ferrite is a significant con-

tributor to outgassing, in the vacuum tank, even after bakeout. In addition, the outgassing increases significantly as temperature of the ferrite rises [69]. Thus, for a given length of the kicker magnet, it is important to keep to a reasonable minimum the thickness of the ferrite in the direction perpendicular to the direction of propagation of the beam. Nevertheless, the thickness must be sufficient to maintain the flux-density in the ferrite yoke, including end effects, to an acceptable level. For 3.3 TeV injection energy and 0.18 mrad deflection angle, the dependence of the magnetic flux density as a function the effective length has been evaluated using Eq. 3.3. The result, neglecting end effects, is shown in Fig. 4.3.

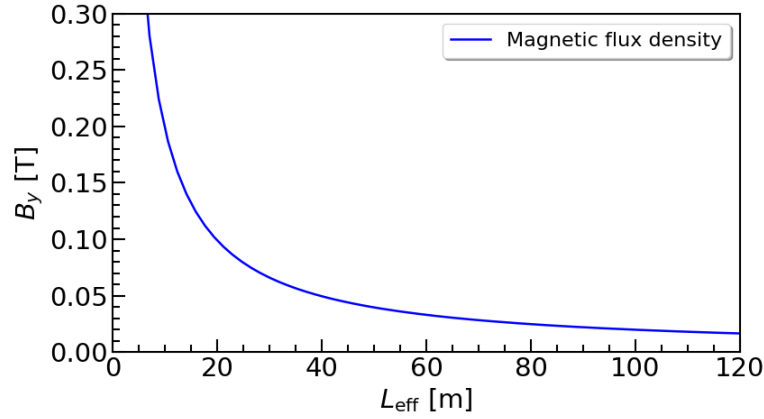


Figure 4.3 – Magnetic flux density in the magnet aperture as a function of the effective length.

To limit the required current, the aperture dimensions should correspond to the minimum value set by the beam parameters with an eventual margin to provide the space for the beam screen. For this reason, expecting that the beam screen will be necessary, we performed the analysis for unshielded and shielded kicker magnets, assuming that  $V_{\text{ap}} = 32$  mm or  $V_{\text{ap}} = 48$  mm, respectively. For both cases, the necessary current as a function of the magnetic flux density is shown in Fig. 4.4. To achieve the fast switching, MOSFETs will be used in the IA or MG: the maximum repetitive design current of the IA, with present generation high voltage and high current SiC MOSFETs, is  $\sim 2.5$  kA [77]. This corresponds to a magnetic effective length of  $\sim 30$  m and a magnetic flux density, in the aperture, of 0.065 T with the beam screen or  $\sim 20$  m and 0.098 T with no beam screen. Note, reducing the current, would decrease the magnetic flux density in the aperture of the magnet and increase the necessary effective magnetic length. A compromise between minimizing the injection kicker system length, due to beam impedance reasons, and ensuring compatibility with the IA, is to choose a pulse current close to the maximum repetitive value of  $\sim 2.5$  kA.

The rise and fall times of the current pulses from the IA are expected to be less than 75 ns [79]. From Eq. 3.9, the allowable propagation delay of the kicker magnet is  $\sim 0.355$   $\mu\text{s}$ . Using Eq. 3.2, with equal horizontal and vertical aperture dimensions, the inductance per meter is  $L_{m/m} = 1.26 \times 10^{-6}$  H/m. From Eq. 3.7, for  $\tau_m = 0.355$   $\mu\text{s}$  and  $Z = 6.25$   $\Omega$ , the total magnet inductance is  $L_m = 2.2 \times 10^{-6}$  H. Thus, the length of each magnet module, calculated using

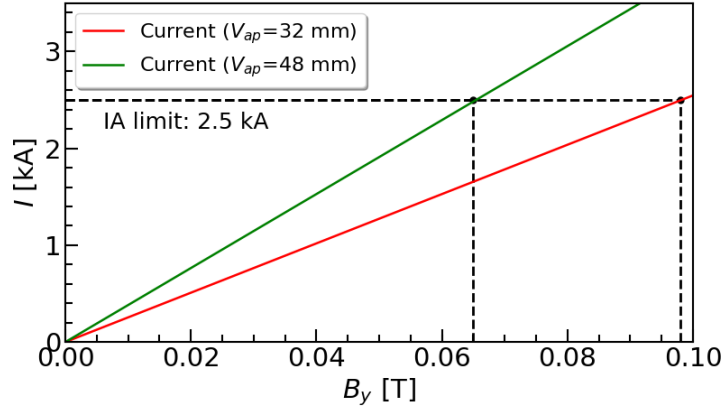


Figure 4.4 – Current as a function of the magnetic flux density (effective length of 20 and 30 m for a 32 mm and 48 mm aperture, respectively).

Eq. 3.6, is 1.765 m. To provide an integer number of modules, the current of the pulse generator must be adjusted within the allowable limit. It follows that the minimum number of unshielded magnets is 12. This corresponds to  $B_y = 0.094$  T,  $L_{\text{eff}} = 21.2$  m and  $I = 2.4$  kA. On the contrary, the minimum number of the kicker magnets with a beam screen is 18. The corresponding parameters are as follows:  $B_y = 0.063$  T,  $L_{\text{eff}} = 31.8$  m and  $I = 2.4$  kA. Note, selecting the minimum number of magnets with the maximum allowable current for the pulse generator will reduce the number of generators and kicker magnets and, hence, the system cost. In addition, the reduced number of magnets allows to minimize the beam coupling impedance.

The magnetic flux through each section of the magnetic circuit is the same. In the air gap region:  $\Theta = B_y \cdot A_c$ , where  $A_c = H_{\text{ap}} \cdot l_{\text{unit}}$  is the cross-section of the air gap. Whereas, in the ferrite core:  $\Theta = B_c \cdot A_c$ , where  $B_c$  is the magnetic flux density in the ferrite core and  $A_c$  is the cross-sectional area of the core. In particular,  $A_c = t \cdot l_{\text{unit}}$ , where  $t$  is the thickness of the ferrite. Therefore, to ensure that the average flux density in the ferrite of a central cell is below 0.1 T, the minimum thickness of the ferrite for the kicker magnet without the beam screen is:

$$t = \frac{0.094 \text{ T} \cdot 0.032 \text{ m}}{0.1 \text{ T}} \approx 30 \text{ mm} \quad (\text{for } V_{\text{ap}} = 32 \text{ mm}). \quad (4.1)$$

In contrast, the minimum thickness of the ferrite for the kicker magnet with the beam screen is:

$$t = \frac{0.063 \text{ T} \cdot 0.048 \text{ m}}{0.1 \text{ T}} \approx 30 \text{ mm} \quad (\text{for } V_{\text{ap}} = 48 \text{ mm}). \quad (4.2)$$

The hardware parameters of the FCC injection kicker system composed either of unshielded or of shielded kicker magnets are summarized in Table 4.1.

## 4.2. Beam coupling impedance of the unshielded kicker

Table 4.1 – FCC injection kicker system parameters including a comparison of the requirements for unshielded and shielded injection kicker magnets.

Parameter	Value	
Injection energy [TeV]	3.3	
Angle [mrad]	0.18	
Pulse duration [ $\mu$ s]	2.0	
Magnetic field flat-top tolerance [%]	$\pm 0.5$	
Magnetic field rise time [ $\mu$ s]	0.43	
Magnet fill time [ $\mu$ s]	0.355	
Voltage [kV]	15	
Current [kA]	2.4	
System impedance [ $\Omega$ ]	6.25	
	<b>Unshielded</b>	<b>Shielded</b>
Effective magnetic length [m]	21.2	31.8
Number of modules	12	18
Flux density in the aperture [T]	0.094	0.063
Aperture height/width [mm]	32/32	48/48
Ferrite thickness [mm]	30	30
Good field region (h/v) [mm]	8/8	8/8

## 4.2 Beam coupling impedance of the unshielded kicker

This section presents an analytical approach to estimating the power deposition in the unshielded kicker magnet, based on a calculated FCC beam spectrum and the Tsutsui model [15]. This analysis is required to determine whether the beam screen is necessary, to choose the final hardware parameters and the number of modules of the FCC injection kicker magnets.

### 4.2.1 FCC beam spectrum

The FCC beam spectrum has been evaluated by calculating the Fourier transform (FT) of a periodic signal consisting of beam bunches. Each bunch is assumed to have a Gaussian distribution with RMS bunch length  $\sigma_{\text{RMS}} = 0.08$  m [7]. In reality, particle distributions can vary for different accelerators [42]. In these studies, the Gaussian distribution is used as an approximation for the bunch shape. Also, the power deposition estimates in LHC MKI have been historically performed assuming Gaussian bunch shape [20, 61, 84]. It will be demonstrated that in the beam spectrum, the observed peaks, at specific frequencies, depend on the filling pattern, the structure of beam bunches and the beam free gaps. Here, we aim to compare the beam spectrum for the nominal filling pattern, which includes the gaps for the kicker magnet field rise time, with the ideal beam spectrum of equally spaced bunches. The two spectra will be used to calculate the total power deposition in the kicker magnet. This analysis is important for the power loss calculation also for other machines. For instance, the estimation of beam induced power deposition in the LHC MKI has been performed without

considering the beam free gaps for the kicker magnet in the filling scheme [84].

### Ideal beam spectrum

First, let us consider a beam consisting of 10400 equally spaced bunches. For the nominal bunch spacing of 25 ns, the total length of the beam in the time domain is 260  $\mu$ s ( $10400 \times 25$  ns). The corresponding beam spectrum is shown in Fig. 4.5. The main lines in the beam spectrum occur every 40 MHz (see zoom in Fig. 4.6), as the period of the signal is 25 ns. In addition, due to the length of the entire signal, the side-band harmonics occur every 3.846 kHz, but their amplitude is negligible (less than  $<0.3\%$  of the main lines). The envelope of the beam spectrum corresponds to the bunch spectrum (see red curve in Fig. 4.5), which is the FT of the bunch line density. In particular, the width of the envelope is inversely proportional to the RMS bunch length [52]. Hence, for short bunches, the beam power spectrum decays more slowly than for long bunches, which can increase the power deposition in an accelerator component.

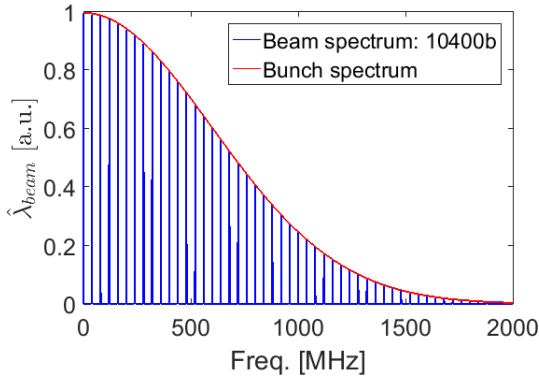


Figure 4.5 – Ideal beam spectrum of equally spaced bunches ( $\sigma_{\text{RMS}} = 0.08$  m, bunch spacing: 25 ns)

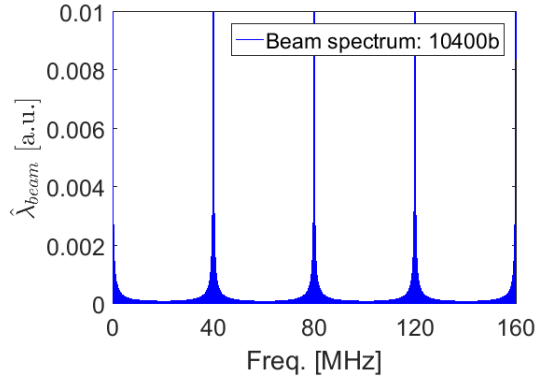


Figure 4.6 – Zoom at main lines in the beam spectrum shown in Fig. 4.5 occurring every 40 MHz.

### Beam spectrum for the nominal filling scheme

In the next step, let us analyze the FCC beam spectrum for the proposed filling pattern (assuming a single beam free gap). In the considered filling scheme there are 80 bunches (80b) per batch and 130 batches, each separated by 0.43  $\mu$ s. The gap for the kicker field rise time corresponds to 17.2 empty bunches (17.2e). The time equivalent of 97.2 bunches (80b+17.2e) separated by 25 ns is 2.43  $\mu$ s, which is the main period of the considered signal. The total length of the beam in the time domain is 315.9  $\mu$ s ( $130 \times 2.43$   $\mu$ s). The corresponding beam spectrum is shown in Fig. 4.7. The beam spectrum consists of main lines separated by 40 MHz (see zoom in Fig. 4.8). However, due to the gaps for the kicker field rise time, the side-band harmonics occur every 0.41 MHz ( $=1/2.43$   $\mu$ s) with an amplitude up to 20% of the main lines. For this reason, the presented beam spectrum is significantly different from the ideal beam spectrum of equally spaced bunches, as the side-band harmonics introduced due to the gaps

for the kicker field rise time have considerable amplitude. This feature will be taken into account in the power loss calculation and further discussed in this chapter. In addition, the side-band harmonics due to the length of the entire signal occur every 3.165 kHz ( $=1/315.9 \mu\text{s}$ ), but their amplitude is negligible over the majority of the frequency range.

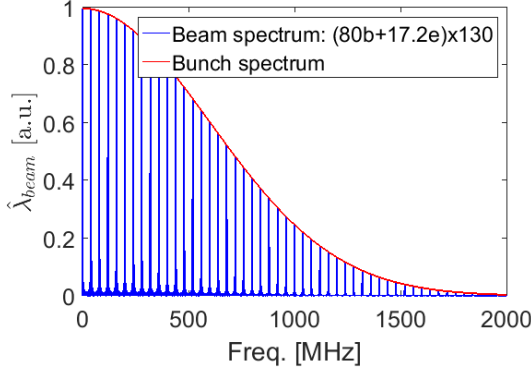


Figure 4.7 – FCC beam spectrum including gaps for the kicker rise time ( $\sigma_{\text{RMS}} = 0.08 \text{ m}$ , bunch spacing: 25 ns).

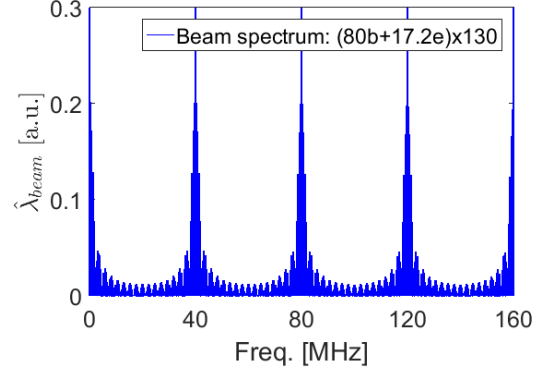


Figure 4.8 – Zoom at main lines in the beam spectrum shown in Fig. 4.7 occurring every 40 MHz.

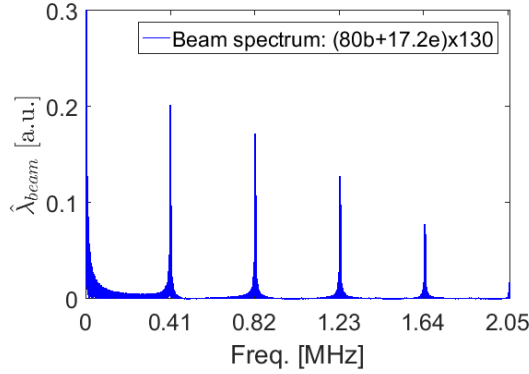


Figure 4.9 – Zoom at the side-band harmonics occurring every 0.41 MHz due to the gaps for the kicker field rise time.

### 4.2.2 Tsutsui model

An analytic calculation of the longitudinal impedance of an unshielded ferrite kicker magnet can be performed using the Tsutsui model. This approach is valid for an ultrarelativistic beam [15]. Although the model does not take into account the C-shape of the magnet yoke, it has been shown to be in a very good agreement with the results of coaxial wire impedance measurements performed for the Super Proton Synchrotron Extraction Kicker Magnet (SPS-MKE) without serigraphy [85]. The geometrical model is shown in Fig. 4.10. It consists of two ferrite blocks surrounded by a perfect electric conductor (PEC). The beam moves along the  $z$  axis (out of the page) and passes through the vacuum region at the position  $x = y = 0$ . The

half-width and half-height of the ferrite aperture are denoted by  $a$  and  $b$ , respectively.

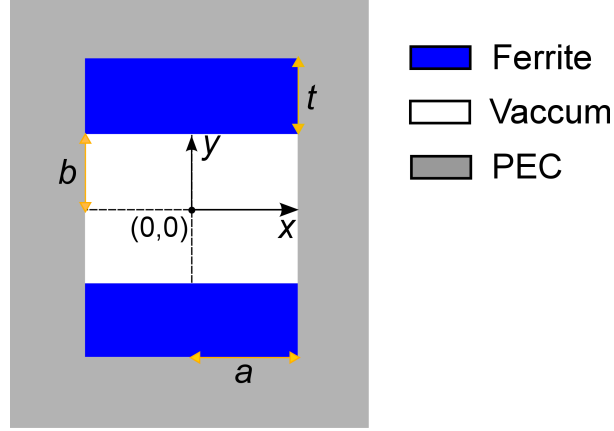


Figure 4.10 – Tsutsui model of the unshielded kicker magnet.

From Ref. [15], the longitudinal beam coupling impedance per unit length ( $\frac{Z_{||}}{L}$ ) is given by:

$$\frac{Z_{||}}{L} [\Omega/m] = j \frac{Z_0}{2a} \sum_{n=0}^{\infty} \left[ \frac{\frac{k_{xn}}{k} (1 + \epsilon_r^* \mu_r^*) \text{sh} \cdot \text{ch} + \frac{k_{yn}}{k} (\mu_r^* \text{sh}^2 \text{tn} - \epsilon_r^* \text{ch}^2 \text{ct})}{\epsilon_r^* \mu_r^* - 1} - \frac{k \text{sh} \cdot \text{ch}}{k_{xn}} \right]^{-1}, \quad (4.3)$$

where  $Z_0 = 377 \Omega$  is the impedance of free space and  $k = \frac{\omega}{c}$  is the angular wave number. The expansion coefficients in the above expression are  $k_{xn} = 2(n+1)\pi/(2a)$  for  $n = 0, 1, 2, \dots$  and  $k_{yn} = ((\epsilon_r \mu_r - 1)k^2 - k_{xn}^2)^{1/2}$ . In addition, the following designations in this formula are used:  $\text{sh} = \sinh(k_{xn}b)$ ,  $\text{ch} = \cosh(k_{xn}b)$ ,  $\text{tn} = \tan(-k_{yn}t)$  and  $\text{ct} = \cot(-k_{yn}t)$ . The relative complex permittivity  $\epsilon_r^*$  and permeability  $\mu_r^*$  of the ferrite are defined by Eqs. 2.70-2.71.

The investigation of the longitudinal beam coupling impedance of an unshielded kicker has been performed for ferrite 8C11 (Ferroxcube) [65]. In particular, this ferrite type is commonly used for the yoke of fast pulsed kicker magnets at CERN. In addition, the EM properties of ferrite 8C11 have been experimentally verified up to  $\sim 2$  GHz [85]. Note, the ferrite permeability data provided by the manufacturer is limited to  $\sim 100$  MHz. Hence, in these studies, the model of ferrite permeability has been obtained by interpolating measurement data published in Ref. [85]. The relative permeability spectra of ferrite 8C11 are shown in Fig. 4.11. For the permittivity model of ferrite 8C11 we assume that  $\epsilon_r' = 12$  and  $\epsilon_r'' = 0$  [15, 85].

#### 4.2.3 Power deposition in an unshielded kicker

Figure 4.12 shows the real part of longitudinal impedance per unit length, calculated using Eq. 4.3, together with the FCC nominal beam spectrum (including gaps for the kicker magnet field rise time in the filling scheme), evaluated for magnet aperture dimensions of both 32 mm ( $a = b = 16$  mm) and 48 mm ( $a = b = 24$  mm). In both cases, it is assumed that  $t = 30$  mm.



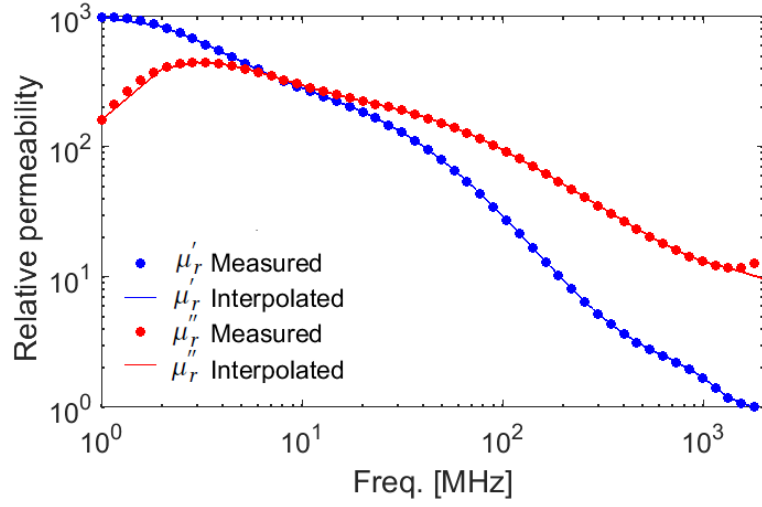


Figure 4.11 – Relative complex permeability of ferrite 8C11 [85].

It can be observed that for the larger aperture dimensions of the unshielded kicker, the real impedance per unit length is higher at frequencies below  $\sim 1.5$  GHz: this is where the real component of the longitudinal impedance contributes most to the total power deposition, as there is higher power in the beam spectrum.

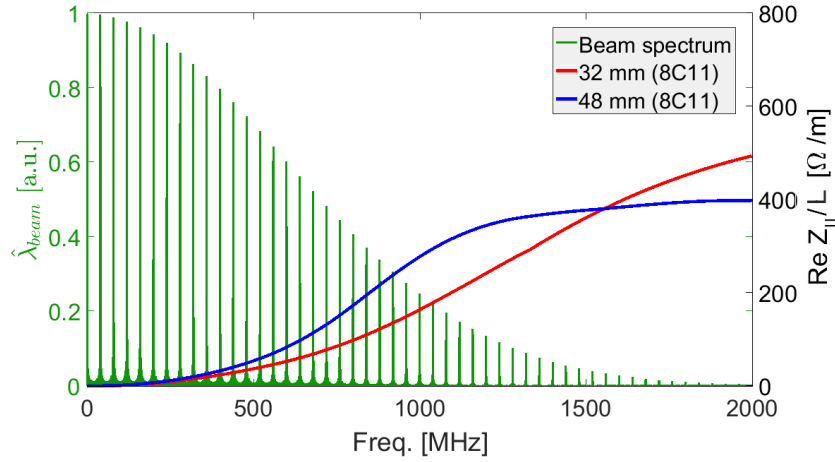


Figure 4.12 – Longitudinal impedance per unit length of unshielded kicker (analytic calculation), for aperture dimensions of  $32 \times 32$  mm and  $48 \times 48$  mm, together with the FCC nominal beam spectrum.

The total power loss, for two kicker aperture dimensions considered, has been calculated using Eq. 2.33. In addition, the predictions for the total power loss have been compared both for the ideal beam spectrum of equally spaced bunches and for the nominal beam spectrum including side-band harmonics due to gaps for the kicker field rise time in the filling pattern. The results are presented in Table. 4.2. The estimates are  $\sim 15$  % higher in comparison with data published in Ref. [18], as in this thesis a more accurate model of 8C11 ferrite permeability

is used. The predicted heat load per meter length of magnet depends on aperture dimensions. In particular, for a rectangular aperture, smaller aperture dimensions are preferable to reduce power deposition in unshielded kicker. A further analysis, using Eq. 2.33, shows that power deposition depends mainly on fundamental harmonics in the beam spectrum: neglecting the gaps in the filling pattern reduces the power deposition by  $\sim 1\%$ . From Ref. [86], measurements show that with a heat load above  $\sim 160$  W/m, the resulting ferrite temperature exceeds the Curie point. Since the FCC injection kicker magnets would consist of similar ferrite as used for the LHC MKIs, which are also housed in a vacuum tank, it is presently assumed that 160 W/m is also an upper limit for the FCC injection magnets. However, further analysis in this thesis will show that power deposition in a FCC injection kicker magnet is not evenly distributed along the length of the ferrite and hence the actual limit can be even more strict (see Chapter 5 and Chapter 7). The presented analysis shows that beam induced heating, of unshielded magnets, would be a major limitation for the injection kicker system. Hence, the beam screen is necessary. Numerical simulations are required to study more complex models of the kicker structures and to investigate solutions for screening the ferrite yoke from high intensity beam.

Table 4.2 – Power deposition estimation, for unshielded kicker magnets with 8C11 ferrite, with an aperture of 32 mm or 48 mm. The predictions for ideal and nominal beam spectrum are compared.

Aperture dimensions [mm x mm]	$P_{8C11}$ [W/m]	$P_{8C11}$ [W/m]
	Ideal beam spectrum	Nominal beam spectrum
32 × 32	227.1	228.1
48 × 48	353.9	355.4

### 4.3 Design of the injection kicker magnet

#### 4.3.1 PSpice simulations

The FCC injection kicker magnet must satisfy challenging demands for fast magnetic field rise and fall times and low ripple during the flat-top to avoid beam losses. The requirements for the FCC injection kicker magnet are listed in Table 4.1. To meet these demanding specifications, the equivalent circuit of the transmission line kicker magnet has been analyzed. In particular, time domain simulations have been performed in Cadence PSpice 16.5 in order to determine the optimum number of cells for a single kicker magnet module. For each design, the kicker magnet waveform has been analyzed. The purpose of these studies was to assess the sensitivity of the field rise time and flat-top to various circuit parameters, including the number of cells. The number of cells is important for beam coupling impedance simulations. For instance, in the frequency range of interest (from few tens of MHz up to few GHz), the segmentation of the injection kickers had a significant effect on the SPS impedance model [85]. Finally, the electrical design has been optimized to reach the required specification.

### 4.3.2 Equivalent circuit

The equivalent circuit of the transmission line type kicker magnet is shown in Fig. 4.13. Let us remark, the presented circuit is more detailed than the model shown in Fig. 3.4, as end effects and parasitic inductance of each cell are taken into account. In addition, a resistor in parallel with the inductance of each cell is introduced as this has previously been shown, for the LHC injection kicker magnets, to reduce the ripple during the flat-top of the field [51]. For the simulations reported below, the imperfections from the pulse power generator are not considered.

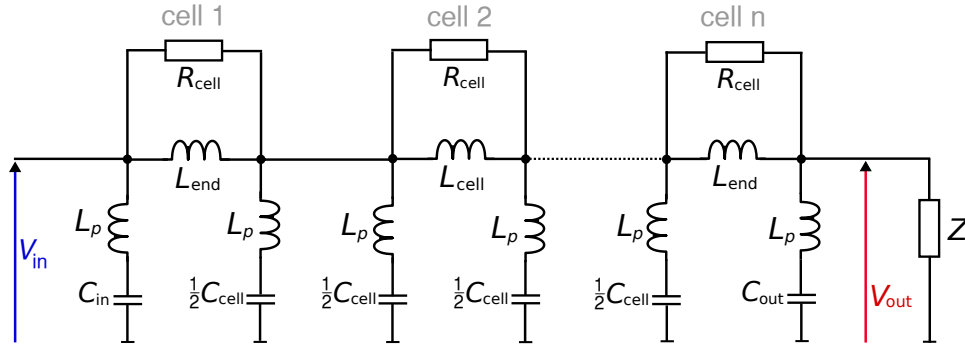


Figure 4.13 – Equivalent circuit of the transmission line kicker magnet - detailed schematic.

The physical length of a central cell ( $l_{cell}$ ) for a kicker magnet composed of  $n$  cells is given by:

$$l_{cell} = \frac{l_{unit}}{n}. \quad (4.4)$$

Due to the fringe fields at both ends of the kicker magnet, the effective inductance of each end cell ( $L_{end}$ ) is greater than that of a central cell ( $L_{cell}$ ). In particular, the additional effective length of an end cell ( $l_{add}$ ), in comparison with the physical length of a central cell ( $l_{cell}$ ), can be estimated using the following formula [49]:

$$l_{add} = l_{cell} + 0.25V_{ap}, \quad (4.5)$$

where  $V_{ap}$  is the aperture dimension in a plane perpendicular to the beam motion (see Fig. 3.3). The inductance of an end cell can be calculated as follows:

$$L_{end} = \frac{l_{add}}{l_{cell}} L_{cell}. \quad (4.6)$$

The parasitic inductance of each cell is denoted by  $L_p$ . In simulations, we assumed 100 nH for parasitic inductance: this value is pessimistic [87]. With the specified characteristic impedance and magnet fill time (see Table 4.1), the capacitance and the inductance of the central cells have been calculated analytically using Eqs. 3.4 and 3.7. For different numbers of cells, the corresponding values are listed in Table 4.3. The capacitance value at the entrance ( $C_{in}$ ) and at the output ( $C_{out}$ ) of the kicker magnet can be adjusted. Hence, the sensitivity to these parameters has been studied to optimize the performance of the FCC injection kicker magnet.

Table 4.3 – Central cell parameters for selected numbers of cells ( $L_m = 2.2 \times 10^{-6}$  H).

Number of cells	$L_{\text{cell}}$ [nH]	$C_{\text{cell}}$ [nF]
16	139	3.55
18	123	3.15
20	111	2.84
24	92	2.36
26	85	2.18
30	74	1.89

### 4.3.3 Field flat-top quality assessment

To analyze the field rise-time and flat-top quality, a figure of merit (FOM) has been introduced. It has been defined as the total area of the excursion from the normalized magnetic flux outside of the tolerance range of  $\pm 0.5\%$ , during the period of the required flat-top, with respect to the time integral of the ideal normalized magnetic flux during the flat-top. A schematic diagram of the kicker magnet waveform is shown in Fig. 4.14. In particular, any flat-top ripples exceeding the acceptance limit of  $\pm 0.5\%$  are marked in red. According to the FCC injection kicker system parameters, the FOM has to be calculated from  $0.43 \mu\text{s}$  after the leading edge of the normalized magnetic flux crosses the  $+0.5\%$  threshold, until  $2.43 \mu\text{s}$  later, which is the end of the flat-top. Ideally, the FOM is equal to zero. Hence, the goal of the study was to determine the number of cells that will satisfy this requirement. Importantly, a smaller number of cells is desirable in order to reduce complexity, construction costs and to ensure good HV performance.

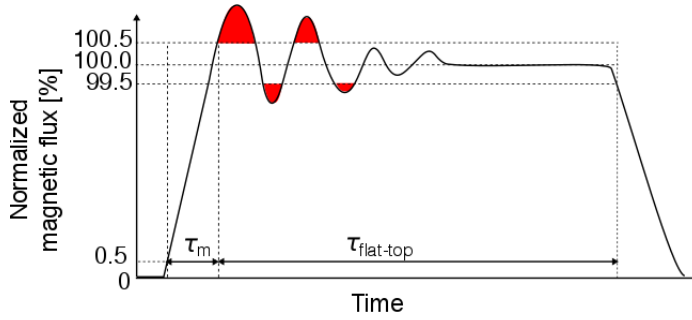


Figure 4.14 – Schematic diagram of the kicker magnet waveform. The flat-top ripple excursions outside of the acceptance limits are marked in red.

To determine relevant parameters of the waveform, such as the rise time, Cadence PSpice provides a set of functions, called "goal functions". In addition, there is a possibility to use mathematical expressions, called "macros", to assist with the analysis of the waveform. Macro definitions are rather simple: a single macro is limited to 80 characters including its name and arguments. In addition, macros can refer to other macros, but recursive definitions are not allowed [14]. In this work, several dedicated macros and goal functions have been developed to evaluate the FOM from the end of the specified rise time to the end of the specified flat-top (see Appendix B).

#### 4.3.4 Optimization of the kicker magnet module

To investigate the optimal number of cells, a first set of simulations has been performed neglecting end effects, thus assuming that each cell of the kicker magnet has the same inductance. In addition, to limit the number of simulations, we considered that the input and output capacitors are identical to the central ones. The cell's inductance and capacitance in the equivalent circuit composed of different number of cells is shown in Table 4.3. For each design, a parametric sweep analysis has been performed by varying the value of resistance  $R_{\text{cell}}$  associated with each cell. The simulation results are presented in Fig. 4.15. It can be observed that the flat-top FOM depends on the total number of cells. In particular, excursions from the ideal normalized magnetic flux become more significant with a smaller number of cells. However, the FOM can be minimized by a proper adjustment of  $R_{\text{cell}}$ . By using at least 24 cells, it is possible to achieve the required field flat-top quality without further optimization. However, to achieve the field flat-top quality specification and reduce the design complexity, a kicker magnet module composed of 20 cells has been proposed for further studies. This choice is driven by the possibility of further reducing the FOM, towards zero, by conducting sensitivity analyses to relevant circuit parameters.

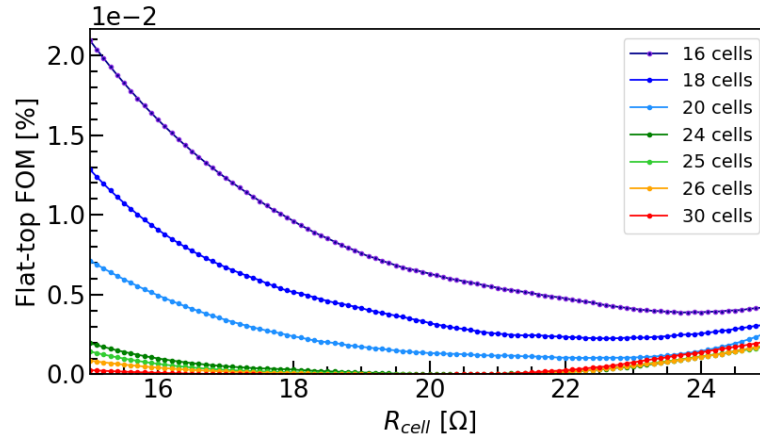


Figure 4.15 – Magnetic field flat-top FOM as a function of  $R_{\text{cell}}$  investigated for different number of cells (see Table 4.3).

#### 4.3.5 20-cell kicker magnet module

In the next step, the waveform of a 20-cell kicker magnet has been analyzed taking into account end effects. The physical length of the proposed FCC injection kicker magnet is  $l_{\text{unit}} = 1.765$  m (i.e. 31.8 m total magnet length comprised of 18 modules). For a kicker magnet composed of 20 cells, a physical length of a central cell can be calculated using Eq. 4.4 and it equals  $l_{\text{cell}} = 0.088$  m. By applying Eq. 4.5, the additional effective length of an end cell is  $l_{\text{add}} = 0.1$  m. From Eq. 4.6 it follows that inductance of an end cell is  $L_{\text{end}} = 126$  nH (i.e.  $111 \text{ nH} \times 0.1/0.088$ ). In addition, to achieve  $6.25 \Omega$  characteristic impedance,  $C_{\text{cell}} = 2.84$  nF:  $C_{\text{in}}$  and  $C_{\text{out}}$  are initially assumed to be  $1.42$  nF each.

First, the impact of  $R_{\text{cell}}$  parameter on the kicker magnet waveform has been investigated. The results are presented in Fig. 4.16. The simulations predict that with higher values of  $R_{\text{cell}}$ , the magnetic field rise time is smaller and the first overshoot increases: the first undershoot is relatively insensitive to the value of  $R_{\text{cell}}$  in the range of 21 to 30  $\Omega$ . A value of  $R_{\text{cell}} = 23 \Omega$  has been selected for further study, as it results in a first peak of field close to 100%.

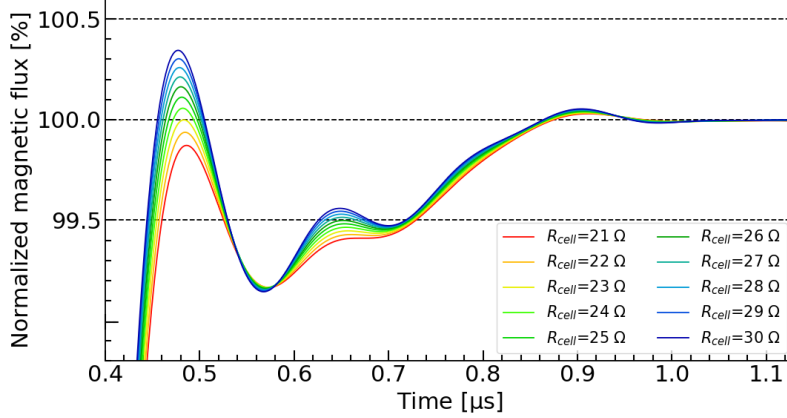


Figure 4.16 – Normalized magnetic flux as a function of time for different  $R_{\text{cell}}$  ( $C_{\text{cell}} = 2.84 \text{ nF}$ ,  $C_{\text{in}} = C_{\text{out}} = 1.42 \text{ nF}$ ,  $L_{\text{cell}} = 111 \text{ nH}$  and  $L_{\text{end}} = 126 \text{ nH}$ ). All waveforms are crossing  $\pm 0.5\%$  threshold of the normalized magnetic flux at  $\sim 15 \text{ ns}$ .

To improve the field flat-top quality, parametric sweep simulations have been performed by varying the value of  $C_{\text{out}}$ . The results show that excursions from the ideal normalized magnetic flux can be greatly reduced by a proper adjustment of this value (see Fig. 4.17). In particular, increasing the value of the output capacitance shifts the flat-top waveform within the acceptance level. The best performance is achieved for  $C_{\text{out}}$  between 1.85 nF and 1.95 nF. All waveforms are crossing  $\pm 0.5\%$  threshold of the normalized magnetic flux at  $\sim 15 \text{ ns}$ . To achieve the required field rise time, each waveform must cross 99.5% of the normalized magnetic flux by an elapsed time of 445 ns (430 ns+15 ns). However, in the aforementioned cases, it has been found that the field rise time is 2 ns longer with respect to the desired value.

For this reason, the parameters have been further optimized. It has been found that the value of  $C_{\text{in}}$  has negligible impact on the kicker magnet waveform. For a 20-cell kicker magnet the specifications both for the field rise time and field flat-top quality are reached with the following parameters:  $R_{\text{cell}} = 25.5 \Omega$ ,  $C_{\text{out}} = 1.82 \text{ nF}$  and  $C_{\text{in}} = 1.42 \text{ nF}$  (see Fig. 4.18). However, in this case, the field flat-top during the first overshoot and the first undershoot is just within the tolerance level of  $\pm 0.5\%$ . To summarize, in these studies, we have shown that the FCC injection kicker magnet should consist of at least 20 cells. To take into account the tolerances of different components, perhaps a design with more number of cells should be considered.

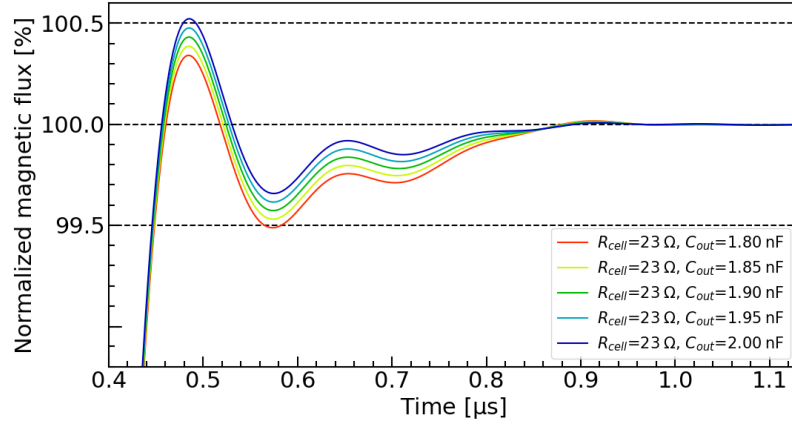


Figure 4.17 – Normalized magnetic flux as a function of time for different  $C_{out}$  ( $R_{cell} = 23 \Omega$ ,  $C_{cell} = 2.84 \text{ nF}$ ,  $C_{in} = 1.42 \text{ nF}$ ,  $L_{cell} = 111 \text{ nH}$  and  $L_{end} = 126 \text{ nH}$ ). All waveforms are crossing  $\pm 0.5\%$  threshold of the normalized magnetic flux at  $\sim 15 \text{ ns}$ .

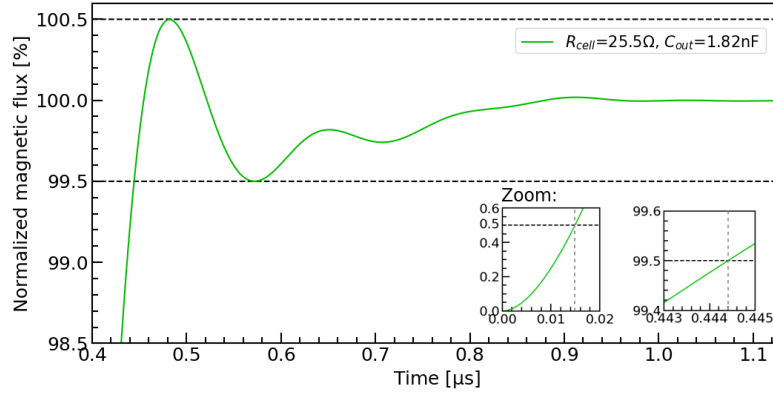


Figure 4.18 – Normalized magnetic flux in the optimized configuration of a 20-cell FCC injection kicker magnet ( $R_{cell} = 25.5 \Omega$ ,  $C_{cell} = 2.84 \text{ nF}$ ,  $C_{in} = 1.42 \text{ nF}$ ,  $C_{out} = 1.82 \text{ nF}$ ,  $L_{cell} = 111 \text{ nH}$  and  $L_{end} = 126 \text{ nH}$ ).





# 5 Beam coupling impedance of the FCC injection kicker magnet

## 5.1 CST Studio Suite

The CST Studio Suite [16] is a commercial software developed to perform 3D EM simulations. It employs several solvers to tackle different problems. In this work, the Wakefield Solver of CST Particle Studio and the Eigenmode Solver of CST Microwave Studio were predominately used.

### The Wakefield Solver

In the Wakefield Solver, we can compute 3D EM fields excited by a bunch distribution in the time domain. The longitudinal beam coupling impedance (Eq. 2.21) is calculated using a Fourier transform of the longitudinal wake potential normalized to the bunch spectrum. Since the transverse position of the exciting bunch and the integration path can be specified in the programme, the dipolar and quadrupolar components of the transverse beam coupling impedance (Eqs. 2.43-2.46) can be also evaluated. The most important simulation settings are discussed below:

- **Wavelength**

The wavelength ( $WL$ ) is proportional to the amount of time the calculation of the wake potential is carried out over. In CST, it is defined as the time equivalent distance expressed in units of length. The simulation time increases linearly with the wavelength. The resolution frequency of the impedance spectrum depends on the total number of points in the calculated wake potential and the so-called timestep. Note, the resolution frequency is inversely proportional to the wavelength.

- **Bunch length**

In the Wakefield simulation, the device is excited by a single bunch of Gaussian line density with  $\sigma_{\text{RMS}}$  being the root mean square bunch length. The maximum frequency in the beam coupling impedance spectrum is inversely proportional to the bunch length.

- **Cells per wavelength**

The Wakefield Solver employs a hexahedral mesh, thus the computational volume is

divided into rectangular cuboids. The accuracy of the simulation increases with a finer mesh at the cost of the computation time. The numerical effort is determined by the total number of timesteps to be calculated. To provide numerical stability, the upper limit of the timestep is bounded by the smallest mesh cell size. In turn, the smallest mesh cell size is constrained by the minimum relevant feature that has to be finely meshed. In addition, the largest mesh cell size cannot be arbitrarily increased to avoid resolution related numerical dispersion errors [88]. For this reason, the shortest wavelength of interest should be sampled with at least 10 mesh cells per wavelength [89]. Hence, the largest mesh cell size is determined by the shortest wavelength of interest, so the highest significant frequency. Thus, by decreasing the bunch length, the wavelength decreases by the same factor. To preserve the required number of mesh cells per wavelength constant, the total number of mesh cells increases and so does the simulation time.

- **Local mesh properties**

To achieve a good balance between simulation time and accuracy, the global mesh settings can be combined with local mesh refinement options, which allow to enhance mesh density of selected elements. For instance, if a mesh cell contains two or more metallic materials due to insufficient spatial discretization, it is represented in the so-called "staircase" mode and filled with PEC material. The staircase cells can create undesired short circuits, which can affect the simulation results.

- **Symmetry planes**

If applicable, the symmetry planes can be specified. For the FCC injection kicker magnet model with the conventional beam screen, the total number of mesh cells can be reduced by a factor of 2 due to mirror symmetry in the  $y - z$  plane. This is not applicable for a spiral beam screen.

- **Boundary conditions**

The boundary conditions used for beam coupling impedance simulations are as follows: electric (tangential component of the electric field  $\vec{E}_t = 0$ ) in  $x$ ,  $y$  planes and open in  $z$ . In particular, the open boundary employs a perfectly matched layer (PML) technique, so that waves can pass this boundary without reflections.

### The Eigenmode Solver

The Eigenmode Solver allows the resonant modes and the corresponding field profiles to be found. The eigenmodes and their frequencies are the solutions of the eigenvalue equation [90]. In the program, the minimum frequency, the maximum frequency and the number of modes to be evaluated must be specified. The Eigenmode Solver calculates the resonant modes above the lower frequency limit in ascending order. If the model contains dispersive materials, it is important to allow the program to interpolate material properties within the user provided frequency range, by activating option "Constant fit and dispersion fit as in Time Domain". The Eigenmode Solver with tetrahedral mesh is capable to handle electrically and/or magnetically lossy problems. In this case, the dialog box "Consider losses in post-processing only" must be

deactivated. To create a mesh more suitable for a given problem, adaptive mesh refinement options are allowed. To reduce the computation time, the symmetry planes can be specified as in the Wakefield Solver. In the Eigenmode Solver, the boundary conditions are electric by default in all planes. Since the Eigenmode Solver and the Wakefield Solver are based on different computational methods, we can use both solvers to compare and verify results. The Eigenmode Solver is a convenient tool to benchmark Wakefield Solver results, especially when the resonant modes are already predicted in the Wakefield simulations.

## **5.2 Computing resources at CERN**

CST EM simulations of the kicker magnet require high performance computing. Depending on the solver used, an appropriate acceleration method must be chosen to run the complex models faster. The Wakefield simulations can be accelerated by multi threading, distributed computing and message passing interface computing, while the Eigenmode simulations can be sped up by multi threading and distributed computing [91]. In general, the time domain simulations run faster with a higher number of cores. The number of cores is important to enable long wavelenght calculations in order to ensure a full decay of the wake potential and a high frequency resolution. However, for time domain simulations, the increase of the simulation speed with a higher number of cores is not linear, as the process becomes memory bound. On the other hand, the frequency domain simulations accelerate with more RAM. In particular, the RAM is important for dense meshing and to perform the analysis of the complex structures.

At CERN, CST simulations can benefit from big memory nodes in the HTCondor Linux cluster. These are machines with 24 physical cores and 1TB of RAM memory or 48 hyper threaded cores (24 physical cores) with 500 GB of RAM. CST simulations can also run on a SLURM Linux cluster, where each machine has 16 or 20 physical cores and 128 GB of RAM. In these studies, both clusters have been successfully tested and used, which allowed to greatly enhance CST performance. For instance, the Wakefield simulation of the kicker magnet with the conventional beam screen requires 2 weeks of computation (using 16 cores), whilst the Eigenmode simulation requires ~500 GB of RAM. For the spiral beam screen, due to the lack of mirror symmetry in the  $y-z$  plane, the computation time doubles. In particular, the HTCondor Linux cluster has been adopted by CERN IT Team as the main tool for complex CST simulations at CERN.

## **5.3 Conventional beam screen: initial design**

At first, the conventional beam screen design has been proposed and studied for the FCC injection kicker magnet. The details of the FCC injection kicker magnet design are discussed in Chapter 4. In the initial beam screen design,  $L_{\text{overlap}} = 56$  mm has been selected (same as for the upgraded LHC MKI8D [61]). Figure 5.1 presents the CST model of the FCC injection kicker

magnet with the conventional beam screen, which we refer to as the full model. As mentioned above, for this model, one can make use of mirror symmetry in  $y - z$  plane. The upstream end of the kicker magnet is zoomed in Fig. 5.2, whilst the downstream end is zoomed in Fig. 5.3.

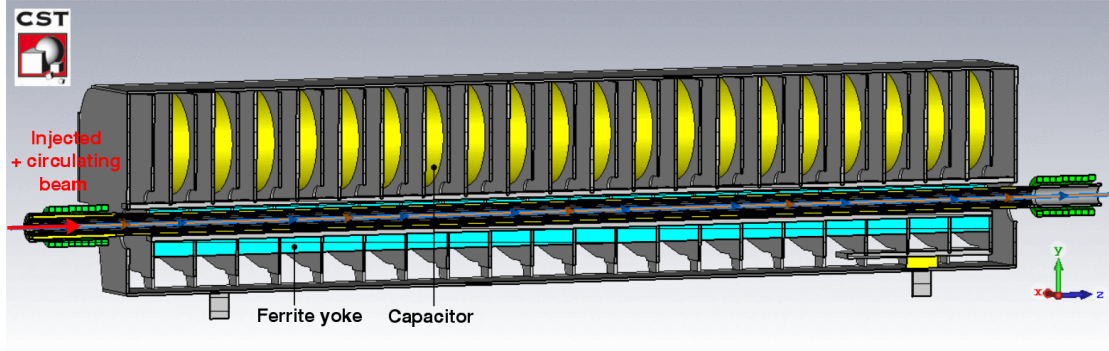


Figure 5.1 – FCC injection kicker magnet with the conventional beam screen (full model).

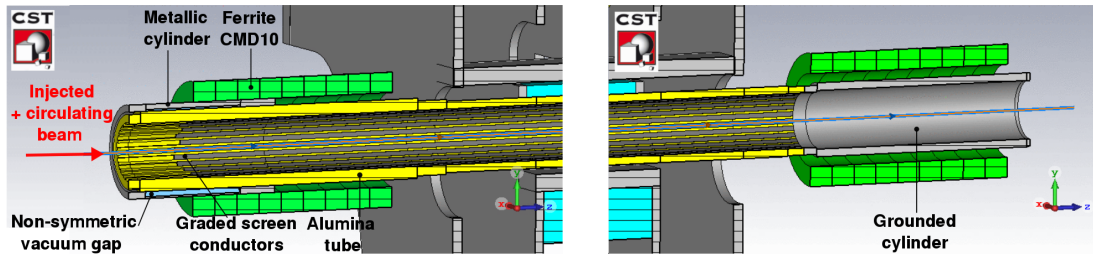


Figure 5.2 – Magnet upstream end (zoom). Figure 5.3 – Magnet downstream end (zoom).

Note, a non-symmetric vacuum gap and screen conductors of graded lengths are modelled at the upstream end. The longitudinal position of the aforementioned elements with respect to the upstream end of the kicker magnet (at which the beam enters the magnet), as well as the radial dimensions of the vacuum gap are patterned after the original "post-LS1" MKI design. However, the inner diameter of the FCC alumina tube is smaller (32 mm) in comparison with the LHC MKI (38 mm). Accelerator grade CMD5005 (National Magnetics, Inc.) [64] is the baseline material for the yoke of the FCC injection kicker magnet. In particular, accelerator grade CMD5005 is preferred over standard grade CMD5005, as accelerator grade is isostatically pressed - which provides superior permeability to uniaxially pressed ferrite [92]. An alternative ferrite to CMD5005 is 8C11 [65]: however, 8C11 is not isostatically pressed. The specification of magnetic materials for fast pulsed kicker magnets is discussed in Chapter 8. The accelerator grade CMD10 (National Magnetics, Inc.) [93] ferrite, also isostatically pressed, is a baseline material for torroidal rings mounted at both ends of the beam screen, as it has a higher Curie temperature ( $T_C \geq 250^\circ$ ) than CMD5005 ( $T_C \geq 125^\circ$ ). This potentially permits high intensity beam operation with better availability.

### 5.3.1 Dispersive materials modelling

In CST Studio Suite, the frequency dependent material properties, such as complex permittivity and permeability, are modelled by applying a polynomial fit to the specified input data. The real and imaginary parts of the complex relative permittivity of ferrites CMD5005 and CMD10 are modelled as  $\epsilon'_r = 12$  and  $\epsilon''_r = 0$  [85, 94]. The complex relative permeability at ambient temperature has been modelled based on the data provided by the manufacturer [64, 93]. However, in the frame of this work, the electromagnetic properties of both ferrites have been experimentally verified (see Chapter 8). Also, we characterized the magnetic properties of ferrites at higher temperatures. Hence, in CST simulations, for analyzing temperature impact on beam coupling impedance, experimental data is used (see Section 5.3.4).

### 5.3.2 Longitudinal beam coupling impedance

Figure 5.4 shows the real part of the longitudinal impedance of the FCC injection kicker magnet with the initial beam screen design, together with the FCC beam spectrum. The beam harmonics occur every 40 MHz, which corresponds to the nominal bunch spacing of 25 ns (see Chapter 4). Let us compare simulation results with the analytical formula (see Eq. 3.11). In the initial design, the screen conductors are graded (see Fig. 5.2) with  $L_{\text{overlap}} = 56$  mm, which is the overlap distance between the metallic cylinder and the longest screen conductor. Hence, the effective overlap distance, calculated as the average overlap length for 24 screen conductors, is 51.95 mm. The real relative permittivity of pure alumina is  $\epsilon_r = 9.9$  [95]. However, the effective relative permittivity ( $\epsilon_{r,\text{eff}}$ ) in the overlap region will be slightly lower due to vacuum gaps. Hence, assuming  $\epsilon_{r,\text{eff}} = 6.3$  [96] and  $\delta_{\text{fringe}}$  from 15 mm to 5 mm, the fundamental resonance is expected to occur between 892 MHz and 1050 MHz, which agrees with the simulation results (see Fig. 5.4). The second harmonic is not an integer multiple of the fundamental resonance: this can be attributed to the frequency dependence of the material electromagnetic properties. In addition, this feature has been also reported for the upgraded LHC MKI8D [97]. Moreover, the main attributes of the longitudinal impedance profile are consistent with the predictions from the longitudinal impedance measurements performed on the LHC MKI (see Chapter 7). For instance, the low frequency mode at  $\sim 2.8$  MHz is observed [97]. For completeness, the imaginary part of the predicted longitudinal impedance and the decay of longitudinal wake potential are presented in Fig. 5.5 and in Fig. 5.6, respectively.

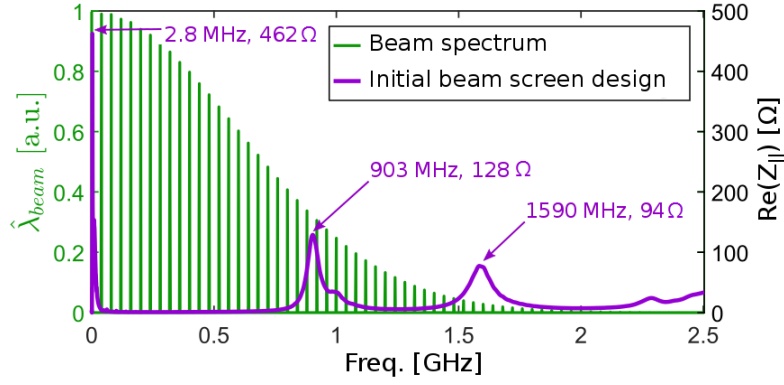


Figure 5.4 – Real part of the longitudinal beam coupling impedance of the FCC injection kicker magnet with the initial beam screen design (full model) together with the FCC beam spectrum.

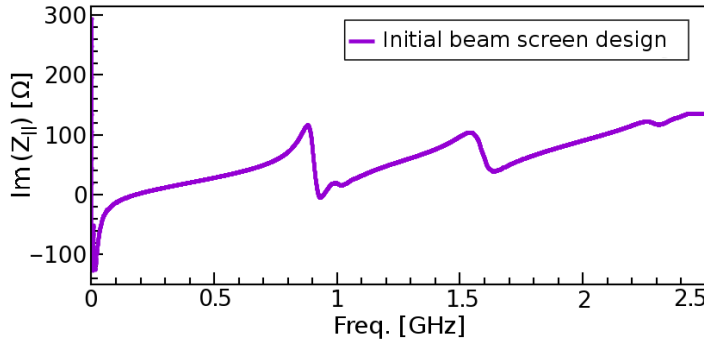


Figure 5.5 – Imaginary part of the longitudinal beam coupling impedance of the FCC injection kicker magnet with the initial beam screen design (full model).

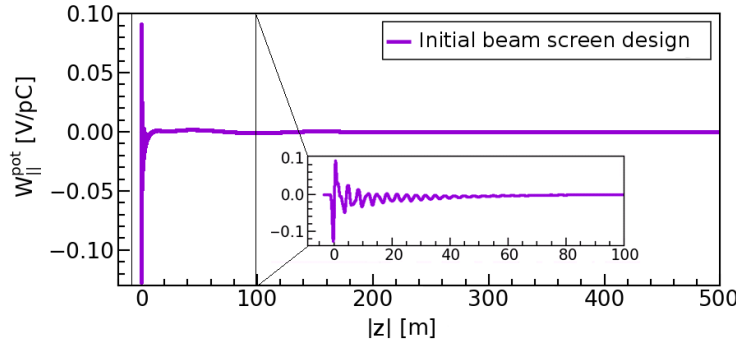


Figure 5.6 – Decay of the longitudinal wake potential ( $WL = 500$  m)

### 5.3.3 Total power loss

The total power loss in the FCC injection kicker magnet calculated using Eq. 2.33 is  $P = 30.2$  W. From Figure 5.4, the low frequency mode in the longitudinal impedance spectrum is below the first beam harmonic at 40 MHz and thus does not contribute to the total power, as will

be shown in Fig. 5.9. The second fundamental harmonic at 1590 MHz is in the frequency range where the beam power is already low. Hence, the highest contribution to the total power loss is due to the first harmonic at 903 MHz. Note: the maximum of this peak is in between two beam harmonics. As a worst case scenario, let us evaluate the total power loss assuming the maximum of the first impedance harmonic coincidences with the beam harmonic at 880 MHz (case 1) or at 920 MHz (case 2). In Figure 5.7, we present the shifted longitudinal impedance spectra together with the FCC beam spectrum. The corresponding total power loss is  $P_{\text{case1}} = 33.4$  W and  $P_{\text{case2}} = 29.3$  W. We conclude that in the considered frequency range of the first harmonic of the fundamental mode, the worst case scenario is within 10% of the predicted total power loss ( $P = 30.2$  W). Thus, the design is tolerant against relatively small shifts in the frequency of the selected resonance.

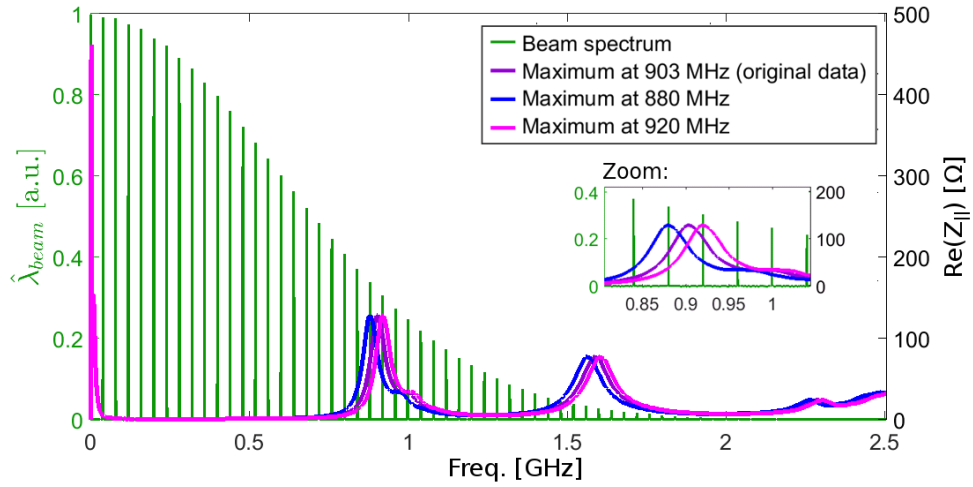


Figure 5.7 – Real part of the longitudinal beam coupling impedance of the FCC injection kicker magnet with the initial beam screen design: original data is compared with the worst case scenario model assuming that first fundamental harmonic is at 880 MHz or at 920 MHz.

#### 5.3.4 Power deposition distribution

For reliable kicker magnet operation, the beam induced power must be properly distributed. The beam screen must be designed in such a way that no more than an acceptable power is deposited in the ferrite yoke. From the real longitudinal impedance one can estimate only the total power lost by the beam, but not its distribution. In this section, we present a computation method to evaluate the power deposition distribution along the magnet and predictions for the FCC injection kicker.

##### Computation method

In the CST Wakefield Solver, the power loss monitors, defined at specified frequencies, can be used to analyze the power loss distribution along a structure. Let us introduce  $P_i^{CST}(\omega_n)$  as the predicted power dissipated in the  $i$ -th solid at an angular frequency  $\omega_n$ . The normalized

power deposition distribution for each of  $N$  solids can be defined in the following way:

$$p_i(\omega_n) = \frac{P_i^{CST}(\omega_n)}{\sum_{i=1}^N P_i^{CST}(\omega_n)}. \quad (5.1)$$

Also, let us introduce  $P(\omega_n)$  as the total power loss at an angular frequency  $\omega_n$ . The total power dissipated in the  $i$ -th solid is:

$$P_i = \alpha \sum_{n=1}^{\infty} P(\omega_n) p_i(\omega_n). \quad (5.2)$$

In the above formula,  $\alpha = \frac{P}{\sum_{n=1}^{\infty} P(\omega_n)}$ , where  $P$  is the total power lost by the beam and deposited in the kicker magnet being considered (see Eq. 2.33). The scaling factor  $\alpha$  ensures that the absolute values of the power loss distribution at each solid are consistent with the total power loss. According to Eq. 2.33, frequencies  $\omega_n = 2\pi f_n$  should consist of all of the multiples of the angular revolution frequency  $\omega_0 = 2\pi f_0$ . However, this would require approximately a million CST power loss monitors distributed until the beam spectrum decays ( $\sim 2.5$  GHz), which is impossible to compute in CST due to memory constraints.

Until now, all the calculations for the LHC MKI have been performed with the CST power loss monitors placed at frequencies  $f_n = n \cdot 40$  MHz, with  $n$  being an integer, under the assumption that power is lost mainly at beam harmonics [20]. However, from the theoretical point of view, this approach is not correct: the contribution to the total power loss cannot be calculated elsewhere than at  $\omega_0$  multiples. Moreover, in the analysis, only a few CST monitors were used.

Hence, in this work we proposed a new approach, which is in line with the theory and can be employed using high performance computing clusters. It involves using CST power loss monitors at selected revolution frequency integer multiples with the highest contribution to the total power loss calculated using Eq. 2.33. In particular, we select frequencies  $f_n = n f_0$ , when the following condition is satisfied:  $P(f_n) \geq P_{\text{level}}$ , where  $P_{\text{level}}$  is a specified limit that can be decreased, while still restricting the number of monitors used to an acceptable number.

### Results

Figure 5.8 presents the power loss evaluated at different frequencies based on CST predictions of real longitudinal impedance and the FCC beam spectrum (see Fig. 5.4). The corresponding cumulative sum of the power loss is shown in Fig. 5.9. From Equation 2.33 and considering multiples of  $f_0$ , the total power loss is  $P = 30.2$  W. The highest contribution to this sum is at  $f_0$  multiples overlapping with beam harmonics and especially with the first impedance harmonic at 903 MHz. The second impedance harmonic at 1590 MHz does not contribute significantly to the total power loss, as the cumulative sum of the power loss does not visibly increase at this frequency (see Fig. 5.9), since the beam current spectrum is already very low. Using the old approach, the power loss evaluated at integer multiples of 40 MHz is 23.8 W, which is 78 %



of the the total power loss. Thus, considering only 40 MHz beam harmonics underestimates the total power loss by 22%. In the new approach, we set  $P_{\text{level}} = 0.1$  W, such that the number of points meeting the adopted criterion is 50. This is a reasonable number given the available computing resources, as the required memory is  $\sim 100$  GB. At selected  $f_0$  multiples, the power loss is 26.6 W, which accounts for 88 % of the total power loss.

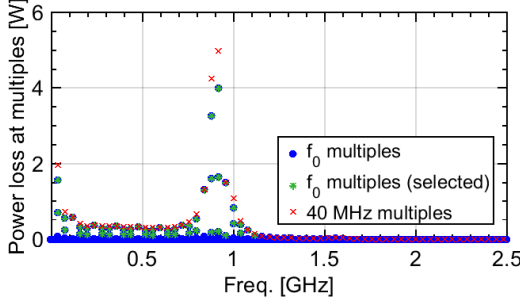


Figure 5.8 – Power loss at different frequencies.

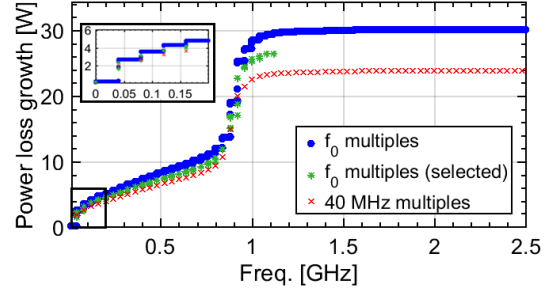


Figure 5.9 – Cumulative power loss.

A comparison of the power deposition distribution in the ferrite rings and the ferrite yokes of the FCC injection kicker magnet with the initial beam screen design, using the two approaches, is shown in Fig. 5.10. The elements are numbered according to their position with respect to the magnet entrance. Note, using the new, proposed approach and skipping frequencies with the lowest contribution to the total power loss ensures that the predicted power loss distribution will be reasonably similar to that calculated using many more monitors, as the skipped points are many and equally distributed over the entire beam spectrum. The analysis shows that using power loss monitors at only 40 MHz multiples can yield differences of more than 10% in an individual solid. Hence, this method is a very important contribution to optimizing computing resources to get adequate accuracy. To conclude, we propose using the new approach since it greatly optimizes the frequencies of the power loss monitors used and enables numerical calculations in line with the theory. For instance, an initial large discrepancy between the predicted power deposition distribution for the LHC MKI and the actual power deposition distribution (and thus the temperature) can now be largely explained by using too few power loss monitors at improper frequencies.

The simulation results confirm that power deposition in the FCC injection kicker magnet is non-homogeneous along its length. The highest portion of the total power is deposited in the ferrite rings at the upstream end of the kicker magnet. In particular, the maximum power is dissipated in ring 5, since this is the first ring fully exposed to the EM radiation and not shielded by the metallic cylinder (see Fig. 5.2). The power loss deposited in the ferrite yokes is significantly smaller and it decreases for the yokes positioned further from the magnet entrance. Finally, the power deposition in the rings at the downstream end of the magnet is negligible. The power deposition distribution along the FCC injection kicker magnet is very similar to that of the upgraded LHC MKI8D [61]. However, the total power loss for the FCC injection kicker magnet ( $P = 30.2$  W) is smaller than for the LHC MKI8D ( $P = 37$  W) [97]. For this reason, the maximum power dissipated in the ferrite rings is also

smaller in comparison with LHC MKI8D. Hence, since the upgraded magnet did not limit operation of the LHC [98], we conclude that the temperature of the ferrite yokes of the FCC injection kickers will certainly not exceed their Curie point. Therefore, we conclude that the heating aspects of the FCC injection kicker magnet are not expected to limit the accelerator performance during operation with nominal beam parameters.

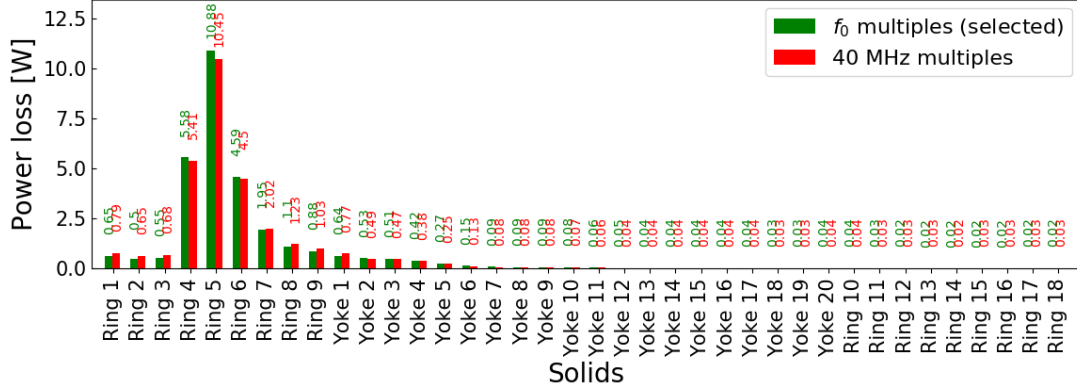


Figure 5.10 – Comparison of the FCC injection kicker magnet power deposition distribution calculated using CST power loss monitors at selected  $f_0$  multiples and at 40 MHz multiples.

### Impact of temperature dependence of magnetic properties

Until now, we used the data-sheet magnetic properties of ferrites, at ambient temperature, provided by the manufacturer. However, we show that complex permeability is temperature dependent (see Chapter 8). Hence, we aim to compare the power deposition distribution using complex permeability data for ferrites CMD5005 and CMD10 at an ambient temperature and at measured 150°C. Note: when using experimental complex permeability data we refer to the temperature measured at the sample holder, thus the actual temperature of the ferrite sample might be lower. Also, the actual temperature is below the ferrites Curie temperature specified by the manufacturer to be  $T_C \geq 125^\circ$  (CMD5005) [64] and  $T_C \geq 250^\circ$  (CMD10) [93].

Figure 5.11 shows the power deposition distribution along the magnet at 25°C (green) and at measured 150°C (orange). For clarity, we indicate the values of the power deposited in each solid only if it is above 0.5 W per solid. In addition, we analyzed the power deposition distribution at 150°C, but assuming that the 9 rings at the upstream end reached their  $T_C$  (blue): there is a significant power loss in the first yokes. In this case, the 9 rings at the upstream end have been modelled as having magnetic properties of vacuum ( $\mu'_r = 1$ ,  $\mu''_r = 0$ ), as we verified that above the Curie temperature, the ferrite is magnetically transparent and lossless (see Chapter 8). In addition, it was assumed that  $\epsilon'_r = 1$  and  $\epsilon''_r = 0$ . The latter simulation shows the importance of maintaining the upstream rings below their Curie temperature in order to limit the heating of the ferrite yoke.

For each model, the corresponding real part of the longitudinal impedance is shown in Fig. 5.12. The results at ambient temperature and at measured 150°C are very similar: the only

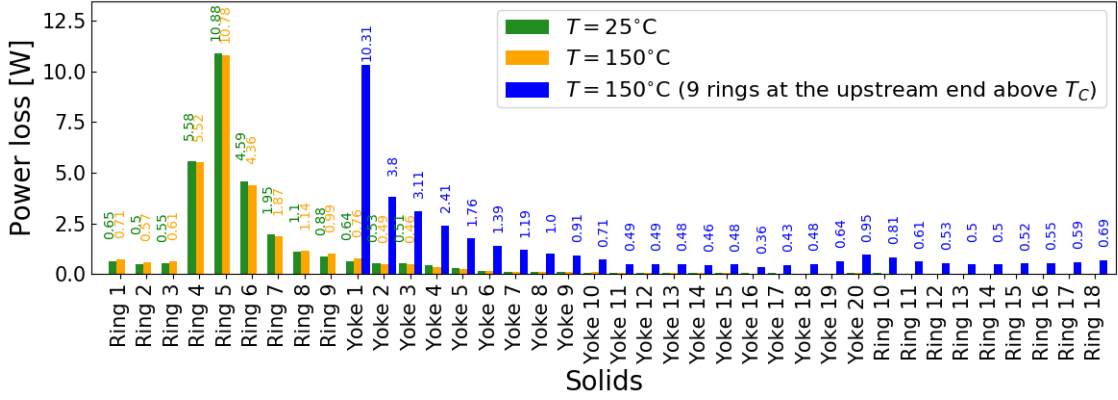


Figure 5.11 – Comparison of the FCC injection kicker magnet power deposition distribution calculated using data-sheet of magnetic properties at ambient temperature and measured magnetic properties at  $150^{\circ}\text{C}$ .

significant difference is observed in the magnitude of the low frequency peak at  $\sim 2.8$  MHz. This is attributed to the fact that a change in the imaginary part of the relative complex permeability due to temperature variation is considerable at frequencies below 100 MHz. At higher frequencies, magnetic losses are similar, thus negligible impact of the temperature on the longitudinal impedance of the kicker magnet is observed. Also, since the low frequency peak does not contribute to the total power loss, as shown in Fig. 5.9, there is no significant difference in the power deposition distribution at  $25^{\circ}\text{C}$  and at measured  $150^{\circ}\text{C}$ . However, if the temperature of the ferrite rings at the upstream end of the kicker magnet exceeds their  $T_C$ , a significant amount of power is deposited into the ferrite yoke. In addition, some low frequency modes at  $\sim 32$  MHz and  $\sim 68$  MHz are observed (see zoom in Fig. 5.12). The source of these resonances is not further investigated here, since they do not occur when the upstream ferrite rings are below their  $T_C$ , which is the aim of these studies.

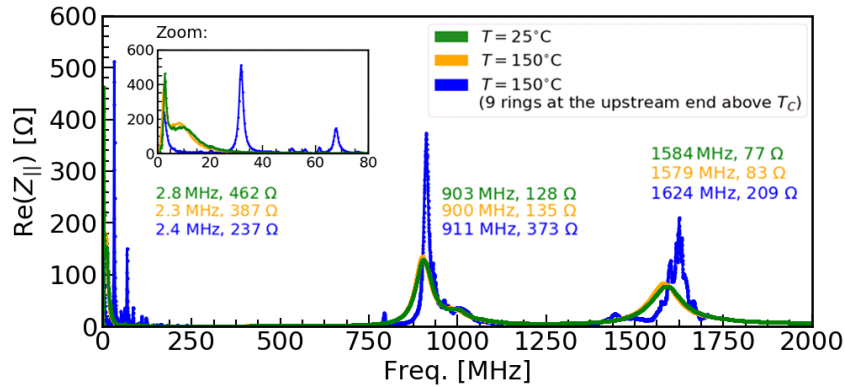


Figure 5.12 – Real part of the longitudinal beam coupling impedance of the FCC injection kicker magnet taking into account temperature dependence of magnetic properties.

### 5.3.5 Investigation of the simplified model and the cut-down model

Next, we analyzed the longitudinal impedance predictions for the following three models:

- **Full model:** kicker magnet with a beam screen (i.e. as shown in Fig. 5.1),
- **Simplified model:** only the beam screen,
- **Cut-down model:** only the capacitively coupled end of the beam screen.

From Figure 5.13, we see that there are no major differences in the impedance spectrum when the full model (green curve) and simplified model (gold curve) are considered: the two curves are almost identical. This demonstrates the high efficiency of electromagnetic shielding of the ferrite yoke and shows that the kicker magnet can be excluded from the simulations to significantly reduce the computation time for calculating the impedance spectrum. The full model requires 2 weeks of computation on a high performance cluster, whereas the cut-down model is analyzed in 48 hours. This observation was found to be very useful for investigating new features of the beam screen that will be discussed in the next sections. Note, however, the full model is required for calculating the power loss distribution along the magnet.

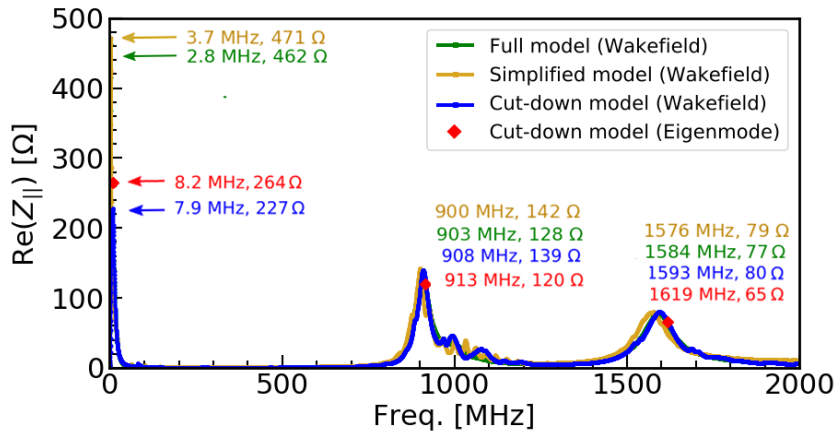


Figure 5.13 – Real part of the longitudinal beam coupling impedance of the initial beam screen design evaluated for the full model, the simplified model and the cut-down model.

Moreover, the analysis of the cut-down model (blue curve), shows that the magnitude and frequency of the harmonics of the fundamental resonance are very similar in comparison with both the full model and the simplified model. This demonstrates that the main resonances are determined by the overlap region and there is no significant impact from the rest of the structure. However, the resonant frequency and the magnitude of the low frequency mode in the impedance spectrum of the cut-down model (7.9 MHz, 227 Ω) are different in comparison with the full model (2.8 MHz, 462 Ω). In this regard, simplifying the model should be treated with caution. However, for the initial beam screen design, the low frequency peak does not contribute to the total power loss, as it is well below 40 MHz (see Fig. 5.9). The total power

loss calculated for the full model, simplified model and the cut-down model is 30.2 W, 32.8 W and 29.1 W, respectively. Hence, the results agree with the full model within 8%. To verify the Wakefield Solver simulations, the cut-down model has been analyzed using the Eigenmode Solver. The results are in good agreement with the Wakefield Solver simulations (see Fig. 5.13).

#### 5.3.6 Impact of the ferrite rings

Using the simplified model of the conventional beam screen, we investigated the influence of the ferrite rings placed at each end of the alumina tube upon the longitudinal impedance. Figure 5.14 shows the results for 3 different configurations considered, assuming ferrite rings placed: at both ends of the beam screen as in the initial design (black curve), only at the downstream end (orange curve) and only at the upstream end (red curve). Note, above 10 MHz the black and red curve overlay each other. From these simulations, it becomes evident that ferrite rings at the upstream end are necessary to damp some low frequency modes, as well as to lower the magnitude of the main harmonics. These predictions are consistent with the longitudinal impedance simulations at higher temperatures, when the temperature of the first 9 ferrite rings is above  $T_C$  (see blue curve in Fig. 5.12).

The longitudinal impedance profiles of the model with ferrite rings placed at both ends and only at the upstream end of the beam screen are very similar: the only difference is observed in the magnitude and frequency of the low frequency mode. If the ferrite rings are placed at both ends of the beam screen, the resonant frequency of the low frequency mode is approximately half of that associated with the design where ferrite rings are placed only at the upstream end. Hence, with ferrite rings placed at both ends, the low frequency mode is more distant from beam harmonic at 40 MHz. This effect is beneficial when shortening the overlap length and optimizing the conventional design (see Section 5.4).

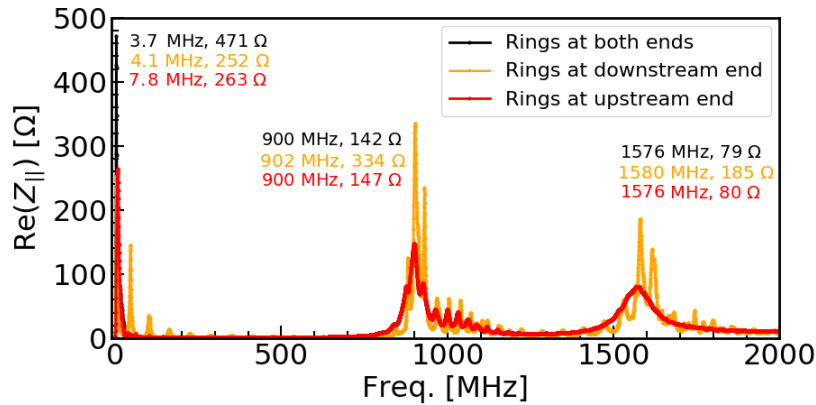


Figure 5.14 – Real part of the longitudinal beam coupling impedance of the initial beam screen design with ferrite rings placed at both ends of the beam screen in comparison with ferrite rings placed only at the downstream or the upstream end (simplified model).

### 5.3.7 The low frequency mode

In this part, we aim to verify the behaviour and the origin of the low frequency mode, which we postulate is due to a resonance between the inductance of the ferrite rings and the capacitance between the overlap of the screen conductors with the external ground. First, let us consider a toroidal ferrite ring characterized by an inner diameter  $d_i$ , an outer diameter  $d_o$  and length  $x$ . The inductance of the magnetic core is:

$$L = \mu_0 \mu_r' N^2 (A_e / l_e). \quad (5.3)$$

In Equation 5.3, the effective magnetic path length ( $l_e$ ) is [99]:

$$l_e = C_1^2 / C_2, \quad (5.4)$$

and the effective cross-sectional area ( $A_e$ ) is [99]:

$$A_e = C_1 / C_2, \quad (5.5)$$

where  $C_1 = \frac{2\pi}{x \ln(\frac{d_o}{d_i})}$  and  $C_2 = \frac{4\pi(\frac{1}{d_i} - \frac{1}{d_o})}{x^3 \ln(\frac{d_o}{d_i})}$ .

The ferrite rings placed at both ends of the beam screen (see Figs. 5.2-5.3) have the following dimensions:  $d_i = 54$  mm,  $d_o = 77.4$  mm,  $x = 13.8$  mm. From Equation 5.4, we calculate  $l_e = 201.9$  mm, while from Eq. 5.5, for each set of 9 rings,  $A_e = 1437.5$  mm<sup>2</sup>. The capacitive coupling ( $C$ ) measured for "post-LS1" LHC MKI with  $L_{\text{overlap}} = 130$  mm is 250 pF. Whereas, for the upgraded LHC MKI8D with  $L_{\text{overlap}} = 56$  mm, we measured 130 pF. Hence, assuming the same properties of the alumina tube, a difference in the overlap length of 74 mm leads to the change in capacitance of 120 pF, which is equivalent to the rate of 1.62 pF/mm or 91 pF/56 mm. For example, by increasing  $L_{\text{overlap}} = 56$  mm by a factor of 2, the coupling capacitance should be equal to 221 pF, i.e. 130 pF + 91 pF. Although in this example we refer to the coupling capacitance measured on the LHC magnets, similar values are expected for the FCC injection kickers, as the beam screen dimensions and material properties are very comparable.

To understand the origin of the low frequency mode, we compared the real part of the longitudinal impedance of the cut-down model for 4 different configurations. Note: the cut-down model includes only the set of 9 ferrite rings at the upstream end. The results are presented in Fig 5.15. Model 1 is the initial design. In other models, only one modification is introduced with respect to the initial design. In model 2, ferrite rings are modelled as having properties of ferrite CMD5005, instead of ferrite CMD10. In model 3, the overlap length is increased by a factor of 2 ( $L_{\text{overlap}} = 112$  mm). In model 4, the length of the screen conductors is increased by a factor of 4, i.e. from 366 mm to 1464 mm. For each model, the simulated resonant frequency of the low frequency mode ( $f_r^{\text{CST}}$ ) is shown in Table 5.1. Also, we present  $\mu_r'$  and  $\mu_r''$  at this frequency taken from the data-sheet [64, 93]. For each model, we include the value of  $L$  calculated using Eq. 5.3 and estimated  $C$  (based on LHC MKI measurements described above). For the RLC equivalent circuit, the resonant frequency is calculated as  $f_r = 1/(2\pi\sqrt{LC})$ .

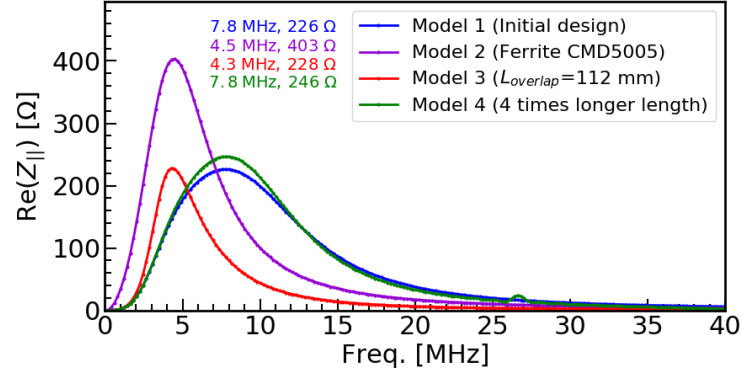


Figure 5.15 – Real part of the longitudinal beam coupling impedance of the initial beam screen design along with modified designs (cut-down model).

Table 5.1 – Results of the low frequency mode analysis (cut-down model).

Model	$\mu'_r$	$\mu''_r$	$L$ [ $\mu\text{H}$ ]	$C$ [pF]	$f_r$ [MHz]	$f_r^{\text{CST}}$ [MHz]
1	253	286	2.3	130	9.2	7.8
2	803	654	7.1	130	5.2	4.5
3	460	350	4.1	221	5.3	4.3
4	253	286	2.3	130	9.2	7.8

From Eq. 5.3, a higher  $\mu'_r$  leads to an increase of inductance and therefore a decrease of the resonant frequency. In addition, an increase of the overlap length causes an increase of both coupling capacitance and inductance and therefore a decrease of the resonant frequency. From Table 5.1, the change in resonant frequency for modified models with respect to the initial design shows the same trends both in simulations and analytical calculations. Moreover, the analytical estimates are reasonably close to the CST predictions. A small discrepancy can be caused due to the capacitance estimation, as this value refers to measurements on an LHC MKI. Importantly, there is no change in predicted resonant frequency when the lengths of the screen conductors are increased. Hence, we confirm that the low frequency mode occurs due to a resonance between the inductance of the upstream ferrite rings and the coupling capacitance. Nevertheless, the results presented in Fig. 5.14 indicate that the ferrite rings at the downstream end contribute to the frequency of this resonance.

## 5.4 Optimization of the conventional beam screen

### 5.4.1 Overlap length reduction

The first approach to improving the performance of the conventional beam screen design, in terms of heating, is to reduce the overlap length. From Eq. 3.11, the frequency of the fundamental resonance is inversely proportional to  $L_{\text{overlap}}$ . Hence, reducing the overlap length moves the first resonance to a higher frequency, where the beam spectrum has a lower

current. The aim of this section is to investigate the reduction in the total power loss by reducing the overlap length. Finally, the limitations of this approach will be demonstrated.

### Graded screen conductors

The first set of simulations has been performed for the simplified model with graded screen conductors (see Fig. 5.2). The overlap length of 56 mm has been reduced in steps of 4 mm by shortening the metallic cylinder at the upstream end. The real part of the longitudinal impedance and the cumulative power loss evaluated at  $f_0$  integer multiples are shown in Fig. 5.16 and Fig. 5.17, respectively. The frequency of the first and second harmonics of the main resonance both increase with a shorter  $L_{\text{overlap}}$ . However, a change in bandwidth of the low frequency peak is observed as well. Let us remark, with a shorter  $L_{\text{overlap}}$ , the low frequency peak is broader and higher in magnitude at frequencies close to the beam harmonics of 40 MHz. For this reason, it contributes considerably to the total power loss when the overlap length is too short. The optimal value is  $L_{\text{overlap}} = 44$  mm (see Fig. 5.18). In this case, a reduction of  $\sim 23\%$  in the total power loss with respect to  $L_{\text{overlap}} = 56$  mm is achieved. This result is vital not only for the optimization of the initial beam screen design for the FCC injection kicker magnet, but also as a means to further improve the LHC MKI performance.

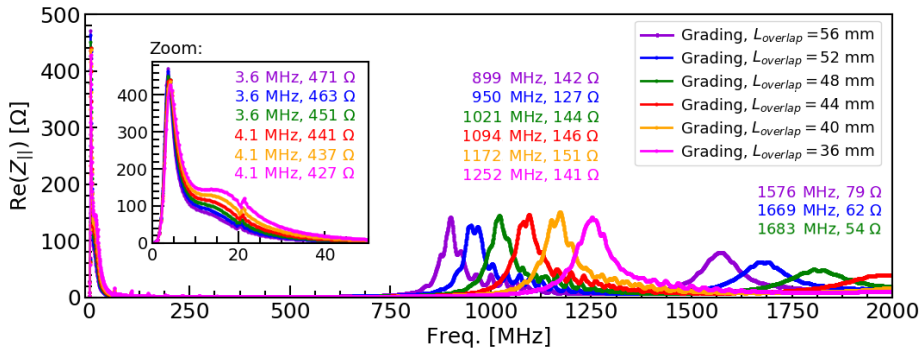


Figure 5.16 – Real part of the longitudinal beam coupling impedance for different  $L_{\text{overlap}}$ , investigated on the simplified model with graded screen conductors.

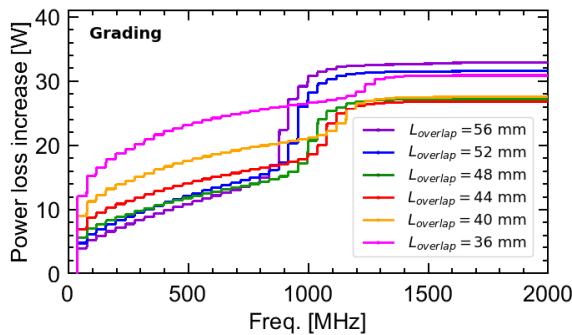


Figure 5.17 – Cumulative power loss for different  $L_{\text{overlap}}$  (graded conductors).

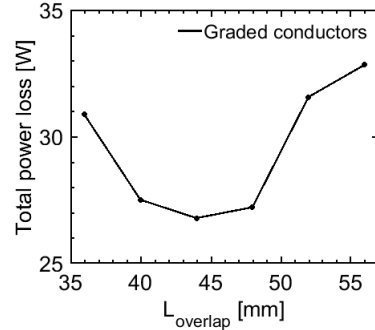


Figure 5.18 – Total power loss as a function of  $L_{\text{overlap}}$  (graded conductors).



### Screen conductors without grading

In the second set of simulations, we investigated a reduction of the total power loss using the simplified model consisting of screen conductors without grading. In reality, the lengths of straight screen conductors for the conventional beam screen design are graded due to HV reasons [55]. However, the analysis of an ungraded configuration is important in case the HV issues were to be mitigated. The results are shown in Fig. 5.19 and Fig. 5.20. For the same overlap length, the frequencies of the first and second fundamental harmonics are lower in comparison to the beam screen composing of graded screen conductors. This is attributed to the fact that the average overlap length is longer with ungraded lengths, whereas, for the graded conductors, the overlap length is defined with respect to the longest screen conductor. In addition, the magnitudes of the main resonances are slightly higher for ungraded conductors. The bandwidth of the low frequency peak increases with a shorter overlap length, hence the optimal value of the overlap length is between 36 mm and 44 mm (see Fig. 5.21). Comparing the curves in Fig. 5.18 and Fig. 5.21 - graded conductors give a relatively broad minimum. Additionally, the absolute minimum is lower for graded conductors.

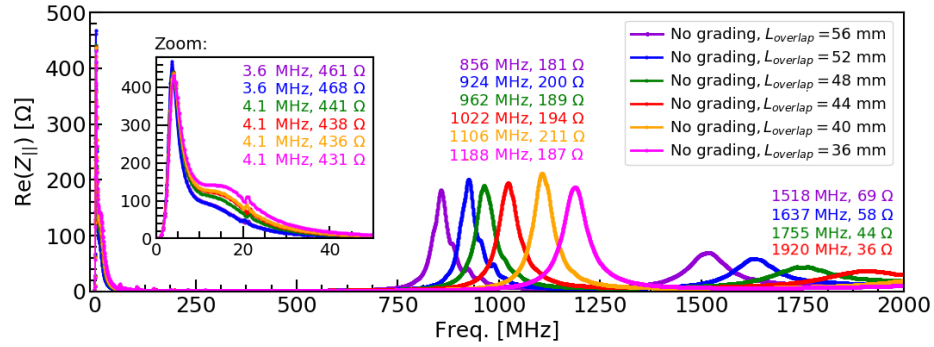


Figure 5.19 – Real part of the longitudinal beam coupling impedance for different  $L_{\text{overlap}}$  investigated on the simplified model with ungraded screen conductors.

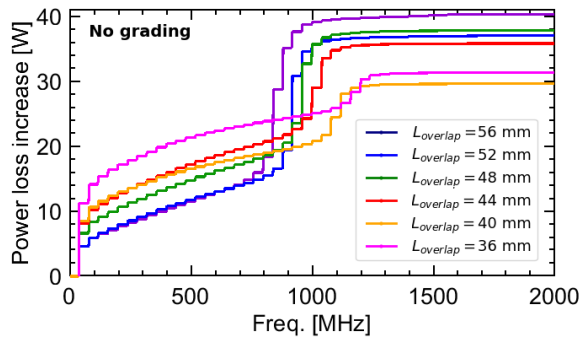


Figure 5.20 – Cumulative power loss for different  $L_{\text{overlap}}$  (no grading).

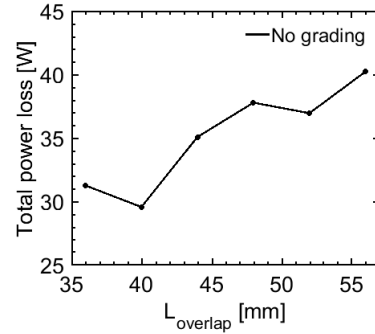


Figure 5.21 – Total power loss as a function of  $L_{\text{overlap}}$  (no grading).

## Conclusions

The analysis shows that the conventional beam screen design can be still optimized in terms of the total power loss. For the beam screen with graded screen conductors the optimal value is  $L_{\text{overlap}} = 44$  mm, while for ungraded screen conductors it can be even shorter. Nevertheless, for the overlaps considered, the minimum of the total power loss is lower with graded conductors ( $\sim 27$  W) than with ungraded conductors ( $\sim 29$  W). In particular, in the next section, we will present a new concept of the beam screen design with an improved high voltage performance for which we can use ungraded screen conductors.

## 5.5 Spiral beam screen

### 5.5.1 New concept

The new concept of the spiral beam screen reduces beam coupling impedance and improves high voltage performance. In this design, the screen conductors are not straight, but each of them is twisted along the length of the alumina tube. To provide a fast magnetic field rise time, the screen conductors are capacitively coupled at the upstream end of the kicker magnet [58]. A schematic diagram of a single spiral conductor is shown in Fig. 5.22.

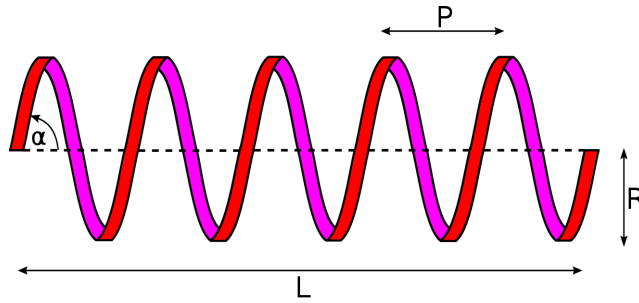


Figure 5.22 – Schematic of a single spiral conductor.

Let us denote  $N_{\text{turn}}$  as the number of turns of the spiral conductor along the length ( $L$ ) of the aperture of the kicker magnet and  $R$  as the spiral radius. The length of the spiral inside the magnet aperture is:

$$s = \sqrt{L^2 + (2\pi R N_{\text{turn}})^2}. \quad (5.6)$$

As each screen conductor extends from the downstream to the upstream end of the beam screen, over a distance  $L_{\text{total}}$ , and assuming a continuous spiral, the total number of turns is given by:  $N_{\text{total}} = \frac{L_{\text{total}}}{L} N_{\text{turn}}$ . The pitch of the spiral is the distance which 1 turn of the spiral spans:  $p = \frac{L}{N_{\text{turn}}}$ . The angle of the spiral screen conductor is:  $\alpha = \arctan(\frac{p}{2\pi R})$ .

### 5.5.2 Induced voltage analysis

The HV issues associated with the conventional design, i.e. breakdowns historically occurring at the upstream end, have been discussed in Chapter 3. Let us analyze the cross-section of the beam screen shown in Fig. 5.23. From Eq. 3.12, in a conventional beam screen, the maximum voltage is induced on the screen conductor closest to the HV busbar (#1 in Fig. 5.23):  $V_1 = \frac{dB}{dt}(d + 2R)L$ , whilst the minimum voltage on the screen conductor adjacent to the GND busbar (#13 in Fig. 5.23) is:  $V_{13} = \frac{dB}{dt}dL$ , where  $R$  is the inner radius of the alumina tube. Note: the spiral would be applied to the inside of the alumina tube so that the alumina provides electrical insulation between the spiral and each of the HV and GND busbars during the field pulse. Voltage breakdown can occur if there is a significant difference in the total induced voltage between adjacent screen conductors or between screen conductors and the outer metallic cylinder, resulting in high electric field [55]. In the new design, we will show that the total induced voltage on every screen conductor is the same, and that the maximum induced voltage is considerably reduced.

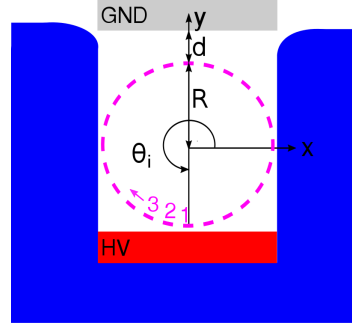


Figure 5.23 – Cross-section of the beam screen.

For the spiral beam screen, the coordinates of a point of the  $i$ -th screen conductor are given by:

$$\begin{cases} x_i(\theta) = R\cos(\theta + \theta_i) \\ y_i(\theta) = R\sin(\theta + \theta_i) \\ z_i(\theta) = \frac{p\theta}{2\pi}; \theta \in [0; 2\pi N_{\text{turn}}], \end{cases} \quad (5.7)$$

where  $\theta_i$  is the initial angle of the  $i$ -th screen conductor at the start of the cross-section (see Fig. 5.23). Assuming 24 conductors,  $\theta_i = \frac{3}{2}\pi - \frac{2\pi(i-1)}{24}$ . The distance from the GND busbar for the  $i$ -th screen conductor changes along the longitudinal direction and can be expressed as:

$$f_i(\theta) = d + R - y_i(\theta). \quad (5.8)$$

Note:  $f_i(\theta)$  does not depend on  $x_i$ . To compute the total induced voltage, for  $\zeta = 2\pi N_{\text{turn}}$ , let  $k = \frac{dB}{dt} \frac{p}{2\pi}$ , hence:

$$V_i = k \int_0^\zeta f_i(\theta) d\theta = k \int_0^\zeta \left( d + R - R\sin(\theta + \theta_i) \right) d\theta = \frac{dB}{dt}(d + R)L - kR \left( \cos(\theta_i) - \cos(\theta_i + \zeta) \right). \quad (5.9)$$

It can be shown that  $V_i$  is independent of  $\theta_i$  when  $N_{\text{turn}}$  is an integer. In this case, the total induced voltage on each screen conductor is the same:  $V_i = \frac{dB}{dt}(d+R)L$ . This is approximately one-half of the worst case voltage induced on a straight screen conductor:  $V_1 = \frac{dB}{dt}(d+2R)L$ . Also, for straight conductors, there can be a significant difference in the induced voltage between adjacent conductors, especially for  $\theta \sim 0$  and  $\theta \sim \pi$ . Whereas, for the spiral design, there is no or little difference at the upstream end for  $N_{\text{turn}}$  equal to an integer value. Although there could be a small difference in induced voltages due to fringe fields at each end of the kicker magnet, a spiral beam screen is expected to provide significantly improved HV performance.

### 5.5.3 Longitudinal beam coupling impedance

#### Impact of the number of turns

The goal is now to study the longitudinal impedance of the spiral beam screen with an integer number of turns along the aperture of the kicker magnet. From an analysis of the conventional design (see Section 5.3.5), the main resonances are in good agreement for simulations performed using the full model, simplified model or the cut-down model. For the spiral design, due to the lack of left-right symmetry present in the conventional design, the computation times double. Hence, the spiral beam screen was analyzed using a simplified or a cut-down model (see Fig. 5.24).

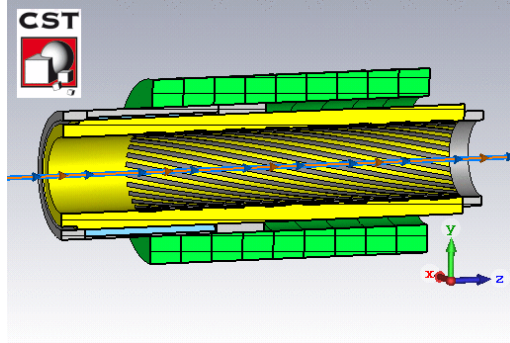


Figure 5.24 – Spiral beam screen (cut-down model).

The parameters of the spiral screen conductors are shown in Table 5.2. The length of a single screen conductor in the overlap region is denoted by  $x_{\text{overlap}}$ . Hence, for spiral screen conductors  $x_{\text{overlap}} > L_{\text{overlap}}$ , whereas for straight ones  $x_{\text{overlap}} = L_{\text{overlap}}$ . The  $n$ -th harmonic of the fundamental resonance in the longitudinal impedance spectrum of the conventional design is denoted by  $f_{\text{conv}}^{(n)}$  (see Eq. 3.11), whereas for the spiral beam screen it is denoted by  $f_{\text{spiral}}^{(n)}$ .

The simulation results show that  $f_{\text{spiral}}^{(n)}$  is determined by the length  $x_{\text{overlap}}$ . This becomes evident when comparing  $f_{\text{conv}}^{(n)} / f_{\text{spiral}}^{(n)}$  with respect to  $x_{\text{overlap}} / L_{\text{overlap}}$ : the two ratios are in good agreement. Hence, Eq. 3.11 should be generalized by using  $x_{\text{overlap}}$  instead of  $L_{\text{overlap}}$ .

when the screen conductors are not straight. As  $x_{\text{overlap}}$  increases with the number of turns, the main harmonics shift to lower frequencies, which increases the power deposition. To address this, we could propose to use the spiral beam screen, with an integer number of turns over the effective length of the kicker magnet, with straight conductors in the overlap region.

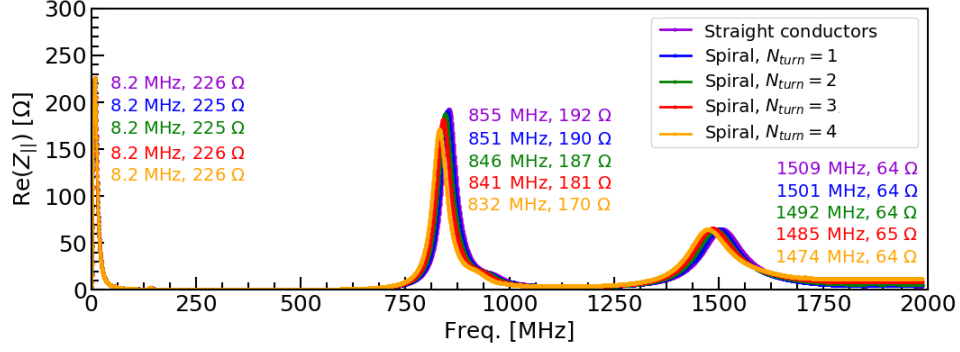


Figure 5.25 – Real part of the longitudinal beam coupling impedance of the spiral beam screen in comparison with the conventional design, evaluated on the cut-down model with ungraded screen conductors, a non-symmetric vacuum gap and  $L_{\text{overlap}} = 56$  mm.

Table 5.2 – Parameters of the spiral beam screen.

Parameter	Spiral			
$N_{\text{turn}}$	1	2	3	4
$N_{\text{total}}$	1.18	2.35	3.53	4.70
$x_{\text{overlap}}$ [mm]	56.09	56.36	56.81	57.43
$x_{\text{overlap}}/L_{\text{overlap}}$	1.002	1.006	1.014	1.025
$f_{\text{conv}}^{(1)}/f_{\text{spiral}}^{(1)}$	1.004	1.011	1.015	1.027
$f_{\text{conv}}^{(2)}/f_{\text{spiral}}^{(2)}$	1.005	1.011	1.015	1.023

### 5.5.4 Optimization process

#### Reduction of the overlap length

In Section 5.4, it has been shown that the overlap region should be reduced to decrease the total power loss. Based on the presented results,  $L_{\text{overlap}} = 44$  mm is proposed for the spiral beam screen. Between the outside of the alumina tube and metallic cylinder, where there is no vacuum gap deliberately introduced, the outside alumina tube must be metallized for HV reasons. An RF contact between the metallization and metallic cylinder ensures good electrical contact for the beam image current. Hence, to provide metallized space of 21.5 mm for the RF contact (see Fig. 5.26) between the metallic cylinder and the alumina tube, as in the initial conventional design (see Fig. 5.27), the overlap length has been reduced by shortening the screen conductors from the left side instead of cutting the metallic cylinder at the right side: this ensures the same length of exposure of the ferrite rings to the beam.

### Implementation of a symmetric vacuum gap

In addition, we introduce a symmetric vacuum gap (see Fig. 5.26), as this feature cancels out the quadrupolar component of transverse impedance (see Section 5.7.3). For the spiral design with an integer number of turns, the total induced voltage, on each conductor, is equal to that of a conductor at a distance of  $d + R$  from the GND busbar in the conventional beam screen (see Fig. 5.23). Hence, for HV reasons [55], the vacuum gap is equal to that at the vertical centre of the conventional design, i.e. 2 mm. As in the conventional design, the vacuum gap extends beyond all the screen conductors for a distance of 22.5 mm, to reduce the electric field [55].

### Screen conductors without grading

For the spiral beam screen, the total induced voltage on the screen conductors is the same, hence inter-conductor voltage breakdowns are expected to be eliminated. Moreover, the induced voltage is lower in comparison with the maximal induced voltage on the straight screen conductors in the conventional beam screen design. For this reason, we will consider the screen conductors without grading in our models of the spiral beam screen (see Fig. 5.26).

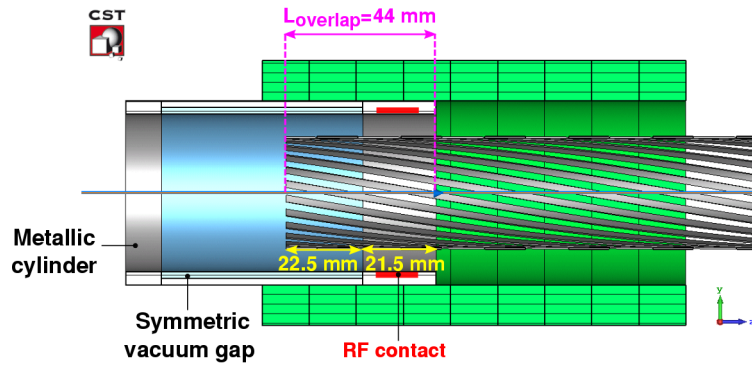


Figure 5.26 – Spiral beam screen with ungraded screen conductors, a symmetric vacuum gap and  $L_{\text{overlap}} = 44$  m (simplified model).

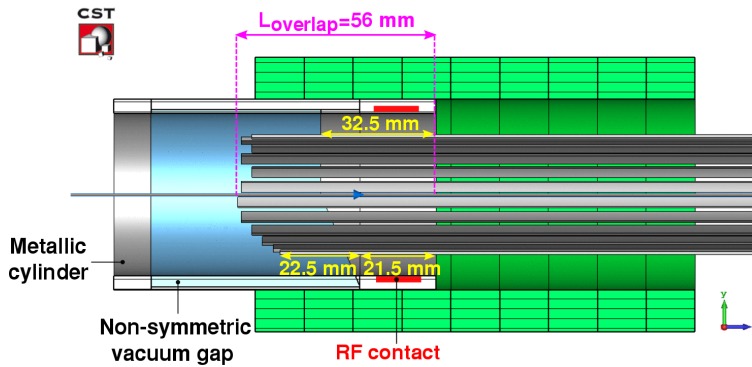


Figure 5.27 – Initial design of the conventional beam screen with graded screen conductors, a non-symmetric vacuum gap and  $L_{\text{overlap}} = 56$  mm (simplified model).

### Screen conductors connected together in the overlap region

Moreover, as the total induced voltage on each spiral conductor is nominally identical, and hence eddy currents should not circulate between conductors, we investigated a design with all spirals connected together in the overlap region (see Fig. 5.28). This idea is very interesting for future machines, e.g. the FCC-hh: if there was a "switch" to connect all screen conductors to the beam pipe, once injection is complete, there would be a continuous path for the beam image current and hence low beam coupling impedance. Whereas, for unconnected screen conductors, a "switch" would be necessary for each screen conductor, what would increase cost and complexity.

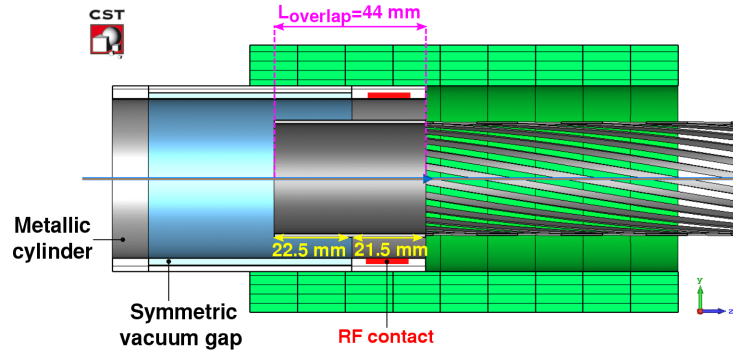


Figure 5.28 – Spiral beam screen with screen conductors connected together in the overlap region, a symmetric vacuum gap and  $L_{\text{overlap}} = 44$  mm (simplified model).

### Results

The longitudinal impedance predictions for the optimized models are presented in Fig. 5.29. The proposed modifications allow us to shift the fundamental harmonics to higher frequencies in comparison with the initial design of the conventional beam screen. The spiral design with conductors all connected together in the overlap region shifts the main harmonic to an even higher frequency. This is due to the length of the overlap being reduced from  $x_{\text{overlap}}$  to  $L_{\text{overlap}}$ . For nominal FCC parameters, the cumulative power loss associated with each configuration of the beam screen is shown in Fig. 5.30. The total power loss for the spiral models is between 31 W (for 1 turn) and 36 W (for 3 turns), while for the FCC conventional design we expect 32 W. For spirals, a significant contribution to the total predicted power loss is between 100 MHz and 800 MHz (see the zoom in Fig. 5.29), where no resonances are expected to occur. Hence, these low- $Q$  resonances are probably an artifact of the simulations for spirals with increased number of turns.

In all cases, the total power loss is lower than for the upgraded LHC MKI8D with nominal LHC parameters (37 W, not scaled) [97]. In addition, similar power deposition distribution will occur in the FCC injection kicker magnets as in the upgraded LHC MKI8D. Hence, since the upgraded MKI has not limited LHC operation [98], we conclude that heating of the FCC injection kickers is acceptable too. The longitudinal impedance of the spiral beam screen

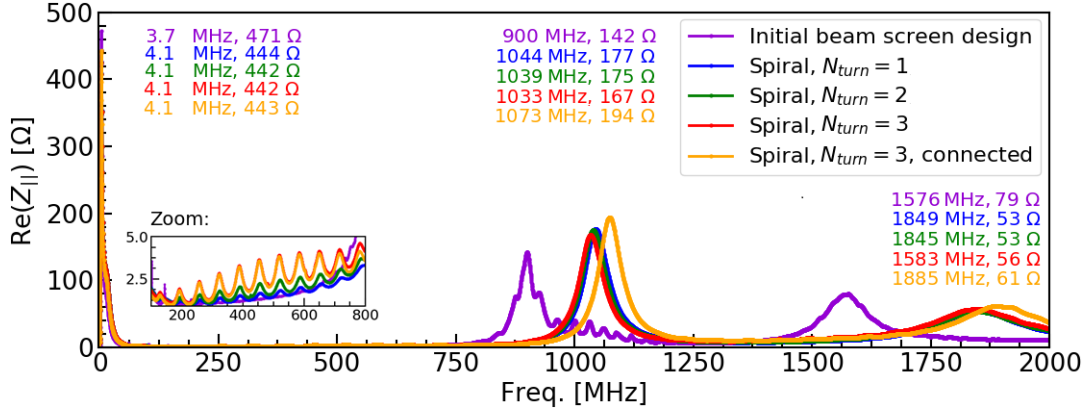


Figure 5.29 – Real part of the longitudinal impedance of the spiral beam screen with a symmetric vacuum gap, ungraded screen conductors and  $L_{\text{overlap}} = 44$  mm in comparison with the initial design of the conventional beam screen (simplified model).

has been experimentally verified. For this purpose, a prototype alumina tube with spiral screen conductors applied using a silver paint, has been installed in a spare LHC MKI for beam coupling impedance measurements. The results are discussed in Chapter 7.

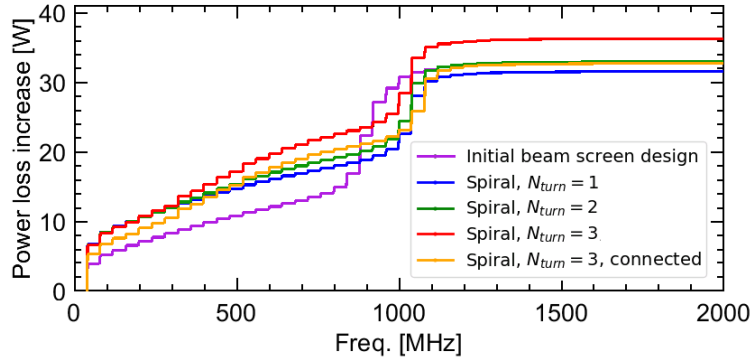


Figure 5.30 – Cumulative power loss for the spiral beam screen of different number of turns, with ungraded screen conductors, a symmetric vacuum gap and  $L_{\text{overlap}} = 44$  mm in comparison with the initial design of the conventional beam screen (simplified model).

## 5.6 Impact on longitudinal beam stability

### 5.6.1 Coupled bunch instability

In this part, we would like to evaluate the longitudinal impedance contribution of the shielded FCC injection kicker magnets to the threshold for the longitudinal coupled bunch instability. The real part of the longitudinal impedance of the conventional and spiral beam screen designs is shown in Fig. 5.29. Let us compare the shunt impedance of the predicted resonances with the threshold for the longitudinal coupled bunch instability (see Eq. 2.52).



Table 5.3 – FCC beam and machine parameters at top energy [7].

Parameter	Unit	Value
Beam energy $E_0$	TeV	50
RF voltage $V_{\text{RF}}$	MV	42
Average beam current $I_0$	A	0.5
Bunch length $\tau_L$	ns	1.07
Slippage factor $\eta$	-	$1 \times 10^{-4}$
Gamma transition $y_t$	-	99.33
Harmonic number $h$	-	130680

To calculate the threshold, the FCC beam and machine parameters at top energy are analyzed (see Table 5.3). The relative energy spread and the relative synchrotron angular frequency spread are estimated using Eqs. 2.53-2.55. In particular,  $\phi_0 = \pi$ , as the machine operates above transition energy. We obtain:  $\frac{\Delta E}{E_0} = 1.2 \cdot 10^{-4}$  and  $\frac{\Delta \omega_{s0}}{\omega_{s0}} = 0.11$ .

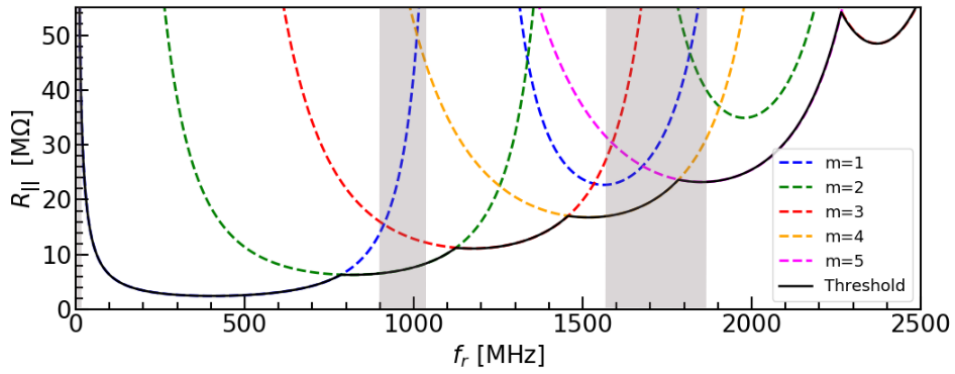


Figure 5.31 – Threshold for the longitudinal coupled bunch instability as a function of resonant frequency. The frequency ranges at which we expect resonances for different beam screen designs are indicated in rectangular windows (in grey).

For a fixed bunch length, the threshold for the longitudinal coupled bunch instability is a function of resonant frequency as shown in Fig. 5.31. Its minimum depends on the order of the Bessel function ( $m$ ). The lowest threshold is found for the resonant frequency of 400 MHz ( $R_{||} \simeq 2 \text{ M}\Omega$ ). The resonant modes at higher or lower frequencies give a smaller probability of driving instability. In the rectangular windows (in grey), we indicate the frequency ranges at which the resonant modes of the FCC injection kicker magnet with the conventional or spiral beam screen design occur. In each range, the threshold is at least a few orders of magnitude above the impedance of one kicker magnet (see Fig. 5.29). In particular, the lowest threshold is found for the first harmonics of the fundamental mode at  $\sim 1000 \text{ MHz}$  ( $R_{||} = 7.5 \text{ M}\Omega$ ). For the conventional and the spiral beam screen, the shunt impedance at this frequency is below  $200 \Omega$ . For 18 kicker magnets, the contribution to the threshold is  $\sim 0.05\%$ . This leads us to the conclusion that FCC injection kickers, either with the conventional or spiral beam screen, are unlikely to drive longitudinal coupled bunch instability.

### 5.6.2 Loss of Landau damping

In FCC, to preserve longitudinal Landau damping, the upper limit for the imaginary effective longitudinal impedance is 200 m $\Omega$ : to provide a safety margin, this is a factor of two higher than for LHC (100 m $\Omega$ ) [7]. To estimate the impedance contribution of shielded FCC injection kicker magnets to the given impedance budget, let us analyze  $\text{Im}(Z_{\parallel}(\omega)/n)$  of the conventional and of the spiral models. As shown in Fig. 5.32, in all cases,  $\text{Im}(Z_{\parallel}(\omega)/n)$  is almost constant, except at low frequencies. To take this effect into account, for each model, we calculated the imaginary effective longitudinal impedance using Eq. 2.56. For this purpose, the angular synchrotron frequency is  $\omega_{s0} = 25$  Hz, as calculated using Eq. 2.14. Table 5.4 presents the contribution (expressed in %) of 18 kicker magnets to the total impedance budget. In particular, we compared different beam screen designs assuming Gaussian and parabolic spectral power densities and  $m = 0$  or  $m = 1$  (see Eq. 2.57). The spectral power densities are shown in Fig. 5.33.

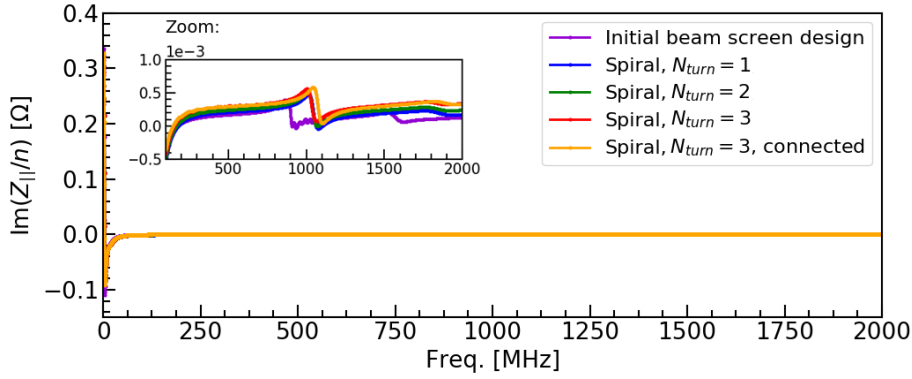


Figure 5.32 –  $\text{Im}(Z_{\parallel}/n)$  as a function of frequency for different beam screen designs.

Table 5.4 – Contribution of the imaginary longitudinal effective impedance of 18 kicker magnets to the threshold for loss of Landau damping (expressed as a % of 200 m $\Omega$ ).

Model	Gaussian	Gaussian	Parabolic	Parabolic
	m=0	m=1	m=0	m=1
Initial design	2.5	2.9	2.6	2.9
Spiral, $N_{\text{turn}} = 1$	4.2	3.8	4.1	3.9
Spiral, $N_{\text{turn}} = 2$	4.7	4.4	4.7	4.5
Spiral, $N_{\text{turn}} = 3$	5.7	5.4	5.7	5.6
Spiral, $N_{\text{turn}} = 3$ , connected	5.7	5.4	5.7	5.6

For a given design, the results are very similar either for Gaussian or parabolic bunch and  $m = 0$  or  $m = 1$ . For 18 kicker magnets with the conventional beam screen, the contribution is between 2.5% to 2.9% of the allowable total machine budget. In the worst case, for the spiral with 3 turns, the contribution is between 5.4% to 5.7%. Overall, we conclude that FCC injection kicker magnets contribute to the total impedance budget at an acceptable level. The studies confirm that optimization of the injection system and the reduction of the total length

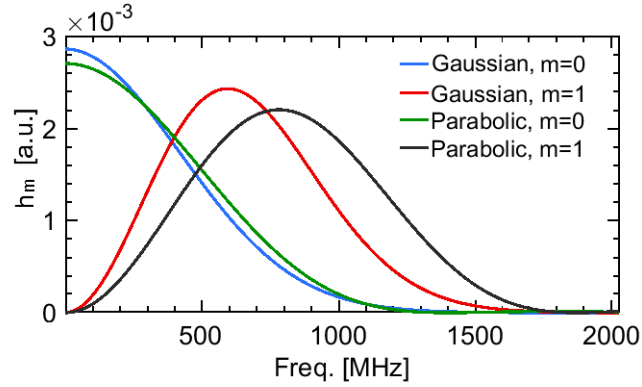


Figure 5.33 – Spectral power densities of Gaussian and parabolic bunch for  $m = 0$  and  $m = 1$ .

of the kicker magnets from  $\sim 120$  m to  $\sim 40$  m, as (see Chapter 4) is very important for reducing the total imaginary effective impedance of the FCC.

## 5.7 Transverse beam coupling impedance

### 5.7.1 Wakefield simulations

In this section, we aim to determine the dipolar and quadrupolar components of the transverse impedance of the conventional and spiral beam screen designs. It is important to disentangle these two components, as they have different effects on beam dynamics. In the Wakefield Solver, to analyze modes with high  $Q$ -factors, the wakelength necessary to compute the impedance spectrum with a good frequency resolution requires several weeks of computation. Otherwise, the impedance calculated from a partially decayed wake potential brings a significant risk of underestimating the shunt impedance of the narrow resonant modes [89]. Let us remark, the conventional beam screen has only left-right symmetry, while the spiral beam screen is asymmetric. Since both structures are not fully symmetric, in the Wakefield Solver, we first evaluated the constant term (see Eqs. 2.35-2.36), when both the source and the test particle are on the nominal beam axis. To calculate the dipolar impedance (see Eqs. 2.43-2.44), we displaced the beam transverse location, while leaving the transverse position of the wake integration path at the nominal beam axis. To obtain the quadrupolar impedance (see Eqs. 2.45-2.46), we displaced the transverse location of the wake integration path, while leaving the beam transverse location at the nominal beam axis.

### 5.7.2 Eigenmode simulations

In the next step, to benchmark Wakefield Solver simulations, we followed the new method of finding the dipolar and quadrupolar modes of an asymmetric structure using the Eigenmode Solver [100]. In this approach, both the dipolar and quadrupolar impedances are found as the sum of the eigenmode solutions using the resonator model (see Eqs. 2.48-2.49). For each

mode found in the Wakefield Solver, we perform Eigenmode simulations on a very narrow frequency range (i.e. 10 MHz). In addition, we allow the program to interpolate material properties within the selected frequency range to properly model the behaviour of ferrites. For each mode found in a single Eignemode Solver simulation, the following function has to be analyzed:

$$f(x) = (R/Q)_{||}(x), \quad (5.10)$$

where  $x$  is the transverse offset around the point of interest  $x_0$ . Analogously, a similar analysis is performed in the  $y$ -plane. Remark: for the shunt impedance, the "circuit" convention is used:  $(R/Q)_{||}(x) = |V_{||}^2(x)/(2\omega_x U)|$ , where  $V_{||}$  is the voltage integrated along the longitudinal direction and  $U$  is the total energy stored in the mode. In addition, we introduce the function [100]:

$$g(\omega) = \frac{Q}{1 + iQ(\frac{\omega}{\omega_x} - \frac{\omega_x}{\omega})}. \quad (5.11)$$

The dipolar and quadrupolar impedances are found as [100]:

$$Z_x^{\text{dip}}(\omega, x_0) = \frac{cg(\omega)}{4\omega} \frac{f'(x_0)^2}{f(x_0)}, \quad (5.12)$$

$$Z_x^{\text{quad}}(\omega, x_0) = \frac{cg(\omega)}{4\omega} \left( -\frac{f'(x_0)^2}{f(x_0)} + 2f''(x_0) \right). \quad (5.13)$$

However, if  $f(x)$  behaves like a parabolic function with a minimum in  $x_0$  and  $f(x_0) \cong 0$ , it follows that  $f'(x_0) = 0$ . In this case, Eqs. 5.12-5.13 become numerically unstable due to 0/0 division. In this case, only the dipolar component is present and can be expressed as [100]:

$$Z_x^{\text{dip}}(\omega, x_0) = \frac{cg(\omega)}{2\omega} f''(x_0). \quad (5.14)$$

### 5.7.3 Results

#### Conventional design

Figure 5.34 presents the real part of the dipolar horizontal transverse impedance of the conventional beam screen with a non-symmetric vacuum gap and  $L_{\text{overlap}} = 56$  mm. The results show excellent agreement of the predicted resonant frequencies using both the Wakefield Solver and the Eigenmode Solver. However, the shunt impedances of the resonant modes evaluated using the Wakefield Solver are remarkably smaller than the Eigenmode results: this is attributed to the impedance calculation from partially decayed wake potential due to time constraints ( $WL = 500$  m modelled). Hence, the shunt impedance of the resonant modes calculated using the Wakefield Solver is underestimated. In Figure 5.34, the resonances occur approximately at: 20 MHz, 61 MHz and 102 MHz. The first mode has the highest shunt impedance of approximately 26 MΩ/m. From an analysis of the electric field patterns (see Fig. 5.35), we assume that

the predicted modes are quarter wavelength resonances, i.e.  $\sim 20$  MHz is a  $\lambda/4$  resonance with  $\lambda$  being the wavelength, while 61 MHz and 102 MHz are odd-integer multiples of  $\sim 20$  MHz. However, an analytic expression for the resonances is hard to define due to the complexity of the structure and this topic requires further investigation. Nevertheless, from the analysis of the cut-down model, we expect that the fundamental harmonic is determined by the length of the screen conductors.

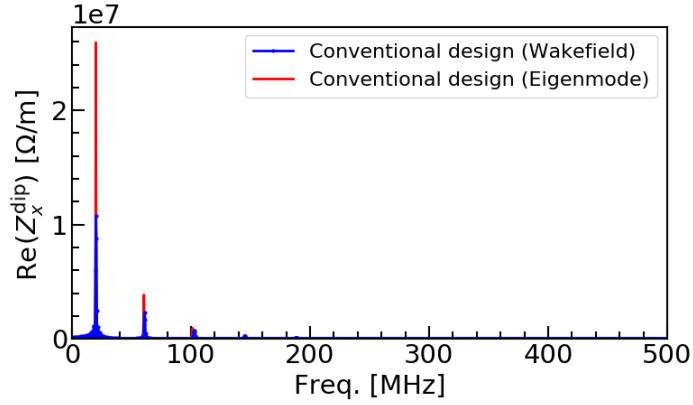


Figure 5.34 – Real part of the horizontal dipolar transverse impedance of the conventional beam screen with a non-symmetric vacuum gap and  $L_{\text{overlap}} = 56$  mm (simplified model).

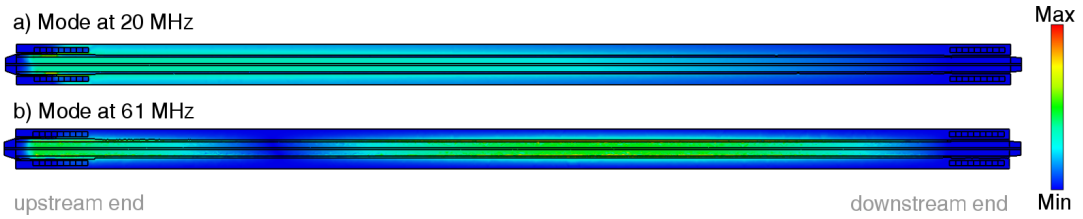


Figure 5.35 – Electric field distributions at a) 20 MHz and b) 61 MHz.

The quadrupolar component of the horizontal transverse impedance is shown in Fig. 5.36. From the Wakefield simulations, the first mode is at  $\sim 17$  MHz - the higher harmonics are weaker and occur every  $\sim 36$  MHz, i.e. at odd-integer multiples of  $\sim 17$  MHz. However, these resonances were not found using the Eigenmode Solver. This can be attributed to the amplitude of the quadrupolar modes being two orders of magnitude lower than the dipolar modes. Note, for the vertical plane, the dipolar and the quadrupolar impedances are very similar to the horizontal plane and the same conclusions apply.

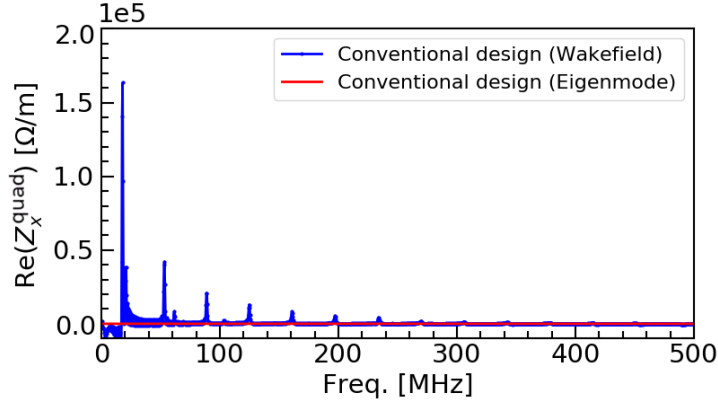


Figure 5.36 – Real part of the horizontal quadrupolar transverse impedance of the conventional beam screen with a non-symmetric vacuum gap and  $L_{\text{overlap}} = 56$  mm (simplified model).

### Spiral beam screen

Next, the transverse impedance of the spiral beam screen with 3 turns, a symmetric vacuum gap and  $L_{\text{overlap}} = 44$  mm has been analyzed. The real part of the dipolar horizontal transverse impedance is shown in Fig. 5.37. Again, an excellent agreement has been achieved in the predicted resonant frequencies using the two different solvers. The magnitudes of the peaks are also very similar, as a full decay of wake potential has been achieved in the Wakefield simulation ( $WL = 500$  m).

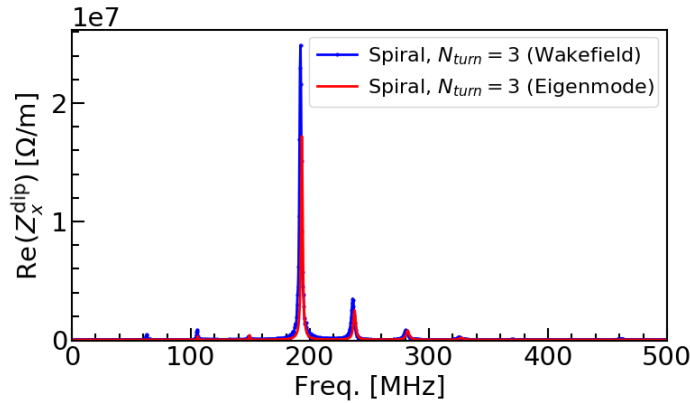


Figure 5.37 – Real part of the horizontal dipolar transverse impedance of a spiral with 3 turns, a symmetric vacuum gap and  $L_{\text{overlap}} = 44$  mm (simplified model).

In Figure 5.37, the resonances occur every 44 MHz and are observed approximately at the following frequencies: 61 MHz, 105 MHz, 149 MHz, 193 MHz, 237 MHz, 281 MHz, 325 MHz. The resonances look like odd-integer multiples of  $\sim 21$  MHz, as per the conventional design, except the first harmonic does not appear. The fundamental harmonic might be slightly different in comparison with the conventional design, as the length of the screen conductors is different due to the shorter overlap length and the twist of the spiral screen conductors. The

strongest mode is observed at 193 MHz, which is not the fundamental harmonic: this attribute of the spiral beam screen is beneficial and will be discussed further. The magnitude of the strongest real mode is  $\sim 18 \text{ M}\Omega/\text{m}$  (Eigenmode Solver) or  $\sim 24 \text{ M}\Omega/\text{m}$  (Wakefield Solver). The electric field pattern at 193 MHz is shown below (see Fig. 5.38).

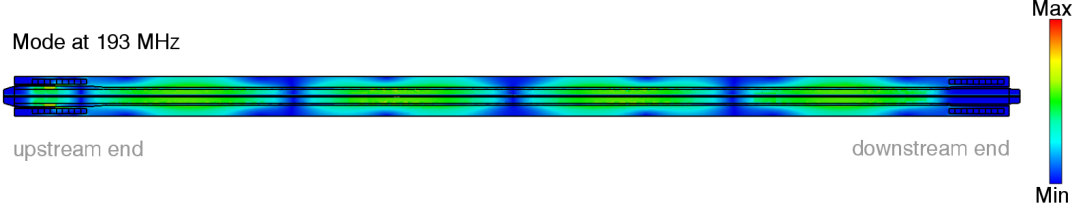


Figure 5.38 – Electric field distribution at 193 MHz (spiral beam screen with 3 turns).

In addition, the spiral beam screen with a symmetric vacuum gap is advantageous, as it cancels out the quadrupolar component of the real and imaginary transverse impedance. In this regard, both of the solvers agree (see Fig. 5.39). To better indicate the negligible magnitude, we use the same scale as in Fig. 5.36. Note, for the vertical plane, the same conclusions apply.

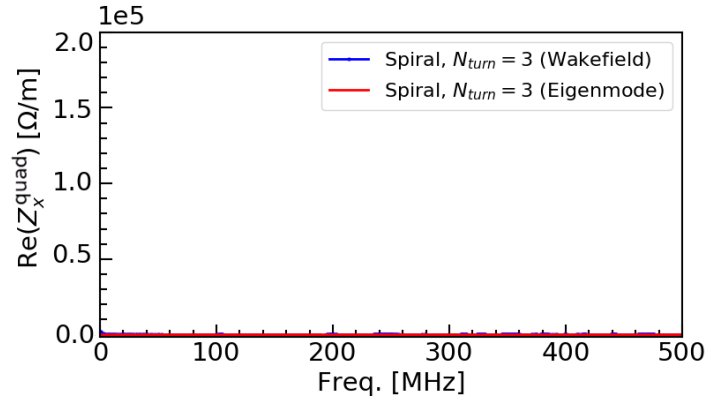


Figure 5.39 – Real part of the horizontal quadrupolar transverse impedance of a spiral with 3 turns, a symmetric vacuum gap and  $L_{\text{overlap}} = 44 \text{ mm}$  (simplified model).

### 5.7.4 Transverse impedance budget considerations

To evaluate the impedance impact of 18 kicker magnets on transverse beam stability in FCC, their contribution has been taken into account in the entire transverse impedance model [101] of the machine. From beam dynamics simulations, only 2 injection kicker magnets with a spiral beam screen with 3 turns would fit into the FCC impedance budget for the coupled bunch instability in the transverse plane [102]. An important advantage of the spiral beam screen is the possibility to tune the resonant frequency of the transverse modes. Provided that the frequencies of the main resonances could be shifted, 9 pairs of detuned kickers would fit into the impedance budget requirements [102]. On the contrary, shifting the resonant frequency for many kicker magnets is not possible with the conventional design, as it would require the overlap of some kickers to be changed and hence it would have destructive impact

on the longitudinal impedance and would cause excessive heating.

### Optimization of the spiral beam screen for 18 kicker magnets

With the spiral beam screen, the strongest mode does not necessarily occur at the fundamental harmonic, as shown in Fig. 5.37. Below, we present a comparison of the dipolar horizontal impedance for a spiral with 1 and 3 turns (see Fig. 5.40). For a 1 turn spiral, the resonances occur at 64 MHz and 108 MHz, in comparison with 61 MHz and 105 MHz for 3 turns. Hence, the difference of the total length of the screen conductors slightly modifies the frequencies of the observed peaks. Moreover, the number of turns determines the frequency of the strongest mode. For a 1 turn spiral, the strongest resonance is at 64 MHz ( $\sim 21 \text{ M}\Omega/\text{m}$ ), while for a 3 turn spiral it is at 193 MHz ( $\sim 18 \text{ M}\Omega/\text{m}$ ). Hence, the change in frequency of the strongest mode is significant. Based on the presented results, to tune the frequencies of the main resonances we can consider several approaches, i.e. different number of turns inside the magnet aperture, the same number of turns inside the magnet aperture but more turns outside of the aperture, or a different length of the beam screen outside of the aperture. However, to provide the exact estimation of the beam coupling impedance, each modified beam screen would have to be analyzed separately.

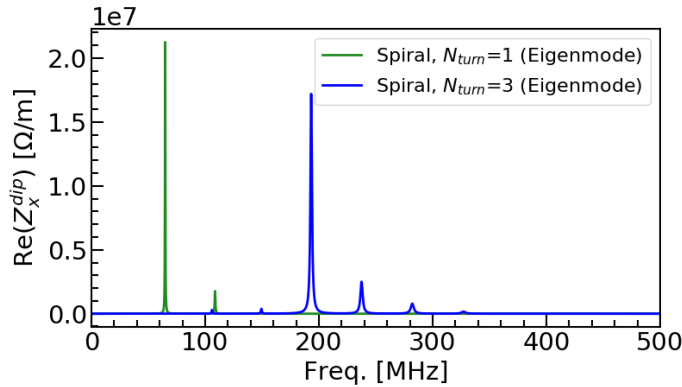


Figure 5.40 – Comparison of the real part of the horizontal dipolar transverse impedance of the spiral with 1 and 3 turns, a symmetric vacuum gap and  $L_{\text{overlap}} = 44 \text{ mm}$  (simplified model).

### Conclusions

The studies show that with the given impedance budget, only the spiral beam screen could be used in an FCC injection system, composed of 18 kicker magnets, by tuning the number of turns - otherwise, the kicker magnets are mechanically, nominally identical. In this thesis, we only present a proof of principle for optimizing the configuration of 18 kickers. For the future studies, each design would have to be separately analyzed. Importantly, we have already reduced the number of kicker magnets and the total length of each FCC injection system as described in Chapter 4, hence considerably reducing the impedance of each injection system. Moreover, for multiple kicker magnets with the conventional beam screen, it is not possible to tune the resonant frequencies without a destructive impact on the longitudinal impedance.



## 6 Impact of a beam screen upon the field response of the kicker magnet

The main goal of this thesis was to develop a beam screen for limiting beam coupling impedance in the pulsed, high voltage environment - a novel beam screen has been proposed and studied. Nevertheless, studies have also been carried out to ensure that the pulsed magnetic field, required to inject beam, is within specification. A beam screen in the aperture of the kicker magnet is expected to influence the field rise time and the field flat-top quality [58]. For this reason, it is important to ensure that, with a beam screen, the required pulse response of the kicker magnet can still be achieved. In particular, the beam screen causes a significant frequency dependence of the inductance of the kicker magnet. In this chapter, such a dependence is quantified using the Finite Element Method (FEM) algorithms implemented in Opera-2D. In addition, the influence of the beam screen upon the predicted field homogeneity is investigated. Predictions for various configurations and electrical conductivity of the screen conductors are compared: hence, an optimal design is selected. The values for an equivalent circuit of the frequency dependent inductance of a cell of the kicker magnet, with the proposed beam screen, are determined using the PSpice Optimizer. The field rise time and the field flat-top quality of the final design are resolved using time domain PSpice simulations.

### 6.1 General considerations

#### 6.1.1 Beam screen with longitudinal or spiral screen conductors

As explained in Section 3.2.2, the beam screen conductors are placed in the inner surface of the alumina tube to carry the beam image current and therefore screen the ferrite yoke from the wake fields induced by the circulating beam, which could cause an excessive heating of the ferrite yoke. The alumina chambers allow the penetration of external fast time-varying magnetic fields produced by the pulse current in the busbars of the kicker magnet. The screen conductors can be either solid (i.e. as for the LHC MKI [58]) or can be applied using a thin coating, i.e. serigraphy [103]. An important advantage of serigraphed screen conductors is ease of manufacture of the alumina tube, as grooved slots are no longer required. The material, width and thickness of the screen conductors must be selected based on several requirements:

(1) adequately low beam coupling impedance must be achieved, (2) the external, pulsed, magnetic field must penetrate the beam screen, (3) the required field rise and fall times must be preserved as must the (4) field flat-top quality, (5) the screen conductors must sustain ohmic heating due to the beam image current and (6) eddy current heating due to the pulsing.

The electrical conductivity of the screen conductors must be rather high to provide a relatively low impedance path for the beam image current. However, at higher frequencies, the eddy currents induced in the screen conductors by the pulsed field will modify the magnetic field produced by the kicker magnet: this can unduly degrade the desired field response. Hence, dedicated studies have to be performed to choose optimum parameters for the screen conductors [58]. Importantly, the selected dimensions and electrical conductivity must be compatible with the requirement of achieving low beam coupling impedance. For a given material, good EM shielding is assumed to be provided when the thickness of the material is at least three skin depths, at the lowest frequency of concern (see Section 2.3). However, according to the literature review, this criterion is rather pessimistic and, in practice, shielding at lower frequencies is achieved as well [104, 105]. For kicker magnet operation, an important concern is the power deposition in the ferrite yoke, which is significant from the first beam harmonic, i.e. at 40 MHz (see Fig. 5.9). Hence, the thickness of the screen conductors must be selected to ensure effective shielding at this frequency and above. However, the thickness must be compatible with the requirement of good adhesion and quality of the coating [106]. The shielding at lower frequencies, and thus the maximum thickness of the screen conductors, is typically limited by the necessity of good pulse field response, as will be shown in Section 6.4.

### 6.1.2 Beam screen with continuous coating

A continuous coating of a thin metallic layer is frequently applied inside the alumina chambers of kicker magnets [107]. However, this solution is typically used for lumped inductance kicker magnets, which are generally used when longer field rise times are allowed [49]. In such a case, despite the shielding effect of the induced eddy currents, the required field response can be achieved. For instance, the alumina tube of the LHC dump kicker has a  $\sim 2\ \mu\text{m}$  thick Ti coating. By contrast, for the LHC or FCC injection kicker magnets, the requirements for field rise and fall times and field flat-top quality are much more demanding and hence transmission line kicker magnets are used. In addition, as a result of the field propagation in a transmission line kicker magnet, eddy currents are induced in the longitudinal direction. For this reason, capacitive coupling to a conductive cylinder, which is connected to the beam pipe, is introduced at one end of the coating to prevent an eddy current loop through the beam pipe: this excludes the possibility of using a continuous coating over the entire surface of the alumina tube.

Studies performed for the LHC MKI have shown that a sheet resistance  $R_s = 10\ \text{k}\Omega/\square$  is required so as not to degrade the magnetic field rise time: however, only below  $R_s = 1\ \text{k}\Omega/\square$  a good quality of coating can be achieved [106]. Hence, assuming a Ti coating of  $R_s = 1\ \text{k}\Omega/\square$ , the thickness would be  $< 0.5\ \text{nm}$ : this brings a significant risk of coating degradation, e.g. when

eddy currents are induced during pulsing or due to impact of beam particles. For the FCC injection kicker magnet, the specifications for field rise and fall times are more challenging than for LHC. For this reason, a continuous coating has not been considered in this case.

## 6.2 Opera-2D

In these studies, to evaluate the impact of a beam screen upon the magnetic field, the transient solver and the steady-state AC solver of the FEM code Opera-2D [17] have been used. The program allows to compute time-varying EM fields, including eddy current effects. In FEM, the model is divided into regions. The regions are simple, non overlapping, areas with specified properties. Finally, a so-called "background" region is specified for the whole model: Opera-2D fits the background around existing regions, greatly simplifying this step. However, the background region is not used for areas where field homogeneity or eddy currents are of significant interest, as it is not possible to control well the size of mesh elements throughout this region. Each region has one of the following characteristics: free space, a conductor with a prescribed conductivity and current density, or permeable material with specified linear or non-linear material characteristics. In FEM, each region is first discretized into small elements connected at nodal points, the so-called "finite elements". In some cases, it might be advantageous to divide one item into several regions in order to improve mesh quality. For each model, the mesh should be verified to ensure that it is suitable: this is especially important in eddy current regions [17]. Next, the user selects whether a linear or quadratic polynomial is used to approximate the solution within each element of a region. Importantly, the electric scalar potential must be defined at one point, at least, in the model to obtain a unique solution of the potential [17].

## 6.3 Unshielded kicker magnet

In this section, we will present the model of an unshielded kicker magnet, modelled in Opera-2D, in order to study the effect of frequency dependent inductance. Next, we will introduce a numerical approach to compute inductance of a magnetic circuit as a function of frequency. The inductance at a relatively high frequency will be compared with an analytic estimate. The benchmarking of this simple model is important before using it to optimize the beam screen for field rise time and homogeneity. Next, we will present the approach to calculate field homogeneity in the aperture of an unshielded kicker magnet using Opera-2D. This method employs several simplifications, which will be outlined. However, it is important to ensure that the field homogeneity in the aperture of an unshielded kicker magnet is adequate. Otherwise, with a beam screen placed in the aperture, the specifications are unlikely to be achievable.

### 6.3.1 Opera-2D model

The Opera-2D model of the unshielded FCC injection kicker magnet is presented in Fig. 6.1. Due to the top-bottom symmetry, it is necessary to model only half of the geometry. The entire model is split into several regions and it consists of the following elements: GND busbar (region 1), HV busbar (region 2), ferrite (regions 3-6), aperture (region 7), background (region 8). The busbars are modelled as a stainless steel with electrical conductivity of  $1.45 \times 10^6$  S/m (see Table 2.1). A non-linear BH curve can be modelled and properly taken into account in an Opera-2D transient analysis. However, for steady-state frequency domain (AC) analysis, Opera-2D can either use a linear or quasi non-linear approach. As discussed in Section 4.1.2, the ferrite dimensions of FCC injection kicker magnet are chosen such that a central cell operates far from saturation. Hence, the non-linear BH curve of the ferrite is neglected in the analysis and the real relative permeability of ferrite is modelled as being constant ( $\mu_r = 2000$ ).

The horizontal and vertical dimensions of the aperture are 48 mm, whereas the thickness of the ferrite is 30 mm (see Chapter 4). The width of the busbars has been specified to be 10 mm. The geometry of the GND busbar and ferrite have been optimized: both elements have rounded corners in order to both reduce electric field strength and ensure adequate field homogeneity in the aperture. The boundary conditions for the entire problem are set as tangential magnetic, except for the axis of top-bottom symmetry ( $y = 0$ ). In the 2D model, it is assumed that for the infinite length of the structure, the field distribution does not vary along the length and there is no component of field parallel to the longitudinal axis ( $z$ ). This approximation is reasonable for estimating the central cell inductance, i.e. neglecting end effects.

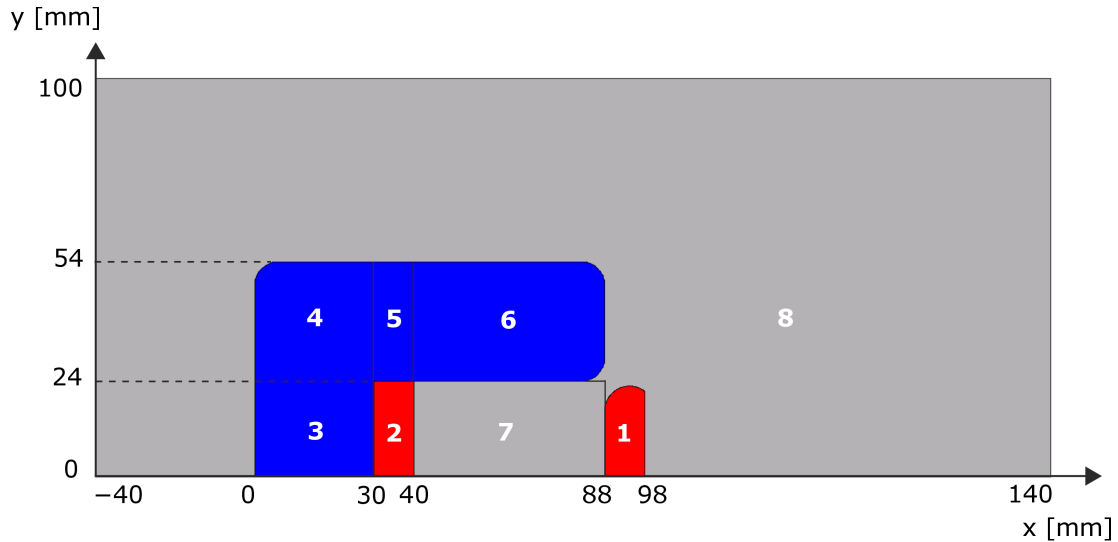


Figure 6.1 – Geometry of the unshielded kicker magnet (Opera-2D model). Due to the top-bottom symmetry only the upper part is modelled. The specific properties of materials are marked with different colours, i.e. conductor (colour red), ferrite (colour blue), free space (colour grey) and the individual regions into which the entire model is divided are numbered.

### 6.3.2 Frequency dependent inductance and resistance

The Opera-2D AC solver has been used to analyze inductance and resistance of a central cell of the magnet, as a function of frequency. The upper frequency limit is determined by the highest frequency of interest in the Fourier Transform of the trapezoidal current pulse:  $f_{\max} \approx \frac{1}{\pi\tau_c}$  [108]. For the FCC injection kicker magnet, the rise time of the current pulse is  $\tau_c = 75$  ns, while the fall time is expected to be longer [78]. Hence, it follows that  $f_{\max} \approx 4.25$  MHz. The Opera-2D simulations have been carried out in steps, from 0.1 Hz to 5 MHz. For stainless steel, the skin depth at 5 MHz is  $\sim 0.2$  mm (see Table 2.2). To achieve reliable results, the busbars are modelled with a regular mesh with at least 3 mesh-cells for the first skin depth, at the highest frequency of interest [17]. While in other regions, the mesh density is appropriately reduced (see Fig. 6.2).

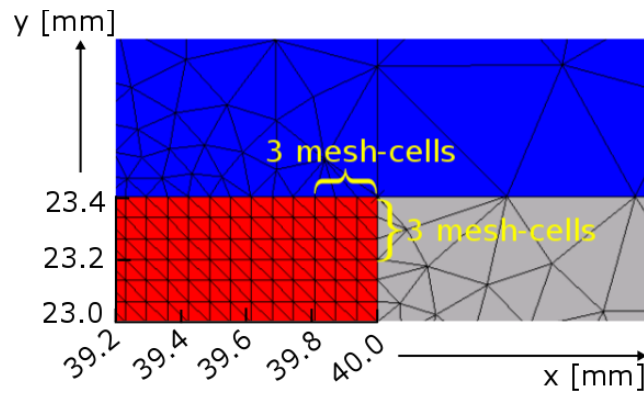


Figure 6.2 – Mesh grid required for simulations up to 5 MHz (zoom of part of HV conductor).

Let us compare the current density at low and at high frequency, i.e. at 10 Hz and at 1 MHz, shown in Figs. 6.3 and 6.4, respectively. At low frequency, the current flows through the entire cross-sectional area of the conductor, such that the current density within the conductor is almost constant. However, at high frequency, the AC current has a tendency to be distributed, such that the current density is highest in the aperture side surface of the conductors, due to both skin and proximity effects. In both cases, the absolute values of the minimum and maximum current density are equal.

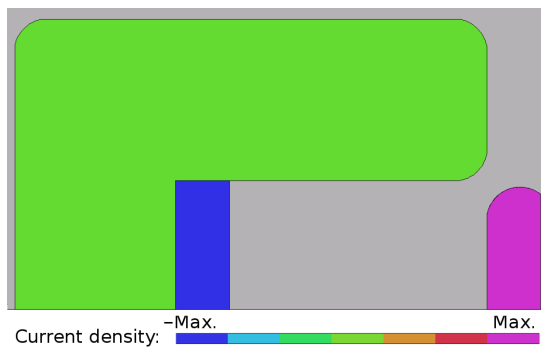


Figure 6.3 – Current density at 10 Hz (unshielded kicker magnet).

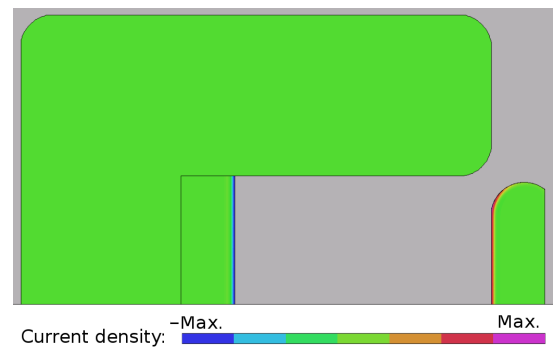


Figure 6.4 – Current density at 1 MHz (unshielded kicker magnet).

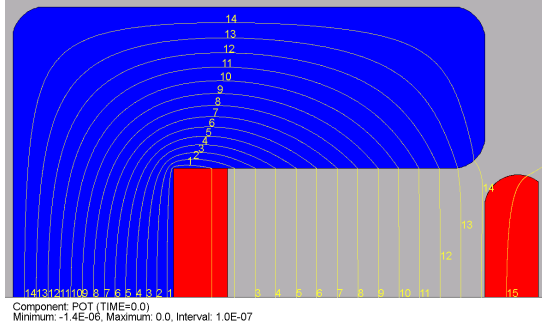


Figure 6.5 – Lines of magnetic flux at 10 Hz (unshielded kicker magnet).

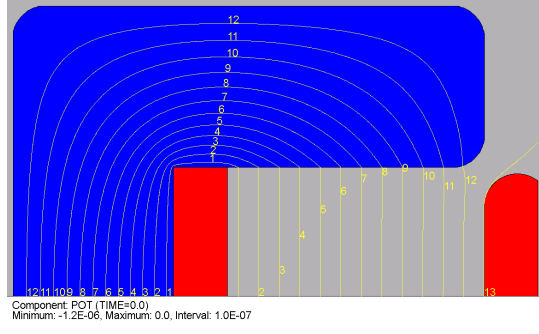


Figure 6.6 – Lines of magnetic flux at 1 MHz (unshielded kicker magnet).

The magnetic field flux lines at 10 Hz and at 1 MHz are shown in Figs. 6.5 and 6.6, respectively. At low frequency, the magnetic flux lines penetrate the busbars. However, at high frequency, eddy currents induced in the busbars produce a reaction field which opposes the original magnetic field generated in the busbars by the pulse current of the magnet (Lenz's law). As a result, the magnetic flux lines do not enter a significant distance into the busbars: this effect must be properly taken into account to calculate field homogeneity and inductance of the central cell.

Let us define  $B_0 \equiv B_y(64, 0)$  as the magnetic flux density at the center of the magnet aperture. The relative magnetic flux density  $B_y/B_0$  (expressed in %) along the  $x$  axis, at different  $y$  positions, both at 10 Hz and 1 MHz, is shown in Fig. 6.7. As can be seen, the strongest variation of the magnetic flux density with respect to  $B_0$  is observed near the GND busbar.

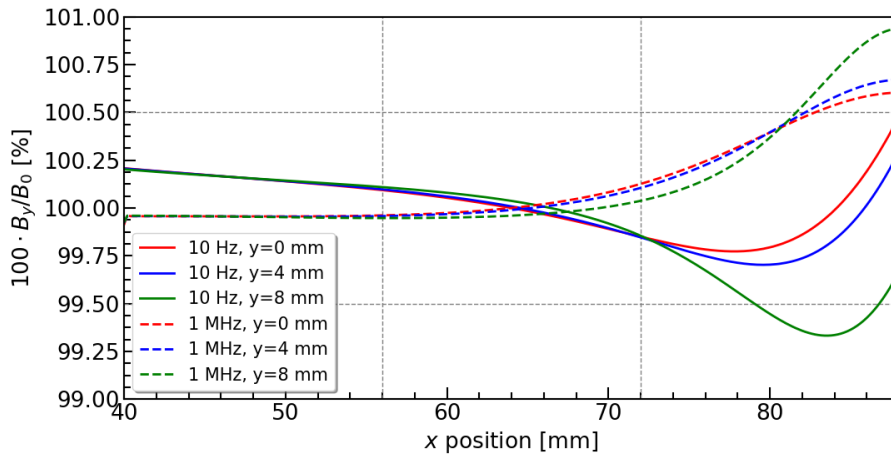


Figure 6.7 – Relative magnetic flux density in aperture of the kicker magnet plotted along the  $x$ -axis for  $y = \{0, 4, 8\}$  mm at both 10 Hz and 1 MHz.

### Equivalent inductance and resistance

In Opera-2D, the predicted stored magnetic energy per unit length ( $E_m$ ) can be calculated either for the entire model or for specific regions. For a linear magnetic circuit and a given excitation current, the total energy stored in the magnetic field must be the same as the electrical energy attributable to the current flowing through an equivalent inductance:

$$L_{\text{cell}}^{\text{Opera-2D}} = \frac{2E_m}{I^2} l_{\text{cell}}. \quad (6.1)$$

In a similar way, from the predicted power per unit length ( $P_m$ ), one can calculate the equivalent resistance associated with a central cell ( $R_{\text{cell}}^{\text{Opera-2D}}$ ):

$$R_{\text{cell}}^{\text{Opera-2D}} = \frac{P_m}{I^2} l_{\text{cell}}. \quad (6.2)$$

The magnetic energy stored in the entire model excluding busbars permits the calculation of the central cell inductance ( $L_{\text{cell}}^{\text{Opera-2D}}$ ) at high frequencies where skin depth in the busbars is negligible.

### Results

The frequency dependent inductance, evaluated for the entire model (green curve), for the entire model excluding busbars (black curve) and only the internal inductance of the busbars (red curve) is shown in Fig. 6.8. At low frequencies, the inductance of the entire model depends on the internal inductance of the busbars. However, during the rise time of the current pulse, the current will flow predominantly on the aperture sides of the busbars (see Fig. 6.4). Hence, the internal inductance of the busbars is negligible during the pulse, as the magnetic field is excluded from the busbars at higher frequencies due to eddy currents (see Fig. 6.6).

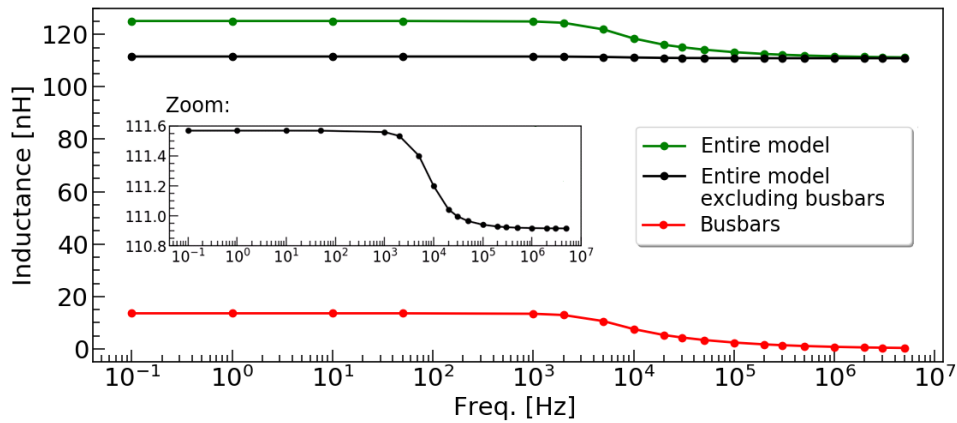


Figure 6.8 – Predicted inductance as a function of frequency evaluated for (a) the entire model of an unshielded kicker magnet, (b) with the internal inductance of busbars excluded and (c) only the internal inductance of busbars.

The predicted central cell inductance for the entire model excluding busbars (see black curve in Fig. 6.8) is constant up to 1 kHz ( $L_{\text{cell}}^{\text{Opera-2D}} = 111.56 \text{ nH}$ ). A small drop ( $\sim 0.6 \text{ nH}$ ) between 1 kHz and 0.1 MHz can be associated with the perturbation of the magnetic flux lines in the aperture and ferrite regions due to reduction of the penetration of the magnetic flux lines within the busbars. However, above 0.1 MHz, the magnetic field lines do not significantly penetrate the busbars (skin depth  $\sim 1.4 \text{ mm}$ ), hence the inductance is more or less constant ( $L_{\text{cell}}^{\text{Opera-2D}} = 110.9 \text{ nH}$ ). The simulation results show excellent agreement with the analytically calculated value of  $L_{\text{cell}} = 111 \text{ nH}$  (see Table 4.3).

### 6.3.3 Field homogeneity

In the next step, the transient solver of Opera-2D has been used to calculate field homogeneity for an unshielded kicker magnet. The fill time of the FCC injection kicker magnet is  $0.355 \mu\text{s}$  and the field flat-top is  $2 \mu\text{s}$  (see Table 4.1). Hence, the current in the busbars has been defined as a trapezoidal pulse with  $75 \text{ ns}$  rise time,  $2.335 \mu\text{s}$  flat-top duration ( $2.0 \mu\text{s} + 0.335 \mu\text{s}$ ) and  $100 \text{ ns}$  fall time. Significant excursions from the ideal magnetic field typically occur at the beginning of the flat-top. For this reason, the field homogeneity has been analyzed at both  $0.43 \mu\text{s}$  and, for comparison, at the end of the flat-top. The relative deviation of the magnetic field ( $\Delta B$ , expressed in %) at the beginning of the flat-top, i.e.  $B_y \equiv B_y(x, y)$  at  $0.43 \mu\text{s}$ , with respect to the magnetic field at the center of the aperture at the end of the flat-top, i.e.  $B_0$  at  $2.43 \mu\text{s}$ , has been calculated as:

$$\Delta B = \frac{B_0 - B_y}{B_0} \cdot 100\%. \quad (6.3)$$

Similarly, at  $2.43 \mu\text{s}$ , the field homogeneity is calculated with respect to the magnetic field at the center of the aperture at  $2.43 \mu\text{s}$ .

The predicted field homogeneity in the aperture of unshielded kicker at  $0.43 \mu\text{s}$  and  $2.43 \mu\text{s}$  is presented in Figs. 6.9 and 6.10. It can be observed that the required field flat-top quality is within the acceptance level of  $\pm 0.5\%$  in the good field region (GFR), at both  $0.43 \mu\text{s}$  and  $2.43 \mu\text{s}$ . There is no significant difference in the GFR between  $0.43 \mu\text{s}$  and  $2.43 \mu\text{s}$  for the field homogeneity predictions. Note, the white areas indicate the regions where the deviation of the magnetic field exceeds the specified limit of  $\pm 0.5\%$ .

Let us remark, in Opera-2D the capacitance of each cell to ground of the transmission line kicker magnet cannot presently be modelled. Hence, neither the propagation delay time of the pulse through the kicker magnet nor the cut-off frequency of a cell is taken into account. For this reason, the analysis of the field homogeneity in Opera-2D, at  $0.43 \mu\text{s}$ , can be considered as a useful approximation with respect to the real case: the prediction at  $2.43 \mu\text{s}$  is more representative of reality as the field should, ideally, have been constant for  $2.0 \mu\text{s}$  and reflections within a well matched transmission line kicker magnet system will be negligible at this elapsed time.



### 6.3.4 Field rise time

As mentioned above, the Opera-2D model does not take into account either the propagation delay time of the pulse through the kicker magnet or the cut-off frequency of a cell. Similarly, end effects are neglected. Hence, the field rise time cannot be evaluated properly with Opera-2D. A more sophisticated method for determining magnetic field rise time and field flat-top quality involves modelling, using PSpice Optimizer, the equivalent circuit of the frequency dependent inductance of each cell in the kicker magnet: this approach will be used to verify the field rise time for the final design of the kicker magnet with a beam screen (see Section 6.4.5).

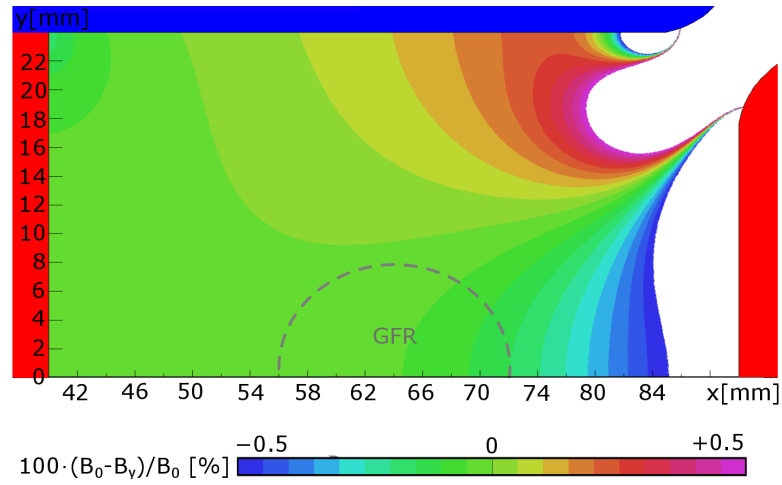


Figure 6.9 – Field homogeneity in the aperture of an unshielded FCC injection kicker magnet at 0.43  $\mu\text{s}$  (i.e. at the beginning of the flat-top), w.r.t.  $B_0$  at 2.43  $\mu\text{s}$ .

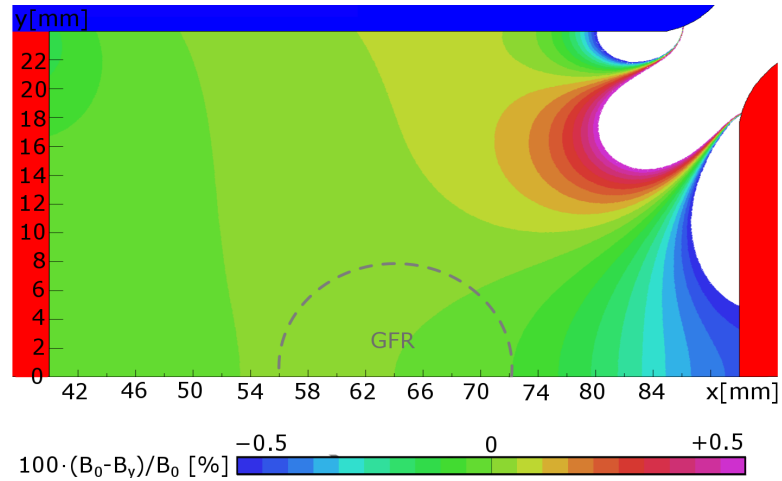


Figure 6.10 – Field homogeneity in the aperture of an unshielded FCC injection kicker magnet at 2.43  $\mu\text{s}$  (i.e. at the end of the flat-top), w.r.t.  $B_0$  at 2.43  $\mu\text{s}$ .

## 6.4 FCC injection kicker magnet with a beam screen

### 6.4.1 Opera-2D model

In the next step, the effects of a beam screen upon central cell inductance and field homogeneity have been analyzed. The geometry of the studied problem is shown in Fig. 6.11. Only the upper part is modelled due to the top-bottom symmetry. In the presented design, the screen conductors are added (regions 7-19). The entire beam screen would consist of 24 screen conductors. The aperture and the background corresponds to regions 20 and 21, respectively. Otherwise, the same assumptions hold as for the model described in Section 6.3.1 (see Fig. 6.1).

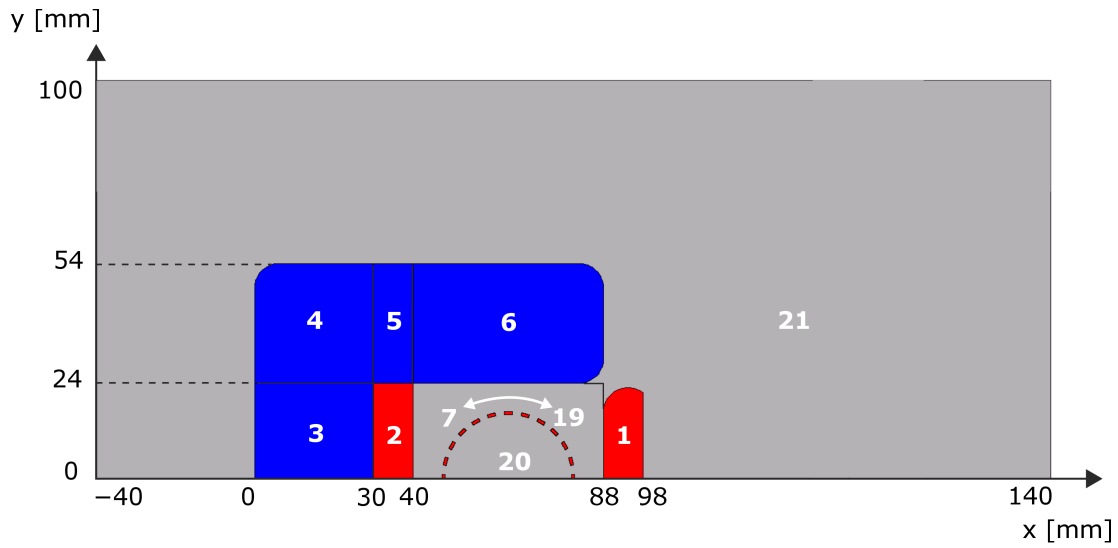


Figure 6.11 – Geometry of the kicker magnet with a beam screen (Opera-2D model). Due to the top-bottom symmetry only the upper part is modelled. The individual regions are numbered.

### 6.4.2 Frequency dependent inductance

#### General principle

Opera-2D AC simulations have been carried out to study eddy currents induced in the screen conductors and to analyze their effect on the inductance of a central cell of the kicker magnet, as a function of frequency. First, let us consider a beam screen with 24 NiCr, rectangular, screen conductors, 2 mm wide and 0.8 mm thick. It should be noted that, since a 2D simulation code is used, the screen conductors are treated as being straight rather than a spiral. In addition, for the spiral conductors, with an integer number of turns in the aperture, the induced voltage is the same for all screen conductors and hence eddy currents would not circulate between conductors, even if they are all connected together in the overlap region. Hence, to correctly simulate this in Opera-2D, the total induced current in any screen conductor is specified to be 0 A, i.e. the integral of current density over the (2D) surface area of any screen conductor is 0 A.

#### 6.4. FCC injection kicker magnet with a beam screen

Figures 6.12 and 6.13 show the current density in the screen conductors at 10 Hz and at 5 MHz, respectively. At 10 Hz the induced eddy currents are of a low magnitude because the rate of change of magnetic flux is relatively small. Whereas, at 5 MHz, significant eddy currents are induced – predominantly in the surfaces of the screen conductors facing the HV busbar. As discussed, the eddy currents generate magnetic fields, which modify the external magnetic field produced by the kicker magnet. Hence, a beam may experience a different magnetic field inside the aperture of the kicker magnet than desired: the induced eddy currents can have a strong impact on the field response of the magnet, and this must be taken into account in the beam screen design.

The magnetic flux lines in the aperture of the kicker magnet at 10 Hz and at 5 MHz are shown in Figs. 6.14 and 6.15, respectively. At low frequencies, the field lines are almost unmodified by the screen conductors, as the magnitude of induced eddy currents are small. However, at high frequency, due to the larger magnitude of induced eddy currents in the screen conductors, the magnetic flux lines in the aperture of the kicker magnet are perturbed, reducing the total flux for a given current in the busbars. As a consequence, both the inductance of the kicker magnet and the magnetic field distribution exhibit a frequency dependence. However, we will demonstrate that the aforementioned effects can be greatly reduced by a proper selection of electrical conductivity, width and thickness of the screen conductors.

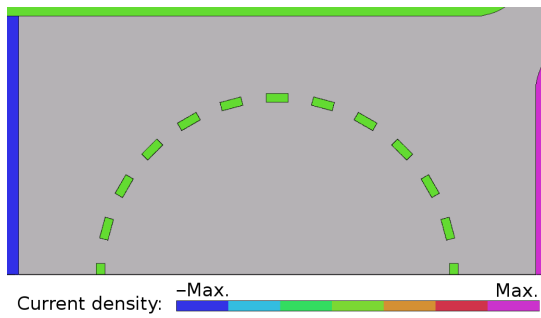


Figure 6.12 – Current density at 10 Hz (shielded kicker magnet).

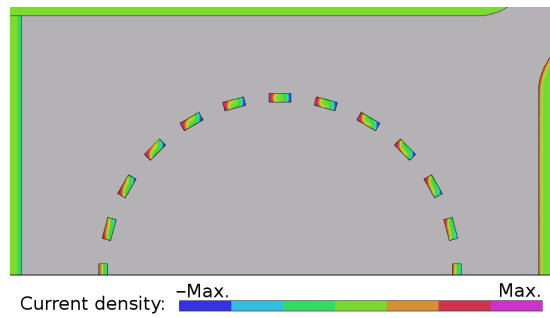


Figure 6.13 – Current density at 5 MHz (shielded kicker magnet).

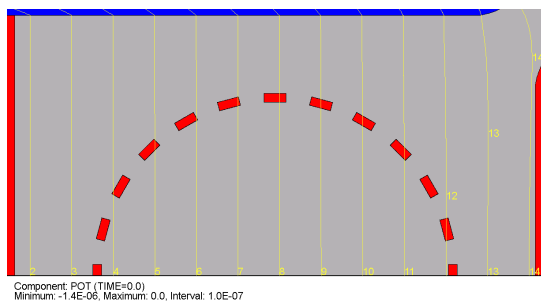


Figure 6.14 – Magnetic flux lines at 10 Hz (shielded kicker magnet).

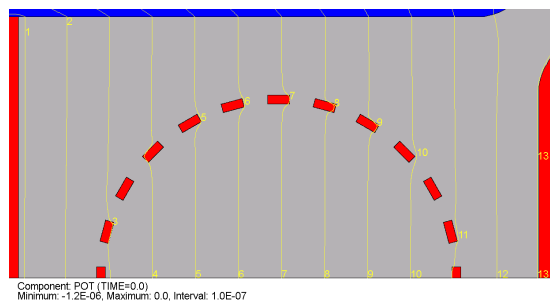


Figure 6.15 – Magnetic flux lines at 5 MHz (shielded kicker magnet).

The relative magnetic flux density, as a function of horizontal distance in the aperture of the kicker magnet with a beam screen, for different vertical positions, both at 10 Hz and 5 MHz is presented in Fig. 6.16. At low frequency, the relative deviation of the magnetic flux density with respect to the value at the center of the aperture does not vary considerably along the  $x$  position. However, at high frequency, the eddy currents induced in the screen conductors cause a significant increase in the relative deviation of the magnetic flux density, which is observed at the positions of the screen conductors. In the GFR, i.e. 8 mm from the center of the aperture (see Table 4.1), the relative deviation stays within  $\pm 0.5\%$ .

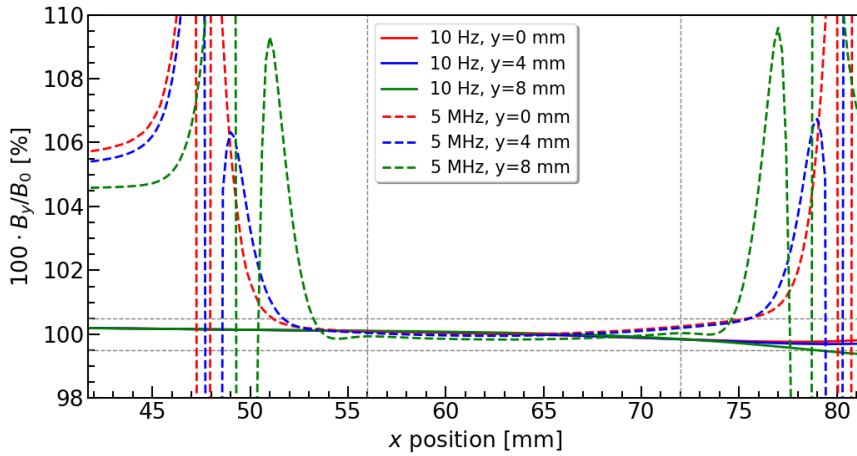


Figure 6.16 – Relative magnetic flux density in the aperture of the kicker magnet with a beam screen plotted along the  $x$ -axis for  $y = \{0, 4, 8\}$  mm, both at 10 Hz and 5 MHz.

### Results

Several materials for screen conductors have been considered, i.e. NiCr, Cu and Ag. The properties of the aforementioned materials are listed in Table 2.2. Also, we studied different geometries of the screen conductors, by varying their width and thickness. As mentioned previously, the cell inductance can be evaluated for the complete 2D model, including internal inductance of the busbars, or excluding the busbars. Here, for each configuration, the central cell inductance (Fig. 6.17) was evaluated for the entire model excluding busbars – this choice will be further explained later. Remark: the black curves in Figs. 6.17 and 6.8 are equivalent.

As expected, at low frequencies ( $\leq 1$  kHz) the eddy currents induced in the screen conductors are relatively small and, hence, all configurations studied have the same value of low frequency inductance, which is close to the analytic value (111.56 nH) for the aperture dimensions.

Let us first analyze solid screen conductors with 2 mm width and 0.8 mm thickness. The simulations confirm that above a certain frequency, the cell inductance, as a function of frequency, strongly decreases for higher electrical conductivity. For instance, the reduction of inductance for Cu (pink curve) or Ag (dark blue curve) screen conductors occurs above 1 kHz. Whereas, for NiCr (light green curve) screen conductors, a significant decrease occurs above 100 kHz.

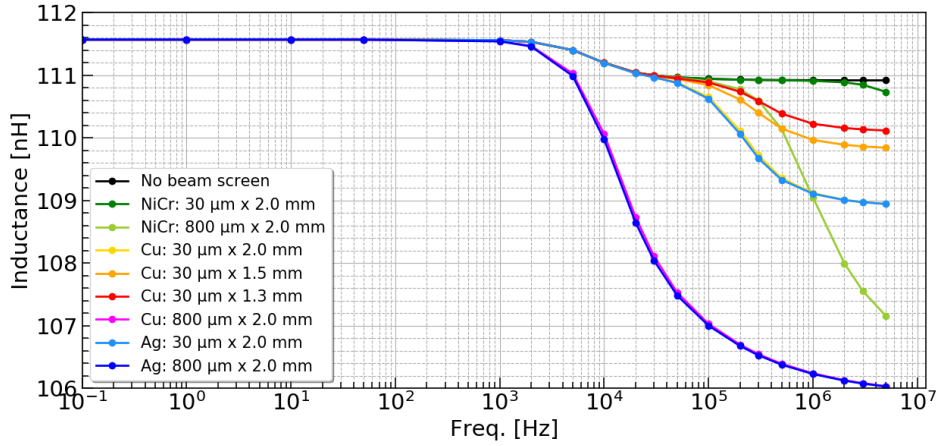


Figure 6.17 – Cell inductance, excluding internal inductance of busbars, as a function of frequency for the FCC injection kicker magnet, with a beam screen, analyzed for different material, width and thickness of the screen conductors.

For Cu and Ag screen conductors the inductance reduces to 106 nH at 5 MHz, whereas for NiCr the inductance reduces to 107.2 nH at 5 MHz: however, the inductance with the NiCr screen conductors is still decreasing at 5 MHz and, at higher frequencies, would be expected to converge to the same value as for the Cu and Ag conductors ( $\sim 106$  nH). The inductance characteristics for the Cu and Ag conductors are expected to have negative impact on field response, as the drop occurs significantly below the highest frequency of interest ( $\sim 4.25$  MHz) and has greater amplitude ( $\sim 4.4\%$ ), than for the NiCr conductors ( $\sim 3.3\%$ ).

Next, let us compare the predictions for Cu (yellow curve, partially hidden under the light blue curve), Ag (light blue curve) and NiCr (dark green curve) screen conductors, 2 mm wide and 30  $\mu\text{m}$  thick with those with the same materials but for 0.8 mm thick conductors. As can be observed, the drop in inductance at higher frequencies can be significantly decreased by reducing the thickness of the screen conductors, e.g. for Ag the inductance at 5 MHz is increased from 106 nH for 0.8 mm thickness to 109 nH for 30  $\mu\text{m}$  thickness. Hence, the reduction in cell inductance is decreased from 4.4% to 1.7%.

Furthermore, considering 30  $\mu\text{m}$  thick screen conductors, for Cu and Ag the inductance is 109 nH at 5 MHz, whereas for NiCr, it is 110.8 nH at 5 MHz. The 30  $\mu\text{m}$  thick configuration has favourable pulse characteristics for NiCr: in this case, the frequency dependence of inductance is similar to that of the unshielded kicker magnet. However, the possibility of applying NiCr coating on alumina would require further studies.

Finally, let us analyze the predictions for Cu screen conductors of 30  $\mu\text{m}$  thickness and widths of 2 mm (yellow curve), 1.5 mm (orange curve) and 1.3 mm (red curve). It can be observed that with reduced width the inductance drop is smaller with increasing frequency. For 2 mm, 1.5 mm and 1.3 mm width, the inductance at 5 MHz is 109 nH, 109.8 nH and 110.2 nH, respectively. These values correspond to a reduction in inductance by 1.9 nH, 1.1 nH and

0.7 nH, respectively, w.r.t. an unshielded kicker magnet. In particular, similar predictions are expected for Ag, as both materials have comparable conductivity (see Table 2.1).

The 30  $\mu\text{m}$  thick Cu or Ag screen conductors are expected to provide low broadband beam coupling impedance from 40 MHz, as their thickness is equal to 3 skin depths at this frequency (see Table 2.2). Also, the screen conductors with this thickness should sustain the beam image current and eddy current heating, as the Ti coating in the LHC dump kicker is only 2  $\mu\text{m}$  thick and has  $\sim 10$  times higher resistivity, but no issues have been reported. However, this requires careful checking as the FCC injection kicker system must operate at 10 Hz burst rate [73].

### 6.4.3 Estimate of power dissipation due to the beam image current and eddy currents

In order to estimate the power deposition in the screen conductors of the proposed beam screen, due to the beam image current, we sampled the nominal beam spectrum (see Fig. 4.7) at the revolution frequency multiples and we calculated the contribution to the total beam current of 0.5 A at these frequencies. In addition, the resistance of Cu rectangular screen conductors (30  $\mu\text{m} \times 1.3$  mm) has been estimated at the revolution frequency multiples, taking into account skin effect (see Eq. 2.79). The power loss in each 3 m long screen conductor is expected to be 7 mW: thus the power loss in 24 screen conductors is approximately 0.5% of the total power dissipated in the magnet.

The energy dissipated in the screen conductors due to the pulsing of the magnet with 2.4 kA current pulse has also been evaluated. For this purpose, the power in the screen conductors at consecutive time stamps of the current pulse has been calculated in Opera transient simulations. In particular, for the spiral beam screen with an integer number of turns, the energy dissipated in every screen conductor due to eddy currents is expected to be the same. The simulations have shown that the energy deposition in a 3 m long screen conductor of such a beam screen will be 0.004 J per pulse. Nevertheless, the impact of the beam image current and eddy current heating on coating quality would require further investigation.

### 6.4.4 Field homogeneity

The transient solver of Opera-2D has been used to determine the field homogeneity in the aperture of the kicker magnet with a beam screen composed of 24 Cu screen conductors with 30  $\mu\text{m}$  thickness and 1.3 mm width. As discussed earlier (see Section 6.3.3 and Eq. 6.3), the field homogeneity is calculated with respect to the field at the centre of the aperture, at 2.43  $\mu\text{s}$ , for the unshielded kicker magnet. The current in the busbars has been modelled as a trapezoidal pulse with 75 ns rise time, 2.335  $\mu\text{s}$  flat-top duration and 100 ns fall time. Figures 6.18 and 6.19 present the field homogeneity in the aperture of the kicker magnet at 0.43  $\mu\text{s}$  and at 2.43  $\mu\text{s}$ , respectively. The simulations show that in both cases, the normalized magnetic field in the GFR stays within the specification of  $\pm 0.5\%$ . However, stronger deviations from the ideal

field occur at the beginning of the flat-top. Despite this, the field is still highly uniform: the excursion from the ideal field flat-top in the GFR varies between 0.2% to 0.4%.

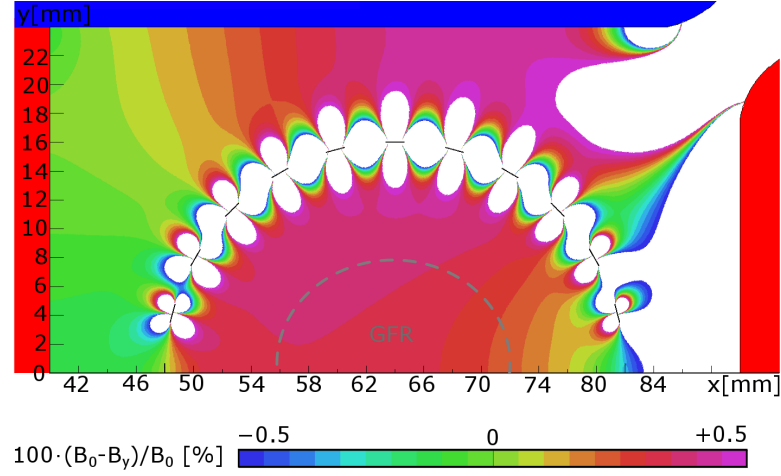


Figure 6.18 – Predicted field homogeneity in the aperture of the FCC injection kicker magnet with a beam screen composed of 24 screen conductors (Cu coating, 30  $\mu\text{m}$  thickness, 1.3 mm width) at 0.43  $\mu\text{s}$  (i.e. at the beginning of the flat-top).

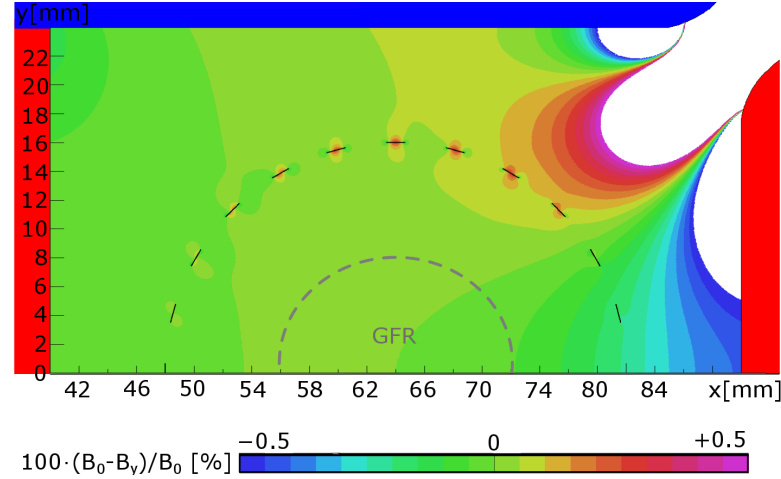


Figure 6.19 – Predicted field homogeneity in the aperture of the FCC injection kicker magnet with a beam screen composed of 24 screen conductors (Cu coating, 30  $\mu\text{m}$  thickness, 1.3 mm width) at 2.43  $\mu\text{s}$  (i.e. at the end of the flat-top).

### 6.4.5 PSpice equivalent circuit

To accurately assess the field rise time and field-flat top quality of the kicker magnet with a beam screen, it is necessary to use an equivalent circuit of the frequency dependent inductance and resistance of a central cell. The basic building block of the equivalent circuit consists of a parallel connected resistor and inductor whose values are frequency independent [109]. To simulate a wide frequency range, several of these blocks are connected in series. In such

a case, the PSpice Optimizer is used to determine the resistance and inductance values which minimizes the RMS error between the Opera-2D predicted frequency dependent inductance and resistance and those of the equivalent circuit. In general, one building block per decade in frequency allows to obtain a reasonable accuracy when fitting the equivalent circuit to the Opera-2D data [109]. For a beam screen composed of 24 Cu screen conductors with 30  $\mu\text{m}$  thickness and 1.3 mm width, the frequency dependent inductance and resistance have been quantified using Opera-2D. The results derived from the Opera-2D predictions, using Eqs. 6.1 and 6.2, are indicated by dashed lines in Fig. 6.20.

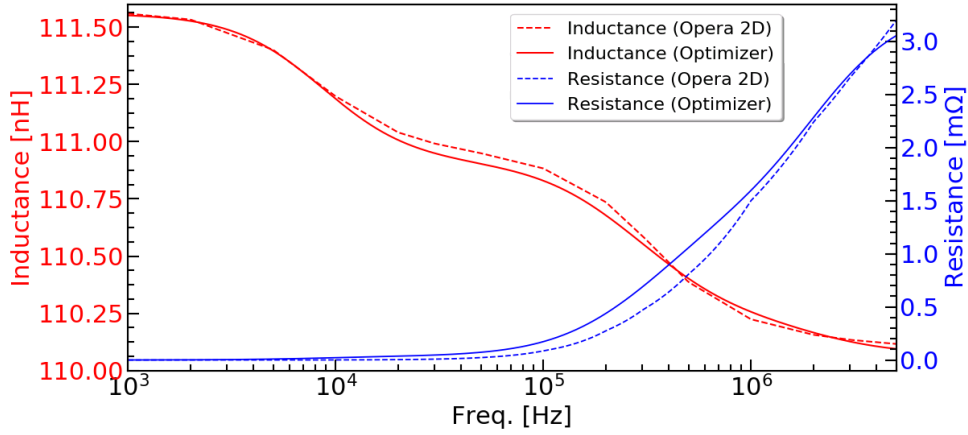


Figure 6.20 – Frequency dependent inductance and resistance of the FCC injection kicker magnet with a beam screen composed of 24 Cu screen conductors (30  $\mu\text{m}$   $\times$  1.3 mm). Opera-2D data is compared with the fit of the equivalent circuit obtained using PSpice Optimizer.

As mentioned previously, during the rise time and the flat-top of the current pulse, the current will flow predominantly on the aperture sides of the busbars. Hence, the internal inductance of the busbars is negligible during the pulse: thus, although the frequency dependence of the internal inductance of the busbars could also be modelled in PSpice, this unnecessarily complicates the model and influences the post-processing of the PSpice predictions. For instance, considering an inductance (of constant value of  $L_{p,1}$ ) and parallel resistance used to simulate frequency dependent inductance, the magnetic field ( $\phi_{bb1}$ ), associated with this inductor, is given by:

$$\phi_{bb,1} = \int V_{Lp,1}(t) \cdot dt = L_{p,1} \cdot I_{Lp,1}(t), \quad (6.4)$$

where  $V_{Lp,1}(t)$  is the instantaneous voltage drop across the inductor and  $I_{Lp,1}(t)$  is the instantaneous current through the inductor. Thus, if there are several of these building blocks in series, without any series resistance modelled, the total magnetic field associated with the  $i$  series blocks,  $\phi_{bb,(1-i)}$  is equal to the sum of the fields in each of the blocks. This can also be expressed as:

$$\phi_{bb,(1-i)} = \int \left( V_{Lp,1(\text{in})}(t) - V_{Lp,i(\text{out})}(t) \right) \cdot dt, \quad (6.5)$$



where  $V_{Lp,1(\text{in})}(t)$  is the input voltage to the first building block and  $V_{Lp,i(\text{out})}(t)$  is the output voltage of the  $i^{\text{th}}$  building block. The same logic can be applied to an  $n$ -cell transmission line magnet, where series resistance of the busbars can be neglected. The field in the kicker magnet ( $\phi_{\text{magnet}}$ ) is given by:

$$\phi_{\text{magnet}} = \int \left( V_{\text{magnet}(\text{in})}(t) - V_{\text{magnet}(\text{out})}(t) \right) \cdot dt, \quad (6.6)$$

where  $V_{\text{magnet}(\text{in})}(t)$  is the instantaneous input voltage to the kicker magnet and  $V_{\text{magnet}(\text{out})}(t)$  is the instantaneous output voltage of the kicker magnet. Using this approach, the magnetic field in the aperture of the kicker magnet can rapidly be evaluated. However, if the internal inductance of the busbar of each cell is represented in the PSpice equivalent circuit, the integral on the right-hand side of Eq. 6.6 no longer represents just the field in the aperture, but also includes the magnetic field in each cell of the busbars, which would thus need to be individually subtracted to determine the field in the aperture. Hence, as per the conventional approach of modelling the frequency independent inductance of a kicker magnet cell, the internal inductance of the busbars is neglected. Remark: Eq. 6.6 is equivalent to Eq. 3.8.

The equivalent circuit utilized to simulate the aforementioned characteristics is shown in Fig. 6.21. It consists of four building blocks to provide an accurate fit ( $\sim 0.01\%$  maximum error for the inductance) within the frequency range from 1 kHz to 5 MHz. At low frequency, the current flows through the parallel inductors, bypassing all the resistors. The sum of the parallel inductors and the inductor in series must be equal to the inductance of a central cell at low frequency, i.e. 111.56 nH (see red curve in Fig. 6.17). As the frequency increases, the impedance of the inductors increases: at very high frequencies the impedance of the inductors will be such that the current flows predominantly through the parallel resistors, bypassing the parallel inductors. Thus, the value of the series inductor must be equal to the high frequency inductance of the cell: in addition, the sum of the resistors should be equal to the resistance of a central cell at high frequency, i.e. 3.2 m $\Omega$  at 5 MHz (see blue dashed line in Fig. 6.20). Hence, the circuit exhibits the following behaviour: as the frequency increases, the effective inductance decreases and the effective resistance increases. The value of the inductance in series with the four "building blocks" is the central cell inductance at the highest frequency of interest, while the value of resistance in series with the "building blocks" is relatively small [109], and is modelled to avoid "inductive loops" in the PSpice model. For the optimization of the values, we provided an initial guess for the component parameters: the initial guesses are based on predictions from trial simulations where all the values were changed randomly within a specified range. This was carried out to find starting values where the errors between the Opera-2D characteristics and those predicted from the equivalent circuit are near a global, rather than a local, minimum. The final component values ("Current" values in Fig. 6.21) have been found using the PSpice Optimizer to minimize the RMS error. During the optimization, the fitting of the inductance characteristic is deliberately weighted more heavily than the fitting of the resistance characteristic, since the inductance is most relevant for calculating the magnetic field in the aperture (see above). The inductance and

resistance characteristics predicted from the optimized equivalent circuit are indicated by solid lines in Fig. 6.20. The maximum error of the equivalent inductance and resistance is 0.01% and 7.8%, respectively. The 0.01% maximum error in the fitted inductance is considered acceptable as it is considerably less than the permissible field error ( $\pm 0.5\%$ ) and, as noted above, the magnetic field is dependent upon the equivalent inductance value and the current through this inductance.

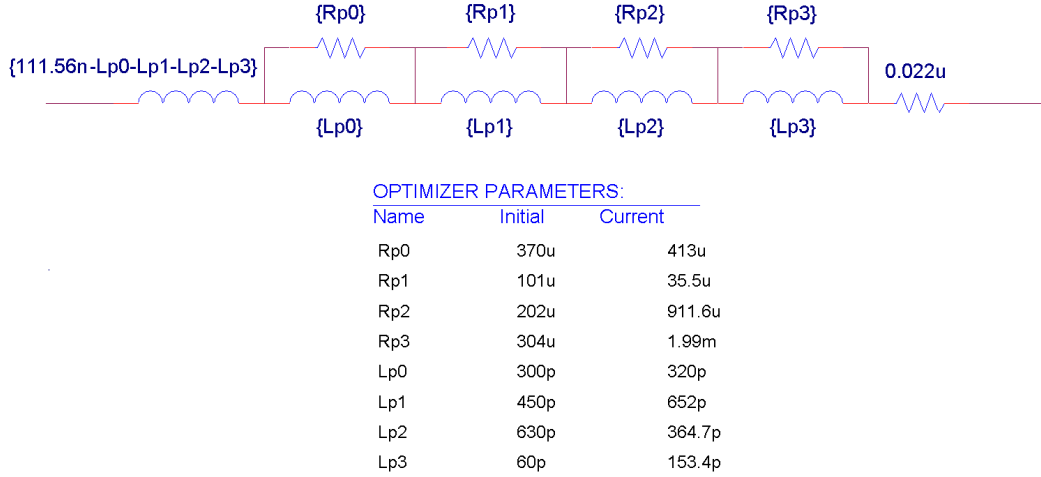


Figure 6.21 – Equivalent circuit of the frequency dependent inductance composed of four building blocks. The initial and optimized ("Current") values of component parameters are indicated below the equivalent circuit.

### 6.4.6 Benchmark simulations of field-rise time and field flat-top quality

To examine the impact of the proposed beam screen upon the field rise time and field flat-top quality, PSpice simulations have been performed. In the equivalent circuit of the transmission line kicker magnet (see Fig. 4.13), the frequency independent inductance of each cell has been replaced by the equivalent circuit of the frequency dependent inductance presented in Fig. 6.21. From Section 4.3.5,  $L_{\text{cell}} = 111 \text{ nH}$  and  $L_{\text{end}} = 126 \text{ nH}$  for a 20-cell FCC injection kicker magnet. Hence, to account for end effects, a series inductance of  $15 \text{ nH}$  ( $L_{\text{end}} - L_{\text{cell}}$ ) has been added at both ends of the kicker magnet, directly in series with the equivalent circuit of the frequency dependent inductance of these cells. For a 20-cell kicker magnet with a beam screen, the specifications for both the field rise time and field flat-top quality are obtained with the following parameters:  $R_{\text{cell}} = 25.5 \text{ } \Omega$ ,  $C_{\text{out}} = 2.33 \text{ nF}$  and  $C_{\text{in}} = 1.2 \text{ nF}$  (see red curve in Fig. 6.22). For comparison, the waveform of the unshielded kicker magnet is presented (see green curve in Fig. 6.22). It can be observed that the beam screen causes a time dependent reduction in the normalized magnetic field with respect to the unshielded kicker magnet. However, the amplitude of the first overshoot and first undershoot is very similar to that of the unshielded kicker magnet. Although this flat-top field is still within specification, and is thus acceptable, it may be possible to modulate the output of the Inductive Adder (IA) (see Fig. 4.2) to compensate for the overshoot, undershoot and the influence of the beam screen - this

#### 6.4. FCC injection kicker magnet with a beam screen

would require further study by the IA experts. During the rise and fall time of the normalized magnetic field, the two curves overlay each other, therefore there is no difference in the kicker field rise time. To conclude, the proposed beam screen is expected to still give a field response which is within specification, but might be further improved by suitable modulation of the IA.

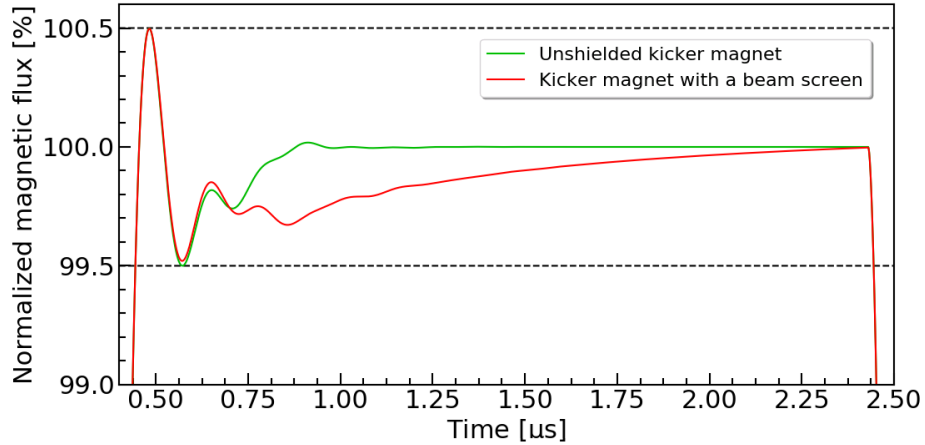


Figure 6.22 – Comparison of the normalized magnetic flux for a 20-cell FCC injection kicker magnet with the beam screen (red curve) and without the beam screen (green curve): the waveform of the unshielded kicker magnet is the same as in Fig. 4.18.



## 7 Experimental validation of predictions using LHC MKI

### 7.1 Single wire measurement techniques

Transmission line methods are widely used for the longitudinal and transverse beam coupling impedance measurements [13, 110]. In this section, we will introduce single wire measurement techniques, which allow to determine the longitudinal impedance of the device under test (DUT). In this approach, the beam is a current source, which we are trying to simulate. The basic principle of a single wire method is that the EM field distribution of an ultrarelativistic beam can be simulated by placing a wire on the beam axis inside the DUT, thus creating a coaxial transmission line, which permits the propagation of the transverse electromagnetic (TEM) waves. In practice, a thin wire is desirable as this gives minimum perturbation of the fields – however, it cannot be too thin as it needs to have adequate mechanical strength: a 0.5 mm diameter wire is a reasonable compromise. The method relies on the fact that the EM field distribution of an ultrarelativistic beam is very similar to that of a TEM line. The source field is provided by feeding a transmission line with an AC signal from the Vector Network Analyzer (VNA). The AC signal will induce an image charge in the inner walls when travelling through the structure. The lossy materials and irregularities will distort the image charge, so that secondary fields (wake fields) will be generated. The attenuation of the signal, due to the secondary fields, can be associated with the energy loss of a bunch while traversing the same structure. In practice, one can use either the classical or resonant single wire method. Below, practical aspects and limitations of the two methods will be discussed. Finally, classical and resonant single wire methods will be used to benchmark longitudinal impedance of the conventional and spiral beam screen installed in the LHC MKI. In particular, only the real part of the longitudinal impedance will be analyzed in order to validate power loss predictions.

#### 7.1.1 Classical method

In the classical method, a single wire is stretched along the DUT at the center of the aperture. Assuming a circular beam screen placed in the aperture of the kicker magnet, the characteristic

impedance of the coaxial line is given by [13]:

$$Z_L = 60 \ln \frac{D_{\text{beam screen}}}{d_{\text{wire}}}, \quad (7.1)$$

where  $D_{\text{beam screen}}$  is the inner diameter of the beam screen and  $d_{\text{wire}}$  is the diameter of the wire, respectively. To provide high characteristic impedance, the wire diameter must be small, but consistent with the requirement of low losses in the wire. In addition, the wire should be straight, i.e. ideally without any sag [13].

To improve the matching of the wire with respect to the impedance  $Z_0$  of the measurement system, carbon matching resistors are used: bulk carbon resistors present relatively low inductance in comparison with some other types of resistors. The matching resistors are housed in a short (40 mm long) metallic, non-magnetic, box (Sucobox) to minimize parasitic inductance of the matching network: nevertheless, this introduces parasitic capacitance. Otherwise, high inductance will result in a significant frequency dependent impedance and thus will cause reflections, which will distort measured signals. The value of the matching resistors is determined using the following formula [13]:

$$Z_{\text{match}} = Z_L - Z_0. \quad (7.2)$$

A schematic drawing of the experimental setup for the classical single wire measurement is shown in Fig. 7.1. The measured transmission coefficient across the DUT is  $S_{21,\text{DUT}}$ , while the transmission coefficient of a reference line is defined as  $S_{21,\text{REF}} = e^{-j\omega L_{\text{DUT}}/c}$ , where  $L_{\text{DUT}}$  is the length of the DUT. There are several formulas to calculate longitudinal impedance, which involve different approximations [13]. For distributed impedance systems, for instance for the LHC MKI, the longitudinal impedance can be evaluated using the so-called "standard log formula" [13]:

$$Z_{||} = -2Z_L \ln \frac{S_{21,\text{DUT}}}{S_{21,\text{REF}}}. \quad (7.3)$$

### 7.1.2 Resonant method

The real part of the longitudinal impedance can also be measured using the resonant single wire method. The setup for this method is similar to that of the classical method, but the input and output matching resistors, shown in Fig. 7.1, are replaced by capacitive coupling. The DUT is a standing wave coaxial resonator with losses in the central conductor and the surrounding materials. The structure resonates when the following condition is satisfied [13]:

$$L_{\text{DUT}} = n\lambda/2, \quad (7.4)$$

where  $n$  is an integer multiple of the resonance.

For each resonance, the loaded  $Q$  factor ( $Q_L$ ) and the magnitude of  $S_{21,\text{DUT}}$  are evaluated. In

particular,  $Q_L$  is the  $Q$  factor of the resonance, which takes into account external losses due to coupling to the measurement circuit outside of the tank, while the unloaded  $Q$  factor ( $Q_0$ ) is the  $Q$  factor of the DUT resonance in isolation. For weak and approximately equal capacitive coupling at both ends, the coupling coefficient can be estimated as [13]:

$$k = \frac{|S_{21,DUT}|}{1 - |S_{21,DUT}|}. \quad (7.5)$$

Using the estimate of  $k$ ,  $Q_0$  from a measured  $Q_L$  can be determined [13]:

$$Q_0 = Q_L \cdot (1 + k) \quad (7.6)$$

The measured line attenuation expressed in nepers per meter (Np/m) is evaluated as [13]:

$$\alpha_{\text{line}} = \frac{\pi}{\lambda Q_0}. \quad (7.7)$$

Let us remark, this attenuation accounts for wakefield effects and for the attenuation due to the finite wire resistivity. However, the losses due to the wire can be determined analytically with the following formula [111]:

$$\alpha_{\text{wire}} = \sqrt{\pi \rho_{\text{wire}} \epsilon f} \cdot \left( d_{\text{wire}} \ln \frac{D_{\text{beam screen}}}{d_{\text{wire}}} \right)^{-1}. \quad (7.8)$$

Hence, the corrected attenuation is  $\alpha = \alpha_{\text{line}} - \alpha_{\text{wire}}$ . From this, the real part of the longitudinal impedance of the DUT can be obtained:

$$\text{Re}(Z_{||}) = 2 Z_L \alpha L_{\text{DUT}}. \quad (7.9)$$

The resonant single wire method provides higher precision in comparison with the classical method and is typically recommended for low loss structures, i.e. LHC MKI [13]. Nevertheless, a major drawback of the resonant method is the limited frequency resolution, which is given by the length of the DUT (see Eq. 7.4). Ideas for artificially extending the length of the DUT have been considered, e.g. by using an appropriate diameter of beam pipe connected to the DUT, but time and resources have not permitted testing of such concepts.

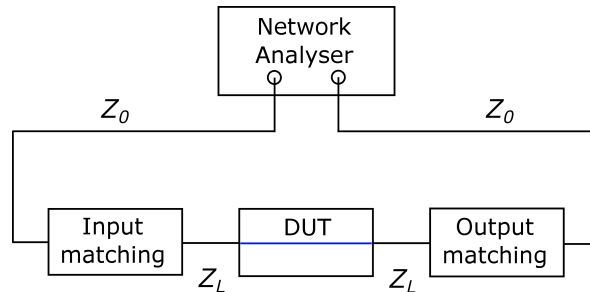


Figure 7.1 – Schematic drawing of the experimental setup for a classical single wire method. In the resonant method, the matching resistors are replaced by capacitive coupling.

## **7.2 Longitudinal impedance of the conventional beam screen**

The beam screen for the LHC MKI kicker magnets consists of screen conductors placed at the inner wall of the alumina tube, which are straight. This is the so-called "conventional" design. As explained in Section 3.2.2, to avoid excessive eddy currents, which would affect rise time of the field pulse, the screen conductors are capacitively coupled at the upstream end of the magnet and directly connected to the local ground at the downstream end. The length of the overlap between the screen conductors and the outer metallic cylinder (see Fig. 3.11) determines the resonances in the longitudinal impedance spectrum (see Eq. 3.11). In particular, decreasing the overlap length shifts the main resonances to higher frequencies. This section summarizes the benchmark measurements that were made to validate the predicted behaviour.

### **7.2.1 Experimental setup**

The impedance measurements have been performed for two configurations of the conventional beam screen. In particular, the post-LS1 LHC MKI ( $L_{\text{overlap}} = 130$  mm) and the upgraded LHC MKI ( $L_{\text{overlap}} = 56$  mm) have been measured. To excite the kicker magnet with a TEM field, a 0.5 mm diameter soft Cu wire (tensile strength of approximately 250 N/mm<sup>2</sup>) with approximately 2.1  $\mu\text{m}$  Ag coating has been stretched through the aperture of the kicker magnet: non-enamelled wire is used to prevent pollution of the kicker during soldering of the wire. Soft copper is preferred to hard copper (tensile strength of approximately 500 N/mm<sup>2</sup>): experience has shown that it is easier to obtain a straight wire in the aperture by using the soft copper. In the analysis, however, we assumed that the conductivity of the wire material is the same as that of pure Cu (see Table 2.1), i.e. the presence of the silver layer is neglected. We calculated that the error introduced due to this is negligible. For instance, when using the conductivity of Ag, the difference in magnitude of the resonances is less than 1%. Moreover, due to the limited frequency resolution of the resonant method, we do not aim to determine the absolute value of the resonances.

The geometrical length of the kicker magnet between the coaxial connectors is  $L_{\text{DUT}} = 3.5$  m. In the classical method, the characteristic impedance of the coaxial line ( $Z_L = 270 \Omega$ ) has been matched to that of the VNA ( $Z_0 = 50 \Omega$ ) by using carbon matching resistors ( $Z_{\text{match}} = 220 \Omega$ ). For the classical method, a reference measurement in a smooth, homogeneous beam pipe has not been performed due to practical reasons. Instead, for the reference we assumed a lossless line of length  $L_{\text{DUT}}$  as in Ref. [110]. In the resonant method, the matching resistors have been replaced with capacitive coupling. The experimental results obtained using classical and resonant single wire methods are compared and discussed below.



### 7.2.2 Results

The measurement results of the classical method, for both configurations, are shown in Fig. 7.2. The oscillatory behaviour of the measured data is attributed to the frequency dependence of matching resistors mounted in the Sucobox. Despite the high noise level, the main resonances can be identified. In the longitudinal impedance spectrum of the post-LS1 LHC MKI, the harmonics of the fundamental mode occur approximately at the following frequencies: 425 MHz, 870 MHz, 1290 MHz and 1685 MHz, while, in the spectrum of the upgraded LHC MKI, at 1155 MHz and 1975 MHz. Importantly, the increase of frequency of the main harmonics, with reduced overlap length, is observed. Also, the expected occurrence of the low frequency mode in such a beam screen (see Section 5.3.7) is confirmed: in both cases, a strong resonance at  $\sim 10$  MHz is observed.

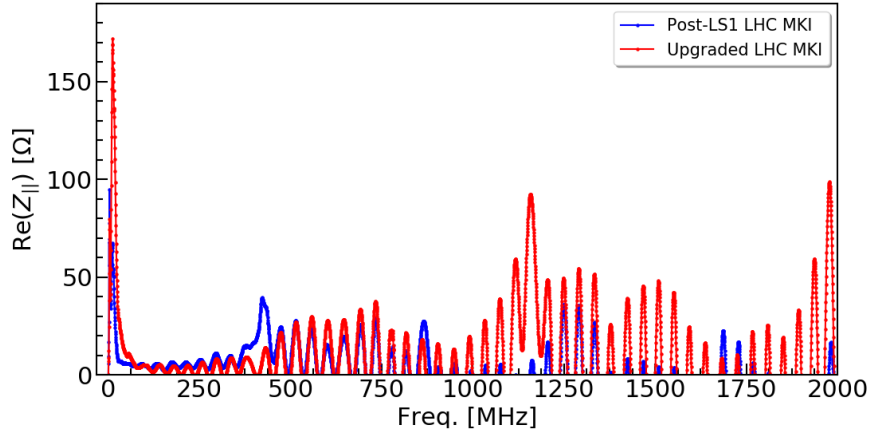


Figure 7.2 – Measurement results of the real longitudinal impedance of the post-LS1 and upgraded LHC MKI (classical method).

The experimental results of the resonant method, for both configurations, are shown in Fig. 7.3. As expected, the real longitudinal impedance is obtained with lower noise floor, at the cost of limited frequency resolution ( $\sim 42.5$  MHz), which is determined by the length of the system ( $L_{\text{DUT}} = 3.5$  m). The resonant frequencies of the main harmonics show good agreement with the classical wire method measurement results. However, due to limited frequency resolution of the resonant method, we do not compare the magnitude of the resonances: the maximum real impedance of each resonance is typically determined from simulations to provide good accuracy over a wide frequency range.

The fact that two measurement methods generally agree is very satisfying: in addition, these measurements show a high impedance, at the corresponding frequencies, as predicted by the analytical model (see Eq. 3.11) and simulations [20]: this gives confidence in the CST model and hence the predictions for the conventional and spiral beam screen solutions proposed for the FCC injection kicker magnet (see Section 5.4). Note, the CST simulations of the LHC MKI are not within the scope of this thesis. However, the comparison of the experimental data with the existing simulation results is further discussed in Ref. [97].

It is important to note that both the classical and resonant measurement techniques give the overall impedance of the DUT, and cannot be used to localize the value or position(s) of any high impedances: an alternative technique is required to do this.

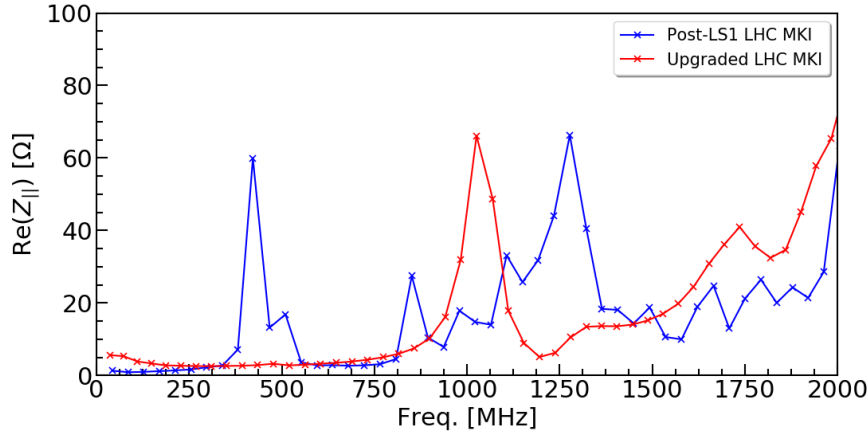


Figure 7.3 – Measurement results of the real longitudinal impedance of the post-LS1 and upgraded LHC MKI (resonant method).

### 7.3 Novel power deposition distribution measurements

The impedance measurements performed on the LHC MKI show that with a beam screen with reduced overlap length, specifically from 130 mm to 56 mm, the first harmonic of the fundamental mode is shifted from approximately 425 MHz to 1155 MHz, where the power in the beam spectrum is significantly lower. For this reason, the total power loss is expected to be reduced. However, it is important to analyze the power deposition distribution along the kicker magnet to ensure that the ferrite yoke will not exceed its  $T_C$ . As discussed in Chapter 3, a characteristic feature of the beam screen are toroidal ferrite rings mounted around each end of the alumina tube, outside of the aperture of the magnet. In the LHC MKI, each set of nine rings consists of two types of alternatively arranged Ferroxcube NiZn ferrites: 4M2 and 4B3, with a  $T_C$  of 200°C [53] and 250°C [54], respectively. These rings serve as a damping material to absorb beam induced power before it is deposited in the ferrite yoke. PT100 sensors are used to monitor temperatures: however, these are not installed directly on the ferrite yokes of the LHC MKI, as the yoke is at high voltage when pulsing the kicker magnet (see Section 3.3). Instead, there are two PT100 sensors for the yoke located on a side plate, which is nominally at ground potential: there is one probe towards each of the upstream and downstream ends, located at the position of the 3<sup>rd</sup> yoke from each end of the magnet. In addition, there is one PT100 sensor associated with each set of ferrite rings, located on a clamp, which is in contact with the ferrite rings [62]. Importantly, temperature probes are not positioned at each ring and yoke of the magnet, hence the longitudinal power deposition distribution cannot be accurately analyzed. Furthermore, temperature predictions for the ferrite yoke are rather qualitative, as PT100 sensors are not in a direct contact with the ferrite yoke.

The operational experience with post-LS1 LHC MKI has shown that the upstream end of the kicker magnet is consistently hotter than the downstream end [19]. For this reason, CST Particle Studio has been used to study non-linearity of the power deposition distribution. For the post-LS1 LHC MKI, the power is predicted to be deposited mainly in the first ferrite yokes, at the upstream end, whereas the ferrite rings absorb a relatively small part of the total power [20]. On the contrary, for the upgraded LHC MKI design, the power is predicted to be deposited mostly in the ferrite rings at the upstream end, leading to a significant reduction of the power deposition in the ferrite yokes [20]. This redistribution can be attributed to the fact that with a shorter length of metallic cylinder, the ferrite rings are more exposed to the EM power radiated due to the resonant behaviour of the overlap at the upstream end.

Note, with an overlap length of 56 mm, a non-symmetric vacuum gap and graded conductors, a similar power deposition distribution is expected for the FCC injection kicker magnet as for the upgraded MKI. For such a configuration, the highest power is predicted to be deposited in the 5<sup>th</sup> ferrite ring, whereas a significantly smaller portion will be deposited in the ferrite yoke (see Fig. 5.10). In addition, for shorter overlap length, i.e. 44 mm, similar results are expected, provided that the length of the screen conductors is reduced, rather than decreasing the length of the metallic cylinder, so that the longitudinal exposure of the ferrite rings to the beam will not change. To provide an experimental verification of the predicted behaviour, novel power deposition distribution measurements have been developed using a single wire method. The experimental technique, technological issues and the results are reported below.

#### 7.3.1 Measurement method

For the power deposition distribution measurement, the same test bench is used as for the single wire measurements: i.e. it consists of a VNA, a single wire stretched along the DUT, input and output matching resistors. In addition, conductive probes are placed around selected ferrite rings or adjacent to a selected yoke: the selected ferrites are those expected to exhibit high losses. For such a structure, a time varying magnetic field will induce voltage in the probes. The goal is to compare the magnetic field that couples from the single wire, representing the beam, to different ferrite elements, as magnetic losses are the main mechanism of power dissipation in the ferrites. Let us remark, the power deposition distribution measurement method does not provide quantitative results. However, it yields qualitative information about the longitudinal power deposition distribution along parts of the kicker magnet and frequency dependent power dissipation in selected ferrite elements.

#### 7.3.2 Experimental setup

The power deposition distribution measurements have been performed for the post-LS1 and upgraded LHC MKI. In both cases, the probes have been placed around the 1<sup>st</sup> and 5<sup>th</sup> rings from the upstream end (see Fig. 7.4). Since the power deposition in the ferrite yoke is crucial, an additional probe has been placed on the aperture side surface of a leg of the 1<sup>st</sup> yoke.

However, the position of this probe was not optimal. Ideally, it would have been placed around the leg of the ferrite yoke, adjacent to the HV busbar: however, due to time constraints and available resources, it was not feasible to disassemble the ferrite yokes of the LHC MKI to install such a probe for this measurement. Note, this particular method to assess longitudinal power deposition distribution may create additional electrical resonances due to the stray capacitance of the pick-up loops and stray inductance of the pick-up cables. However, since we are interested in analysing the relative results, i.e. comparing two designs, the influence of the probes and cables should be similar in both cases, as the same experimental setup is used.

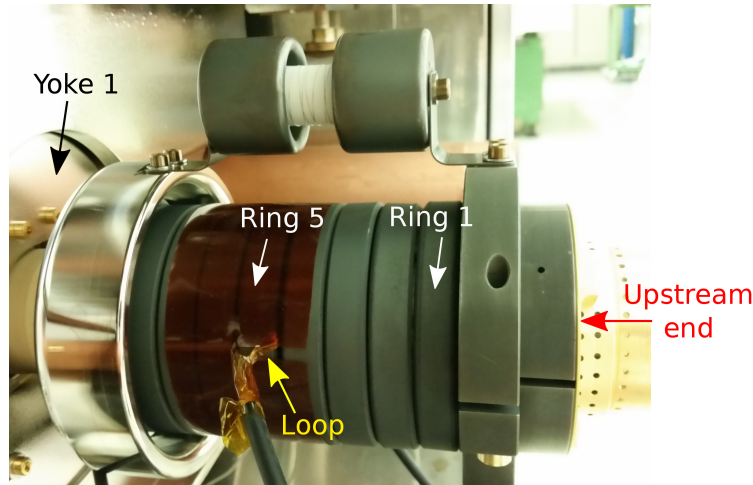


Figure 7.4 – Photograph of the measurement setup for the power deposition distribution analysis. The conductive wire is mounted around 5<sup>th</sup> ring (with respect to the upstream end).

### 7.3.3 Results

Figure 7.5 presents a comparison of the signals measured at the 1<sup>st</sup> and the 5<sup>th</sup> rings of the post-LS1 LHC MKI design with  $L_{\text{overlap}} = 130$  mm (see Fig. 3.11). In both cases, relatively high losses occur approximately at 425 MHz, which is the first fundamental harmonic in the impedance spectrum of this design (see blue curves in Figs. 7.2 and 7.3). The amplitudes of the measured signals at this frequency are comparable for each of the two measurements. The higher harmonics of the fundamental mode are not clearly distinguishable from the noise. However, it is the first mode which contributes the most to the total power loss. Importantly, the amplitudes of the measured signal at both rings are very similar over the entire frequency range. Hence, a similar portion of the total power is expected to be deposited in these rings: this experimental result agrees with the simulations performed for the post-LS1 LHC MKI [20].

A comparison of the signals induced in the probes around the 1<sup>st</sup> and the 5<sup>th</sup> rings of the upgraded LHC MKI with  $L_{\text{overlap}} = 56$  mm is shown in Fig. 7.6. The shorter overlap length causes the shift of the fundamental mode to higher frequency, thus the peak at 425 MHz is no longer visible for the 1<sup>st</sup> and the 5<sup>th</sup> ring. Note, in the signal measured at the 1<sup>st</sup> ring, two peaks around 150 MHz and 450 MHz can be distinguished, however their origin is not understood:

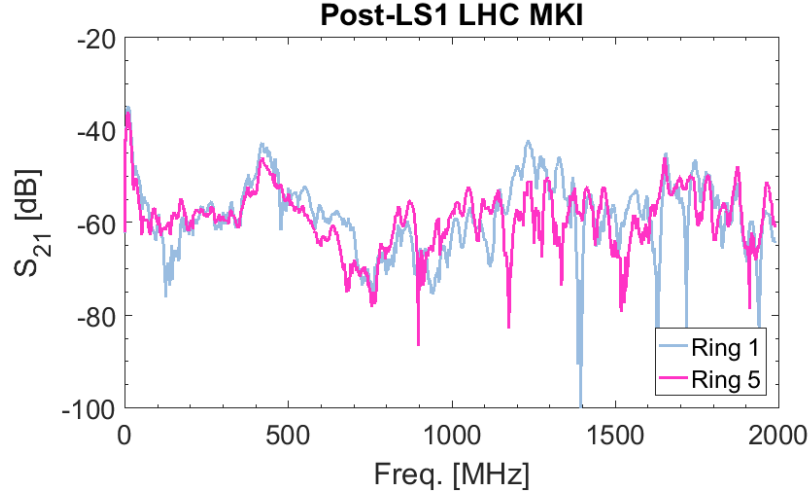


Figure 7.5 – Forward transmission coefficient as a function of frequency measured at the 1<sup>st</sup> and the 5<sup>th</sup> rings of the post-LS1 LHC MKI design.

they are not expected to be present. Also, with an overlap length of 56 mm, a significantly higher power is expected to be deposited in the 5<sup>th</sup> ring than in the 1<sup>st</sup> ring (see Fig. 5.10): this behaviour has not been confirmed by the experiment and would require further studies [20].

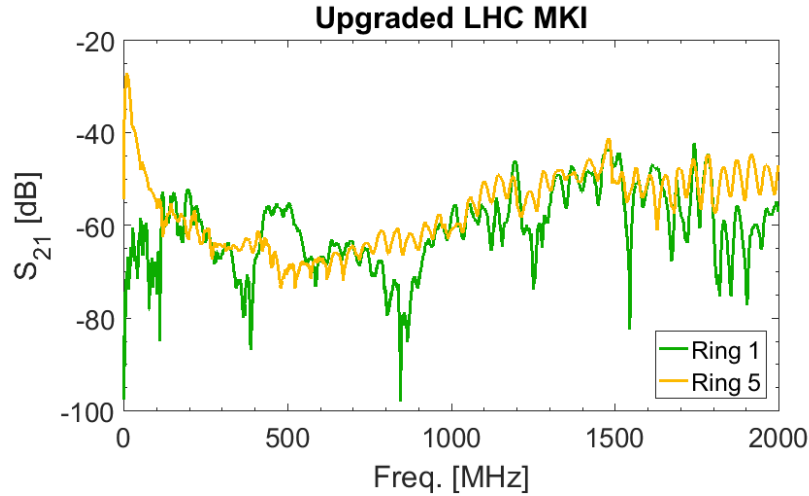


Figure 7.6 – Forward transmission coefficient as a function of frequency measured at the 1<sup>st</sup> and the 5<sup>th</sup> rings of the upgraded LHC MKI design.

Of particular interest is the measured signal at the 1<sup>st</sup> yoke, for both configurations of the LHC MKI beam screen. A direct comparison of the induced signal at this probe for the post-LS1 LHC MKI (blue curve) and upgraded LHC MKI (red curve), is shown in Fig. 7.7. The experimental results confirm that the performance of the kicker magnet with reduced overlap length will be significantly improved, as a reduction of 20 dB to 30 dB is observed between 400 MHz and 1 GHz. In addition, the measured signal for the 1<sup>st</sup> yoke of the upgraded LHC MKI is weaker in

the frequency range from 200 MHz to 2 GHz than for the post-LS1 design. Hence, the heat load in the first yoke is expected to be reduced, in agreement with simulations. Let us remark, due to the differences of the probe at the 1<sup>st</sup> yoke compared with those at 1<sup>st</sup> and the 5<sup>th</sup> rings, we do not compare the magnitude of the induced signal at the yoke with that at the rings.

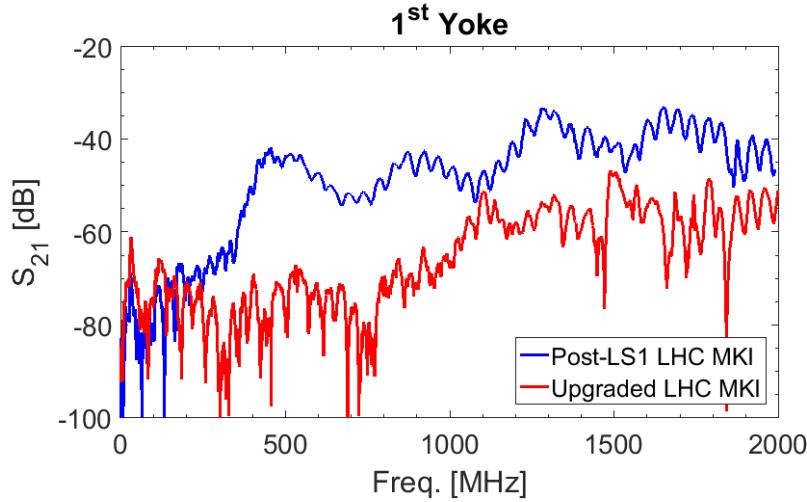


Figure 7.7 – Comparison of the forward transmission coefficient as a function of frequency measured at 1<sup>st</sup> yoke of the post-LS1 and upgraded LHC MKI.

## 7.4 Benchmark measurements of the spiral beam screen

### 7.4.1 Prototype

A prototype of the spiral beam screen has been manufactured at CERN. It consists of 21 screen conductors, applied using vacuum compatible Ag paint ( $\sigma = 3.78 \times 10^7$  S/m) from Heraeus [112]. To produce the spiral beam screen, the inner surface of the alumina tube was coated uniformly with Ag paint. After sintering, a photoresist was applied over the entire surface of the coating. In the next step, a patterned mask with the spirals made of Cu paint, applied to a clear sheet, was inserted in the alumina tube and a specially built 3 m-long light tube, designed to give a UVA spectrum over 360 degrees, was mounted inside the tube. In this process, the mask is used to block the light, so that the UVA effects the photoresist where there is no Cu, hence it can be later removed by etching. The applied mask must be in good contact with the substrate to prevent the UVA effecting the photoresist under the Cu. Finally, an etching agent was used to remove Ag in areas where the mask was not placed: this is a difficult step, i.e. if the photoresist is damaged, where it should be protected, this can result in the etching agent giving breaks in the Ag paint. In addition, it is difficult to have a uniform Ag layer after sintering - small voids can be often visible after this process. Thus, in the future, it is proposed that more than one layer of uniform Ag is applied to the inside of the alumina tube.

In a prototype beam screen, each screen conductor has a width of  $\sim 3$  mm, but the thickness is

#### 7.4. Benchmark measurements of the spiral beam screen

not precisely defined. The prototype spiral extends over  $\sim 4.5$  turns along the aperture of the LHC MKI. The length of the alumina tube is 3 m: this is 7 mm less than the total length of the original alumina tube installed in the LHC MKI. For this reason, special components were manufactured to extend the spiral tube at the grounded end, so that the spiral beam screen could be installed in the spare LHC MKI. A photograph of the prototype spiral beam screen is shown in Fig. 7.8. Parameters of the prototype spiral tube are summarized in Tab. C.1. The average thickness of a spiral is calculated from measured end-to-end resistance: it should be noted that this is  $\sim 12\ \mu\text{m}$ , in comparison to  $39\ \mu\text{m}$  required to give 3 skin depths at 40 MHz. Measured parameters of the spiral screen are reported further in Section 7.4.4 and in Appendix C.

Note, however, the existing spiral beam screen is not optimized either for the FCC nor for the LHC MKI injection kicker magnets in terms of beam coupling impedance and HV operation. Nevertheless, the goal was to validate the performance of the spiral beam screen with the new features installed in a spare LHC MKI, with the limited resources available, by performing benchmark impedance measurements. Hence, longitudinal impedance measurements, using a spiral beam screen with the proposed features, i.e. symmetric vacuum gap, ungraded screen conductors and shorter overlap length ( $L_{\text{overlap}} = 44\ \text{mm}$ ), which are described in Section 5.5.4, were carried out. For this purpose, all the necessary components were designed and produced. However, unfortunately, the spiral beam screen had defects (see Section 7.4.4).



Figure 7.8 – Photograph of the prototype spiral beam screen with 21 screen conductors applied using Ag paint and  $\sim 4.5$  turns along the length of the alumina tube installed in an LHC MKI.



### 7.4.2 CST model

The prototype spiral beam screen has been modelled in CST. The simulations have been performed using the simplified model (i.e. full length beam screen, with ferrite rings at both ends, but excluding the magnet), due to limited computational resources (see Chapter 5). A zoom of the upstream end of the beam screen is shown in Fig. 7.9. The thickness of the metallic cylinder has been adjusted to fit in the original 4M2 and 4B3 ferrite rings, which are alternatively arranged at both ends of the LHC MKI alumina tube. Note, in the CST model, we assume that the screen conductors have a thickness of at least 3 skin depths (see Chapter 5).

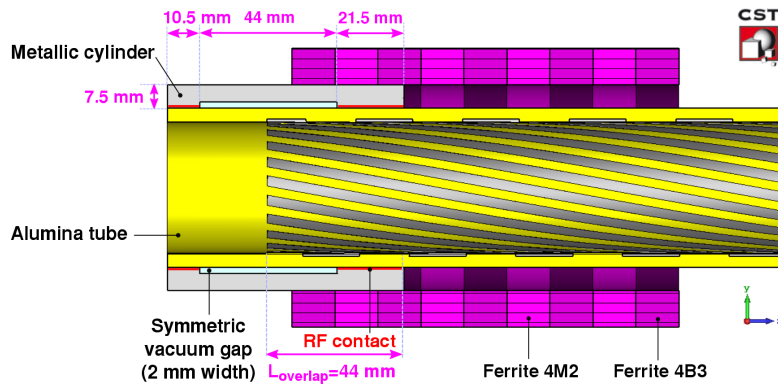


Figure 7.9 – CST model of the spiral beam screen (simplified model).

### 7.4.3 Experimental setup

In the practical realization, an important aspect is the Ag metallization, indicated by the red colour in Fig. 7.9, that has to be applied to part of the outside diameter of the alumina tube to ensure a good, homogeneous, contact between the metallic cylinder and the alumina tube. Photographs of the metallization applied at both ends of the prototype spiral tube are shown in Figs. 7.10 and 7.11, respectively.

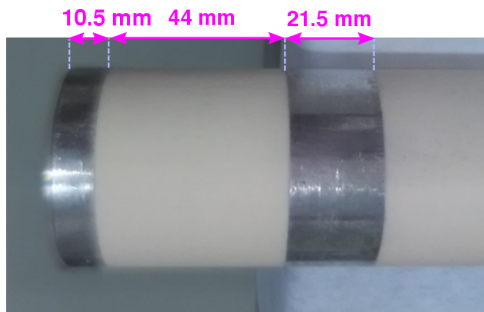


Figure 7.10 – Metallization at the capacitively coupled end.

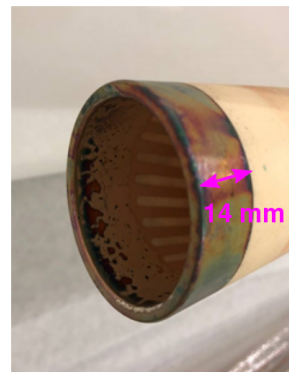


Figure 7.11 – Metallization at the grounded end.



#### 7.4. Benchmark measurements of the spiral beam screen

A photograph of the measurement setup for impedance measurements is shown in Fig. 7.12. The test bench consists of an LHC MKI with a spiral beam screen. A single 0.5 mm diameter Cu wire with a  $\sim 2.1 \mu\text{m}$  Ag coating has been stretched through the aperture of the DUT. In addition, we used a VNA, calibration kit (85032B/E) and RF measurement cables (ST18A/11N468/11N468) from Huber+Suhner [113]. For the classical method, Sucoboxes, each containing a "non-inductive"  $220 \Omega$  matching resistor, have been utilized (see Fig. 7.13). Ideally, however, the Sucoboxes used in this method should be shorter to minimize the parasitic inductance and capacitance in order to improve the accuracy at higher frequencies. For the resonant method, Sucoboxes with the capacitive coupling have been used (see Fig. 7.14). The geometrical length of the LHC MKI between the coaxial connectors is  $L_{\text{DUT}} = 3.5 \text{ m}$ .

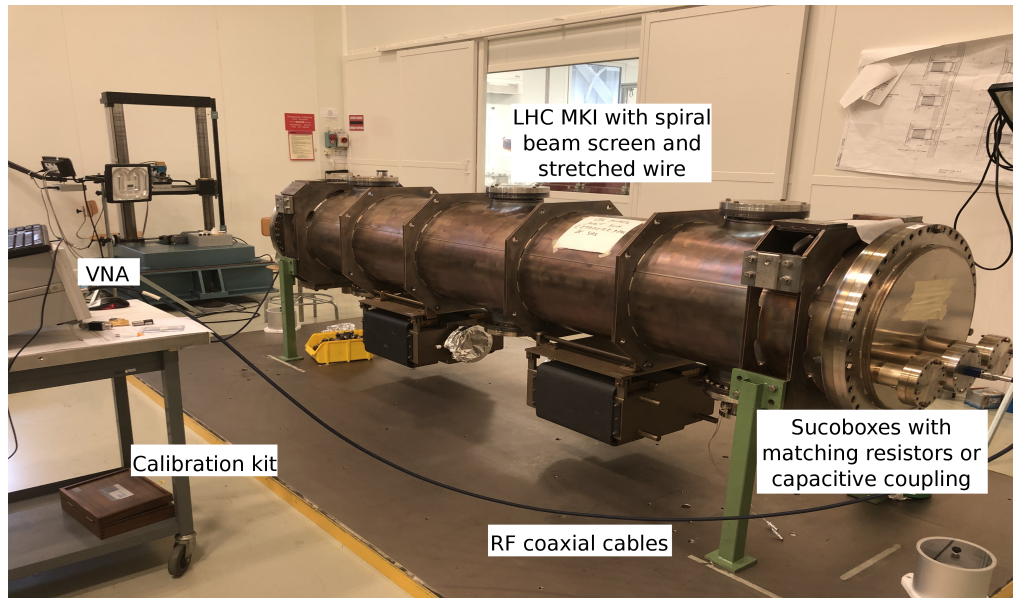


Figure 7.12 – Photograph of the experimental setup with the individual elements indicated.

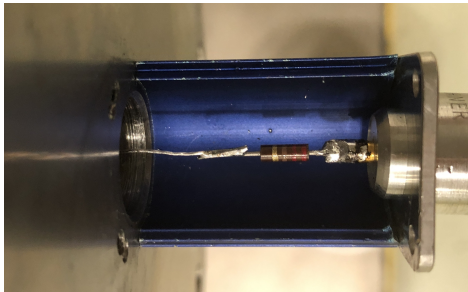


Figure 7.13 – Sucobox with a wire connected to a  $220 \Omega$  matching resistor.

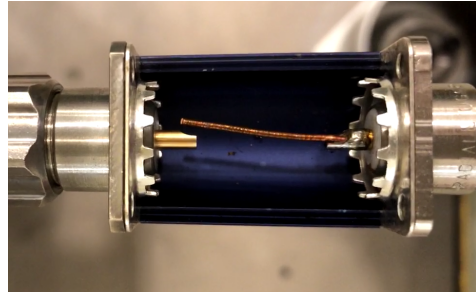


Figure 7.14 – Sucobox with the capacitive coupling.

#### 7.4.4 Results

The experimental results obtained using classical (grey curve) and resonant (red points) single wire methods are shown in Fig. 7.15. The measurement data is compared with CST predictions (blue curve). Reasonable agreement between simulations and the two measurement methods has been achieved. From simulations, the fundamental mode is expected at  $\sim 1230$  MHz. Indeed, the measurements show that the impedance peak due to the overlap at the upstream end of the beam screen is pronounced between 1200 MHz and 1350 MHz. In addition, the results of the classical wire method indicate small resonances between 20 MHz and 150 MHz, which are not present in the impedance spectrum of the LHC MKI with two different configurations of the conventional beam screen (see Fig. 7.2). However, an increase of the real part of the longitudinal impedance in the low frequency range (except up to 10 MHz) can be attributed to the defects of the spiral, i.e. thickness of only  $12\ \mu\text{m}$  and breaks in the silver of 12 spirals, in unknown location(s) along their length: this aspect will be discussed below.

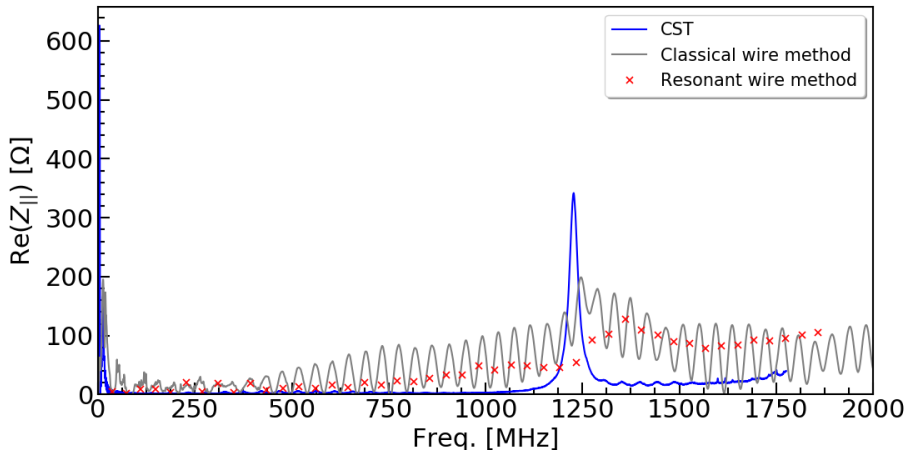


Figure 7.15 – Results of the longitudinal impedance measurements performed on the LHC MKI with a prototype spiral beam screen using classical and resonant single wire methods. The experimental data is compared with the CST predictions.

To assess the quality of the Ag spirals, additional measurements have been carried out. For this purpose, the voltage drop due to applying a DC current from end-to-end of each spiral has been measured, as well as the capacitance from end-to-end of the spirals with breaks. The results are shown in Table 7.1. It has been found that 12 stripes are broken. Such a problem could arise during production process of the spiral beam screen. As mentioned in Section 7.4.1, eventual damage of the photoresist in the areas where it should be protected can result in the etching agent giving breaks in the Ag paint. For this reason, the manufacturing process at CERN should be improved to give more reliable results. In addition, significant differences in the measured end-to-end capacitance, of broken spirals, indicate that overall damage and possibly the number of breaks varies between spirals. From Equation 2.78, assuming  $L = 3\ \text{m}$ ,  $W = 3\ \text{mm}$  and  $\sigma = 3.78 \times 10^7\ \text{S/m}$ , the average thickness is estimated to be  $\sim 12\ \mu\text{m}$ : this is

#### 7.4. Benchmark measurements of the spiral beam screen

approximately one skin depth at 40 MHz. Hence, an increase of the real part of the longitudinal impedance in the low frequency range is presumably attributed to reduced shielding and the aforementioned breaks. Since the capacitive impedance of the break is inversely proportional to frequency, this effect is dominant at low frequencies. To conclude, a prototype spiral beam screen with improved coating quality and larger coating thickness, i.e. 40  $\mu\text{m}$  to provide 3 skin depths at 40 MHz, is proposed as a subject for future impedance measurements.

Table 7.1 – Results of quality assessment of the prototype spiral beam screen.

Nb.	Current [A]	Voltage [V]	End-to-end resistance [ $\Omega$ ]	Average thickness [ $\mu\text{m}$ ]	End-to-end capacitance [pF]
1	0	–	–	–	151
2	0.409	0.894	2.19	12.1	–
3	0.417	0.894	2.14	12.3	–
4	0.417	0.894	2.14	12.3	–
5	0.408	0.894	2.19	12.0	–
6	0.395	0.895	2.27	11.7	–
7	0	–	–	–	143
8	0.383	0.895	2.34	11.3	–
9	0.363	0.896	2.47	10.7	–
10	0	–	–	–	98
11	0	–	–	–	73
12	0	–	–	–	63
13	0	–	–	–	57
14	0	–	–	–	55
15	0	–	–	–	54
16	0	–	–	–	56
17	0	–	–	–	62
18	0	–	–	–	67
19	0	–	–	–	105
20	0.376	0.896	2.38	11.1	–
21	0.387	0.896	2.32	11.4	–



## 8 Characterization of electromagnetic properties of ferrites

### 8.1 Specification of magnetic materials for pulsed kicker magnets

The properties of a magnetic material are critical parameters for the performance of a fast pulsed kicker magnet in a particle accelerator. The choice of an appropriate material for the magnetic yoke is based on considerations of suitable permeability curves over the required operational range, a high electric resistivity to minimize eddy current losses, reasonably high saturation magnetic flux density to minimize the overall length of kicker magnets required and limit the volume of magnetic material e.g. for outgassing reasons, suitable frequency response in order that field rise and fall times follow those of the drive current, a low remanent flux density to minimize the influence upon circulating beam, and compatibility with an ultra high vacuum environment. Typically, the standard material for the yoke of the kicker magnet is a NiZn ferrite. The aperture of the kicker magnet is typically rectangular (see Fig. 3.3), in order that machining of the ferrite - an expensive process - is minimized.

In particular, the permeability of the magnetic material (see Section 2.3) is a key parameter to be carefully studied. The real part of the permeability has to be relatively high until the highest significant frequency of the pulse current in order that the core reluctance is low with respect to that of the aperture, and thus the required magnetic field strength is achieved without the need to significantly increase the magnitude of the pulse current (or pulse voltage, for a given characteristic impedance), which could cause an excessive electric stress on the pulse generator, magnet, cables and connectors. In addition, a relatively high real part of permeability is necessary to achieve good field homogeneity in the rectangular aperture. On the contrary, a low imaginary permeability is desirable to minimize magnetic losses in the yoke of the kicker magnet. Hence, an accurate model of the ferrite's permeability is crucial to understanding its behaviour and for accurate beam coupling impedance simulations. In the situation where power loss significantly increases the temperature of the ferrite yoke, the permeability is of interest over a range of temperatures, from ambient up to the Curie temperature ( $T_C$ ).

Beam induced power deposition, due to the circulating beam passing through the kicker

aperture, can cause an increase in ferrite temperature. More specifically, the power deposition in the ferrite is dependent upon the interaction of the beam spectrum with the real component of the longitudinal beam coupling impedance of the magnet (see Eq. 2.33). A change in ferrite properties, due to the effect of temperature, will also influence the beam coupling impedance. Hence, a good knowledge of EM properties of ferrites up to the GHz frequency range, which corresponds to the range of the beam spectrum for example in LHC or FCC, is important for a correct beam coupling impedance evaluation and allows us to obtain a reliable estimate of beam induced power deposition in the magnet and impact on beam stability [31].

At CERN, CMD5005 (National Magnetics, Inc.) [64] or 8C11 (Ferroxcube) [65], both of which have  $T_C \geq 125^\circ\text{C}$  as indicated by the data-sheet of the manufacturer, are typically used for the yoke of kicker magnets. However, 8C11 is not isostatically pressed in the production process, hence it has a lower initial permeability in comparison with CMD5005. From Ref. [92], it follows that CMD5005 can be isostatically pressed for accelerator purposes and therefore it is characterized by higher initial permeability in comparison with commercial samples. Hence, ferrite CMD5005 isostatically pressed is a baseline material proposed for the FCC injection kicker magnet yoke. However, a major concern is that beam induced heating of the ferrite yoke will result in severely degraded performance of the kicker magnets, especially during operation with long fills with high beam intensity [114].

Employing an alternative ferrite, e.g. CMD10 which has a higher Curie temperature ( $T_C \approx 250^\circ\text{C}$ ) than CMD5005 and 8C11, in the MKI magnet, was considered [69], but its initial permeability [64] is lower than required for the MKI [115]. As a result, a ferrite of a 50/50 mixture in powder of CMD5005 and CMD10 is being considered and it will be tested in a prototype SPS-MKP injection kicker magnet [116]. In particular, this blended ferrite, CMD10B, will have a higher Curie temperature ( $T_C \approx 190^\circ\text{C}$  expected) than CMD5005 or 8C11, but with a higher initial permeability than CMD10. If the performance of CMD10B is satisfactory, replacement of some of the hottest yokes in the MKI could be considered: nevertheless, although this would provide additional margin for the ferrite temperature, it is undesirable to operate at higher temperature as this increases outgassing and thus the probability of an electrical breakdown in the kicker magnet [117]. In addition, for NiZn ferrites the permeability data provided by the manufacturer is typically limited up to 10's of MHz, which is inadequate for beam coupling impedance simulations (GHz range typically required). In this chapter, we will present the results of measurements of electromagnetic properties of ferrites as a function of frequency and temperature. The following ferrite types are characterized: CMD5005, CMD10 and CMD10B. The results presented in this chapter are published in Ref. [22].

### 8.2 Electromagnetic characterization of materials

The response of a material to an applied electromagnetic field is quantified by the material's complex permeability  $\mu^*$  and permittivity  $\varepsilon^*$  (see Eqs. 2.68- 2.71). The electromagnetic properties of the materials can be determined using coaxial line measurement methods [45, 118].

A sample of the ferrite is placed within a 50  $\Omega$  coaxial line test fixture and S-parameters are measured using a vector network analyzer (VNA). The sample holder consists of a Dezifix connector (for detailed description see Ref. [119]) around which the material sample is clamped. At the sample's position within the line, the cross section of the line should be completely and homogeneously filled by the sample and hence appropriate machining of the sample is required. The material properties are extracted from measured S-parameters using algorithms, which will be discussed in the following sections. In this work, two different non-resonant measurements were used: transmission and short-circuit line methods. Below we present the configuration of the coaxial line test fixture for both experimental methods (see Figs. 8.1-8.2).

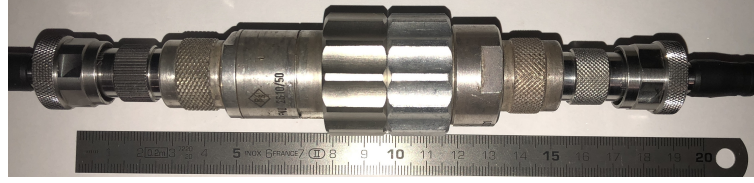


Figure 8.1 – Coaxial line test fixture with Dezifix in transmission.

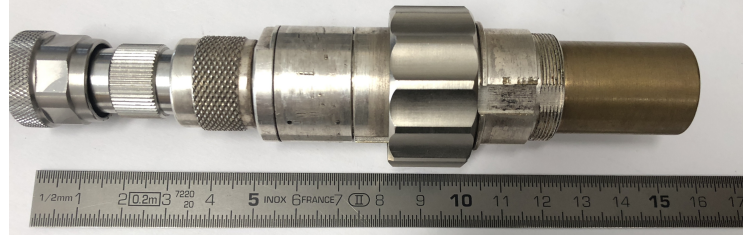


Figure 8.2 – Coaxial line test fixture with Dezifix terminated in short.

### 8.3 Transmission method

The transmission method [118] allows for a simultaneous measurement of  $\mu_r^*$  and  $\epsilon_r^*$ . A toroidal sample of length  $x$  loads a section of the transmission line, that has a total length  $L = L_1 + L_2 + x$  (see Figs. 8.3-8.5). In the free space region, the characteristic impedance of the transmission line is  $Z_0$  and the wave number is  $k_0 = \omega \sqrt{\mu_0 \epsilon_0}$ , while in the ferrite loaded region:  $Z = Z_0 \sqrt{\frac{\mu_r^*}{\epsilon_r^*}}$  and  $k = k_0 \sqrt{\mu_r^* \epsilon_r^*}$ . In addition, the reflection coefficient at material boundaries is  $R = \pm \frac{Z - Z_0}{Z + Z_0}$ .

In this method, the expressions for  $\mu_r^*$  and  $\epsilon_r^*$  in terms of  $k$ ,  $k_0$  and  $R$  are given by:

$$\epsilon_r^* = \epsilon_r' - j\epsilon_r'' = \frac{k}{k_0} \left( \frac{1 - R}{1 + R} \right), \quad (8.1)$$

$$\mu_r^* = \mu_r' - j\mu_r'' = \frac{k}{k_0} \left( \frac{1 + R}{1 - R} \right), \quad (8.2)$$

where a single-prime and double-prime donates the relative real and imaginary components, respectively. The S-parameters defined at the material-vacuum boundaries, thus assuming

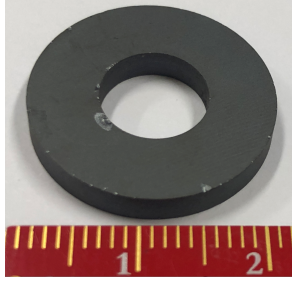


Figure 8.3 – Ferrite sample ( $x = 3.0$  mm,  $d_i = 9.2$  mm,  $d_o = 20.9$  mm).

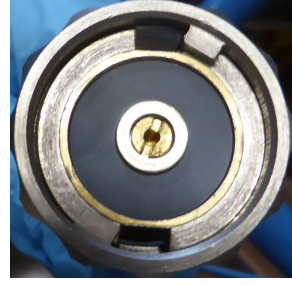


Figure 8.4 – Ferrite sample placed inside Dezifix connector.

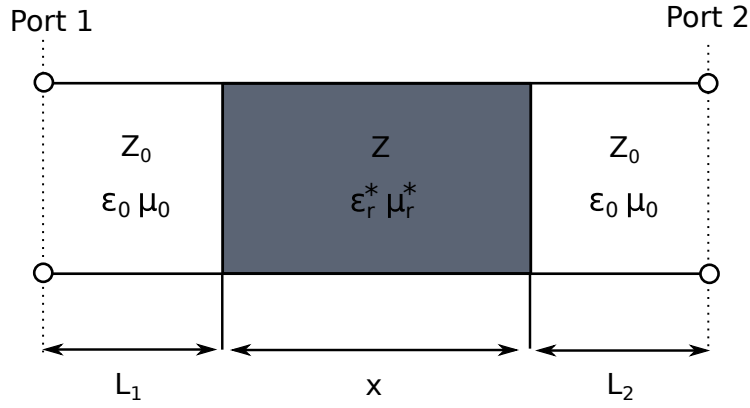


Figure 8.5 – Simplified diagram of the measurement setup.

$L_1 = L_2 = 0$ , are given by [120]:

$$S_{11}^* = \frac{R(1 - e^{-j2kx})}{1 - R^2 e^{-j2kx}}, \quad (8.3)$$

$$S_{21}^* = \frac{(1 - R^2)}{e^{jkx} - R^2 e^{-jkx}}. \quad (8.4)$$

In practice, however, the S-parameters are measured at the reference points: port 1, port 2. For this reason, the delay in the air filled regions of the transmission line has to be taken into account. Hence, the final expressions for the measured S-parameters are as follows [45, 118]:

$$S_{11} = \frac{R(1 - e^{-j2kx})e^{-jk_0 2L_1}}{1 - R^2 e^{-j2kx}} = \frac{R(e^{jkx} - e^{-jkx})e^{-jk_0 2L_1}}{(e^{jkx} - R^2 e^{-jkx})} = \frac{2jR \sin(kx)e^{-jk_0 2L_1}}{(e^{jkx} - R^2 e^{-jkx})}, \quad (8.5)$$

$$S_{21} = \frac{(1 - R^2)e^{-jk_0(L_1+L_2)}}{e^{jkx} - R^2 e^{-jkx}}. \quad (8.6)$$



In the transmission method developed by W. Barry [118], it is additionally assumed that  $L_1 = L_2$ . In particular, this method was followed in these studies. In such a case, Eqs. 8.5-8.6 can be solved simultaneously for  $k$  and  $R$  in terms of measured S-parameters:

$$k = \frac{1}{x} \cos^{-1} \left( \frac{e^{-j2k_0L} + S_{21}^2 - S_{11}^2}{2e^{-jk_0L}S_{21}} \right), \quad (8.7)$$

$$R = \frac{S_{11}}{e^{-jk_0L} - S_{21}e^{-jkx}}. \quad (8.8)$$

## 8.4 Short-circuit line method

Under conditions that  $L_2 = 0$  in Fig. 8.5 and a short-circuit is placed on port 2, we have a short circuit line method (see Ref. [45, 119]). Since only  $S_{11}$  is measured and the sample is placed against a short-circuit, only  $\mu_r^*$  is extracted and  $\epsilon_r^*$  must be known. In this study,  $\epsilon_r^* = 12$  was used [85], which was confirmed by the results of the transmission line measurement method, which are discussed in the next section (see Fig. 8.6). Let us introduce  $S_{11}^{\text{filled}}$  and  $S_{11}^{\text{empty}}$  as the measured S-parameters of the filled and empty sample holder, respectively. In this method, the following equation, shown in [45], is solved for  $\mu_r^*$  using the Newton-Raphson algorithm:

$$\frac{S_{11}^{\text{filled}}}{S_{11}^{\text{empty}}} + e^{j2k_0L_1} \frac{\tanh(k_0\sqrt{\mu_r^*\epsilon_r^*}L_1) - \sqrt{\frac{\epsilon_r^*}{\mu_r^*}}}{\tanh(k_0\sqrt{\mu_r^*\epsilon_r^*}L_1) + \sqrt{\frac{\epsilon_r^*}{\mu_r^*}}} = 0. \quad (8.9)$$

## 8.5 Results

Note, in both methods, the length of each part of the sample holder has been evaluated by measuring the electrical delay of the impulse response in the empty sample holder in the time domain and assuming the propagation speed of  $3 \times 10^8 \text{ ms}^{-1}$ . In the transmission method, the measured length of both parts of the sample holder was 175 mm, while in the short circuit method the length of one side of the sample holder was equal to 86.5 mm. The small difference in the length of two parts of the sample holder should be accounted as a possible source of error in the transmission method, hence the short method was predominately used in these studies. In both methods, we applied a correction to the magnitude of measured S-parameters, by calibrating out the losses of the empty sample holder. Below, we present the results.

### 8.5.1 Measurements at room temperature

The  $\mu_r^*$  and  $\varepsilon_r^*$  have been derived from the transmission method performed at 25°C. Figure 8.6 shows  $\varepsilon_r'$  for three types of ferrite. In particular, for frequencies above 400 MHz we found a good agreement with the expected value of  $\varepsilon_r^* \sim 12$  [85, 94].

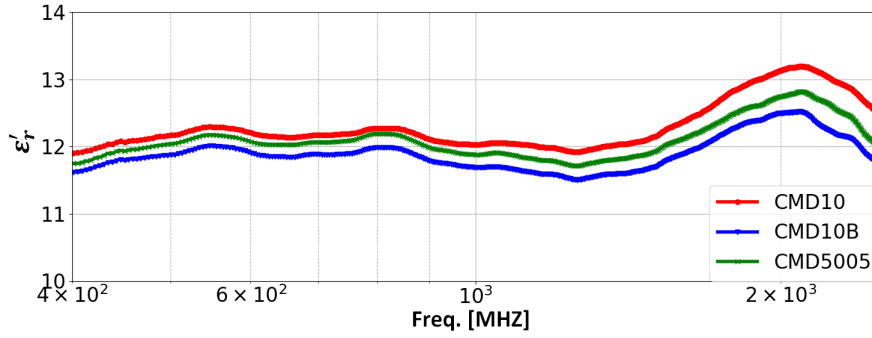


Figure 8.6 – Measured  $\varepsilon_r'$  for three types of ferrites at 25°C.

Figure 8.7 shows  $\mu_r^*$  for CMD5005 ferrite: there is good agreement between the two measurement methods and the data-sheet [64]. However, since the transmission line method is more prone to error as mentioned before, the short-circuit line technique was predominantly used in these studies.

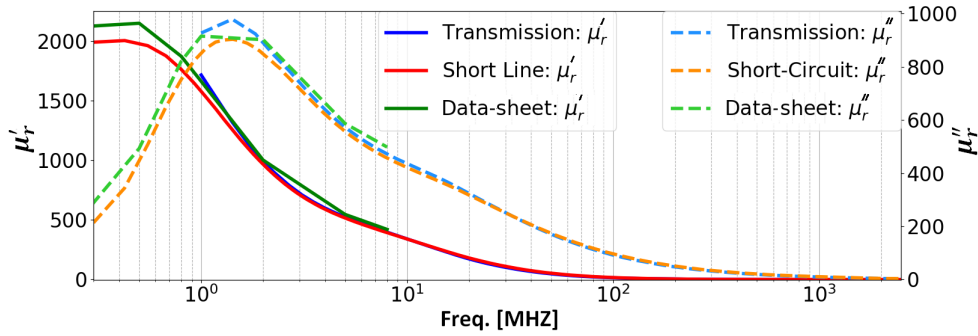
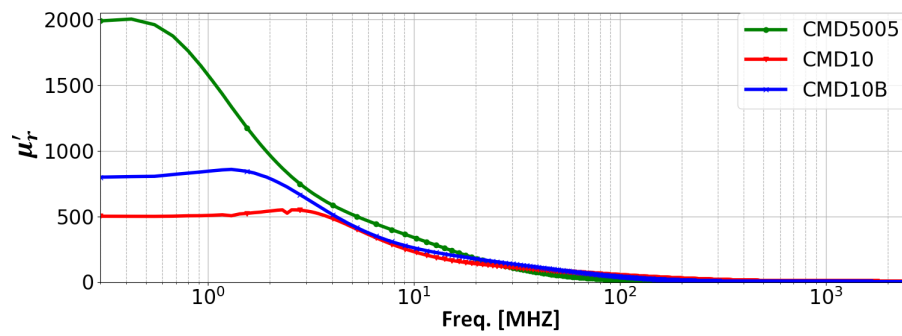
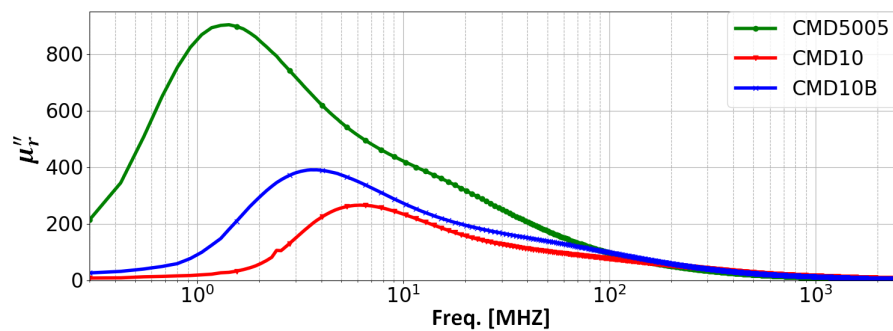


Figure 8.7 – Measured  $\mu_r^*$  of CMD5005 ferrite at 25°C in comparison with data-sheet [64].

Figures 8.8 and 8.9 show  $\mu_r'$  and  $\mu_r''$ , respectively, for the three ferrite types, measured using the short-circuit line method. Since CMD10B is a 50/50 blend of CMD10 and CMD5005, its  $\mu_r^*$  is in between those of these ferrites, as expected. In general, below 100 MHz the  $\mu_r^*$  of the three ferrites is quite different.

Figure 8.8 – Measured  $\mu'_r$  of ferrites at 25°C.Figure 8.9 – Measured  $\mu''_r$  of ferrites at 25°C.

### 8.5.2 Heated sample measurements

Heated sample measurements were performed using a power supply powering a heating braid that was wrapped around the outside of the coaxial line test fixture (see Fig. 8.10). The required temperature was set and the output of the supply was controlled by feedback from a temperature sensor attached to the heating braid. As a cross-check on the temperature, a PT100 sensor and non-reversible temperature indicators were used on the outside of the sample holder.



Figure 8.10 – Coaxial line test fixture with Dezifix terminated in short, PT100 temperature sensor, heating braid with temperature sensor and non-reversible temperature indicators.

However, it was not possible to measure the temperature of the ferrite sample directly. Hence, we would like to emphasize that temperatures shown in this paper are those set, i.e. on the outside of the test fixture: the ferrite sample would be cooler than this, because of thermal conduction via the cables to the VNA. In the experiment, the set temperature was increased in steps, ensuring thermal equilibrium of the sample was reached at each step by monitoring the stability of the S-parameters, before the S-parameters were recorded and used in the analysis.

To prevent damage to the test fixture, set temperatures were limited to  $T_{\max} = 175^{\circ}\text{C}$ , therefore only the CMD5005 reached its Curie point, indicating that its temperature was above  $125^{\circ}\text{C}$ . Figures 8.11 and 8.12 show  $\mu'_r$  and  $\mu''_r$ , respectively. At  $150^{\circ}\text{C}$  set, the CMD5005 was still below its Curie temperature ( $\sim 125^{\circ}\text{C}$ ). The increase of the set temperature from  $150^{\circ}\text{C}$  to  $175^{\circ}\text{C}$ , results in the reduction of  $\mu'_r$ , at frequencies below 500 kHz, from above 2000 to almost 1, hence showing the ferrite reached its Curie point. Below  $\sim 10$  MHz,  $\mu'_r$  generally increases with temperature, while at higher frequencies the opposite effect is observed. Hence, two mechanisms of losses can be distinguished in the  $\mu'_r$  spectra: resonance-type for the domain wall motion and relaxation-type for the spin rotation [121, 122]. In general, above  $125^{\circ}\text{C}$  set,  $\mu'_r$  and  $\mu''_r$  are both significantly reduced. From Figure 8.13, if the temperature of ferrite reaches its  $T_C$  (at  $T_{\max} = 175^{\circ}\text{C}$ ), then  $S_{11} \sim 0$  dB at all measurement frequencies. In such a case,  $\mu'_r \sim 1$  and  $\mu''_r \sim 0$ , hence ferrite is magnetically transparent and lossless.

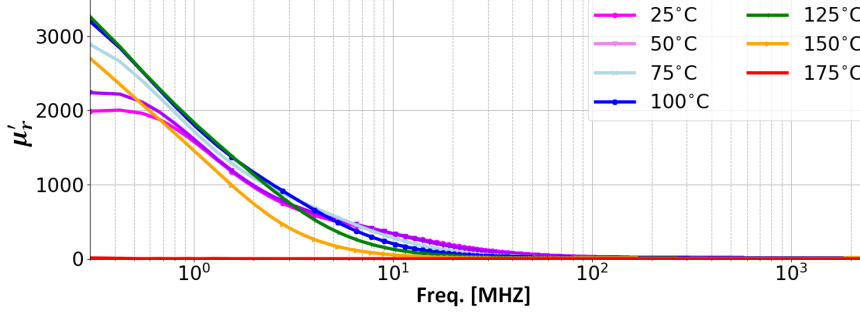


Figure 8.11 – Measured temperature dependence of  $\mu'_r$  for CMD5005.

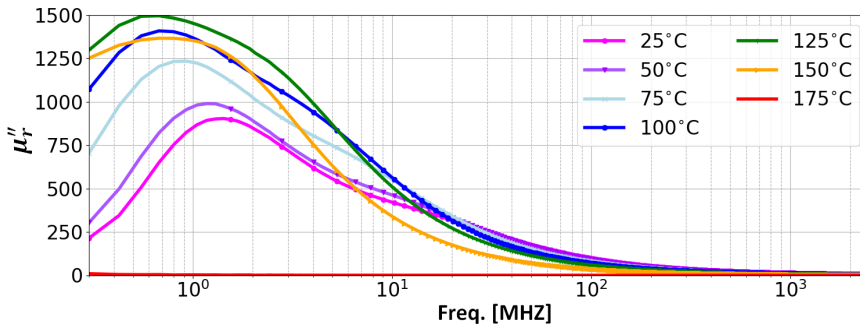


Figure 8.12 – Measured temperature dependence of  $\mu''_r$  for CMD5005.

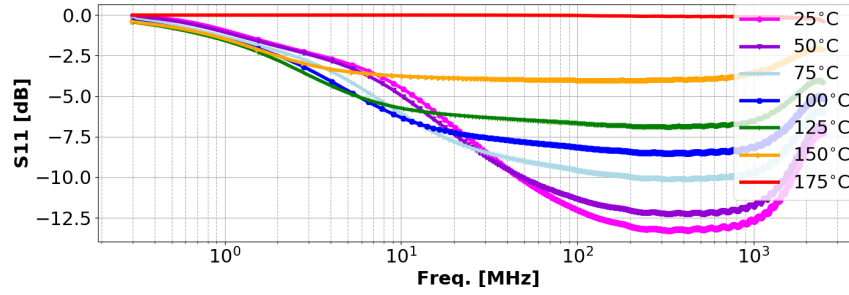


Figure 8.13 – Measured temperature dependence of  $S_{11}$  for CMD5005.

The above mentioned results are highly relevant to equipment containing ferrite which heats up during operation of an accelerator. The nominal bunch spacing for LHC and FCC is 25 ns: this results in line harmonics at multiples of 40 MHz, which can significantly contribute to power deposition in the ferrite. The measurement results show that, above 40 MHz,  $\mu_r''$  decreases with increasing ferrite temperature: for a given beam, this would result in a reduction in beam induced power deposition as the ferrite heats up. On the other hand, for the LHC and FCC injection kicker magnet beam screen, this would indicate that the ferrite rings of the beam screen cannot absorb power and most of the beam induced power is, instead, deposited into the magnet yoke: this would increase the rate of heating of the yoke until it too reached its Curie point. Hence, temperature dependence of the electromagnetic properties of ferrites is an important input for beam coupling impedance simulations and thermal simulations.

An interesting analysis is the comparison of  $\mu_r^*$  for all three ferrite types at higher temperatures. At frequencies below  $\sim 10$  MHz, which is the highest significant frequency in a pulse with 30 ns rise time,  $\mu_r'$  must be above 500 to provide the required field strength for the LHC MKI with the nominal magnitude of the pulse current [115]. Note, the rise time of the current pulse for the FCC injection kicker magnet is similar (75 ns), hence the same requirements should be fulfilled. However, already at  $50^\circ\text{C}$  set  $\mu_r'$  is  $\sim 350$ , for CMD5005, at 10 MHz (Fig. 8.14), and is less than 100 at  $150^\circ\text{C}$  set (Fig. 8.15). For both CMD10 and CMD10B at 10 MHz  $\mu_r'$  is below 300 at  $50^\circ\text{C}$  set (Fig. 8.14) and it slightly increases at  $150^\circ\text{C}$  set (Fig. 8.15). In addition, for the LHC MKI, the homogeneity of the field stays within specification when the relative permeability is above 100 up to 10 MHz [115]. For ferrite CMD5005, this condition is satisfied up to  $150^\circ\text{C}$  set.

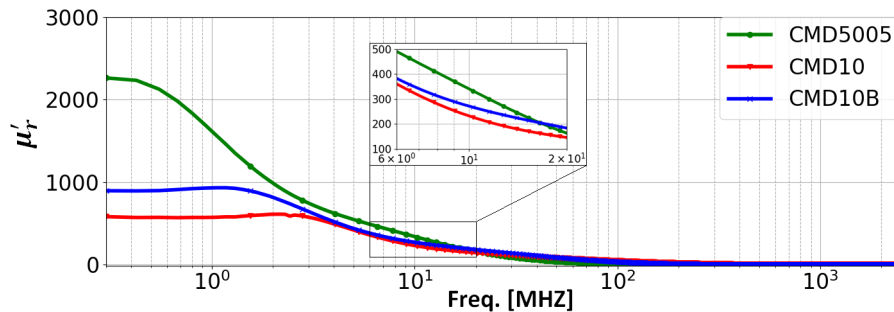


Figure 8.14 – Measured  $\mu_r'$  at  $50^\circ\text{C}$  set, for the three types of ferrites.

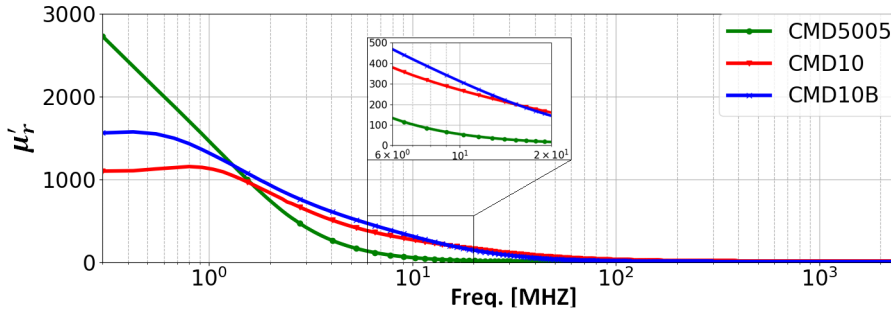


Figure 8.15 – Measured  $\mu'_r$  at 150°C set, for the three types of ferrites.

## 8.6 Importance of the results

The electromagnetic properties of CMD5005, CMD10 and CMD10B ferrites have been successfully characterized, into the GHz range, using transmission and short circuit measurement methods. A good agreement between the two methods, as well as the available low frequency data from the manufacturer, has been achieved for the CMD5005. The results are important both for understanding the  $\mu_r^*$  of ferrites and for the accurate simulation of beam coupling impedance. It is also necessary to have accurate  $\mu_r^*$  data for ferrites as a function of temperature, especially approaching and exceeding the Curie point: this can occur with high intensity beam circulating for many hours. A comparison of the properties of the three types of ferrite shows that the new type, CMD10B, maintains its initial  $\mu'_r$ , at 10 MHz, to higher temperatures than CMD5005. The presented results also show that, above 40 MHz,  $\mu'_r$  decreases with increasing ferrite temperature: for a given beam, this would result in decreased functionality of ferrite absorbers and increased power deposition into the ferrite yoke of the kicker magnet. Hence, the measurement results at 25°C and at higher temperature are vital input for beam coupling impedance simulations and to understand the kicker magnet performance.

## 9 Conclusions

### 9.1 Summary of work achievements

This PhD thesis aimed to study and optimize the beam screen for the injection kicker magnets of the Future Circular Collider for hadrons (FCC-hh). This topic is particularly challenging due to the large size and complexity of the kicker magnet design from the electromagnetic point of view, and due to many technical constraints inherent to the functional specifications of the kicker magnet. In the scope of this project, we proposed an innovative design - the spiral beam screen, to meet the demanding requirements for fast pulsed kicker magnets of the FCC. The spiral beam screen allows to achieve adequately low beam coupling impedance and improved high voltage performance in comparison with the "conventional", i.e. straight conductors, beam screen designs used to date. A comparison of the spiral beam screen alongside the conventional model has been performed from a theoretical, numerical and experimental point of view, and the results obtained are consistent. These results are relevant, not only for the FCC, but they also helped to better understand, and thus improve, the operation of the LHC kicker magnets. Below, the main achievements of this work are discussed in more detail.

Chapter 3 reviewed technological aspects of the injection kicker systems and introduced the conventional beam screen design used in the LHC MKIs. First, we explained the operational principle and main features of the conventional beam screen. Secondly, we reported the major drawbacks associated with this design amongst which are: (1) high voltage breakdown of the beam screen and (2) heating problems of the ferrite yoke. The novel concept of the spiral beam screen, described in Chapter 5, addresses both of these issues. To better understand the thermal behavior of the LHC MKI, we developed an online analysis of the parameters of the current waveform measured in the kicker magnet terminating resistor: this analysis is carried out following a beam dump and a Soft Start. As a result, we characterized the dependence of parameters such as current rise time and delay time upon yoke measured temperatures. This analysis method is presently the only reliable method to verify that the temperature of the ferrite yoke is below its Curie temperature. Hence, a new validation tool was implemented in operation to ensure a safe injection into the LHC. In addition, a significant difference of the

## Chapter 9. Conclusions

---

temperatures measured at the upstream and downstream ends of the kicker magnet paved the way for numerical and experimental studies performed later on in this project (see Chapters 5 and 7).

In Chapter 4, a new layout of the FCC injection kicker system was proposed. The main goal of the design process was to create a feasible and optimized solution. The total length of the kicker system was reduced by a factor of three, from the initially assumed 120 m down to  $\sim 40$  m, which greatly decreased the number of magnets and pulse power generators, hence costs and complexity are reduced. This optimization was crucial, since it allowed to reduce to an acceptable level the contribution of the injection kicker magnets to the overall machine impedance budget, as confirmed by analytical calculations and beam dynamics simulation results reported in Chapter 5. The analysis of the derived nominal FCC beam spectrum, together with the analytical Tsutsui model of the longitudinal impedance of an unshielded kicker magnet, showed a critical need for a beam screen, as otherwise the resulting power deposition is unacceptably high at above 160 W/m. Also, we calculated power loss firstly for the nominal filling scheme including gaps for the kicker field rise time and subsequently for an ideal filling scheme with equally spaced bunches. The comparison yielded differences below 1%. In particular, only the latter method has been used so far for the power loss calculations for the LHC MKI. For FCC, to enable injection at 3.3 TeV with an angle of 0.18 mrad, we optimized the total effective magnetic length of the kicker system, in conjunction with the person designing an inductive adder pulse generator, to be 31.8 m: this length is consistent with the capability of the inductive adder to supply 2.4 kA of pulse current, with today's SiC MOSFET technology, and the need to increase the aperture dimensions to accommodate a beam screen. To allow a fast rise time of the inductive adder, but consistent with the field rise time requirements of the kicker magnet, a  $6.25\ \Omega$  system impedance was chosen: this gives a magnet voltage of 15.0 kV. The kicker system will consist of 18 ferrite-loaded transmission line type magnets. The field rise time cannot exceed  $0.43\ \mu\text{s}$  (including any field overshoot, undershoot or ripple outside of the tolerance of  $\pm 0.5\%$ ), the flat-top duration is specified to be  $2\ \mu\text{s}$ . In this work, we developed a PSpice model of the FCC injection kicker magnet and optimized certain circuit parameters to achieve the required field rise time and flat-top quality: the optimizations showed that at least a 20-cell transmission line kicker magnet must be used to satisfy the requirements.

In Chapter 5, a detailed CST model of a 20-cell FCC injection kicker magnet was developed. At first, the longitudinal beam coupling impedance of the kicker magnet with the conventional beam screen and  $L_{\text{overlap}} = 56\ \text{mm}$ , as per upgraded LHC MKI, was analyzed. The expected total power loss was 30.2 W in comparison with 37 W for the LHC MKI8D. In addition, a new, efficient, power deposition distribution calculation method was proposed, which eliminates errors in the existing procedure used for the LHC MKI and improves accuracy. The highest power dissipation is expected in the 5<sup>th</sup> ring, at the upstream end, while the power deposition in the 1<sup>st</sup> yoke is significantly reduced. Based on these observations: (1) the total power loss is lower in the screened FCC injection kicker and (2) the power deposition distribution is similar to that of the upgraded LHC MKI. Hence, since the upgraded magnet did not limit LHC



operation, no heating issues are expected for FCC kicker magnets. Moreover, we can reduce even further the total power loss, by decreasing the overlap length: however the limits of this approach were explained and an optimal overlap of 44 mm was proposed. In addition, it was demonstrated that peaks in the longitudinal impedance spectrum are determined by the resonant behaviour of the overlap region, so that predictions for the full model (with the kicker magnet), simplified model (just the beam screen) and cut-down model (capacitively coupled end of the beam screen) are very similar. This allowed to simplify and therefore significantly speed up the CST simulations: prior to this, the duration of the simulations was limiting the ability to optimize the design. Confidence in the CST model has been established both by (1) characterizing and simulating EM properties of ferrites used in this design, as a function of frequency and temperature, in newly developed measurements (see Chapter 8) and (2) by performing new power deposition distribution and beam coupling impedance measurements on the LHC MKI (see Chapter 7). Next, we developed the concept of a spiral beam screen. We showed that for an integer number of turns in the aperture, the induced voltage on every screen conductor is nominally the same and this is approximately one-half of the worst case induced voltage of the conventional design. For this reason, the spiral beam screen is expected to provide significantly improved high voltage performance, while the longitudinal impedance is controlled and determined by the length of the screen conductors in the overlap region. To improve the design, new features were proposed, i.e.  $L_{\text{overlap}}$  reduced to 44 mm, a symmetric vacuum gap and ungraded screen conductor lengths. The prototype of the spiral beam screen was successfully benchmarked in beam coupling impedance measurements on an LHC MKI (see Chapter 7). For the conventional and spiral beam screen, the impact on the longitudinal beam stability was estimated. The analytical calculations revealed that for 18 kicker magnets: (1) the contribution to the threshold for the longitudinal coupled bunch instability, at the frequency of the fundamental mode ( $\sim 1000$  MHz), is below 0.05% and (2) the maximum contribution to the threshold for loss of Landau damping is  $\sim 5.7\%$ . Both of these contributions were reduced by a factor of approximately three due to the optimization of the kicker system length (see Chapter 4). Next, we evaluated the transverse impedance for both the conventional and spiral designs. In most cases, we obtained excellent agreement between the CST Wakefield and Eigenmode simulation solvers, but also we highlighted the areas where the agreement is not perfect and requires further investigation. The studies showed that with the spiral beam screen and a symmetric vacuum gap, the transverse quadrupolar impedance is zero in both planes. In addition, with the spiral beam screen, the transverse dipolar impedance can be controlled, i.e. by adjusting the number of turns, which allows to tune the resonant frequencies of the dipolar modes. Also, we showed that with the given impedance budget, only the spiral design can be used in an FCC kicker system: For multiple magnets with the conventional beam screen, it is not possible to tune resonant frequencies without a destructive impact on the longitudinal impedance.

In Chapter 6, we investigated the impact of a beam screen upon the field response of the kicker magnet. For this purpose, we performed Opera-2D simulations to evaluate the frequency dependence of the equivalent inductance and resistance associated with a central cell of the

kicker magnet. First, we established confidence in our model, by showing that the simulation results for an unshielded kicker magnet showed excellent agreement with analytically calculated inductance. Next, the simulations were performed for different beam screen design options. To achieve the desired performance, the equivalent inductance should be relatively constant up to the highest significant frequency of the current pulse ( $\sim 4.25$  MHz). We demonstrated that, for certain designs, the induced eddy currents in the screen conductors cause a significant decrease of the inductance at higher frequencies. However, this reduction can be limited with a suitable conductivity of the screen conductors and/or with a decreased width and thickness, while still providing adequately low beam impedance. The simulations showed that for Cu or Ag screen conductors,  $30\text{ }\mu\text{m}$  thick and  $1.3\text{ mm}$  wide, the inductance droop is suitably limited and the field homogeneity in the GFR stays within the specification. Also, the screen conductors are predicted to provide low broadband beam coupling impedance from  $40\text{ MHz}$ , as their thickness is equal to 3 skin depths at this frequency. Based on experience with the LHC dump kicker and initial estimates of power loss in the screen conductors, we concluded that, with the selected thickness, they will sustain the beam image current and eddy current heating. However, this topic requires further investigation. Next, to examine the impact of the proposed beam screen upon the field rise time and field flat-top quality, we derived an equivalent circuit to accurately model the frequency dependent inductance and resistance of a central cell using PSpice. These simulations show that the proposed beam screen will give a field response which is within specification.

Chapter 7 discussed the impedance related measurements carried out on an LHC MKI. The first goal was to measure the longitudinal impedance of the kicker magnet with the conventional beam screen, both with  $L_{\text{overlap}} = 130\text{ mm}$  (post-LS1 MKI) and  $L_{\text{overlap}} = 56\text{ mm}$  (upgraded MKI): this was to demonstrate that, with the shorter overlap length, the first fundamental harmonic is shifted to a higher frequency, as predicted by CST simulations and an analytical model. For this purpose, we used classical and resonant single wire measurement techniques. For both methods, the obtained results are in agreement with predictions. The second task was to verify the power deposition distribution along the magnet for two different configurations of the conventional beam screen. To accomplish this, a new experimental method was developed. In particular, we compared the magnetic field that couples from the single wire, stretched along the device, to different ferrite elements, as magnetic losses are the main mechanism of power dissipation in ferrites. The experiment confirmed, qualitatively, that for the beam screen with a shorter overlap length, the power loss in the 1<sup>st</sup> yoke of the kicker magnet is significantly reduced. This result enhances confidence in the solutions proposed for FCC. Finally, we measured the longitudinal impedance of the prototype spiral beam screen, consisting of 21 screen conductors, applied using a vacuum compatible Ag paint. In benchmark measurements of the spiral beam screen we confirmed that the longitudinal impedance is determined by the capacitive coupling and the first peak is, as expected, pronounced between  $1200\text{ MHz}$  to  $1350\text{ MHz}$ . Small resonances below  $150\text{ MHz}$  were attributed to both defects of the spiral conductors and an average thickness of only  $12\text{ }\mu\text{m}$ , which corresponds to only one skin depth at  $40\text{ MHz}$ .

Finally, in Chapter 8, novel measurements of the EM properties of ferrites, as a function of frequency and temperature, were performed. The experimental studies were conducted using the transmission line and the short-circuit line methods for three types of ferrites: CMD10, CMD10B and CMD5005. The EM properties of these ferrites, from 100 MHz to 2 GHz, were formerly unexplored. However, these materials are widely used in CERN accelerators and good knowledge of their EM properties is essential for beam impedance simulations. At room temperature, we determined the relative complex permittivity and permeability: a good agreement between the two methods and the low frequency data available from the manufacturer was achieved. Also, we characterized the temperature dependence of the permeability spectra and we demonstrated that above the Curie temperature, the ferrite becomes magnetically transparent and lossless. These results are highly relevant to equipment containing ferrites, which heats up during operation of an accelerator. For example, we showed in Chapter 5, that when the temperature of the ferrite rings at the upstream end of the beam screen reaches the Curie point, the total power is mainly deposited into the first yokes of the magnet, which gives a significant risk that the beam will be mis-injected. Thus, it is critical to ensure that the ferrite rings also remain below their Curie temperature.

## **9.2 Scientific contributions**

The research carried out in the scope of this PhD thesis provided a full spectrum of the design, analysis, optimization and measurements of a new beam screen for achieving low beam coupling impedance for a fast, transmission line, kicker magnet. Subsequently studies were carried out to optimize the screen and magnet design to ensure that the predicted field rise time and flat-top quality met specifications. The achieved results provide a solid base for future studies towards the implementation of a spiral beam screen in new or existing machines. The new contributions to the field of kicker magnets are listed below:

- Real-time data analysis of the output waveform of the MKIs to ensure safe injection into the LHC,
- Optimization of the length of the FCC injection kicker system,
- Optimization of the beam screen design of the FCC injection kicker magnet (CST, Opera-2D, and PSpice),
- Proposal and development of the novel spiral beam screen concept and subsequently demonstrate the feasibility of this concept,
- Proposal and development of a new calculation method for determining power loss distribution, from simulations, in the yoke of a kicker magnet,
- Performed novel measurements of power loss distribution at several ferrite components of a kicker magnet, to validate CST predictions - in particular, the benefits of reduced overlap,

- Novel measurements of the EM properties of ferrites as a function of frequency and temperature. In particular, these contributed to improved CST models and the understanding of the need to maintain the temperature of the ferrite rings below their Curie point.

### 9.3 Recommendations for future research

The research work on the LHC and FCC injection kicker systems showed that a spiral beam screen is a promising solution not only for future accelerators, but also for the existing machines. For example, this screen has been analyzed theoretically and numerically for FCC, and benchmarked in measurements on an LHC MKI: the results show that it should provide significantly improved performance with respect to the existing design. Nevertheless, further developments are required to suitably apply the spiral to an alumina tube: to guarantee effective shielding, an improved coating quality, without breaks and with adequate thickness, should be achieved. To validate a significant reduction in the maximum induced voltage, low voltage measurements of voltage on each screen conductor, followed by high voltage tests, should be performed. The spiral beam screen offers the potential to connect the screen conductors together, outside of the magnet aperture, and thus to electrically connect the screen to the beam pipe, following the completion of injection: this will further reduce beam coupling impedance with circulating beam. However, this could lead to an increase in field rise time if there are differences in induced voltage between screen conductors, e.g. due to fringe fields at the ends of the kicker magnet - this would require further, detailed, investigation. In addition, the influence of the beam image current and induced eddy currents, upon thin conductors, needs to be studied. Also, the concept of tuning of the resonant frequencies of the transverse dipolar modes requires further investigation together with benchmarking of the beam coupling impedance for two spiral designs with different number of turns. In order to determine the transverse impedance contribution of the kicker magnets to the overall FCC impedance budget, each configuration of the spiral beam screen would require separate simulations. Finally, the proposed design of the FCC injection kicker magnet requires prototyping.

# A The Panofsky-Wenzel theorem

There is a relationship between longitudinal and transverse wake function, known as the Panofsky-Wenzel theorem. Below, we present a derivation of this formula, based on Ref. [29]. Let us refer to the system presented in Fig. 2.3. First, to simplify equations we introduce  $A = \{\vec{r}_1, s_1, \vec{r}, s, t\}$ . In order to derive desired relation, we use the integral form of the Faraday's law of induction, where  $\vec{\nabla} = \{\frac{\partial}{\partial x}, \frac{\partial}{\partial y}, \frac{\partial}{\partial s}\}$ :

$$\vec{B}(\vec{A}) = - \int_t^{t_1} (\nabla \times \vec{E}(\vec{A})) dt. \quad (\text{A.1})$$

The Lorentz force acting on the test charge (see Eq. 2.15) can be therefore re-written:

$$\vec{F}(\vec{A}) = q \left[ \vec{E}(\vec{A}) - \vec{v} \times \int_t^{t_1} \vec{\nabla} \times \vec{E}(\vec{A}) dt \right] = q_2 \left[ \vec{E}(\vec{A}) - \int_t^{t_1} \left( \vec{\nabla}(\vec{v} \cdot \vec{E}(\vec{A})) - \vec{v}(\vec{\nabla} \cdot \vec{E}(\vec{A})) \right) dt \right]. \quad (\text{A.2})$$

From the above relation, the longitudinal and transverse components of the Lorentz force are:

$$F_{\parallel}(\vec{A}) = q_2 E_{\parallel}(\vec{A}), \quad (\text{A.3})$$

$$\vec{F}_{\perp}(\vec{A}) = q_2 \left[ \vec{E}_{\perp}(\vec{A}) - \beta c \int_t^{t_1} \left( \vec{\nabla}_{\perp} E_{\parallel}(\vec{A}) - \frac{\partial \vec{E}_{\perp}(\vec{A})}{\partial s} \right) dt \right], \quad (\text{A.4})$$

where  $\vec{\nabla}_{\perp} = \{\frac{\partial}{\partial x}, \frac{\partial}{\partial y}\}$ . Using relations (A.3 - A.4), the longitudinal wake function (Eq. 2.16) and

## Appendix A. The Panofsky-Wenzel theorem

---

transverse wake function (Eq. 2.34), can be expressed in the following way:

$$W_{\parallel}(\vec{r}_1, \vec{r}, z)[V/C] = -\frac{1}{q_1} \int_0^L \vec{E}_{\parallel}(\vec{A})|_{t=\frac{s-z}{\beta c}, s_1=s-z} ds \quad (\text{A.5})$$

$$\vec{W}_{\perp}(\vec{r}_1, \vec{r}, z)[V/C] = -\frac{1}{q_1} \int_0^L \left[ \vec{E}_{\perp}(\vec{A}) - \beta c \int_t^{t_1} \left( \vec{\nabla}_{\perp} E_{\parallel}(\vec{A}) - \frac{\partial \vec{E}_{\perp}(\vec{A})}{\partial s} \right) dt \right] |_{t=\frac{s-z}{\beta c}, s_1=s-z} ds \quad (\text{A.6})$$

Following Ref. [29], a derivative of transverse wake potential with respect to  $z$  has to be calculated. Since  $s = s_1 + z$ , we obtain  $\partial/\partial z = \partial/\partial s$ . In addition since  $t = \frac{s-z}{\beta c}$ , we obtain  $\partial/\partial z = -\partial/(\beta c \partial t)$ . In a result, the first and the third term of Eq. A.6 cancels out:

$$\frac{\partial}{\partial s} \vec{W}_{\perp}(\vec{r}_1, \vec{r}, z) = -\frac{1}{q_1} \int_0^L \left[ \frac{\partial}{\partial s} \vec{E}_{\perp}(\vec{A}) + \frac{\partial}{\partial t} \int_t^{t_1} \left( \vec{\nabla}_{\perp} E_{\parallel}(\vec{A}) - \frac{\partial \vec{E}_{\perp}(\vec{A})}{\partial s} \right) dt \right] ds \quad (\text{A.7})$$

From the above, we obtain:

$$\frac{\partial}{\partial z} \vec{W}_{\perp}(\vec{r}_1, \vec{r}, z) = -\frac{1}{q_1} \int_0^L \vec{\nabla}_{\perp} E_{\parallel}(\vec{A}) ds \quad (\text{A.8})$$

The Panofsky-Wenzel theorem, using Eq. A.5, is expressed as:

$$\frac{\partial}{\partial z} \vec{W}_{\perp}(\vec{r}_1, \vec{r}, z) = \vec{\nabla}_{\perp} W_{\parallel}(\vec{r}_1, \vec{r}, z). \quad (\text{A.9})$$

Using Fourier transform, the longitudinal and transverse beam coupling impedance are therefore related by:

$$\vec{Z}_{\perp}(\vec{r}_1, \vec{r}, z) = \frac{\nu}{\omega} \vec{\nabla}_{\perp} Z_{\parallel}(\vec{r}_1, \vec{r}, z). \quad (\text{A.10})$$

## B PSpice macros and goal functions

PSpice syntax is a powerful tool to define customized expressions in order to determine important parameters of the waveforms. Below, we present macros and goal functions that have been developed to analyze the field flat-top quality of the FCC-hh injection kicker magnet at the design stage. First, we define constants that are used in the proposed expressions. Next, the macro to calculate the normalized magnetic flux with and without considering end effects is presented. In addition, the macro to calculate a time integral of the magnetic flux excursion from the acceptance level is shown. In particular, the last expression is necessary to evaluate the FOM. Finally, the goal function to calculate the FOM during the flat-top period is presented.

### Constants:

```
1 tau_fill=355n
2 tau_flattop=2000n
3 Vmax=15.7k
4 normalization=0.002824628461800
5
6 *tau_fill - magnet fill time
7 *tau_flattop - flat-top duration
8 *Vmax - maximum magnet voltage
9 *normalization - field at the flat-top (depends on number of cells)
```

### Normalized magnetic flux (neglecting end effects):

```
1 Norm_field(Vin,Vout)=s(Vin-Vout)*2*100/tau_fill/Vmax
2 *Vin - input voltage
3 *Vout - output voltage
```

### Normalized magnetic flux (including end effects):

```
1 Norm_fieldEE(Vin,Vout)=s(Vin-Vout)/normalization*100
```

Depending on whether the end effects are taken into account or not, the user must select an appropriate function to calculate the normalized magnetic flux, i.e. [Norm\\_field](#)(Vin, Vout)

## Appendix B. PSpice macros and goal functions

or `Norm_fieldEE`(Vin, Vout). The expressions listed below are valid in both cases, provided that a proper function is selected. For instance, the examples presented below are used for the analysis without considering the end effects, as function `Norm_field`(Vin, Vout) is specified.

### Time integral of the magnetic flux excursion from the acceptance level:

```
1 Area_outside(Vin, Vout, level1, level2)=
2 Area_down(Vin, Vout, level1)+Area_up(Vin, Vout, level2)
3 *level1 - lower acceptance limit in % (i.e. 0.5 for 99.5%)
4 *level2 - upper acceptance limit in % (i.e. 0.5 for 100.5%)
5
6 Area_up(Vin, Vout, level2)=
7 s((abs(Norm_field(Vin, Vout) - (100 + level2)) + (Norm_field(Vin, Vout) - (100 +
8   level2))) / 2)
9
10 Area_down(Vin, Vout, level1)=
11 s((abs(Norm_field(Vin, Vout) - (100 - level1)) - (Norm_field(Vin, Vout) - (100 -
12   level1))) / 2)
```

### FOM as a function of time:

```
1 FOM(Vin, Vout, level1, level2)=
2 Area_outside(Vin, Vout, level1, level2)/(flattop)
```

### FOM calculated during the flattop duration:

```
1 FOM_FLAT_TOP(1,2,transit,flattop,level3) = Y3 - Y2
2 * WAVEFORM 1 = Norm_field(V(in),V(out))
3 * WAVEFORM 2 = FOM(Vin, Vout, level1, level2)
4 * transit - field rise time
5 * flattop - flat-top duration
6 * level3 - threshold of the field rising edge in % (i.e. 0.5 for 0.5%
7   {
8     1|SF/B/#2#LE(level3,P)!1;
9     2|SXV(X1)
10    SXV(.+transit)!2
11    SXV(X2)
12    SXV(.+flattop)!3;
13  }
```



## C Prototype spiral beam screen

Below, we present the dimensions of the prototype spiral beam screen manufactured at CERN. The schematic drawing of the spiral beam screen is presented in Fig. C.1, whereas its cross-section is shown in Fig C.2. Individual dimensions are marked with letters. The description of the measured parameters and their exact values are listed in Tab. C.1.

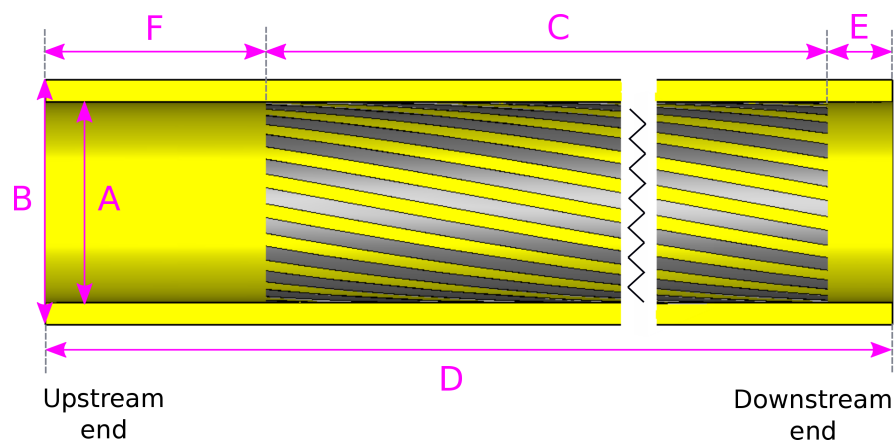


Figure C.1 – Schematic drawing of the prototype spiral beam screen.

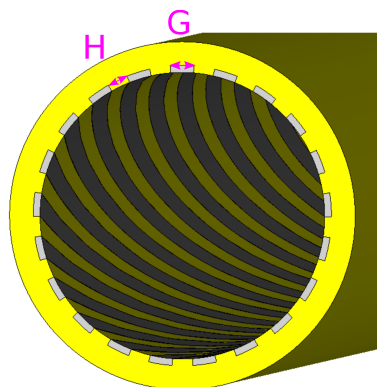


Figure C.2 – Schematic cross-section of the prototype spiral beam screen.

## Appendix C. Prototype spiral beam screen

---

Table C.1 – Dimensions of the prototype spiral beam screen.

Parameter	Description	Value [mm]
A	Inner diameter	42
B	Outer diameter	51
C	Height of spiral	2948
D	Tube length	3000
E	Tube length from capacitively coupled end	32
F	Tube length from grounded end	20
G	Width of single screen conductor	3
H	Separation of the screen conductors	3.3

# Bibliography

- [1] CERN Official Website, “The Higgs boson.” <https://home.cern/science/physics/higgs-boson>. Accessed: 2019-08-15.
- [2] J. Beacham *et al.*, “Physics Beyond Colliders at CERN. Beyond the Standard Model Working Group Report,” tech. rep., CERN, Geneva, Switzerland, 3 2019. CERN-PBC-REPORT-2018-007.
- [3] G. Dvali, “A Lecture on the Hierarchy Problem and Gravity.” <https://cds.cern.ch/record/2120792/files/CERN-2013-003-p145.pdf>. Accessed: 2019-09-06.
- [4] M. McCullough, “Physics at FCC.” FCC Week 2017, Berlin, Germany (May 2017). <https://indico.cern.ch/event/556692/contributions/2483388>, Accessed: 2019-09-06.
- [5] W. Herr and B. Muratori, “Concept of luminosity.” <https://cds.cern.ch/record/941318/files/p361.pdf>. Accessed: 2019-09-06.
- [6] G. Apollinari *et al.*, “High-Luminosity Large Hadron Collider (HL-LHC) Preliminary Design Report,” tech. rep., 12 2015. No. CERN-2015-005; FERMILAB-DESIGN-2015-02.
- [7] M. Benedikt *et al.*, “Future Circular Collider Study: Vol. 3 The Hadron Collider (FCC-hh),” tech. rep., 12 2018. No. CERN-ACC-2018-0058.
- [8] Compact Linear Collider Official Website, <http://clic-study.web.cern.ch>, Accessed: 2019-09-09.
- [9] International Linear Collider Official Website, <https://ilchome.web.cern.ch>, Accessed: 2019-09-09.
- [10] F. Bordry *et al.*, “Machine Parameters and Projected Luminosity Performance of Proposed Future Colliders at CERN,” 10 2018. arXiv:1810.13022v1.
- [11] A. Milanese, B. Goddard, and M. Solfaroli Camillocci, “Faster Magnet Ramps for Using the LHC as FCC Injector,” *ICFA Beam Dyn., Newslett.*, no. 72, pp. 113–121, 2017.
- [12] M. Benedikt and F. Zimmermann, “Overview and status of the Future Circular Collider Study.” FCC Week 2019, Brussels, Belgium (June 2019). <https://indico.cern.ch/event/727555/sessions/275519/#20190624>, Accessed: 2019-09-06.

## Bibliography

---

- [13] T. Kroyer, F. Caspers, and E. Gaxiola, “Longitudinal and Transverse Wire Measurements for the Evaluation of Impedance Reduction Measures on the MKE Extraction Kickers,” tech. rep., CERN, Geneva, Switzerland, 8 2000. No. CERN-SL-2000-050-AP.
- [14] Cadence Official Website, “Allegro PSpice Simulator.” <https://www.cadence.com>. Accessed: 2017-11-06.
- [15] H. Tsutsui, “Longitudinal impedances of some simplified ferrite kicker magnet models,” In Proc. of European Particle Accelerator Conference 2000 (EPAC’00), Vienna, Austria (June 2000), No. CERN-SL-2000-050.
- [16] CST Studio Suite, <https://www.cst.com>, Accessed: 2019-03-06.
- [17] Opera Simulation Software Suite , “Opera-2D Reference Suite,” 6 2018. (Version 18R2).
- [18] A. Chmieleńska *et al.*, “Preliminary estimate of beam induced power deposition in a FCC-hh injection kicker magnet,” In Proc. of International Particle Accelerator Conference 2017 (IPAC’17), Copenhagen, Denmark (May 2017), paper WEPVA095, pp. 3475-3478.
- [19] A. Chmieleńska and M. J. Barnes, “New Spiral Beam Screen Design for the FCC-hh Injection Kicker Magnet,” In Proc. of International Particle Accelerator Conference 2019 (IPAC’19), Melbourne, Australia, (May 2019), paper MOPGW074, pp. 270-273.
- [20] V. Vlachodimitropoulos, M. Barnes, and A. Chmieleńska, “Preliminary results from validation measurements of the longitudinal power deposition model for the LHC injection kicker magnet,” In Proc. of International Particle Accelerator Conference 2018 (IPAC’18), Vancouver, Canada (May 2018), paper WEPMK005, pp. 2636-2639.
- [21] A. Chmieleńska, “New Spiral Beam Screen Design for the FCC-hh Injection Kicker Magnets.” FCC Week 2019, Brussels, Belgium (June 2019). <https://indico.cern.ch/event/727555/contributions/3461029/>, Accessed: 2019-09-09.
- [22] A. Chmieleńska *et al.*, “Measurements of electromagnetic properties of ferrites as a function of frequency and temperature,” *Journal of Physics: Conference Series.*, vol. 1067, p. 082018, 9 2018. IOP Publishing.
- [23] D. A. Edwards and M. J. Syphers, *An introduction to the physics of high energy accelerators*. John Wiley & Sons, 2008.
- [24] S. Y. Lee, *Accelerator physics*. World scientific publishing, 2018.
- [25] E. Métral and D. Möhl, “Transition crossing,” in *Fifty years of the CERN Proton Synchrotron* (S. Gilardoni and D. Manglunki, eds.), vol. 1, pp. 59–60, CERN, Geneva, Switzerland, 6 2011.
- [26] K.Y. Ng, *Physics of intensity dependent beam instabilities*. World Scientific, 2006.

- 
- [27] E. Métral, “Longitudinal beam dynamics.” JUAS 2018, Archamps, France (January 2018). [https://indico.cern.ch/event/683638/contributions/2801711/attachments/1585987/2515503/LongitudinalBeamDynamics\\_JUAS2018\\_EM\\_Handout.pdf](https://indico.cern.ch/event/683638/contributions/2801711/attachments/1585987/2515503/LongitudinalBeamDynamics_JUAS2018_EM_Handout.pdf), Accessed: 2019-09-15.
- [28] A. Chao, “Lecture notes on topics in a accelerator physics,” tech. rep., SLAC, Menlo Park, USA, 11 2002. SLAC-PUB-9574.
- [29] B. W. Zotter and S. A. Kheifets, *Impedances and Wakes in High-Energy Particle Accelerators*. World Scientific, 1997.
- [30] L. Palumbo, V.G. Vaccaro, and M. Zobov, “Wake Fields and Impedance,” tech. rep., INFN - Laboratori Nazionali di Frascati, 9 1994. LNF-94/041 (P).
- [31] G. Rumolo, “Beam Instabilities,” In Proc. of the CAS - CERN Accelerator School: Advanced Accelerator Physics Course 2013, Trondheim, Norway (Aug 2013), pp. 199-219.
- [32] P. B. Wilson, “Introduction to wakefields and wake potentials,” tech. rep., Stanford Linear Accelerator Center, 1 1989. SLAC-PUB-4547.
- [33] A. Chao and W. Chou, *Reviews of accelerator science and technology*. World Scientific, 2008.
- [34] A. Chao, *Physics of Collective Beam Instabilities in High Energy Accelerators*. Wiley, 1993.
- [35] G. V. Stupakov, “Wake and Impedance,” tech. rep., Stanford Linear Accelerator Center, 10 2000. SLAC-PUB-8683.
- [36] E. H. Lieb and M. Loss, *Graduate studies in mathematics. Analysis*. American Mathematical Society, 2001.
- [37] S. Heifets, A. Wagner, and B. Zotter, “Generalized Impedances and Wakes in Asymmetric Structures,” tech. rep., Stanford Linear Accelerator Center, 1 1998. SLAC/AP110.
- [38] G. Rumolo, *Private communication*. Date: 2019-02-10.
- [39] W. K. H. Panofsky and W. Wenzel, “Some considerations concerning the transverse deflection of charged particles in radio-frequency fields,” *Review of Scientific Instruments*, vol. 27, pp. 967–967, 11 1956.
- [40] E. Shaposhnikova, “Longitudinal stability of the LHC beam in the SPS,” tech. rep., CERN, Geneva, Switzerland, 8 2001. SL-Note-2001-031-HRF.
- [41] T. Argyropoulos, *Longitudinal Beam Instabilities in a Double RF system*. PhD thesis, National Technical University of Athens, Greece, 1 2015. CERN-THESIS-2015-421.
- [42] J. E. Müller, *Longitudinal intensity effects in the CERN Large Hadron Collider*. PhD thesis, École Polytechnique Fédérale de Lausanne, Switzerland, 6 2016. CERN-THESIS-2016-066.

## Bibliography

---

- [43] A. Lasheen, *Beam measurements of the longitudinal impedance of the Cern Super Proton Synchrotron*. PhD thesis, University of Paris-Sud, France, 1 2017. CERN-THESIS-2017-068.
- [44] K. Zhang *et al.*, *Electromagnetic theory for microwaves and optoelectronics*. Springer, 1998.
- [45] J. B. Jarvis *et al.*, “Measuring the Permittivity and Permeability of Lossy Materials: Solids, Liquids, Metals, and negative-Index Materials,” tech. rep., National Institute of Standards and Technology, California, USA, 2 2005. NIST TN-1536.
- [46] ThoughtCo. Official Website, “Table of Electrical Resistivity and Conductivity.” <https://www.thoughtco.com/table-of-electrical-resistivity-conductivity-608499>. Accessed: 2019-08-06.
- [47] Alloy Wire International Official Website, “80/20 NiCr Datasheet.” <https://www.alloywire.us.com/products/8020-ni-cr-nickel-chrome-resistance-wire>. Accessed: 2019-08-06.
- [48] H. W. Ott, *Electromagnetic Compatibility Engineering*. John Wiley & Sons, 2011.
- [49] M. J. Barnes *et al.*, “Injection and extraction magnets: kicker magnets,” In Proc. of the CAS - CERN Accelerator School: Specialised Course on Magnets 2009, Bruges, Belgium (June 2009), pp. 141-166.
- [50] J. Uythoven *et al.*, “Beam induced heating of the SPS fast pulsed magnets,” In Proc. of European Particle Accelerator Conference 2014 (EPAC’04), Lucerne, Switzerland (June 2004), pp. 623-625.
- [51] L. Ducimetière *et al.*, “The LHC injection kicker magnet,” In Proc. of Particle Accelerator Conference 2003 (PAC’03), Portland, Oregon, USA, (May 2003), paper TPAC036, pp. 1162-1164.
- [52] H. Day, *Measurements and Simulations of Impedance Reduction Techniques in Particle Accelerators*. PhD thesis, The University of Manchester, 2013.
- [53] Ferroxcube Official Website, “4M2 Material Specification.” <https://www.ferroxcube.com>. Accessed: 2019-02-25.
- [54] Ferroxcube Official Website, “4B3 Material Specification.” <https://www.ferroxcube.com>. Accessed: 2019-02-25.
- [55] M. J. Barnes *et al.*, “Reduction of surface flashover of the beam screen of the LHC injection kickers,” In Proc. of International Particle Accelerator Conference 2017 (IPAC’13), Shanghai, China (May 2013), paper MOPWA032, pp. 735-737.
- [56] M. J. Barnes *et al.*, “High voltage performance of surface coatings on alumina insulators,” In Proc. of Particle Accelerator Conference 2016 (IPAC’16), Busan, Korea (May 2016), paper THPMW028, pp. 3603-3605.

- 
- [57] M. J. Barnes *et al.*, “An improved beam screen for the LHC injection kickers,” In Proc. of Particle Accelerator Conference 2017 (PAC’07), Albuquerque, New Mexico, USA (May 2007), paper TUPAN086, pp. 1574-1576.
- [58] M. J. Barnes *et al.*, “The Beam Screen for the LHC Injection Kicker Magnets,” tech. rep., CERN, 1 2006. LHC Project Report 909.
- [59] M. J. Barnes *et al.*, “An upgraded LHC injection kicker magnet,” In Proc. of International Particle Accelerator Conference 2018 (IPAC’18), Vancouver, Canada (May 2018), paper WEPMK003, pp. 2632-2635.
- [60] H. Day *et al.*, “Current and future beam thermal behaviour of the LHC injection kicker magnet,” In Proc. of Particle Accelerator Conference 2016 (IPAC’16), Busan, Korea (May 2016), paper THPMW031, pp. 3615-3618.
- [61] V. Vlachodimitropoulos *et al.*, “Study of an improved beam screen design for the LHC injection kicker magnet for HL-LHC,” In Proc. of International Particle Accelerator Conference 2015 (IPAC’17), Copenhagen, Denmark (May 2017), paper WEPVA094, pp. 3471-3474.
- [62] L. Vega *et al.*, “Conception and design of a cooling system for the lhc injection kicker magnets,” *Nuclear Instruments and Methods in Physics Research Section A: Accelerators, Spectrometers, Detectors and Associated Equipment*, pp. 296–305, 2 2019.
- [63] R. A. Barlow *et al.*, “KISS conditioning of the LHC injection kickers,” tech. rep., CERN, 3 2010. CERN TE-Note-2010-008.
- [64] National Magnetics Group, “CMD5005 Datasheet.” <https://www.magneticsgroup.com>. Accessed: 2018-03-30.
- [65] Ferroxcube Official Website, “8C11 Material Specification.” <https://www.ferroxcube.com>. Accessed: 2018-03-30.
- [66] M. Barnes *et al.*, “An improved beam screen for the LHC injection kickers,” In Proc. of Particle Accelerator Conference 2007 (PAC’07), Albuquerque, New Mexico, USA (June 2007), pp. 1574-1576.
- [67] W. Bartmann, *Private communication*. Date: 2017-05-05.
- [68] CERN Scripting Tools: PyTimber, <https://wikis.cern.ch/display/ST/Python>, Accessed: 2019-02-28.
- [69] M. J. Barnes *et al.*, “Analysis of Ferrite Heating of the LHC Injection Kickers and Proposals for Future Reduction of Temperature,” In Proc. of International Particle Accelerator Conference 2012 (IPAC’12), New Orleans, Louisiana, USA, (May 2012), paper TUPPR090, pp. 2038-2040.
- [70] CERN Scripting Tools, <https://gitlab.cern.ch/scripting-tools>, Accessed: 2019-02-28.

## Bibliography

---

- [71] CERN Gitlab, <https://gitlab.cern.ch/achmieli>, Accessed: 2019-02-28.
- [72] W. Bartmann *et al.*, “Beam transfer to the FCC-hh collider from 3.3 TeV booster in the LHC tunnel,” In Proc. of International Particle Accelerator Conference 2015 (IPAC’15), Richmond, Virginia, USA, (May 2015), paper THPF089, pp. 3901-3904.
- [73] E. Renner, “Machine Protection of the Future Circular Hadron Collider FCC-hh: Injection and Extraction,” Master’s thesis, Vienna University of Technology, Vienna, Austria, 8 2018. CERN-THESIS-2018-261.
- [74] F. Burkart *et al.*, “Injection and extraction straight and dump lines.” FCC Week 2017, Berlin, Germany (May 2017). <https://indico.cern.ch/event/556692/contributions/2484253/>, Accessed: 2019-07-06.
- [75] T. Kramer *et al.*, “Considerations for the Injection and Extraction Kicker Systems of a 100 TeV Centre-of-Mass FCC-hh Collider,” In Proc. of International Particle Accelerator Conference 2016 (IPAC’16), Busan, Korea (May 2016), paper WEPVA095, pp. 3901-3904.
- [76] M. J. Barnes, “Kicker Systems,” In Proc. of the CAS - CERN Accelerator School: Beam Injection, Extraction and Transfe, Erice, Italy (March 2017), pp. 229-283.
- [77] M. J. Barnes *et al.*, “Future circular collider injection and extraction kicker topologies and solid state generators,” *Physical Review Accelerators and Beams*, vol. 22, p. 071001, 7 2019.
- [78] D. Woog *et al.*, “Design of an Inductive Adder for the FCC injection kicker magnet pulse generator,” In Proc. of International Particle Accelerator Conference 2017 (IPAC’17), Copenhagen, Denmark (May 2017), paper WEPVA024, pp. 3312-3314.
- [79] D. Woog *et al.*, “First prototype Inductive Adder for the FCC injection,” In Proc. of International Particle Accelerator Conference 2017 (IPAC’17), Vancouver, Canada (May 2018), paper WEPMF076, pp. 2553-2556.
- [80] L. M. Redondo, A. Kandrasyeu, and M. J. Barnes, “Marx Generator Prototype for Kicker Magnets Based on SiC MOSFETs,” *IEEE Transactions on Plasma Science*, vol. 46, pp. pp. 3334–3339, 10 2018.
- [81] J. Holma, *A Pulse Power Modulator with Extremely Flat-top Output Pulses for the Compact Linear Collider at CERN*. PhD thesis, Aalto University, Helsinki, Finland, 11 2015. CERN-THESIS-2014-359.
- [82] M. J. Barnes *et al.*, “Inductive Adders for Replacing Thyatron Based Modulators at CERN,” In Proc. European Conference on Power Electronics and Applications (EPE’15 ECCE Europe), Geneva, Switzerland (September 2017).
- [83] L. Vos, “Longitudinal impedance from ferrite,” tech. rep., CERN, 3 2010. CERN CERN-SL-2000-010 AP.



- 
- [84] D. Woog *et al.*, “Studies towards the new beam screen system of the LHC injection kicker magnet for HL-LHC operation,” In Proc. of International Particle Accelerator Conference 2019 (IPAC’19), Melbourne, Australia (May 2019), paper THPRB074, pp. 3982-3985.
- [85] C. Zannini, *Electromagnetic Simulation of CERN Accelerator Components and Experimental Applications*. PhD thesis, École Polytechnique Fédérale de Lausanne, Switzerland, 3 2013. CERN-THESIS-2013-076.
- [86] Z. Sobiech *et al.*, “Cooling of the LHC injection kicker magnet ferrite yoke: measurements and future proposals,” In Proc. of International Particle Accelerator Conference 2014 (IPAC’14), Dresden, Germany (June 2014), paper MOPME075, pp. 544-546.
- [87] M. J. Barnes *et al.*, “PSpice Analysis of the AGS A10 Kicker magnets,” tech. rep., TRIUMF, 6 2005. TRI-DN-05-15.
- [88] CST Studio Suite, “Understanding Time Domain Meshing in CST MICROWAVE STUDIO,” 7 2010. (available online).
- [89] CST Studio Suite, “HF design and analysis,” 12 2003. (available online).
- [90] CST Studio Suite, “3D EM Simulations,” 7 2009. (available online).
- [91] CST Studio Suite, “CST HPC Webinar for CERN.” Webinar, CERN, Geneva, Switzerland, 11 2018.
- [92] J. Cao, “Initial Permeability and Loss vs Frequency For Various Ceramic Magnetics Ferrites.” Hathaway Consulting Services, 1 2001.
- [93] National Magnetics Group, “CMD10 Datasheet.” <https://www.magneticsgroup.com>. Accessed: 2019-02-30.
- [94] J. A. Dinkel and C. Jensen, “Comparison of Ferrite Materials for Pulse Applications,” In Proc. of IEEE Pulsed Power Conference 1993, Albuquerque, New Mexico, USA (June 1993), pp. 300-303.
- [95] R. J. Hussey and J. Wilson, *Advanced Technical Ceramics Directory and Databook*. Springer Science & Business Media, 9 2012.
- [96] M. J. Barnes, *Private communication*. Date: 2019-02-10.
- [97] V. Vlachodimitropoulos *et al.*, “Longitudinal impedance analysis of an upgraded LHC injection kicker magnet,” In Proc. of International Particle Accelerator Conference 2018 (IPAC’18), Vancouver, Canada (May 2018), paper WEPMK002, pp. 2628-2631.
- [98] M. J. Barnes *et al.*, “Operational Experience of a Prototype LHC Injection Kicker Magnet with a Low SEY Coating and Redistributed Power Deposition,” In Proc. of International Particle Accelerator Conference 2019 (IPAC’19), Melbourne, Australia (May 2019).

## Bibliography

---

- [99] International Standard IEC 60205, "Calculation of the effective parameters of magnetic piece parts."
- [100] S. Arsenyev and B. Salvant, "A method for computing driving and detuning beam coupling impedances of an asymmetric cavity using eigenmode simulations," 4 2019. arXiv:1904.04680.
- [101] CERN Impedance Website, FCC-hh Impedance, <https://impedance.web.cern.ch/impedance/fcchh/impedances.html>, Accessed: 2019-05-30.
- [102] S. Arsenyev, *Private communication*. Date: 2019-04-30.
- [103] A. Adraktas *et al.*, "Influence of conducting serigraphy upon field pulse shape of the SPS extraction kicker systems," In Proc. of International Particle Accelerator Conference 2017 (IPAC'17), Copenhagen, Denmark (May 2017), paper WEPVA099, pp. 3491-3494.
- [104] S. S. Kurennoy, "Using a Ceramic Chamber in Kicker Magnets," In Proc. of Particle Accelerator Conference 1993 (PAC'93), Washington D.C., USA, (May 1993), pp. 3420-3422.
- [105] F. Caspers *et al.*, "RF Screening by Thin Resistive Layers," tech. rep., CERN, 4 1999. LHC Project Report 300.
- [106] M. J. Barnes, "Sparking of Screen Conductors during MKI HV Pre-Conditioning." MKI Strategy Meeting, CERN, Geneva, Switzerland, 6 2012.
- [107] M. J. Barnes *et al.*, "Calculation of Metallization resistivity and thickness for MedAustron kickers," In Proc. of International Particle Accelerator Conference 2011 (IPAC'11), San Sebastian, Spain (September 2011), paper THPO033, pp. 3412-3414.
- [108] K. L. Kaiser, *Electromagnetic compatibility handbook*. CRC press, 2004.
- [109] M. J. Barnes, "Spice models optimized to accurately simulate frequency-dependent impedances," *Personal Engineering & Instrumentation News*, 12 1996.
- [110] F. Caspers *et al.*, "Impedance measurement of the SPS MKE kicker by means of the coaxial wire method," tech. rep., CERN, Geneva, Switzerland, 2 2000. PS/RF/Note-2000-004.
- [111] P. G. Fontollet, *Systèmes de télécommunications*, vol. 17. PPUR presses polytechniques, 1999.
- [112] Heraeus Electronics Official Website, "Products and Solutions." <http://www.heraeus-electronics.com>. Accessed: 2019-08-30.
- [113] Huber+Suhner Official Website, "Radio Frequency Products." <http://www.hubersuhner.com>. Accessed: 2019-08-30.

- 
- [114] M. J. Barnes *et al.*, “Studies of Impedance-Related Improvements of the SPS Injection Kicker System,” In Proc. of International Particle Accelerator Conference 2016 (IPAC’16), Busan, Korea (May 2016), paper THPMW030, pp. 3611-3655.
  - [115] M. J. Barnes and L. Ducimetière, “Vacuum, Ferrite, Cooling, Beam Impedance and Pre-Scrubbing.” MKI Strategy Meeting, CERN, Geneva, Switzerland, 2 2012. CERN.
  - [116] M. J. Barnes *et al.*, “Discussion: Baseline, Mid-term and Long-term Strategy for MKP-L.” MKP Strategy Meeting, CERN, Geneva, Switzerland, 6 2017.
  - [117] M. J. Barnes *et al.*, “Analysis of ferrite heating of the LHC injection kickers and proposals for future reduction of temperature,” In Proc. of International Particle Accelerator Conference 2012 (IPAC’12), New Orleans, Louisiana, USA, (May 2012), paper TUPPR090, pp. 2038-2040.
  - [118] W. Barry, “A Broad-Band, Automated, Stripline Technique for the Simultaneous Measurement of Complex Permittivity and Permeability,” *IEEE Transactions on Microwave Theory and Techniques*, vol. 1, no. 34, p. 80, 1986.
  - [119] C. Vollinger, F. Caspers, and E. Jensen, “Permittivity and Permeability Measurement Methods for Particle Accelerator Related Materials,” In Proc. of International Particle Accelerator Conference 2014 (IPAC’14), Dresden, Germany (May 2014), paper THPRI054, pp. 3893-3895.
  - [120] I. Nathan, *Engineering electromagnetics*, vol. 3. Springer, 3 ed., 2015.
  - [121] F. Fiorillo *et al.*, “Loss and Permeability Dependence on Temperature in Soft Ferrites,” *IEEE Transactions on Magnetics*, vol. 10, no. 45, pp. 4242–4245, 2009.
  - [122] T. Tsutaoka *et al.*, “High Frequency Permeability of Mn-Zn Ferrite and its Composite Materials,” *J. Phys. IV France*, vol. C1, no. 7, p. 557, 1997.



# AGNIESZKA CHMIELIŃSKA

Born: 10.05.1991 ♦ Mobile: +48 609750050 ♦ Mail: agassa91@gmail.com

## EDUCATION

---

### Ph.D. in Accelerator Physics

August 2016 – December 2019

École Polytechnique Fédérale de Lausanne, Lausanne, Switzerland

Department of Accelerator Physics

Advisors: Prof. Dr. Leonid Rivkin (EPFL), Dr. Michael Barnes (CERN)

Thesis: Design and optimization of the beam screen for the FCC-hh injection kicker magnets.

### M.Sc. in Applied Physics

March 2014 – April 2016

AGH University of Science and Technology, Cracow, Poland

Department of Physics and Applied Computer Science

Advisors: Dr. Jan Kulka (AGH-UST), Dr. Mauro Taborelli (CERN)

Thesis: Secondary electron yield at low temperature for selected accelerator materials.

### B.Sc. in Applied Physics

October 2010 – February 2014

AGH University of Science and Technology, Cracow, Poland

Department of Physics and Applied Computer Science

Advisors: Dr. Jan Kulka (AGH-UST), Dr. Paulo Gomes (CERN)

## RESEARCH EXPERIENCE

---

### Doctoral Student in the TE-ABT-PPE section at CERN

August 2016 – August 2019

- Developed a new concept of the spiral beam screen for the FCC-hh injection kicker magnets including theoretical analysis, electromagnetic simulations, beam dynamics studies and experimental verification.
- Novel measurements of electromagnetic properties of ferrites as a function of frequency and temperature.

### Technical Student in the TE-VSC-SCC section at CERN

March 2015 – March 2016

- In charge of measurements of the secondary electron yield (SEY) for selected accelerator materials and analysis of beam conditioning, at room temperature and in cryogenic conditions, to better understand the development of the electron cloud in particle accelerators.

### Trainee Student in the TE-VSC-SCC section at CERN

July 2014 – September 2014

- Investigation of multiple activation of non-evaporable getter (NEG) thin film coatings with elemental composition analysis using X-ray photoelectron spectroscopy (XPS).

### Trainee Student in the TE-VSC-ICM section at CERN

February 2014 – March 2014

- Improvement of the precision of voltage-pressure conversion in PLC and SCADA for the proper ultra-high vacuum maintenance in particle accelerators at CERN.

### Trainee Student in the TE-VSC-ICM section at CERN

July 2013 – September 2013

- PSpice simulations and measurements of the ion pump controller electronic system used for the vacuum control in the Proton Synchrotron Complex (CPS) and in the Large Hadron Collider (LHC) at CERN.

## PROFESSIONAL EXPERTISE

---

- **Accelerator operation, upgrade and commissioning of the LHC injection kicker magnet** (LHC MKI) with particular focus on beam coupling impedance measurements, power deposition distribution measurements and beam based waveform measurements of the LHC MKI.
- **Analysis and optimization of the FCC-hh injection system.** Identifying requirements for beam optics and hardware parameters. Developed a new concept of a spiral beam screen for the kicker magnets with an improved high voltage performance, fast field rise and fall times, good field homogeneity and reduced beam induced power deposition.
- **Studies of the longitudinal and transverse beam stability** in the FCC-hh. Optimization of the beam coupling impedance contribution of the injection kicker magnets to the total impedance budget.
- **Data analysis of the LHC MKI parameters** after a beam dump and a Soft-Start. Implemented new operational validation tool in Python, allowing for real-time performance analysis with the output data synchronized to the CERN Timber database.
- **Electromagnetic simulations and measurements** of beam coupling impedance. Analysis of the magnetic field rise time and field homogeneity of the kicker magnets using the Finite Element Method. Developed numerous scripts to automate data processing, which are shared on CERN gitlab. Helped CERN-IT Group to configure, beta-test and deploy the Linux High Performance Computing cluster.
- **Publishing scientific results both in conference proceedings and in peer-reviewed journal** (IOP Journal of Physics).

## TECHNICAL SKILLS

---

<b>Programming Languages</b>	Python, C/C++, Java, MATLAB
<b>Design Software</b>	CST Particle Studio, CST Microwave Studio, Opera 2D, Cadence PSpice
<b>Project Management</b>	MS Office, LiClipse, Gitlab ( <a href="https://gitlab.cern.ch/achmieli">https://gitlab.cern.ch/achmieli</a> )

## AWARDS AND ACCOMPLISHMENTS

---

**AGH-UST Rector's scholarship** awarded for the highest scores in semestral examinations over the years 2013-2015. Ranked in top 5%.

**The European Union scholarship** received for the academic achievements in years 2010-2015 (offered to the top 20 students at the AGH-UST Department of Physics and Applied Computer Science).

## ACCELERATOR COURSES AND SCHOOLS

---

Longitudinal Beam Dynamics & RF Engineering	Juas 2018, Archamps, France
Accelerator Physics (including MAD-X tutorials)	2018, EPFL, Lausanne, Switzerland
Beam Injection, Extraction and Transfer	CAS 2017, Erice, Sicily
Introduction to Accelerator Physics	CAS 2016, Budapest, Hungary
Physics of Synchrotron Radiation	2015, Jagiellonian University, Cracow, Poland
Accelerators	2014, AGH, Cracow, Poland

## LANGUAGES

---

<b>English:</b> Professional proficiency	<b>French:</b> Intermediate knowledge	<b>Polish:</b> Native speaker
------------------------------------------	---------------------------------------	-------------------------------

## ADDITIONAL INFORMATION:

---

**Personality:** Conscientious, Sociable, Highly motivated, Hardworking

**Hobbies:** Triathlon, Cross country skiing, Mountain hiking